UNIVERSITÉ D'ORLÉANS

ÉCOLE DOCTORALE : Énergie - Matériaux - Sciences de la Terre et de l'Univers

Institut des Sciences de la Terre d'Orléans (ISTO)

THÈSE présentée par :

Nathan Bernard

soutenue le : **7 novembre 2025**

pour obtenir le grade de : **Docteur de l'Université d'Orléans**

Discipline/ Spécialité : Sciences de l'Univers

Dynamics of CO_2 trapping by capillary effects for carbon sequestration : experimental and numerical microfluidics

Dynamique du piégeage par capillarité pour le stockage géologique du CO2 : microfluidique expérimentale et numérique

THÈSE dirigée par :

Mme ROMAN Sophie	Maîtresse de conférences, Université d'Orléans
M. SOULAINE Cyprien	Chargé de recherche CNRS, ISTO

RAPPORTEURS :

M. DE ANNA Pietro	Associate Professor, Université de Lausanne
M. BERHANU Michael	Directeur de recherche CNRS, Laboratoire MSC

JURY :

M. ROUET Jean-Louis	Professeur des universités, Université d'Orléans, **Président du jury**
Mme ROMAN Sophie	Maîtresse de conférences, Université d'Orléans
M. SOULAINE Cyprien	Chargé de recherche CNRS, ISTO
M. BERTIN Henri	Directeur de recherche émérite CNRS, I2M
Mme PROTIERE Suzie	Directrice de recherche CNRS, Institut Jean le Rond d'Alembert
M. DE ANNA Pietro	Associate Professor, Université de Lausanne
M. BERHANU Michael	Directeur de recherche CNRS, Laboratoire MSC

Acknowledgment

Experiments have been performed at Nanoμlab, a nano-microfluidic laboratory in Orléans (France) that is part of the ECCSEL consortium and of the project StoRIES (STorage Research Infrastructure Eco-System) - European Research Infrastructures capacities and services to address European Green Deal challenges. The research leading to these results has received support from the French Agency for Research (Agence Nationale de la Recherche, ANR) through the grant GeoMIME ANR-21-CE50-0038, the Labex Voltaire ANR-10-LABX-100-01. This work was also supported by LAAS-CNRS micro and nanotechnologies platform, a member of the Renatech french national network. This project has received financial support from the CNRS through the MITI interdisciplinary programs and Cellule Energie of CNRS through the project EsCapaDeS.

I want to thank my PhD advisors, Sophie Roman and Cyprien Soulaine, for their invaluable help during this work and for the numerous scientific discussions that shaped this manuscript. Your expert knowledge and continuous support throughout the 3 years of this thesis were invaluable. Thank you both for your kindness and patience.

I would also like to thank my friends and colleagues at the institute for their support and help, in the lab or outside. I am deeply sorry for my rambling about the physics and mathematics of bananas at every lunch break.

Finally, I also want to thank my mom and my dad, who always supported me throughout the years, as well as my brothers, for these late-night gaming sessions.

Résumé étendu

Les mécanismes du stockage géologique du CO_2

Le réchauffement climatique constitue l'un des défis majeurs de ce siècle. L'augmentation de la concentration atmosphérique en CO_2 provoque un renforcement de l'effet de serre, entraînant une hausse des températures moyennes, l'accentuation des phénomènes climatiques extrêmes et des bouleversements écosystémiques. Face à cette crise, plusieurs stratégies sont envisagées pour réduire les émissions nettes de gaz à effet de serre. Parmi elles, la capture et le stockage du carbone, ou CCS, apparaît comme une solution prometteuse et en plein développement, capable de limiter les rejets industriels massifs de CO_2 en les stockant dans le sous-sol. Après capture en sortie d'usine, le CO_2 est injecté dans des réservoirs géologiques profonds, tels que des aquifères salins ou des réservoirs de pétrole et de gaz épuisés. Ces réservoirs sont loin des grandes poches de fluides souterraines de l'imaginaire populaire. Ils sont en fait composés de roches poreuses, dans lesquelles les fluides peuvent circuler et être stockés, et sont déjà saturés en eau. Lors de l'injection de CO_2 dans un réservoir souterrain, on a affaire à un écoulement diphasique, comprenant de l'eau et du CO_2, qui est dans un état supercritique aux conditions de température et de pression du réservoir, dans des milieux poreux.

La réussite du CCS repose sur la fiabilité du stockage à long terme, en effet, tout risque de fuite doit être écarté avant de pouvoir envisager d'implémenter cette solution à large échelle. Or, une fois injecté dans le réservoir, composé de roches poreuses, le CO_2 migre vers le sommet du réservoir sous l'effet de sa flottabilité. La sécurité du stockage dépend donc de plusieurs mécanismes de piégeage (cf. Figure 1) : le piégeage structural sous la couverture imperméable qui recouvre le réservoir, le piégeage par dissolution du CO_2 dans la saumure, le piégeage par minéralisation, où le CO_2 précipite sous forme de carbonates, et enfin le piégeage résiduel. Ce dernier se déroule durant la migration du CO_2, lorsque les forces capillaires immobilisent une partie du CO_2 sous forme de ganglions et de gouttes dispersées dans le milieu poreux. Cette méthode de piégeage joue un rôle essentiel dans la sécurisation du stockage, et il est estimé que ce mécanisme est le garant d'une immobilisation à 100 % du CO_2 injecté [100].

Cependant, le piégeage résiduel reste encore mal compris et son impact sur la capacité de stockage des réservoirs fait débat. La plupart des études s'appuient sur des approches quasi-statiques qui relient saturation résiduelle et pression capillaire, mais ces méthodes ignorent les nombreux phénomènes dynamiques se produisant à l'échelle du pore. Ces lacunes entraînent des incertitudes importantes dans l'évaluation de la capacité effective de stockage. L'objectif de ce travail est donc d'améliorer la compréhension des processus dynamiques contrôlant le piégeage résiduel du CO_2 à l'échelle du pore.

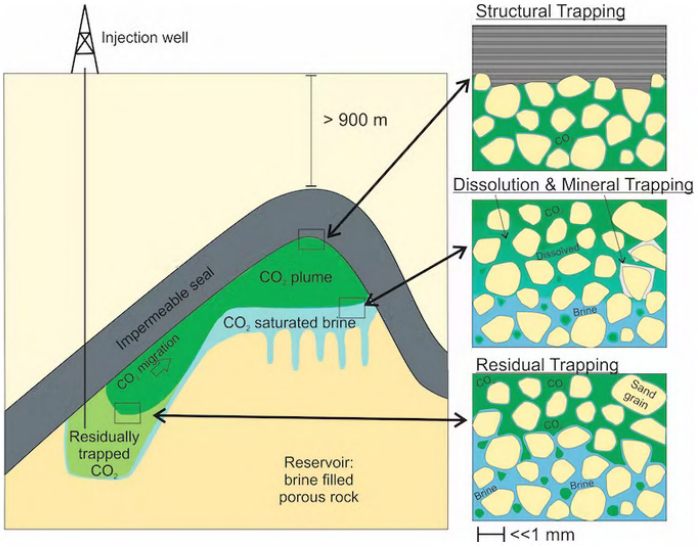

Figure 1: Illustration du stockage géologique du CO_2 et des quatre mécanismes de piégeage: structurel, résiduel, par dissolution et par minéralisation.

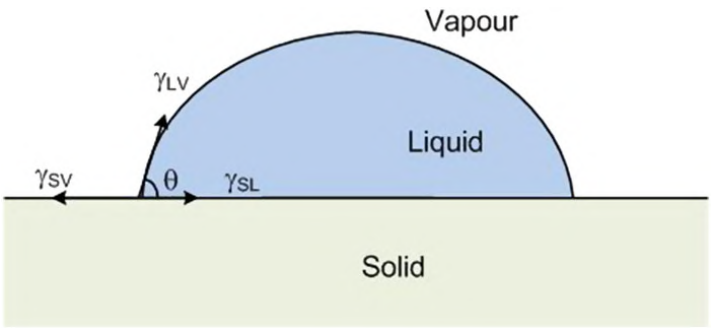

Figure 2: Angle de contact d'une goutte d'eau sur un solide en présence d'air. Ici, l'angle est inférieur à 90°, le liquide mouille le solide, alors que la vapeur est ici le fluide non-mouillant [126].

Ecoulements diphasiques en milieux poreux

Pour mieux comprendre le piégeage du CO_2, il est important d'introduire la notion de mouillabilité du solide composant la roche poreuse. Lorsque deux fluides sont en contact avec le solide, un des deux fluides recouvre préférentiellement le solide. On dit alors que c'est le fluide mouillant, et l'autre phase devient alors le fluide non-mouillant. La mouillabilité peut être caractérisée par l'angle de contact formé par l'interface entre les deux fluides et la surface du solide (cf. Figure 2). On sépare alors l'invasion d'un milieu poreux en deux catégories: le drainage, où un fluide non-mouillant déplace un fluide mouillant, et l'imbibition, où c'est le fluide mouillant qui déplace le fluide non-mouillant.

Le comportement des écoulements diphasiques dans les milieux poreux a fait l'objet de nombreuses recherches au cours des années. Les travaux de Lenormand (1990) ont identifié trois régimes d'écoulement: invasion stable, invasion percolante et invasion en doigts visqueux, en fonction du nombre capillaire et du rapport de vis-

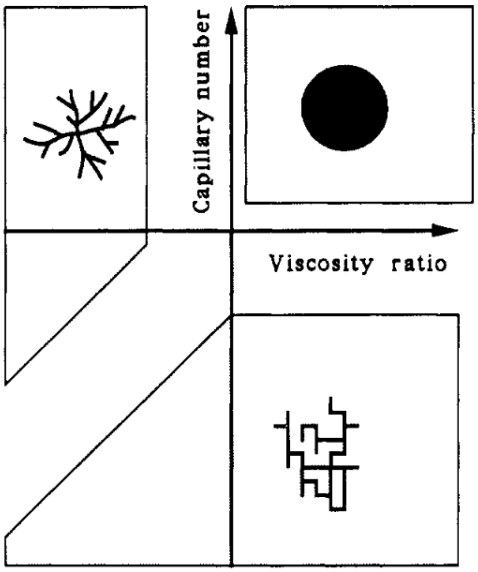

Figure 3: Les trois régimes d'invasion observés pendant le drainage d'un réseau de pores, en fonction du nombre capillaire (en ordonnée) et du rapport de viscosité (en abscisse) [107].

cosité entre les fluides. Ces régimes, illustrés sur la Figure 3, bien que simplificateurs, constituent une base pour comprendre les déplacements immiscibles. Cependant, plusieurs phénomènes propres à l'échelle du pore complexifient la dynamique et modifient la quantité de fluide piégée durant l'écoulement:

- les films de mouillage (films de Bretherton, ou films de coins), présents le long des parois du solide. Ils modifient et altèrent l'écoulement des fluides, jusqu'à modifier la stabilité de l'écoulement,
- le snap-off, qui cause le détachement d'une gouttelette de fluide non-mouillant lors du passage d'une constriction, est un mécanisme important du piégeage résiduel,
- les sauts de Haines, où le ménisque franchit brutalement une constriction, ce qui peut rendre l'inertie, phénomène généralement négligé, localement importante.

Les études expérimentales et numériques de la littérature aboutissent parfois à des conclusions divergentes, notamment sur le rôle de la géométrie et sur les limites entre régimes. Ces incertitudes justifient la mise en place d'approches intégrant à la fois modèles idéalisés et expérimentations contrôlées.

Méthodes de l'étude

Pour étudier les mécanismes dynamiques du piégeage résiduel, cette thèse a mobilisé deux méthodes principales :

- les expériences microfluidiques (cf. Figure 4) : elles permettent d'observer directement les déplacements diphasiques dans des géométries transparentes reproduisant certaines caractéristiques des milieux poreux. Les pores doublets, en

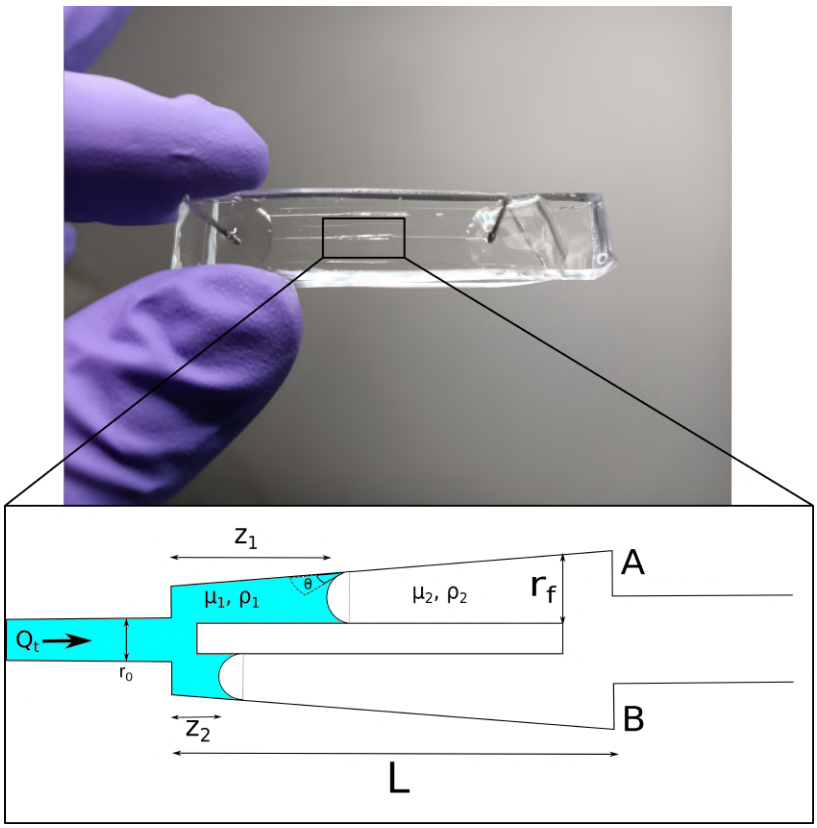

Figure 4: Exemple d'une puce microfluidique utilisée pour les expériences. Ce micromodèle présente une géométrie de pore doublet utilisée dans ce manuscrit.

particulier, offrent une représentation simplifiée mais pertinente des processus d'invasion et de piégeage

- les modèles numériques : la résolution des équations de Navier–Stokes dans des pores doublets permet de simuler précisément la dynamique des interfaces, en incluant des paramètres tels que la tension interfaciale, la viscosité ou encore l'inertie

Ces deux approches se complètent : l'expérimentation valide les modèles, tandis que les simulations explorent des gammes de paramètres difficiles à atteindre en laboratoire.

Piégeage résiduel durant le drainage d'un micromodèle.

Dans un micromodèle reproduisant la structure d'une roche du sous-sol, nous avons mené des expériences de drainage à différents débits, tout en mesurant la quantité de fluide piégée au cours de l'expérience. Ces essais avaient pour objectif d'analyser à la fois les sauts de Haines et la présence généralisée de films mouillants durant le drainage. Nos résultats ont mis en évidence le rôle majeur des sauts de Haines dans l'invasion du milieu poreux, ainsi que l'importance des films mouillants dans la dynamique de l'écoulement (cf. Figure 5).

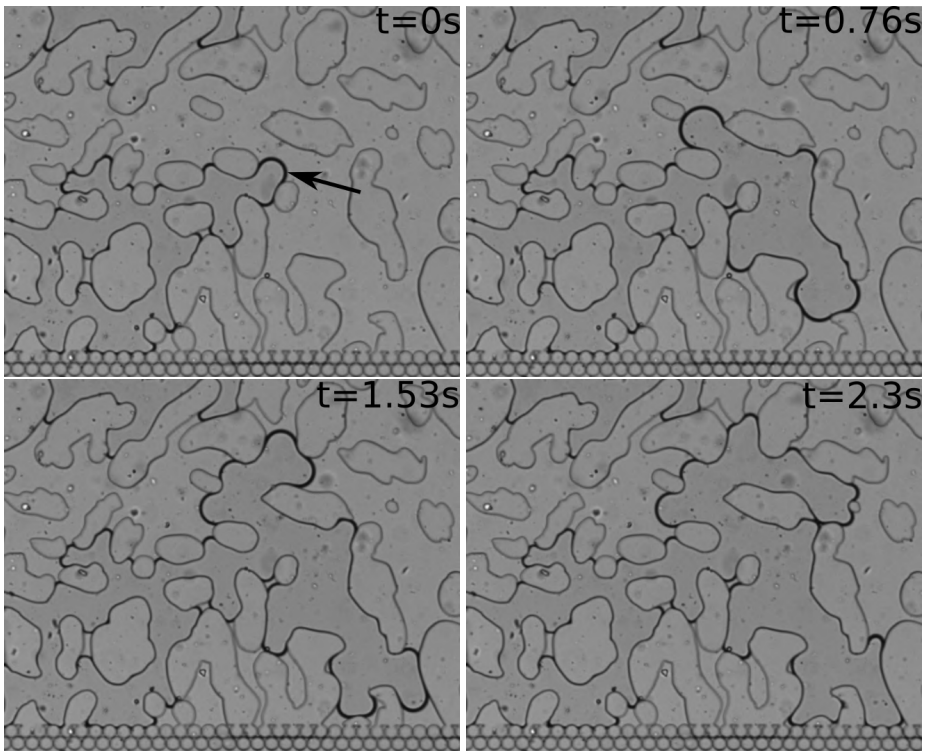

Figure 5: Saut de Haines durant un drainage dans une expérience utilisant un micromodèle complexe. À t=0 s, un des ménisques présents se déstabilise, ce qui conduit à une invasion en cascade des pores suivants, jusqu'à ce que les interfaces se stabilisent, à t=2,3 s. Durant ce saut, la vitesse est un ordre de grandeur supérieure à la vitesse moyenne de l'invasion.

Face à la complexité de l'invasion, nous montrons aussi le besoin d'étudier ces phénomènes au niveau des pores, plus particulièrement au niveau de l'embranchement entre les pores.

Impact des films de mouillage sur la stabilité des écoulements diphasiques

Lors de l'écoulement des fluides, que ce soit lors de l'imbibition ou du drainage, des films de fluide mouillant engendrés par les forces capillaires apparaissent le long des parois du solide. Ces films sont souvent négligés lors des études en pores doublets, par souci de simplicité.

Lors de cette étude expérimentale et théorique, nous avons étudié une instabilité causée par la compétition entre les forces capillaires et les forces visqueuses. Nous avons montré que la présence ou non de cette instabilité impacte grandement la quantité de fluide piégée dans un pore doublet. Surtout, nous avons mis en lumière l'impact des films mouillants sur l'écoulement des fluides dans ces modèles, et comment ils altèrent les conditions d'apparition de l'instabilité. Les résultats de cette étude montrent que :

- les films peuvent agir comme des lubrifiants favorisant la propagation de la phase non mouillante, ou au contraire comme des freins selon le rapport de viscosité,

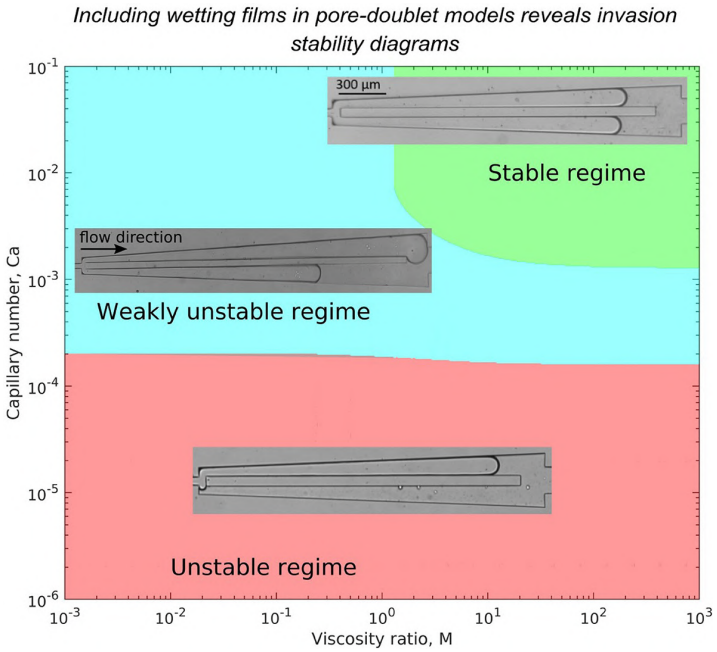

Figure 6: Régimes de stabilité dans un pore doublet divergent en fonction du nombre capillaire et du rapport de viscosité. Les modèles théoriques ne valident les expériences que si les films mouillants sont pris en compte.

- ces films modifient la stabilité du drainage dans un pore doublet (cf. Figure 6),
- leur rôle doit être pris en compte pour prédire correctement la saturation résiduelle.

La prise en compte des films de mouillage permet de réconcilier les modèles théoriques avec certaines observations expérimentales.

Impact de l'inertie causée par les sauts de Haines sur l'invasion

Les sauts de Haines sont des mouvements rapides des ménisques entre les deux fluides. Ils apparaissent majoritairement lors du drainage, lorsqu'un ménisque est dans une gorge (la constriction de faible rayon entre deux pores). Durant le drainage, la pression dans le fluide non-mouillant ainsi que la pression capillaire augmentent, ce qui force la courbure du ménisque à augmenter en conséquence, selon la loi de Young-Laplace. Or, à un certain point, la géométrie de la constriction ne permet plus au ménisque d'augmenter sa courbure. On observe une instabilité, où le ménisque 'saute' pour atteindre la prochaine configuration stable. Ce saut est souvent très rapide, et il est commun qu'un ou plusieurs pores soient envahis.

Ces sauts de Haines sont des événements irréversibles d'un point de vue thermodynamique et sont responsables d'une partie importante de l'hystérésis observée durant les cycles de drainage et d'imbibition. Lors de ces sauts, la vitesse du ménisque peut atteindre des vitesses jusqu'à trois ordres de grandeur supérieures à la vitesse moyenne d'invasion. Classiquement, ces événements sont analysés uniquement sous l'angle des forces capillaires, mais étant donné leurs vitesses, les forces inertielles, habituellement négligées, peuvent devenir importantes et altérer l'écoulement.

Nos travaux montrent que :

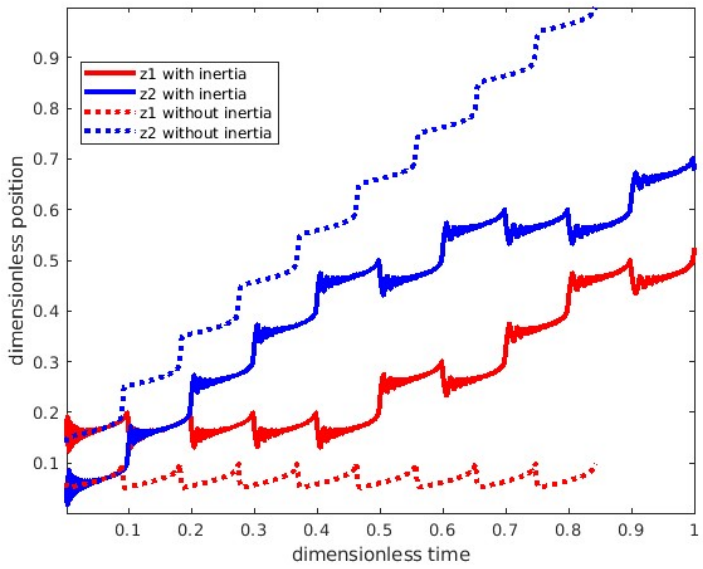

Figure 7: Simulation numérique de la dynamique des ménisques dans un pore doublet dans le régime capillaire. Les courbes en pointillés présentent l'évolution des ménisques dans le cas où l'inertie est négligée. Les courbes en continu correspondent au modèle développé qui prend en compte l'inertie. On voit que la prise en compte de l'inertie est importante pour prédire correctement la quantité de fluide piégé.

- des oscillations de l'interface, typiquement associées aux effets inertiels, peuvent apparaître lors des sauts de Haines,
- ces oscillations influencent la succession des sauts en 'poussant' les interfaces dans les gorges séparant les pores, ce qui mène potentiellement à un autre saut de Haines. Cela altère l'ordre d'invasion des pores, et donc la répartition finale des fluides piégés (cf. Figure 7).

Ainsi, l'inertie, bien que souvent ignorée, joue un rôle non négligeable dans le contrôle du piégeage résiduel.

Ce phénomène est plus important dans de gros pores, qui présentent un volume de fluide plus important, ce qui entraîne une plus grande inertie lors du saut. Les expériences réalisées n'ont pas permis de mettre en lumière ces oscillations dues à l'inertie, mais de nouveaux micromodèles ont été conçus à l'aide du modèle numérique développé dans cette étude. Ces nouveaux pores doublets nous permettront de confirmer nos résultats théoriques à l'aide d'expériences microfluidiques. Le modèle numérique sera alors utilisé pour explorer une gamme plus importante de conditions et de déterminer sous quelles conditions les effets inertiels impactent le piégeage résiduel.

Altération de la mouillabilité de la calcite en présence d'eau et de CO_2

La mouillabilité des surfaces minérales est un paramètre crucial pour le piégeage du CO_2. L'angle de contact formé par l'interface fluide-fluide avec le solide est une caractéristique importante pour tous nos travaux qui ont été conduits jusqu'ici. Si la valeur

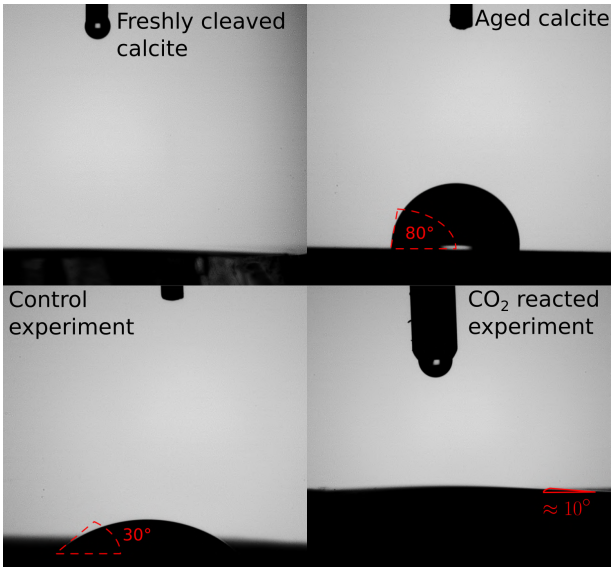

Figure 8: Mesures d'angle de contact entre une surface de calcite fraîchement clivée, une surface de calcite qui a été altérée après plusieurs mois en contact avec l'atmosphère, une surface issue d'une expérience témoin sans CO_2 et enfin une surface issue d'une expérience avec du CO_2. La présence de CO_2 pendant la réaction diminue l'angle de contact entre l'eau et la calcite, ce qui s'explique par l'augmentation de la rugosité [213].

de cet angle change dans le temps, le comportement du système peut aussi évoluer, et du CO_2 qui était piégé dans des pores peut alors se libérer et potentiellement se frayer un chemin jusqu'à la surface. Si ce changement est vraiment important, c'est-à-dire si l'angle de contact entre l'eau et la roche, qui est usuellement inférieur à 90°, devient supérieur à 90°, alors le CO_2 devient le fluide mouillant du système. Ce phénomène, appelé renversement de mouillabilité, peut avoir des conséquences catastrophiques sur le stockage du CO_2. En effet, si la roche couverture, qui est responsable du piégeage structurel au sommet du réservoir, subit ce renversement de la mouillabilité, elle a plus de chances de laisser fuir le CO_2, qui peut ensuite se retrouver dans l'atmosphère, compromettant l'intégrité du stockage.

Or, la littérature indique que la présence de CO_2 et de saumure au contact de certains minéraux peut altérer la mouillabilité de ces derniers. Ceci nous a conduits à réaliser nos propres expériences, en exposant de la calcite, l'un des principaux minéraux du sous-sol, à de la saumure et à de la CO_2 à 100 bar et 65 °C. Ces valeurs représentent les conditions de pression et de température moyennes des réservoirs considérés pour le stockage du CO_2. Ces expériences ont eu lieu dans des autoclaves fermés, contenant de l'eau, une quantité variable de CO_2, et de l'argon, un gaz noble, utilisé pour atteindre la pression de 100 bar. La pression partielle de CO_2 dans l'autoclave varie entre 0 bar (expérience sans CO_2, utilisée comme témoin) et 10 bar.

Les échantillons de calcite ont été analysés avant et après les expériences afin de mesurer les changements de surface qui se sont opérés pendant la réaction dans l'autoclave. Ces techniques d'analyse sont au nombre de trois: les mesures d'angle de contact (cf. Figure 8), pour déterminer l'évolution de la mouillabilité, la microscopie par force atomique, pour observer les changements de topologie de surface, et la spectroscopie Raman, pour suivre la composition chimique de l'échantillon. Ces analyses nous ont appris que :

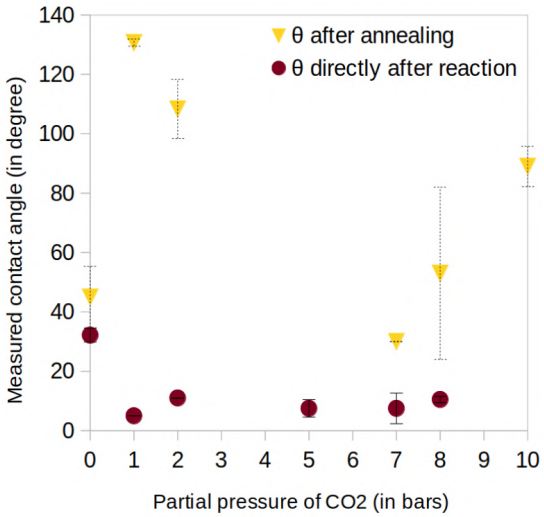

Figure 9: Résultats expérimentaux des mesures d'angles de contact.

- notre échantillon ne comporte que de la calcite: il n'y a pas de précipitation d'un autre minéral à la surface de l'échantillon durant la réaction,
- le CO_2 attaque la surface, augmentant la rugosité de l'échantillon,
- cette rugosité rend la surface plus hydrophile, conformément à la théorie de Wenzel.

Ce résultat va à l'opposé de la majorité de la littérature, qui conclut généralement à une hydrophobie accrue après contact avec du CO_2 et de l'eau. Mais ce genre d'étude n'a jamais été réalisé sur de la calcite avant nos travaux, et les mécanismes généralement avancés pour expliquer cette augmentation du caractère hydrophobe (altération des liaisons chimiques contenant du silicium) ne s'appliquent pas à notre système. Par ailleurs, des tests complémentaires ont montré que la déshydratation de la calcite après exposition au CO_2 et à l'eau induit une augmentation drastique de l'angle de contact entre la calcite et l'eau, menant à un renversement de la mouillabilité (cf. Figure 9). Nous avons proposé une explication topologique de ce phénomène, mais des tests supplémentaires sont requis pour mieux le comprendre. Des expériences plus complexes avec davantage d'espèces chimiques dans la saumure sont aussi prévues, afin d'identifier les phases qui pourraient se former à la surface de l'échantillon et de mesurer leur impact sur la mouillabilité.

Conclusions de la thèse

Les trois chapitres principaux sur l'impact des films mouillants, de l'inertie et de l'altération de la mouillabilité sur la dynamique de l'écoulement diphasique mettent en lumière l'importance des phénomènes dynamiques et physico-chimiques souvent négligés dans l'analyse du piégeage résiduel. Les approches statiques, telles que les courbes de pression capillaire/saturation, sont insuffisantes pour pleinement comprendre le piégeage résiduel. Ce dernier ne peut donc être correctement prédit qu'en intégrant inertie, films de mouillage et altération de la mouillabilité. Cette étude a pour l'instant été menée à l'échelle du pore, et une démarche multi-échelle, couplant ob-

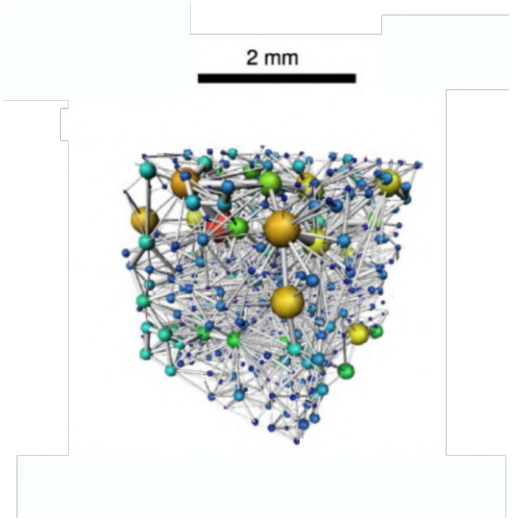

Figure 10: Exemple d'un réseau de pores obtenu par scanner à rayons X. La géométrie des pores a été simplifiée pour ne garder que la topologie. En utilisant des lois décrivant l'écoulement dans les canaux reliant les pores, telle que la loi d'Hagen-Poiseuille, il est possible de décrire l'écoulement de fluide dans ce réseau [29].

servations locales et modèles globaux, est nécessaire pour transposer nos résultats à l'échelle du réservoir.

Perspectives de ces travaux

Plusieurs pistes émergent pour poursuivre et finaliser ces travaux. Tout d'abord, des expériences complémentaires doivent être menées pour vérifier notre modèle prenant en compte l'inertie dans les pores-doublets. Une fois ce modèle vérifié, nous voulons combiner tous nos travaux sur les écoulements diphasiques en pore doublet, afin de créer un modèle qui permette de prédire la dynamique des ménisques dans des géométries variées, tout en prenant en compte les films mouillants, l'inertie et des propriétés de mouillabilité variables.

Ce modèle pourra ensuite servir au développement d'un modèle de réseau de pores (cf. Figure 10) permettant de simuler des écoulements diphasiques dans un milieu poreux sur une échelle de quelques millimètres.

Concernant l'altération de la mouillabilité de la calcite, il nous faut élargir les protocoles expérimentaux à des systèmes chimiques plus réalistes et des techniques d'analyse plus poussées pour l'étude de l'altération de la mouillabilité

En révélant la complexité et l'interdépendance de ces mécanismes, ce travail montre que le piégeage résiduel ne peut être décrit par des approches statiques simplifiées. Il ouvre la voie à des modèles plus complets, capables de prédire avec plus de fiabilité la sécurité du stockage de CO_2 à long terme.

Ainsi, ce travail contribue à l'effort collectif visant à faire du CCS une solution robuste et efficace pour atténuer le changement climatique.

Contents

Chapter 1

Introduction

In this chapter, we explore the principles of carbon capture and storage (CCS), its role in the energy transition, its underlying mechanisms, and current real-world implementations. Then, we focus on the potential of residual trapping for CCS. Finally, the objectives of the PhD are introduced.

1.1 The role of carbon capture and storage in the energy transition

1.1.1 Principles and storage potential

The ongoing global warming is one of, if not the most challenging, problems facing humanity in the current century. The non-stop use of fossil fuels and the huge amount of CO_2 that they release into our very thin atmosphere (99% of the gas around our planet is below 80 km of altitude) has drastically increased the concentration of carbon dioxide in the air. This year, it has reached 420 ppm, which is 50% more than the pre-industrial level, which was stable at around 280 ppm for 6000 years, according to the US National Oceanic and Atmospheric Administration [216], see Fig. 1.1. The elevated concentration of CO_2 in the atmosphere significantly amplifies the greenhouse effect, leading to a rise in Earth's average temperature. This warming triggers a range of harmful consequences, including the melting of polar ice caps, desertification, more frequent and intense extreme weather events, and increased evolutionary pressure that accelerates the extinction of plant and animal species.

According to the latest IPCC report [7], limiting global warming to a 'still bad but not disastrous' 2°C would require reducing the CO_2 emissions to a net zero by the second half of the 21st century. Despite the continuous improvement in carbon-neutral energy, like solar, wind, hydraulic, or nuclear power, some carbon sources are still irreducible, such as gas processing, chemical, fertilizer, cement, iron, and steel production. This is due to the nature of these industries, where CO_2 is a by-product of the chemical reactions. For example, the cement production requires calcium carbonate ($CaCO_3$) to be turned into lime (CaO). This reaction releases nearly 900 kg of carbon dioxide per ton of lime, without taking into account the energy used for heating the calcium carbonate, a step necessary for the reaction to occur. Similarly, iron and steel emit a lot of CO_2 in the atmosphere when the oxide is reduced to produce iron, or when iron is enriched in carbon to form steel. With the constantly growing need for cement and steel in construction, these CO_2 emissions have reached an astonishing 13% of the total CO_2 emissions in the world or 5 Gt per year!

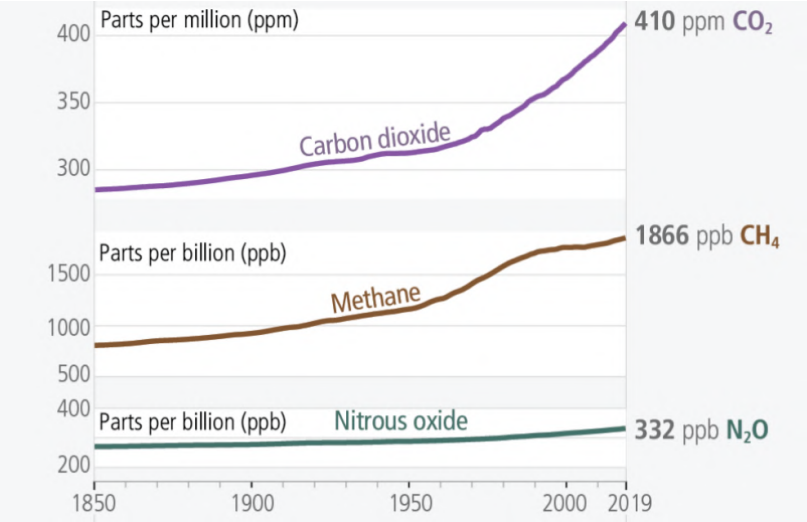

Figure 1.1: Evolution of the concentrations of greenhouse gases in the atmosphere since 1850 [7].

Until other strategies are developed to reduce the emissions of CO_2, such as green steel, where H_2 is used to reduce the iron oxide, Carbon Capture and Storage (CCS) is the only solution to reduce the emissions for these industries. This technique relies on the capture of CO_2 from the emissions of a power plant/industrial facility, or directly from the air. This captured CO_2 is then injected underground in a geological formation, like a saline aquifer or depleted oil/gas reservoirs, where the CO_2 will be trapped and unable to escape. According to the European Commission, this technique is essential to reach carbon neutrality by 2050, and the EU aims at storing at least 50 Mt of CO_2 per year by 2030.

CCS faces several challenges that hinder its large-scale implementation. Estimating the storage potential of the underground formation is hard, and local communities often oppose projects because of perceived risks such as induced seismicity or CO_2 leakage. Economic incentives are also weak: capturing, transporting, and storing one ton of CO_2 costs between €80 and €150 [32], with the capture being the most expensive stage of the process. Meanwhile, exceeding legal emission limits costs only between €20 and €100 per ton of CO_2 on the European carbon market.

Although CCS is poised to play a crucial role in the energy transition, we still lack robust methods to estimate reservoir storage capacity, quantify leakage risks, determine optimal injection strategies that maximize stored CO_2, and reduce overall costs. Answering these questions requires a closer examination of the physical processes that occur inside a geological formation when CO_2 is injected.

1.1.2 Underground storage of CO_2

1.1.2.1 Thermodynamics of CO_2

For most storage sites, the formation of interest should be at least 900 m underground. This is a requirement for the pressure and the temperature of the formation to be clearly above 73 bar and 31 °C. This pressure-temperature condition is the supercritical point of CO_2, where it is neither liquid nor gas, but in a state sharing the properties of both [186], see Fig. 1.2. This supercritical CO_2 (also referred to as $scCO_2$) has a much higher density than gaseous CO_2, increasing the amount of carbon dioxide that can be

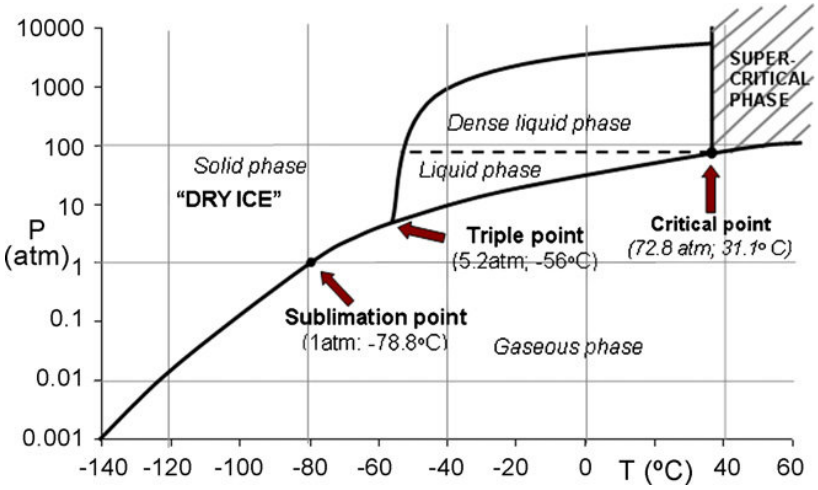

Figure 1.2: Phase diagram of CO_2, from Mazzoldi and Hill (2008).

stored in the same volume of reservoir, see Fig. 1.3. For an aquifer, the salinity of the brine must also be above 1 $g \cdot L^{-1}$, making sure that no usable water is used for the storage of CO_2. The geological context must also be examined to avoid leaks through faults or geothermal wells.

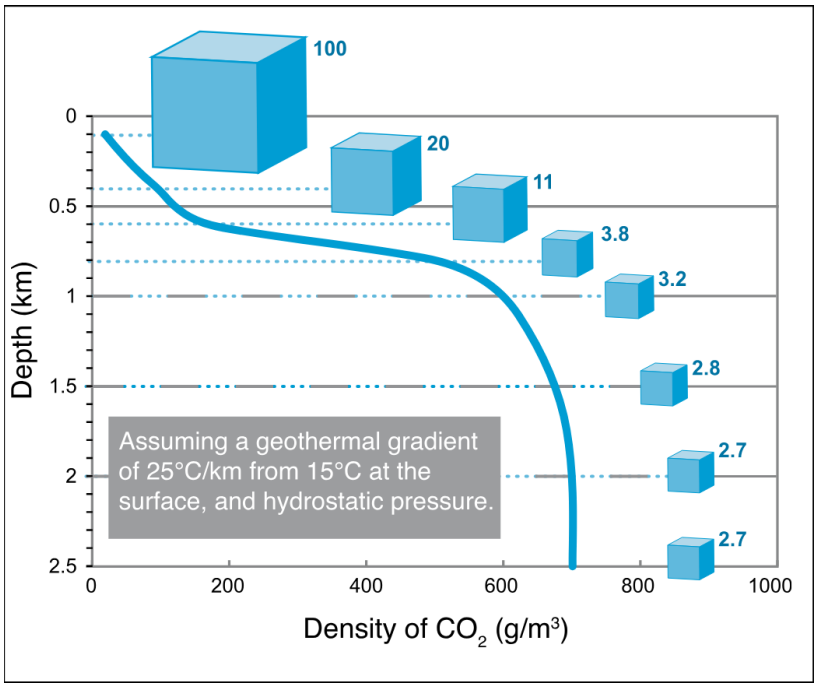

Figure 1.3: Evolution of CO_2 density with depth, assuming pure CO_2. The cubes and the numbers in blue represent the relative volume occupied by a constant mass of gas at different depths, from B.Metz et al. (2005).

Once a suitable reservoir is identified, supercritical CO_2 ($scCO_2$) is injected, displacing the native fluid, typically brine. During this process, the brine and $scCO_2$ remain as two immiscible phases, each with distinct physical properties such as den-

sity and viscosity. Under typical storage conditions, the density of $scCO_2$ does not exceed 700 $kg \cdot m^{-3}$ (see Fig. 1.3), whereas brine has a higher density ranging from 1000 to 1300 $kg \cdot m^{-3}$, depending on its salinity [143]. Due to this density contrast, $scCO_2$ tends to migrate upward within the reservoir, forming a buoyant plume. Four key mechanisms act to prevent the CO_2 from reaching the surface, see Fig. 1.4 [100].

1.1.2.2 Trapping mechanisms

Structural trapping It occurs when the $scCO_2$ rises in the reservoir and encounters the impermeable top layer of the geological formation known as the caprock. This stops the plume from reaching the surface. This layer can be, for example, made out of clays, known for their very low permeability. This mechanism occurs quickly after the injection and immobilizes the largest part of the CO_2 (see Fig. 1.5), but its efficiency relies on the integrity of this impermeable layer. Faults created by drilling, seismic activities, or overpressure of the reservoir might break this layer, leading to a leak of CO_2.

Residual trapping This mechanism is caused by the capillary force that creates droplets of CO_2 during the migration of the fluids. These droplets, or ganglia, can then be immobilized in the porous matrix by capillary forces. The contribution of this mechanism is the hardest to estimate, as many parameters change the amount of fluid trapped, and the droplets have the potential to reconnect to the bulk of the CO_2. Residual trapping is a complex topic and will be discussed in further detail in the following sections.

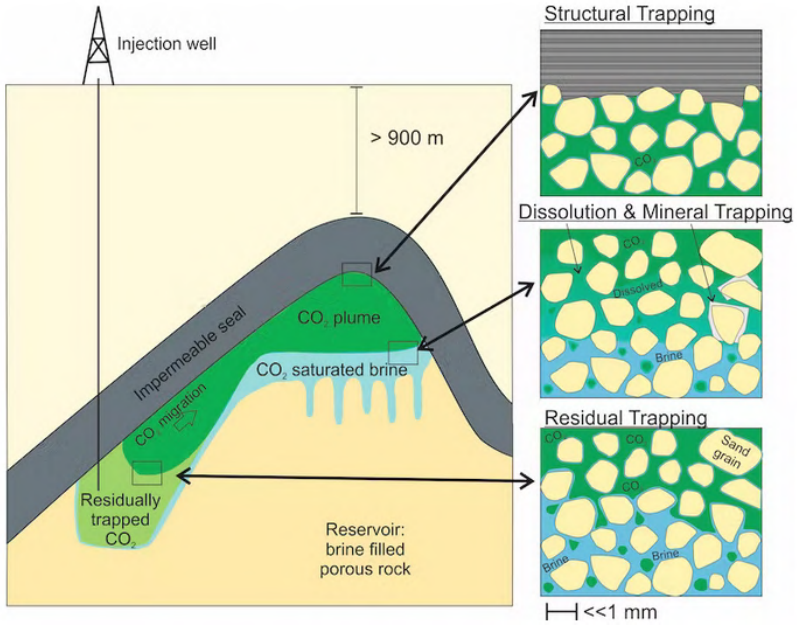

Figure 1.4: Illustration of CCS, with the four mechanisms that trap CO_2 underground, from the conversation.com.

Solubility trapping Dissolution of CO_2 from the supercritical phase into the aqueous phase happens on a longer time scale than the structural and residual trapping. Despite their immiscible nature, $scCO_2$ can slowly dissolve into the brine. This leads to the saturation in CO_2 of the brine at the interface between both fluids. Or, fresh

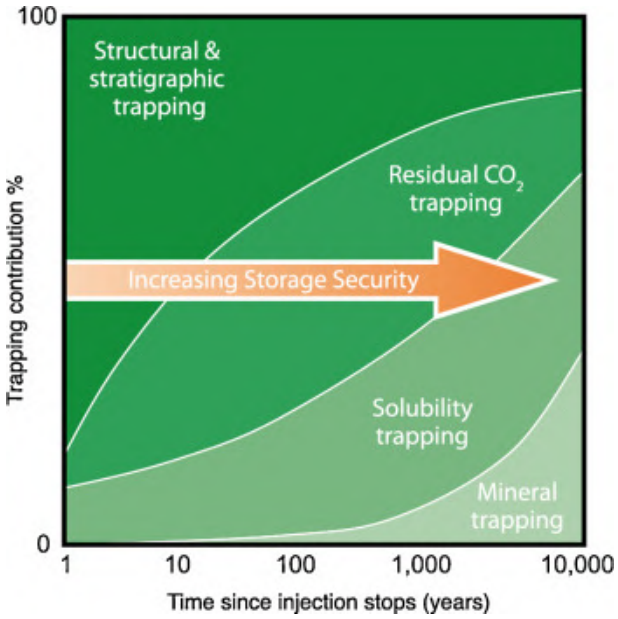

Figure 1.5: Evolution of the relative importance of each trapping mechanism with time from the stopping of the injection, from Kelemen et al. (2019).

brine is less dense than the CO_2-saturated brine. This leads to a convection cell, where the CO_2 saturated brine sinks at the bottom of the aquifer, taking the carbon further away from the surface, see Fig. 1.4.

Mineral trapping The dissolved CO_2 presents itself as carbonate ions (CO_3^{2-}, HCO_3^-, or H_2CO_3 depending on the pH of the brine), which can react with bivalent ions from the brine, such as Ca^{2+} or Mg^{2+} to form minerals such as calcite ($CaCO_3$) or magnesite ($MgCO_3$), trapping carbon for geological times. This is the safest form of trapping, as nothing short of a volcanic eruption can free the CO_2 from the minerals, but it is also the slowest trapping mechanism, see Fig. 1.5.

CO_2 trapping is a complex and dynamic process. A deeper understanding of the efficiency and timescales of these processes is essential for improving our ability to accurately evaluate a reservoir's capacity and to design injection protocols that maximize storage efficiency while minimizing the risk of leakage, ultimately accelerating the development of CCS.

1.1.3 Existing CCS projects

In 2024, according to the Global CCS Institute, 50 carbon capture and storage (CCS) facilities were in operation, collectively storing 51 million tonnes (Mt) of CO_2 per year. An additional 44 facilities are under construction, with a combined storage capacity of 51 Mt of CO_2 annually. Beyond these, more than 500 CCS projects are in various stages of development, aiming to increase total storage capacity to 416 Mt per year, see Fig. 1.6. This rapid expansion reflects growing collaboration between the public and private sectors, along with significant national investments aimed at reducing net greenhouse gas emissions. Among the operating facilities, four of them operate by directly capturing the CO_2 in the air, in a process known as Direct Air Capture (DAC).

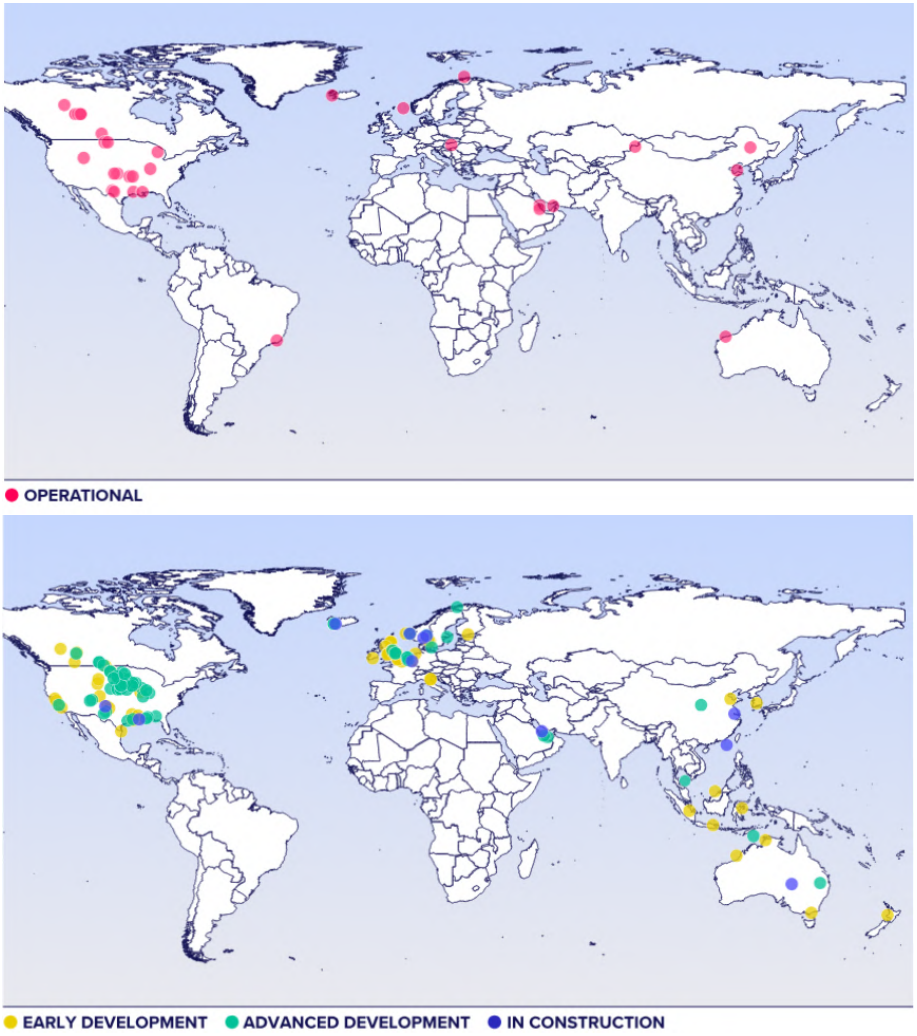

Figure 1.6: World map of CCS facilities at various stages of development in 2022, from the 2022 Status Report of the Global CCS Institute.

The oldest CCS plant still in operation is the Occidental Terrell facility, which started operation in 1972 in the United States, capturing 0.5 Mt of CO_2 per year for enhanced oil recovery (EOR). The idea behind EOR is to inject a fluid, here CO_2, to increase the production of hydrocarbon at another well. Other noteworthy projects are the Sleipner project, opened in Norway in 1996, which is the first offshore CCS facility, but also the first where CO_2 is injected purely for storage, and not to enhance the recovery of hydrocarbons. It is currently storing CO_2 at a rate of 1 Mt per year. In France, a pilot CCS facility was created in the Lacq basin in southwest France. It was used between 2010 and 2013 to inject 51 kt of CO_2 into the Rousse formation, a depleted gas reservoir. This pilot, launched by Total, is still monitored, and its results are used for the development of new, bigger storage facilities in France and Europe.

We also need to mention the Carbfix project in Iceland, which is certainly one of the most famous CCS projects in Europe. Iceland is part of the Mid-Atlantic Ridge, and its underground consists only of basaltic rocks, which means that no sedimentary basins (deep aquifers or depleted reservoirs) are available. It is thus impossible to

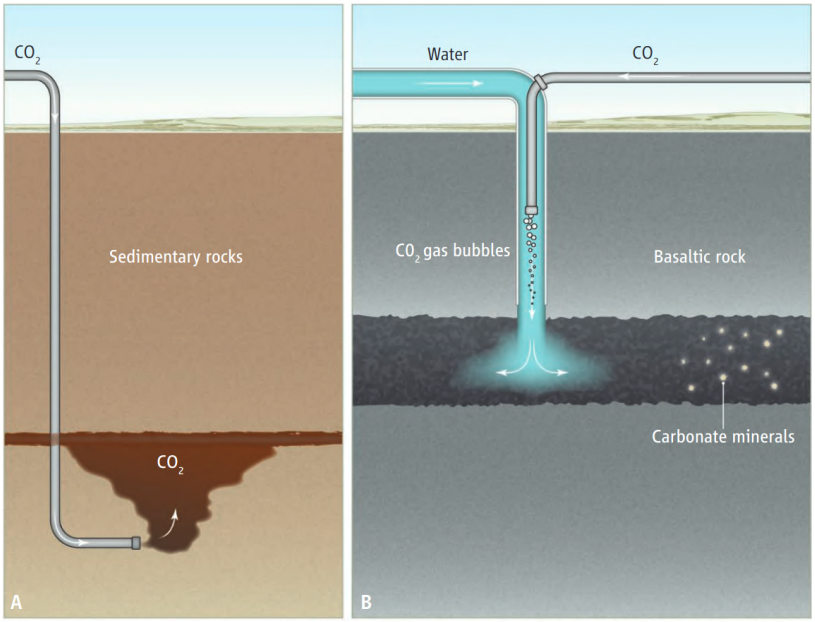

Figure 1.7: (A) Carbon storage in sedimentary rocks, with an impermeable layer at the top of the formation. The structural, residual, dissolution and mineralization trapping prevent the injected $scCO_2$ from escaping the formation. (B) Carbon storage as designed for the Carbfix project, where the CO_2 is co-injected with seawater. Only the dissolution trapping (CO_2-saturated brine being denser than the formation brine) and mineralization trapping stop the CO_2 from reaching the surface [69]. Figure from Gislason and Oelkers (2014).

inject CO_2 in supercritical form, as no structural trapping can occur. The idea that made Carbfix so famous was to inject CO_2 not in its pure form, but already dissolved in seawater. The CO_2 saturated brine, denser than the formation brine, sinks in the formation (dissolution trapping), and its acidic nature, caused by the CO_2 lead to the dissolution of the basaltic rocks, creating bivalent cations favoring the precipitation of CO_2 containing minerals, such as calcite, siderite or magnesite [69], see Fig. 1.7. This leads to most of the carbon being fixed in minerals in less than a year underground via mineral trapping. This project, initially started as an experiment, showed its feasibility, and is still ongoing now, with the recent addition of the world's largest DAC plant, leading to a capture rate of 0.03 Mt per year. This relatively small capture capacity is caused by the need to pump more fluids to capture the same amount of CO_2, leading to lower efficiency. Despite this, more facilities using the co-injection of CO_2 and water are under development in the world. As previously discussed, carbon capture and storage (CCS) plays a vital role in mitigating global warming, and is currently seeing an important growth, notably because of government investments.

1.1.4 Assessment of storage potential

CCS has the potential to store around 10,000 Gt of CO_2, or 250 years' worth of the current global emissions [100] [16]. Recently, the EVASTOCO2, a project coordinated by the BRGM (Bureau de Recherches Géologiques et Minières), reported on the CO_2 storage capacity of metropolitan France. They concluded that 3.7 Gt of CO_2 could be stored in the different sedimentary basins [63]. To estimate the storage capacity, two

main calculation methods are used.

Storage assessment using the Storage Efficiency Factor The first method takes into account the volume of the reservoir considered (Surface area ×Depth× porosity of the formation), data acquired through a geological survey, the density of CO_2 (which depends on pressure and temperature of the reservoir), as well as the Storage Efficiency Factor (SEF). This represents the percentage of the formation volume that is occupied by the CO_2 after injection. Typical values are between 4% and 15%. The calculation reads as [17, 13],

$$m_{CO2} = V_{res} \times \rho_{CO2} \times SEF. \tag{1.1}$$

The SEF is based on several real-life studies of CO_2 storage in aquifers, as well as on some numerical simulations of CO_2 injection. It depends on certain geological parameters, such as the type of rocks constituting the reservoir, the structure of the reservoir,... The SEF is known to be poorly accurate, and to over-predict the actual amount of storable CO_2.

Storage assessment using compressibility and reservoir confinement The second method relies more on physical considerations, and considers that the injection of CO_2 increases the pressure in the reservoir, compressing the rocks and water of the aquifer. This overpressure will also compress the neighboring formation, leaving more space for the CO_2. This calculation reads as [17, 13],

$$m_{CO2} = V_{res} \times \rho_{CO2} \times Ct \times \Delta P \times \left(1 + 2\overline{W_D}(t_D)\right) \tag{1.2}$$

with C_t representing the combined compressibility of the reservoir and the brine, ΔP the overpressure in the reservoir, typically around 20% above the initial formation pressure, and $\left(1 + 2\overline{W_D}(t_D)\right)$ the edge correction, taking into account the effect of overpressure on the neighboring reservoirs. In this method, two parameters introduce approximations. The first is the overpressure, which cannot be increased excessively without risking the fracture of the impermeable caprock. Second, the edge corrector depends on the permeability of the formation and whether the aquifer is enclosed or open to one or more aquifers surrounding it. This leads, again, to some uncertainties on the amount of CO_2 that can be stored, and in general, it gives a more conservative estimate than the first method. Nevertheless, accurate prediction of the amount of carbon that can be stored in a given formation is hard to assess, and we have very little feedback on the behavior of the stored CO_2 in the long term.

These two methods only take into account the structurally trapped CO_2 and completely ignore the three other mechanisms that are known to store significant amounts of CO_2. Being able to take all four of the trapping mechanisms into account would greatly improve our assessment capacity, aiding the development of the CCS technology.

1.2 The potential of residual trapping for CCS

As we have seen in the previous sections, a better understanding of the CO_2 trapping mechanisms could lead to significant improvement in the safety and capacity of the underground carbon storage. In this section, we focus more in depth on residual trapping and how it has significant potential to enhance the storage capacity.

1.2.1 Residual trapping for storing CO_2

Residual/capillary trapping is one of the main mechanisms that traps CO_2 underground. While dissolution and mineralization occur on the long time scale (on the hundreds to thousands of years), residual trapping occurs as soon as the injection starts.

In porous media, the two-phase flow is greatly impacted by capillary forces, which lead to the formation of ganglia that can then become immobilized in the matrix. This plays a crucial role in the distribution of CO_2 in the reservoir, and thus impacts the other trapping mechanisms. Indeed, the trapping of ganglia during the rise of the CO_2 plume reduces the amount of CO_2 under the impermeable layer, diminishing the pressure on the caprock and the risk of leaks. The presence of the trapped droplets surrounded by brine also increases the contact area between both fluids, increasing the mass transfer of CO_2 into brine, speeding the dissolution trapping.

Moreover, residual trapping is one of the trapping mechanisms that can be influenced by how we inject the CO_2 inside the formation. Alternated injection between CO_2 and water could help increase the amount of capillary trapping [76]. Additives can also be added to the injected CO_2 to alter its properties and enhance the trapping. One example of this is nanoparticles, used to improve the injection by reducing the viscous instability (see Chapter. 3) and to prevent the reconnection of the trapped ganglia to the bulk of the CO_2 [4]. But some other impurities in the CO_2, such as O_2 or N_2 reduce the trapping capacity by reducing the density of the supercritical phase [100]. It is shown that the mechanisms of residual trapping could be exploited to improve the overall effectiveness of the injection process and achieve immobilization of 100 % of the CO_2 in a plume over time, according to Kumar et al. (2020).

One of the limitations of residual trapping is that it is not always permanent. Under certain conditions, trapped CO_2 ganglia can become remobilized. A notable example is Ostwald ripening, in which smaller CO_2 droplets dissolve and redeposit onto larger ones. This process is driven by capillary pressure, which energetically favors the growth of larger droplets over smaller ones [67, 35]. As these larger ganglia grow, they experience increased buoyant forces that may eventually overcome the capillary forces that keep them trapped.

Another remobilization mechanism is wettability alteration, where the surface properties of the porous matrix change over time. This alters the capillary pressure balance and can lead to the release of previously trapped CO_2 [42]. Additionally, hydrodynamic forces or reconnection with the main CO_2 phase during subsequent injection cycles can further reduce the extent of residual trapping. These processes can increase the amount of CO_2 that becomes structurally trapped beneath the caprock, potentially raising the risk of fracture or leakage.

All of this shows that a better understanding of residual trapping is necessary for efficient and safe carbon storage.

1.2.2 Snap-off vs bypass: mechanisms for trapping

The rocks and minerals constitutive of geological reservoirs are, for the most part, water-wet, meaning that during the injection $scCO_2$ is the non-wetting phase and water is the wetting phase. The displacement of the brine by the CO_2 during the initial injection is what is called a drainage, where a non-wetting fluid is injected and displaces a wetting fluid. After the injection, when the plume of CO_2 rises to the top of the formation, the opposite occurs, with water refilling the pores that CO_2 left at the bottom of the plume. This is called an imbibition, where a wetting fluid displaces a non-wetting fluid. Residual trapping occurs both during drainage and imbibition, but with different mechanisms.

Drainage and imbibition are complex phenomena that depend on a wide range of parameters, from the physical properties of the fluids (interfacial tension, viscosity, density,...) to the characteristics of the porous media (porosity, permeability, size of the pores, wettability, connectivity,...). Still, during the flow, there are two main ways for a ganglion of fluid to be trapped in a pore: snap-off and bypass [38, 122].

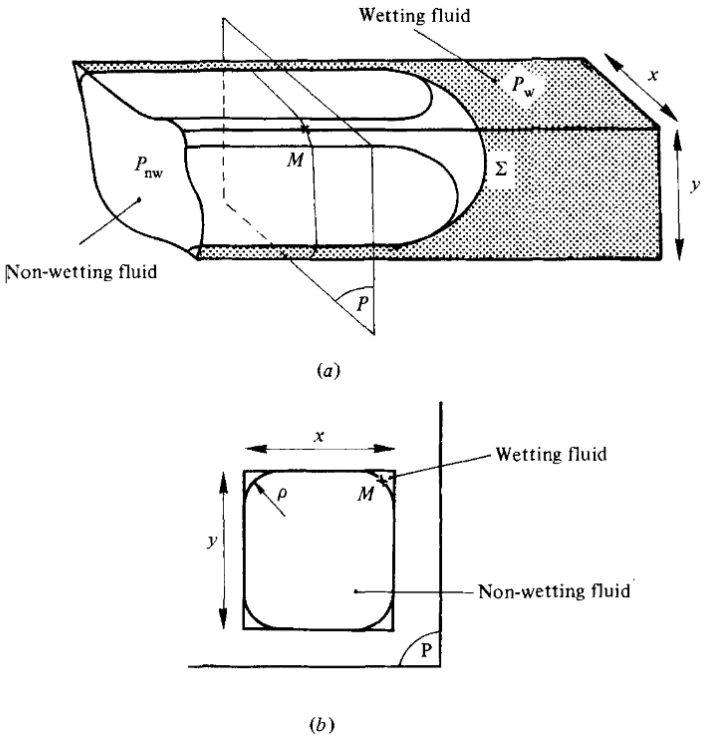

Figure 1.8: Invasion of a rectangular capillary by a non-wetting fluid, highlighting the presence of wetting layers behind the front meniscus (a) perspective view and (b) sectional view. Image from Lenormand et al. (1983).

Snap-off This mechanism, first introduced by Roof (1970), leads to the disconnection of ganglia of fluid from the bulk of non-wetting fluid because of an imbalance in the capillary forces. These ganglia can then be transported and trapped in the porous matrix [122], or can reconnect to the bulk of the fluid [165]. A more in-depth discussion of this mechanism is presented in Sec. 3.2.2.

Bypass This phenomenon occurs when the invading fluid does not invade a part of the porous medium, leaving it saturated with the initial fluid. This can be due to capillary pressure during drainage, where the invading fluid cannot access the small pores because of their high entry capillary pressure. This can also be caused by the formation of preferential flow paths, where some parts of the media are not invaded [36]. The Saffman-Taylor instability [174] is one example of the formation of these preferential flows when a less viscous fluid displaces a viscous fluid. This leads to viscous fingering, where only a fraction of the porous medium is invaded, leaving a lot of residual fluid behind the invasion front. An example of bypass can be seen in Fig. 1.9, where the invading fluid takes a preferential path around a cluster of non-wetting fluid due

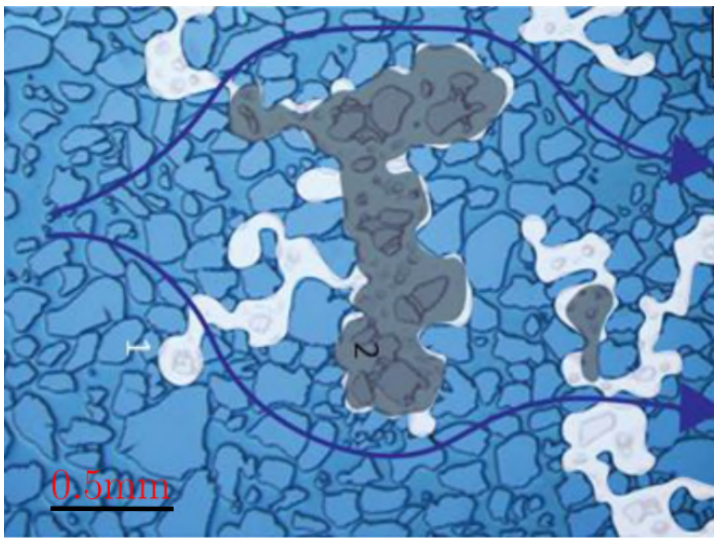

Figure 1.9: Example of bypass trapping presented in Lysyy et al. (2022). Here, the fluid highlighted in gray is hydrogen and is trapped in a space surrounded by small pores, preventing the non-wetting hydrogen from escaping.

to hydrodynamic conditions.

From these mechanisms, it is clear that residual trapping arises from pore-scale phenomena. The proportion of fluid trapped by each of these mechanisms during CCS is not properly studied, and seems to depend on the characteristics of the media, the properties of the fluids, and the injection rate [165].

1.2.3 Estimation of the amount of CO_2 stored by capillary trapping

Predicting the amount of CO_2 stored by capillary trapping is difficult, because even with tracers [69], CO_2 is difficult to track underground. Estimations range from only 2% of the injected trapped by capillary forces [4] to more than 40% [79, 196]. This wide variation in value depends on the porous medium used, the wettability of the solid, the injection rate, the fluids used,... This shows that residual trapping needs to be better understood if we want to make accurate predictions about the quantity of CO_2 that it traps.

1.3 Objectives of the PhD thesis

1.3.1 Scientific questions

This chapter examines the carbon capture and storage technology, highlighting its potential and the numerous questions that remain unanswered for its implementation. We saw that residual trapping plays a key role in CCS, by trapping an important part of the injected CO_2, as well as impacting the efficiency and safety of other trapping mechanisms. Residual trapping is thus a crucial mechanism to understand, predict, and achieve a safe and efficient CO_2 trapping.

These challenges around residual trapping raise scientific questions:

- How do the properties of the two fluids, such as interfacial tension, viscosity, or density, affect the capillary trapping?
- How do the geometry of the porous media and the flow rate control the trapping of fluid?
- How can we better predict the amount of CO_2 immobilized by residual trapping?
- How can the study of residual saturation at the pore scale translate to the field scale?

1.3.2 Open challenges

The study of residual trapping is a particularly complex task, as we are faced with different scientific challenges that limit our ability to study this subject.

Multi-scale phenomenon The first of these challenges is the profoundly multiscale nature of the problem. Indeed, we are interested in what happens at the large scale, since the reservoir in which the CO_2 is injected can span hundreds of kilometers. But at the same time, the physics of the flow occurs in pores, cracks, and fractures whose typical length scales are around a few hundred micrometers. Even worse, wettability and capillary forces, two major factors in two-phase flow, emerge from the molecular scale, see Fig. 1.10. The question of residual trapping thus spans more than 15 orders of magnitude, making the study of residual trapping extremely intricate.

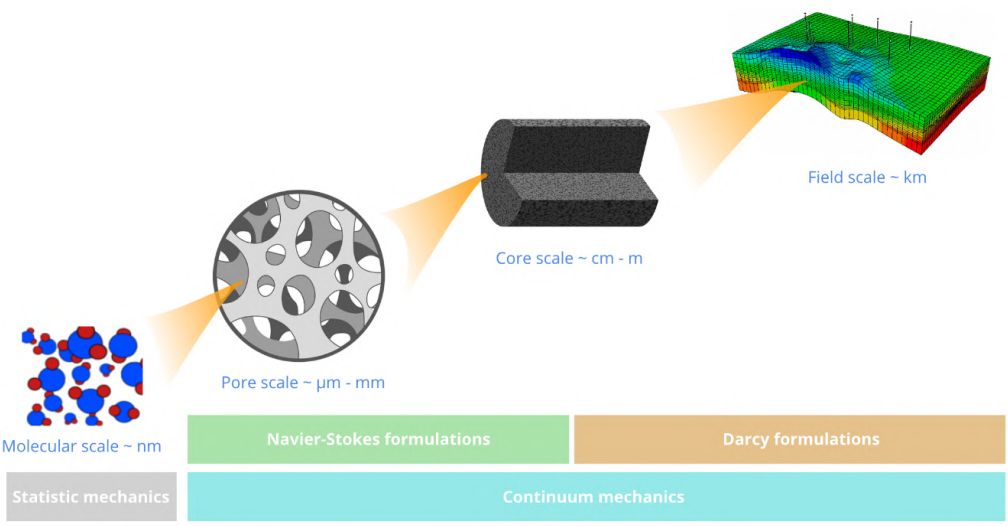

Figure 1.10: The different length-scales of interest in geological porous media, and the different laws used to model each scale, from Maya Fogouang (2024).

Non-linear behavior Another challenge in this study is the coupling of multiple physical phenomena. While capillary forces and surface tension dominate the system, other factors —such as viscosity and inertia— also play a significant role in influencing the flow. The intricate interplay between these forces results in nonlinear fluid behavior, further complicating the analysis and interpretation of the system.

Multi-physics coupling Another difficult aspect of this study is the coupling between the physics of the flow and the chemical reactions that occur. For example, the dissolution and precipitation of minerals are significantly influenced by the transport of reagents through the flow of fluids. Similarly, the flow of fluid is directly affected by the geometry of the pore space, which can evolve based on chemical reactions at the minerals' surface. These couplings between the different phenomena occurring during CCS make this study challenging.

Difficulty in the visualization of two-phase experiments One important issue in the study of the flow of fluids in porous media is visualization. Most, if not all, geological porous media are opaque to visible light, making it impossible to image the flow at the pore scale using standard methods such as optical microscopy.

1.3.3 Scientific strategy: a pore-scale approach

Studying residual trapping at the field scale (hundreds of kilometers) is extremely challenging. Even at the meter scale, describing a two-phase flow experiment requires an overwhelming amount of information. The observed behavior is influenced by a wide range of parameters —such as pore structure, connectivity, wettability, injection rate, and fluid properties— and small variations in these parameters can lead to significantly different outcomes. As a result, such studies typically yield only empirical relationships, which are often difficult —or even incorrect— to extrapolate to different porous media.

For this reason, we focus on investigating residual trapping at the pore scale, where the mechanisms responsible for residual saturation, such as snap-off and bypass, can be directly observed. At this scale, the governing physics is better understood, key parameters like wettability can be precisely controlled, and the porous structure is easier to characterize. A pore-scale approach enables us to gain deeper insight into how residual saturation forms, under what conditions it becomes significant, and which geometrical features promote or inhibit it. This improved understanding of the phenomenology of residual trapping provides a more solid foundation for developing predictive models that can be extended to a broader range of porous media.

1.3.4 Thesis outline

To answer these questions, we employ an approach that combines experimental and numerical investigations at the pore scale. The study presented in this manuscript is part of a project directed by Sophie ROMAN, which aims to examine the underlying mechanisms that control residual and solubility trapping in porous media during multiphase flow by providing more details on pore-scale fluid behavior, financed by the ANR GéoMIME. This study will focus on the residual trapping part of the research, and is organized as follows:

In Chapter. 2, we go over the fundamental notions of fluid mechanics in porous media.

In Chapter. 3, we discuss the different methods used in the study of residual trapping and their results.

In Chapter. 4, we will go over the principles of microfluidics and the experimental methods used in this study.

This is followed by an illustration of residual trapping in a complex heterogeneous porous media in Chapter. 5.

In Chapter. 6, we present our numerical approach based on pore-doublet modelling.

In Chapter. 7, we go over how the wetting layers present during two-phase flow impact the flow of the fluids and alter the stability of the invasion.

In Chapter. 8, we cover the impact of inertia during drainage and how it can alter the stability of the invasion.

In Chapter. 9, we take a closer look at how the presence of both brine and $scCO_2$ can alter the wettability of the rocks, and how it plays a significant role in the capillary trapping of CO_2.

Finally, in Chapter. 10, we present the conclusions of this work as well as the perspectives of this PhD.

Chapter 2

Fundamentals of fluid mechanics in porous media

In this chapter, we introduce the fundamentals of fluid mechanics as well as the defining parameters of porous media. Then, we examine the various methods for modeling two-phase flow in porous media.

2.1 Elements of fluid mechanics

We have taken an interest in the injection of CO_2 displacing brine in a geological reservoir. This problem involves the flow of fluids, and some introduction to the principles of fluid mechanics is required for a proper understanding of the situation.

2.1.1 What is a fluid?

A fluid is a medium that continuously moves and deforms under an applied shear stress (to a few exceptions). It means that they cannot resist any shear applied to them, whereas a solid can. This definition includes both liquid and gas, as well as plasma. Fluids are made up of a large number of molecules interacting with each other and the walls of their containers. By knowing the interacting forces between the molecules of the system, it would be possible to fully describe the entire system, down to the single molecules. This approach, also called molecular dynamics, can resolve about a few hundred molecules at the same time. For reference, a liter of water contains more than 10^{25} molecules. Currently, a fully resolved simulation of a system of even a few picoliters for any relevant duration of time would be way above the capacity of even the biggest supercomputers on Earth [137].

Thankfully, we don't need to simulate the individual position of each particle to understand how a fluid flows. The huge amount of molecules means that we can use a statistical approach to determine the properties of the motion of a very large number of molecules. For this, we describe the fluid not as an array of molecules, but as a continuum, by introducing the concept of a fluid particle. It is composed of many molecules, contained in a relatively small volume. The size of this volume needs to be above the mean free path of the molecules, and small enough compared to the total fluid domain, so that by averaging properties over it, we recover some meaningful properties. These properties are then associated with the center of the fluid particle. This means that at every point in the domain occupied by the fluid, we have a fluid particle with defined dynamic properties. For liquid flow, the scale of such a fluid

particle is around 1 µm. Below this size, the continuum approach presented above starts to break down and is no longer valid. This is important to keep in mind, as many porous media have pores below this size, meaning that the behavior of fluid inside these pores cannot be accurately described by the laws that we will see.

2.1.2 Main fluid properties

Fluid density The density of a fluid ρ is the mass per unit volume of this fluid. It depends on the temperature and the pressure of the fluid. The rate of change in the density is written as,

$$\frac{\partial \rho}{\rho} = -\alpha\, dT + \kappa_T\, dP \qquad \text{with} \begin{cases} \alpha \equiv \frac{-1}{\rho}\left(\frac{\partial \rho}{\partial T}\right)_P & \text{the thermal dilation coefficient ,} \\ \kappa_T \equiv \frac{1}{\rho}\left(\frac{\partial \rho}{\partial P}\right)_T & \text{the isothermal compressibility coefficient.} \end{cases} \tag{2.1}$$

A fluid is considered incompressible when its density is considered constant (if it does not change by more than a few percent) over the range of pressure and temperature in the flow. A few models exist for the expression of the dilation and compressibility coefficient: The Boussinesq approximation is a first-order Taylor development of the dilation coefficient and reads as,

$$\rho(T,P) \approx \rho_0\,[1 - \alpha_0(T - T_0)], \tag{2.2}$$

where the α_0 is the dilation coefficient computed for the reference value T_0. For the compressibility, a similar development is used,

$$\rho(T,P) \approx \rho_0\,[1 + \kappa_T(P - P_0)], \tag{2.3}$$

where the compressibility coefficient is calculated for a value P_0 of the pressure. In all of the following manuscripts, we will consider incompressible fluid, meaning that the density will be taken as constant.

Fluid viscosity As we have seen, one of the main ways to define a fluid is that it continuously moves when a shear is applied to it. But not all fluids flow the same. For example, air deforms easily and offers little resistance to the motion, while pitch is so hard to deform that it resembles more a solid than a liquid. This is highlighted in the famous pitch drop experiment at the University of Queensland, where in 1927 [60], pitch was put in a glass funnel and allowed to drip out, see Fig. 2.1. Since the beginning of the experiments, only nine drops have fallen out of the funnel.

The parameter that measures the response of the fluid to shear is called the viscosity. If we denote $\boldsymbol{\tau_{yx}}$ the shear stress exerted in the x direction on the surface of a fluid particle whose normal is along the y direction, then the fluid response to this shear is given by,

$$\boldsymbol{\tau_{yx}} = \mu \frac{\partial \mathbf{u}}{\partial y}, \tag{2.4}$$

where μ is known as the dynamic viscosity of the fluid, and $\mathbf{u}$ denotes the velocity of the fluid. Non-scalar parameters are written in bold, and their dimensions can be deduced from the equations. The viscosity of air is very low, around 1.81×10^{-5} Pa·s at 15 °C, water has a viscosity of 1.0×10^{-3} Pa·s at 20 °C while the pitch of the pitch drop experiments is estimated to have a viscosity of 2×10^{8} Pa·s, 11 order of magnitude above the viscosity of water! For most fluids, viscosity decreases with temperature.

For simple fluids, known as Newtonian fluids, μ is independent of the shear stress: the fluids that do not follow this rule are called non-Newtonian fluids. Among them,

Figure 2.1: Picture of the pitch-drop experiment, highlighting how pitch, despite looking like a solid, flows like a fluid over long time scales [154].

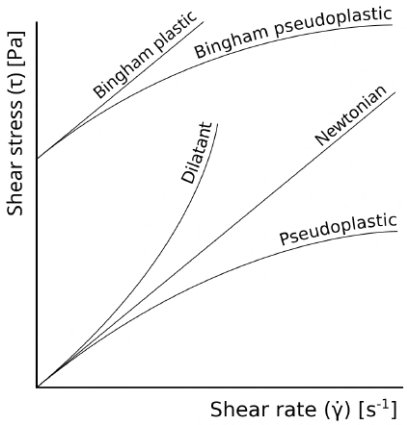

Figure 2.2: Example of a rheogram for different types of fluids. The gradient of the curves at each point gives the viscosity for each shear rate[142].

one can mention the shear-thinning fluid (such as paints, soap, and grease), whose viscosity decreases with increasing stress, and shear-thickening fluids, such as wet sand, where the viscosity increases with stress. This is represented on a rheogram, which gives the shear rate of the fluid when exposed to different shear stress, see Fig. 2.2.

2.1.3 Governing equations

Conservation of mass The conservation of mass of a fluid is written as,

$$\frac{\partial \rho}{\partial t} + \nabla.(\rho \mathbf{u}) = 0. \tag{2.5}$$

If the density ρ of the fluid is constant on the flow lines, it is pulled out of the derivative, which leads to

$$\nabla.\mathbf{u} = 0. \tag{2.6}$$

This is true for most liquids, but gases are compressible. Nevertheless, for a flow of low speed, the change in absolute pressure in the flow is small, and the gas is considered incompressible.

Conservation of the momentum By doing a momentum balance on a small element of fluid, one can find Cauchy's equation, which reads as,

$$\rho \frac{D\boldsymbol{u}}{Dt} = \nabla.\boldsymbol{\sigma} + \rho \mathbf{g} \tag{2.7}$$

where $\frac{D}{Dt} = \frac{\partial}{\partial t} + \mathbf{u}.\nabla$ is the material derivative, and $\boldsymbol{\sigma}$ is the total stress tensor. This total stress tensor is written as,

$$\boldsymbol{\sigma} = \boldsymbol{\tau} - P\mathbf{I} \tag{2.8}$$

where $\boldsymbol{\tau}$ is the shear stress, P is the pressure, and $\mathbf{I}$ is the identity tensor. For an incompressible Newtonian fluid, the shear stress tensor $\boldsymbol{\tau}$ is written as,

$$\boldsymbol{\tau} = \mu\left(\nabla\mathbf{u} + (\nabla\mathbf{u})^T\right). \tag{2.9}$$

Combining Eqs. (2.7) and (2.9) leads to,

$$\rho \frac{D\mathbf{u}}{Dt} = \rho\mathbf{g} - \nabla P + \mu\Delta\mathbf{u} \tag{2.10}$$

which is known as the Navier-Stokes equation. In the cases where viscosity dominates inertia, and when the flow is steady, the Navier-Stokes equation is simplified under the Stokes equation that reads as,

$$\rho\mathbf{g} - \nabla P + \mu\Delta\mathbf{u} = 0. \tag{2.11}$$

Boundary conditions at the solid surface In most cases, a viscous fluid in contact with a rigid wall will adhere to the wall and move with it. This is called the no-slip boundary condition. This means that at the interface between fluid and solid, we have

$$\boldsymbol{u}_{fluid} = \boldsymbol{u}_{wall}. \tag{2.12}$$

This equation is used for most domains of fluid mechanics, but is known to fail for non-Newtonian fluids, or when the mean free path of the fluid is close to the dimension of the conduit. This can occur in porous media for a rarefied gas, where the mean free path of the gas molecule is in the order of magnitude of the pore size. This is

characterized by the Knudsen number Kn, which is the ratio of the mean free path l to the representative physical length L, with $Kn = \frac{l}{L}$. When $Kn > 0.01$, we enter a regime where the no-slip boundary condition no longer holds, because the continuum approximation starts to fail. This has been experimentally shown by Klinkenberg in 1941 [90]. To better describe these flows, the Navier-Slip boundary condition is generally used and reads as,

$$u_{fluid} - u_{wall} = \lambda \frac{\partial u_{fluid}}{\partial y}, \tag{2.13}$$

where y is the coordinate normal to the wall, and λ is the slip length, which is proportional to l.

For a non-viscous fluid, also called a perfect fluid, we have no adherence between the fluid and the solid, and instead of having a no-slip condition, we have what we call a slip boundary condition, which reads as,

$$\boldsymbol{u}_{fluid}.\boldsymbol{n} = \boldsymbol{u}_{wall}.\boldsymbol{n}, \tag{2.14}$$

meaning that the fluid cannot enter the solid, but no statement is made on the tangential flow along the wall. In practice, this boundary condition is rarely seen in use.

2.2 Two-phase flow

We have seen the laws that govern the flow of the bulk of the fluid. We now take an interest in the case where we have two fluids flowing simultaneously in the system.

2.2.1 Surface tension: molecular origin

Consider two immiscible fluids separated by a well-defined interface. In the bulk of one fluid, molecules interact strongly with their neighbors and exist in a low-energy state. However, at the interface, molecules experience fewer cohesive interactions with their kind and instead interact with molecules of the other fluid, interactions that are typically weaker. As a result, molecules at the interface are in a higher energy state compared to those in the bulk. This energy difference implies that creating an interface

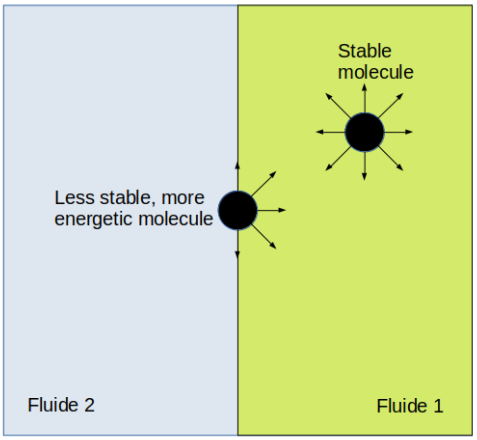

Figure 2.3: Schematic of surface tensions, with a stable molecule in the bulk of the fluid interacting with all of its neighbors, while a more energetic molecule is represented at the interface between both fluids, with only half as many interactions.

between two immiscible fluids requires energy input, as illustrated in Fig. 2.3. When one of the fluids is air, this energy per unit area is referred to as the surface tension of the fluid. When both phases are liquids or other fluids, the term used is interfacial tension. Both of them are usually noted with the Greek letter σ.

The consequence of this interfacial tension is that immiscible fluids try to decrease their surface of contact by 'pulling' the surface molecules inwards. This creates a pressure jump across the interface between two fluids, known as capillary pressure, P_c. This capillary pressure is given by Young-Laplace's equation, which reads,

$$P_c = P_i - P_0 = \sigma\left(\frac{1}{R_1} + \frac{1}{R_2}\right) = \sigma\kappa. \tag{2.15}$$

Here, P_i is the pressure of the fluid on the convex side of the interface, P_0 is the pressure on the other side of the interface, and R_1 and R_2 are the radii of curvature of the interface along two orthogonal directions, see Fig. 2.4. κ is the curvature of the interface, deduced from these radii. The pressure is always higher on the convex side of the interface.

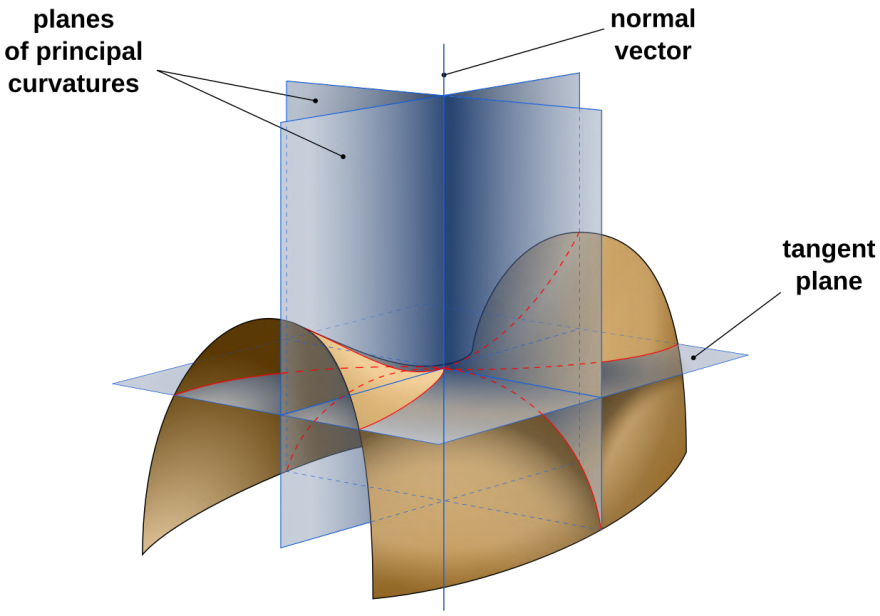

Figure 2.4: Schematic of the two radii of curvature of a surface. To determine the two radii of curvature, we need to take two orthogonal planes that pass through the vector normal to the point where we wish to measure the curvature. These two planes intersect the interfaces along two curves (in red). On these curves, we use osculating circles to define the two radii of curvature, R_1 and R_2. These radii are algebraic parameters: they can be positive as well as negative. If the center of the circle defining the radius R_i is inside the saddle, R_i is positive. If it is outside, the radius is counted as negative in the Young-Laplace equation [48].

For example, a drop of water in the air, if it is only affected by the capillary forces, is always a sphere. This is because a spherical shape minimizes the contact between water and air. Since the drop is convex, the pressure of the water is higher than the pressure of the air. The capillary pressure is expressed as $P_c = \frac{2\sigma}{R}$ since the radius of curvature of the drop, in any direction, is R.

2.2.2 Boundary conditions at the interface between the two fluids

At the interface between two fluids, we observe a different set of conditions:

- First, we have the continuity of the velocity. If there is no mass transfer between both fluids at the interface, and they both have a viscosity, we can write that, see Fig. 2.5

$$\boldsymbol{u_{II}} = \boldsymbol{u_I}. \tag{2.16}$$

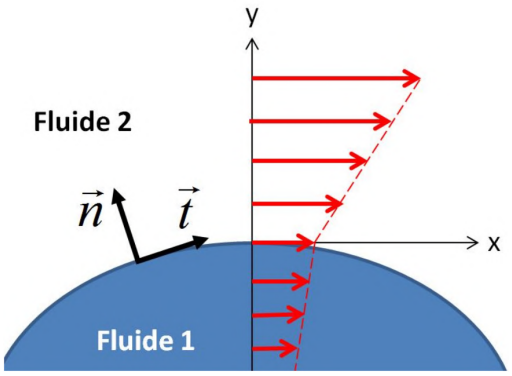

Figure 2.5: Boundary condition between two fluids. Credits to Olivier Bonnefoy, professor at the Ecole des Mines de Saint-Etienne.

- Secondly, since the interface is thin and cannot dissipate any stress, we have continuity of the stress through the interface. This reads as,

$$\boldsymbol{n}.\left[-P_I\boldsymbol{I} + \mu_I\left(\nabla\boldsymbol{u_I} + \nabla^T\boldsymbol{u_I}\right)\right] = \boldsymbol{n}.\left[-P_{II}\boldsymbol{I} + \mu_{II}\left(\nabla\boldsymbol{u_{II}} + \nabla^T\boldsymbol{u_{II}}\right)\right] + \sigma\kappa. \tag{2.17}$$

  At equilibrium, the normal stress balance simplifies to the Young-Laplace equation (2.15).

At the solid boundary, we observe the same no-slip boundary conditions as introduced in Sec. 2.1.3. This poses an issue at the triple line, where the interface between the two fluids meets the wall. The flow of this triple line violates the no-slip condition. This leads to a significant amount of ongoing research. This topic is explored more in depth in Huh and Scriven (1971) and De Gennes (1985), or Snoeijer and Andreotti (2013).

2.2.3 Dimensionless numbers to characterize the flow

Reynolds number From Eq. (2.10), one can easily derive one important dimensionless number used to describe the flow: the Reynolds number, which is expressed as $Re = \frac{\rho u L}{\mu}$ where u and L are respectively the average speed of the flow and the length scale over which the speed varies (such as the diameter of a conduit, for example). This number represents the ratio of inertia to viscous forces and is used to categorize the flow into two general categories: turbulent and laminar flow. For high Reynolds numbers, i.e., $Re > 1000$, the flow is turbulent, the fluid flows in a disorganized pattern, eddies form, and mixing occurs. When the Reynolds number is small, i.e., when $1 < Re < 1000$, the flow is laminar. This means that overall, all of the fluid flows in a single direction in a regular pattern, with no movement perpendicular to the general flow direction. For a very low Reynolds ($Re < 1$), we are in the creeping flow regime, where inertia is negligible and the Stokes equation describes the flow (2.11), which is

Figure 2.6: Time reversibility of Stokes. Fluid has been injected between two concentric cylinders, with dyes injected inside the fluid. One of the cylinders is then slowly rotated to be in the Stokes regime, which smears the dye, making it appear mixed. The rotation is then reversed, and we recover the same initial pattern, highlighting the reversibility of Stokes flow [191].

reversible (i.e., if we replace t by $-t$ in (2.11)), the equation stays the same). This means that the entropy generated by the flow is very small, and if we reverse the flow, we can recover the initial situation, see Fig. 2.6. For most geological applications, we are in the creeping flow regime, with the Reynolds number below one.

Capillary number Other dimensionless numbers are crucial for this study but do not directly arise from (2.10), such as the capillary number Ca that compares the viscous forces with the capillary forces. A general expression of this number is $Ca = \frac{\mu u}{\sigma}$. In the scope of CO_2 storage and for most two-phase flow in geological formations, this number takes a value between 10^{-5} and 10^{-10}, meaning that the capillary forces are important during the injection.

Bond number To take into account the relative importance of gravity, the Bond number $Bo = \frac{\Delta\rho g L^2}{\sigma}$ is defined as the ratio of the gravity and the capillary forces, with $\Delta\rho$ the density difference between the fluids. For CO_2 storage, the values taken by the Bond number lie between 10^{-4} and 1.

Viscosity ratio Finally, we introduce the viscosity ratio $M = \frac{\mu_{in}}{\mu_{out}}$ where μ_{in} is the viscosity of the displacing phase and μ_{out} is the viscosity of the displaced phase. For CO_2 storage, M is between 0.03 and 0.2 [144], meaning that the brine is always more viscous than the $scCO_2$.

2.3 Wettability conditions

We have defined the boundary condition between one fluid and the solid, as well as the boundary conditions between both fluids. But what happens at the line where both fluid and the solid meet? This is what we discuss in this section.

2.3.1 Concept of contact angle

Definition of the contact angle Wettability describes the ability of one fluid to stay in contact with a solid substrate in the presence of a second immiscible fluid. It is the result of the balance of the cohesive forces between the two fluids and the solid. This equilibrium is characterized by measuring the angle formed by the fluid-fluid interface with the solid substrate, see Fig. 2.7. This angle, also called the contact angle,

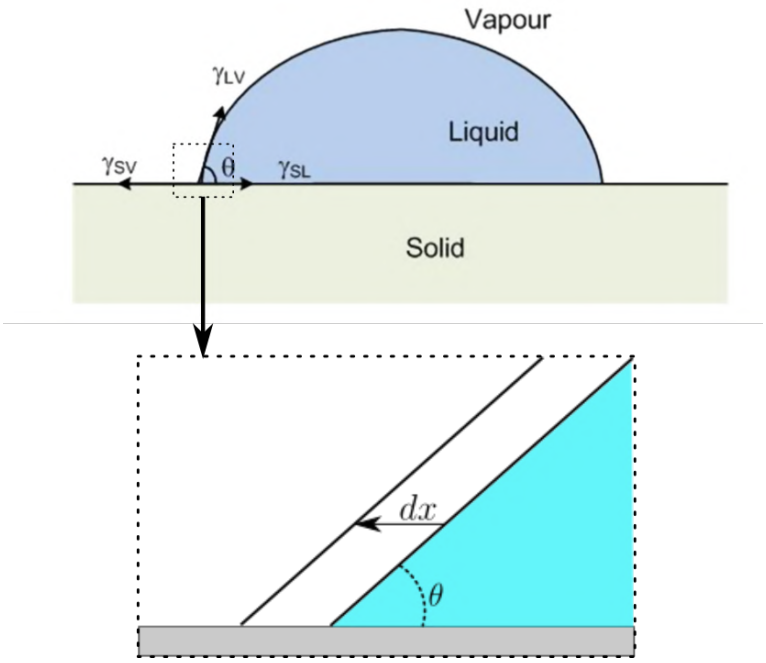

Figure 2.7: Contact angle at a three-phase contact line, adapted from Makkonen (2017) with a zoom on the contact line, with the small displacement dx used to find the variation in surface energy.

is measured through one of the fluids (in Fig. 2.7, it is measured through the liquid) and characterizes the affinity of the surface for this fluid. If this angle is below 90°, it means that the fluid is wetting; if it is above 90°, it is non-wetting, and the other fluid becomes the wetting fluid. If the contact angle drops to 0°, the fluid spreads over the entire solid and forms a film. This is called complete wetting, or spreading. In the case of a drop at the surface of a solid, Fig. 2.7, three interfacial energies arise: the interfacial energy between the solid and the liquid σ_{S-L}, the solid and the vapour σ_{S-V} and between the liquid and the vapour σ_{L-V}. To find the contact angle θ, we want to find the situation where the energy of the system is minimal. For this, we consider a small displacement dx of the contact line, and we look at the corresponding variation in surface energy, see Fig. 2.7. This reads as,

$$dE = \sigma_{S-L}dx - \sigma_{S-V}dx + \sigma_{L-V}\cos\theta dx. \tag{2.18}$$

By minimizing the energy variation of the system, we find that the contact angle is given by,

$$\sigma_{S-V} = \sigma_{S-L} + \sigma_{L-V}\cos\theta, \tag{2.19}$$

which is the famous Young-Dupré equation [221].

Capillary rise The contact angle affects the curvature of the interface between the fluids. For example, in the well-known case of a capillary rise, where a cylindrical tube of radius R is dipped in water, a meniscus forms inside the tube, and the capillary pressure created forces water to rise inside the tube above the initial water level, see Fig. 2.8. But if the liquid is mercury, the opposite occurs, and the mercury-air interface

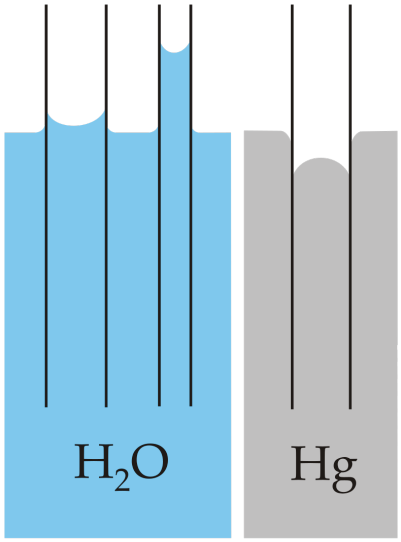

Figure 2.8: Capillary rise in a glass cylindrical tube. Water is wetting the glass and rises inside the tube, while mercury is non-wetting to the glass and recedes from the tube [119].

is below the initial mercury level. This is explained by Jurin's law, which states that for a cylindrical tube immersed in liquid, the height of the capillary rise h is given by

$$h = \frac{2\sigma \cos\theta}{R\rho g}, \tag{2.20}$$

where ρ is the density of the fluid and g the Earth's gravitational constant. If the fluid is non-wetting, i.e., $\theta > 90°$, h is negative, and the meniscus drops below the initial liquid level, as is the case for mercury.

Contact angle hysteresis We have seen that for an ideal, flat surface, the contact angle takes one value given by the Young equation. But real solids often present defects, either chemical ('spots') or physical (irregularities of the surface). This non-ideality makes the contact angle non-unique! It can take values between two extremums, called the advancing contact angle and the receding contact angle. This phenomenon is called the contact angle hysteresis, and it is the reason why we can observe drops on a slightly tilted leaf (see Fig. 2.9) or water trapped in a small capillary. These two angles are determined by creating a drop on a substrate and tilting it until the drop moves under the action of gravity, and measuring the contact angle at the front and back of the drop. The contact angle at the front is the advancing contact angle, and represents the maximal angle, and the angle at the back, the receding angle, is the minimal value taken by the contact angle, see Fig. 2.9.

This hysteresis occurs when the triple line, which is the contact line between the two fluids and the solid, is pinned on a defect of the solid, either an edge or a spot that is more hydrophilic than the rest of the surface.

2.3.2 Effect of heterogeneous surface

As we have seen, surfaces with defects, such as chemical impurities or roughness, lead to contact angle hysteresis, but it is not the only impact it has, as it also changes the apparent contact angle!

Figure 2.9: Droplets of water sliding along a tilted substrate, from Makkonen (2017).

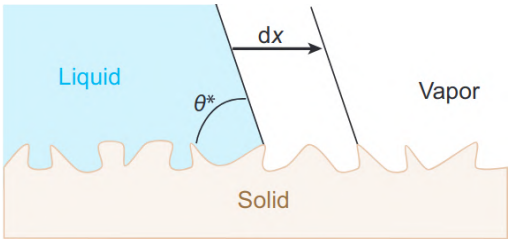

Figure 2.10: Wenzel's model. Assuming that the drops follow the solid roughness, the apparent contact angle θ^* is obtained by looking at the variation of surface energy.

Surface roughness: Wenzel's model One example of that is the impact of rugosity on the contact angle, as described by Wenzel (1949). For this situation, we introduce a rough solid substrate and its roughness r, defined as the ratio of the real and apparent surface area. The real surface area is the one that is measured at the small scale, while the apparent one is measured at the large scale. r takes values between 1 (perfectly flat surface) to ∞, for an infinite fractal surface. We consider that locally, the contact angle obeys the Young equation with a contact angle of θ_E, and the apparent contact angle is written θ^*, see Fig .2.10. When we take into account the increase in surface area due to the roughness of the solid, (2.19) is rewritten to :

$$r\,\sigma_{S-V} = r\,\sigma_{S-L} + \sigma_{L-V}\cos\theta^*. \tag{2.21}$$

This leads to Wenzel's law:

$$\cos\theta^* = r\cos\theta_E. \tag{2.22}$$

According to this law, rugosity always has the same effect: it increases the natural tendency of the solid. If the solid is already wetted by the fluid ($\theta_E < 90°$), the roughness makes it wetter, with an even lower contact angle. If the solid is not wetted by the fluid ($\theta_E > 90°$), the contact angle will get even higher. This law predicts that it is possible to reach a contact angle of 0°, i.e., a surface where the fluid spreads entirely, with a solid that is only partially wetted by the fluid (i.e., where $\theta_E > 0$), if the surface is rough enough.

Chemically heterogeneous surface: Cassie-Baxter's model Let's now consider a flat surface composed of two materials 1 and 2, each with a distinct contact angle, given by

the Young equation, θ_1 and θ_2, with the drop. We assume that the size of the chemical heterogeneity is small compared to the size of the drop.

If we take a similar approach to the one presented for the rough surface, we end up with the following equilibrium condition,

$$f_1 (\sigma_{S-L} - \sigma_{S-V})_1 + f_2 (\sigma_{S-L} - \sigma_{S-V})_2 = -\sigma_{L-V} \cos\theta^*. \tag{2.23}$$

f_1 and f_2 are the fraction of the surface occupied by the materials 1 and 2 respectively. The indices 1 and 2 refer to the properties of the corresponding materials. This equation leads to the Cassie-Baxter law, where the apparent contact angle on this chemically heterogeneous surface θ^* is given by [34],

$$\cos\theta^* = f_1 \cos\theta_1 + f_2 \cos\theta_2. \tag{2.24}$$

For a chemically heterogeneous substrate, the apparent contact angle is the weighted average of the contact angles of the two materials.

2.3.3 Deeper look at textured substrates

Shibuichi et al. (1996) studied how texturing the substrate alters the apparent contact angle, depending on the initial wettability of the solid. Their results are shown in Fig. 2.11. On the right side of the X-axis (for hydrophilic substrates), the apparent

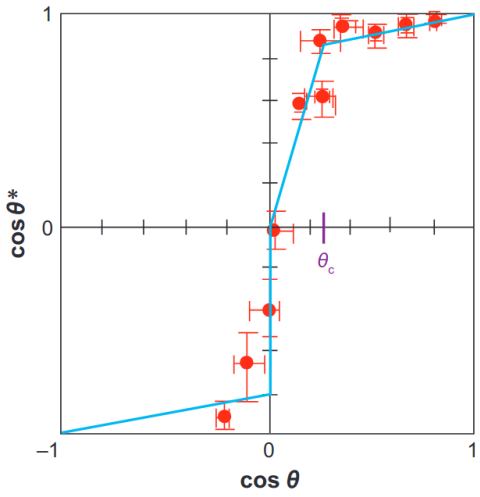

Figure 2.11: Experimental results from Shibuichi et al. (1996). The X-axis represents the Young contact angle of the solid, before texturation, while the Y-axis shows the apparent contact angle, after texturation. The right side of the X-axis represents hydrophilic substrates ($\theta < 90°$) while the left-hand side of the X-axis represents a hydrophobic substrate. θ_c is the critical contact angle above which the Wenzel law breaks down. Figure from Quéré (2008).

contact angle increases linearly, with a slope greater than 1. This behavior is explained by Wenzel's law, where the roughness increases the natural hydrophilicity of the substrate. In this case, the slope of the curve is given by r, the roughness of the solid. But Wenzel's law appears to break down for a certain value of the inherent contact angle, the evolution of the apparent contact angle changes, and reaching $\cos\theta^* = 1$ requires $\cos\theta = 1$. On the hydrophobic side (left-hand side of the figure), our first observation is the limited number of experiments for high inherent contact angle. This is due

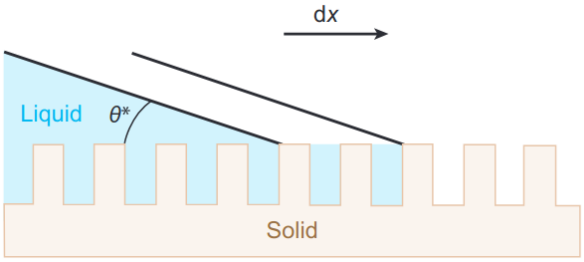

Figure 2.12: Example of a hydrophilic solid substrate with well-defined crevices filled with water [156].

to the difficulty in manufacturing a hydrophobic material with a contact angle with water above 120. When the solid becomes rough, we observe a quick and significant increase in the apparent contact angle, in a behavior that cannot be explained simply by Wenzel's law.

These results highlight the complex behavior of the apparent contact angle and suggest that Wenzel's law does not describe the entire picture, and that other phenomena are needed to explain this behavior.

Hydrophilic surface Another way to look at a textured substrate is to see it as a porous medium, where it is possible that some of the fluid escapes the drop and enters some crevices ahead of the contact line. When the drop reaches these crevices, they are already full of fluid, meaning that the drop spreads over a patchwork of solid and fluid. To determine what would be the contact angle for this situation, we consider an idealized surface with well-defined geometrical features, see Fig.2.12, that are already filled with water, and the rest of the substrate is composed of a solid with a contact angle of θ. Considering that the fraction of the surface occupied by liquid is f_l and the one occupied by the solid is $1 - f_l$, we use the Cassie-Baxter law to write that,

$$\cos\theta^* = f_l + (1 - f_l)\cos\theta. \tag{2.25}$$

This result explains why we cannot reach complete wetting by texturing the surface. There is always a fraction of the surface that is left exposed, which prevents the contact angle from reaching 0.

For this description to be accurate, the liquid needs to be able to invade the crevices of the surface, which leads to the creation of a surface between the liquid and the air. Let us consider the liquid film advancing along the surface presented in Fig. 2.12. The variation of surface energy is written as,

$$dE = (r - (1 - f_l))(\sigma_{S-L} - \sigma_{S-V}) + f_l\sigma_{L-V}. \tag{2.26}$$

The term $(r - (1 - f_l))$ arises since the inside of the crevices is wetted, but not the top of the solid, which is still dry. This means that the imbibition of the crevices by the liquid is energetically favorable if

$$\cos\theta > \frac{f_l}{(r - (1 - f_l))} = \cos\theta_c. \tag{2.27}$$

This critical angle θ_c defines the limit where the imbibition of the crevices by the liquid becomes possible and where Wenzel's law no longer works.

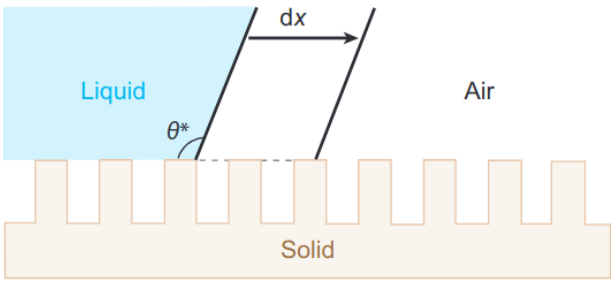

Figure 2.13: Case of textured hydrophobic solid capturing air in its roughness, increasing the apparent contact angle[156].

Hydrophobic surface To explain how the apparent contact angle decreases so much with roughness in Fig. 2.11, we take a similar approach of a solid substrate with well-defined crevices, but instead of being inherently hydrophilic, the solid is now hydrophobic. The crevices are thus preferentially filled by air, and not by water, see Fig. 2.13. Now the contact line moves over a patchwork of solid and air, with the fraction of the air written as f_l. According to the Cassie-Baxter equation, the apparent contact angle is given by:

$$\cos\theta^* = -f_l + (1 - f_l)\cos\theta, \tag{2.28}$$

since the contact angle between air and the liquid is π. The behavior predicted by (2.28) is very different from the one predicted by Wenzel model. As soon as air pockets are trapped under the drop, the contact angle jumps to a high value, but it is almost impossible to reach a value of 180° because one cannot remove the solid entirely under the drop. This is again, in contradiction to Wenzel's law, which predicts that we have an angle of 180° as soon as we reach $r\cos\theta = -1$.

For these pockets of air to be stable under the drop, the inherent contact angle must be above a certain critical angle θ_c, which is found similarly as earlier, and reads as

$$\cos\theta_c = \frac{-f_l}{(r - (1 - f_l))}. \tag{2.29}$$

The trapping of air pockets beneath a droplet enables the fabrication of solids with surface topologies specifically designed to maximize air retention, resulting in highly hydrophobic materials. This phenomenon is also observed in nature, for example, in lotus leaves. Their superhydrophobicity not only repels water but also reduces contact angle hysteresis, allowing water droplets to roll off easily, picking up dust and parasites, effectively cleaning the leaf surface. A review on the design and the uses of such superhydrophobic materials is found in Quéré (2008).

2.3.4 Wettability alteration in the context of CCS

In the context of the CCS and porous media in general, measuring the contact has proved to be challenging. Firstly, pressure, salinity, and temperature have a significant impact on the interfacial tensions, which, according to Young's equation, modify the contact angle. Several studies using high-pressure cells highlight that the surface tension of CO_2 increases with the density of the fluid (so increases with the CO_2 pressure and decreases with temperature). This leads to higher interfacial tension between the minerals/water and the CO_2, which tends to increase the contact angle between water and the minerals, making the solid less hydrophilic [8, 9, 92, 175]. These experiments, which do not involve any chemical changes, are not always in agreement

with each other, as they find different values of contact angle for the same conditions. Some hypothesize that these discrepancies in measurements are caused by the methods used to clean the solid surface before the measurements, which fail to eliminate some contaminants that can have a massive effect on the measured contact angle [88, 87].

Secondly, chemical reactions and exchanges between the fluids and the minerals constitutive of the underground are possible. This has been found by many different studies to change the wettability of the porous matrix [208, 150, 120, 83, 98]. Usually, the CO_2 is the non-wetting phase in the underground reservoirs. But if the surface properties of the minerals change, we can observe a wettability reversal of the minerals, where the CO_2 becomes the wetting phase. This would profoundly alter the dynamic of the carbon storage. Indeed, if the contact angle changes, the bubbles trapped by the capillary forces might remobilize and escape the pore they were trapped in. More concerningly, structural trapping relies on the layer of rocks at the top of the formation to have an entry capillary pressure above the pressure of CO_2 to prevent it from invading this impermeable layer. If this wettability reversal occurs for the caprock, we might observe imbibition of the CO_2 inside of the sealing cover of the reservoir. This would be catastrophic, as the structural trapping would fail and leak all of the CO_2 it trapped in the surrounding formations.

Different mechanisms have been proposed to explain the observed alteration in wettability. Some studies suggest that the increased acidity of the brine due to the dissolution of CO_2 starts to dissolve the minerals and increase their roughness, altering the contact angle according to the Cassie-Baxter or Wenzel model. Others believe that this is due to the alteration of certain chemical groups on the surface of the minerals, changing their interfacial tension between the CO_2 and the minerals [98, 123].

2.4 Physics of flow in porous media

Now that we have introduced fluid mechanics, we take an interest in porous media, how they are defined, and what characterizes them.

2.4.1 Notion of scales in porous media science

We have discussed in the previous section about the geological storage of CO_2 in porous geological formations, but we have not yet properly defined a porous medium. Two scales are important to define a porous medium: the large (Darcy) scale and the pore scale.

What is a porous medium? Porous materials are commonly encountered in our everyday lives. To be described as a porous medium, a material needs to follow the following criteria [57]:

- *(i)* It must contain a relatively small space free of solid, embedded in the solid matrix. These spaces, called pores, are typically filled with fluids.
- *(ii)* It must be permeable to fluids. It means that fluids should be able to penetrate through one face of the material and emerge on the other side.

These criteria fit a wide variety of everyday materials, such as wood, cement, textiles, and paper. It also concerns biological tissues, including the lungs, blood vessels, kidneys, bones, and skin. This also works for soil or underground rocks.

Pore scale Porous media are composed of a multitude of pores surrounded by solids. If one looks at the material at the scale of a few pores (≈ 100 µm), one can accurately describe their geometry and the connection between the pores. It is then possible to numerically solve the Navier-Stokes equation inside this geometry, giving a full description of the velocity, pressure, and/or chemical concentration inside the pore network, solving the problem entirely. But for typical applications, the porous materials are several orders of magnitude bigger than this pore size, and solving the Navier-Stokes equation in a network of this size becomes absurdly computationally expensive. For example, an static X-ray scan of a 1 mm × 1 mm × 1 mm at a resolution of 1 µm takes around one terabit of data. The description of the flow at the pore-scale in a sample of this size would require a supercomputer, but we would still be far from the field scale, which can be kilometers long ... To describe porous material at a convenient scale, we need to describe the porous medium using a continuous description.

Continuum approach to porous media This continuous approach for the description of the porous medium is similar to the one presented in Sec. 2.1.1 when we introduced the notion of fluid particle. Instead of describing each pore individually, we take the average of the velocity, pressure, and other relevant parameters over a control volume inside the porous medium. For this, we need to determine the size of a representative control volume around any point of the porous medium. It should be much smaller than the total size of the media, in order to recover some meaningful properties, but must also be much larger than the individual pore to include enough pores so that the averaged properties make sense. For instance, if the averaging volume is similar to the characteristic pore size, it may contain only void space or only solid material, yielding an apparent porosity of either 1 or 0, both of which deviate significantly from the true porosity. To obtain meaningful values, the averaging volume must therefore be increased until it captures both the solid and fluid phases in proportions representative of the material as a whole. The smallest volume over which macroscale parameters are consistently defined is known as the Representative Elementary Volume (REV). Its size depends strongly on the heterogeneity of the porous medium: media composed of regularly repeating structures, such as packed glass beads, typically have a small REV, whereas highly heterogeneous materials require a much larger one.

Experimentally, the REV is determined by measuring the average value of a parameter ϕ, typically porosity or permeability, over progressively larger increments of volume V. When the measured value of ϕ stabilizes and no longer changes significantly with further increases in V, the REV has been reached (see Fig. 2.14). Care needs to be taken when we have a heterogeneous medium that contains, for example, large-scale fractures. If we keep increasing the averaging volume, we might start to include the fractures, which will drastically change the value of the parameters. We also need to keep in mind that a REV for the porosity might not be a REV for the permeability.

By introducing the concept of REV to the porous media, we have replaced the actual medium with its complex network of pores with a theoretical continuous medium, where each point can be associated with an averaged value.

2.4.2 Continuum-scale properties of porous media

Now that we have defined the porous medium as a continuum, we introduce some properties defined at the large scale that are essential for the understanding of the flow of fluids through it. These are:

Porosity The porosity is defined as the fraction of the material volume occupied by the pores. Depending on the porous media, this value ranges from almost zero (i.e.,

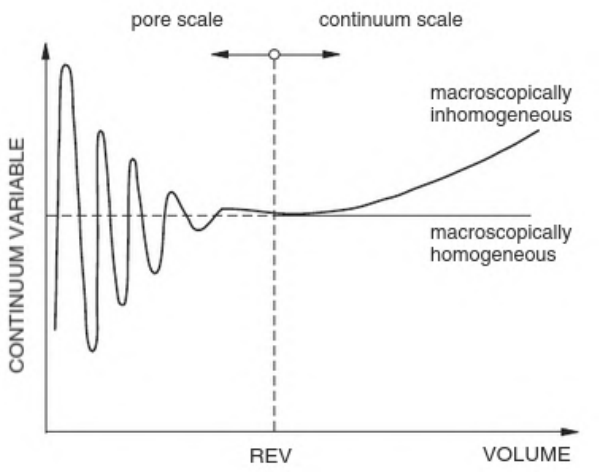

Figure 2.14: Example of the determination of a REV. When the parameter stops depending on the size of the averaging volume, then we are in a REV, from White et al. (2006).

no pores) to almost unity (i.e., only pores). For example, glass and metals generally have almost no porosity, while foam is almost entirely composed of pores. Two kinds of pores exist within a porous medium: the connected or effective porosity and the closed porosity. The closed pores are only surrounded by the solid matrix and cannot participate in the flow of fluid, given their isolation, while the connected pores allow for the flow of fluids through them.

Permeability As we saw earlier, for a material to be porous, fluid needs to be able to flow through it. The intrinsic conductivity of the porous medium to a Newtonian fluid is called the permeability, noted k. The higher the permeability, the easier it is to force a fluid to flow through the material. This property is intrinsic to the material and depends only on the pore structure. The permeability arises from the famous Darcy's law [50], which states that for a sufficiently slow, unidirectional and steady flow through a porous medium, we have;

$$Q = \frac{kA}{\mu}\frac{\Delta P}{L}, \tag{2.30}$$

where Q is the volumetric flow rate, A is the normal cross-sectional area of the sample, μ is the viscosity of the fluid, ΔP is the pressure difference on either side of the sample, and L is the length of the sample. It is important to note that porous media are rarely isotropic. The permeability along the x-axis of a material is rarely the same as the one along the y-axis, making the permeability a tensor.

Specific surface area The specific surface of a porous medium is defined as the total interfacial surface between the pores and the solid matrix per unit of mass or volume. For porous media, this value is usually very high, above 1 m^2/kg. This property is crucial for many applications of porous media, such as the adsorption capacity or the effectiveness of catalysts. It also shows that for porous media, the ratio of the surface of contact to the bulk volume of fluid is extremely high compared to other applications of fluid mechanics. This highlights the crucial role that interfacial tension plays in porous media.

Figure 2.15: Both a torus and a coffee mug share the same connectivity of one, because they each present only one handle, or hole, inside of their geometry.

The parameters defined above at the large scale arise from the small scale, where the sizes of the pores, their geometry, and their connectivity are the controlling parameters.

Connectivity Connectivity is a parameter that measures how well the pores are connected to each other and is related to the topology of the material. A theorem in topology tells us that the connectivity of a geometry is equal to its 'genus', with the 'genus' being the number of 'cuts' that can be made in the geometry without disconnecting any part of it. It is seen more intuitively as the number of holes in the geometry. For example, a sphere has a genus of 0, while a donut has a genus of 1.

As connectivity only cares about the genus, geometries that appear very different share the same connectivity value. A coffee mug and a torus look quite different from each other, but both of them only have one handle, so they are of genus 1, see Fig. 2.15

Pore size distribution Another important parameter for porous media is the size of the pores, as it has a direct impact on all the large-scale parameters that we saw earlier. One of the ways to measure the sizes of the pores in a sample is to use mercury porosimetry. This is done by injecting a non-wetting fluid at high pressure inside a porous medium and measuring the volume of fluid injected as a function of the fluid pressure. This is often done using mercury, as it is a non-wetting fluid for many materials. Then, from the measured pressure, we can recover the diameter d of the invaded pores using Laplace's equation,

$$d = \frac{4\sigma \cos\theta}{\Delta P}. \tag{2.31}$$

Where ΔP is the difference between the pressure of the mercury and the gas. By starting with a small pressure in the mercury and by gradually increasing it, we invade smaller and smaller pores until all the pores are filled with mercury. This gives us a distribution, where for each value of pressure (and thus pore-size), we have the volume of mercury injected. This can then be translated to a distribution of the pore size, see Fig.2.16.

This technique suffers from numerous issues, as it only measures the entry capillary pressure of a pore or a network of pores, and not directly its size. For example, a big pore connected to the surface through a small constriction will only be invaded when the pressure in the mercury is high enough to enter the constriction, which will lead to a gross overestimation of the volume of small pores. Secondly, it assumes that all the pores are spherical, which is rarely the case. Other techniques, such as X-ray

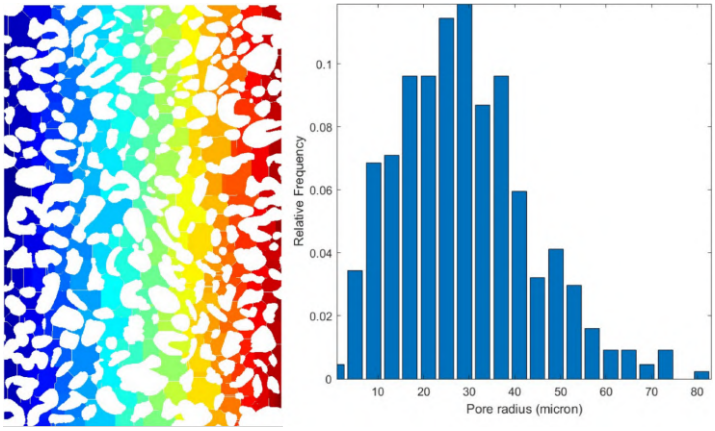

Figure 2.16: Example of a pore-size distribution. On the left is the porous medium analyzed, where all the different pores have been segmented and characterized using specialized software [158, 157]. On the right is the resulting pore size density.

microtomography coupled with powerful image processing algorithms, have been developed to scan the sample and separate pores from each other, producing the pore-size distribution.

2.4.3 Darcy-scale equation of two-phase flow in porous media

We have seen how to characterize a porous medium, its controlling parameters, as well as the fundamental laws of fluid mechanics. Now, we will examine how fluids flow within a porous medium, with a focus on two-phase flow.

Darcy law One of the most fundamental laws for the flow of fluid through porous media is the Darcy law, named after the French engineer Henry Darcy. It was introduced in its publication, 'Les fontaines publiques de la ville de Dijon' [50]. It is a linear law that relates the flow of a single fluid of viscosity μ through a porous medium to a gradient of pressure, at the steady state, and in the Stokes regime, and reads as,

$$\boldsymbol{v} = -\frac{k}{\mu}\boldsymbol{\nabla} P, \tag{2.32}$$

where k is the previously defined continuum scale permeability, which depends only on the structure of the materials. $\boldsymbol{v} = \frac{\partial Q}{\partial A}\boldsymbol{n}$ is the filer speed, or the Darcy velocity, which is the average speed inside the voids of the porous media. This law was found experimentally in 1856, but has since been proven analytically [214].

Capillary pressure curve Let's start with a porous medium initially saturated with wetting fluid, in which we inject a non-wetting fluid by slowly increasing its pressure. For this, the outlet of the sample is covered by a porous diaphragm that stops the non-wetting fluid, but the wetting fluid is free to flow through [57]. We now slowly raise the capillary pressure by small increments, and we give time for the fluids to equilibrate after each increase. When the capillary pressure increases, the non-wetting fluid displaces the wetting fluid, and the saturation of the latter decreases. Since the displacement is slow and the fluids have time to equilibrate, it means that we are in the

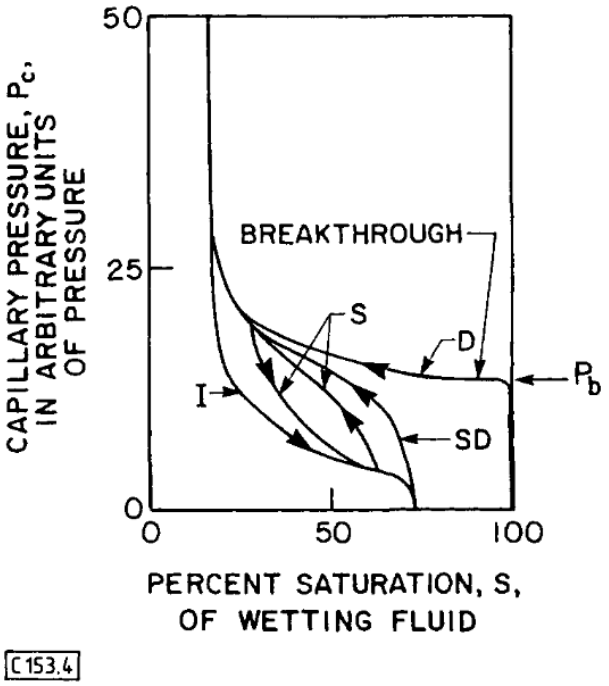

Figure 2.17: Example of capillary pressure curve showing primary drainage (D), imbibition (I), secondary drainage (SD), as well as two scanning curves (S). From this graph, one can recover the breakthrough pressure P_b as well as the irreducible water saturation. This graph also highlights the hysteresis that occurs during this quasi-static displacement. Figure from Dullien (1988).

quasi-static case, where time is no longer a parameter, and the wetting fluid saturation only depends on the imposed capillary pressure, such that

$$P_{nw} - P_w = P_c(S_w) \tag{2.33}$$

where S_w is the wetting fluid saturation, defined as the fraction of pore space occupied by the wetting fluid. Immediately, the saturation in non-wetting fluid can be written as $S_{nw} = 1 - S_w$.

This allows us to draw the capillary pressure curves, see Fig. 2.17. On this figure, the porous media is initially at at 100% of wetting fluid saturation. The drainage is started (curve D), and we can see that the non-wetting fluid does not invade the sample immediately; it must first reach a threshold in capillary pressure to enter the porous medium. This threshold is known as the breakthrough pressure, or the displacement pressure. When the capillary pressure is increased, the wetting fluid saturation decreases, at first very fast, but then it slows down before reaching the irreducible wetting phase saturation. Nowadays, it has been shown that this minimal saturation can reach much lower values than initially thought, because of the existence of wetting films in the roughness of the pores that increase the connectivity of the wetting phase and allow the ganglia of trapped wetting fluid to drain [56, 134]. Once this irreducible fraction is reached, the capillary pressure is slowly lowered step by step, allowing the wetting fluid to imbibe the porous media (curve I in Fig. 2.17). This imbibition is over at $P_c = 0$, where we recover a residual saturation of the non-wetting phase. A secondary drainage can then be made (SD). We observe that the drainage and imbibition curves do not match with each other: the value of the function $P_c(S_w)$ is not uniquely defined.

This hysteresis of the capillary pressure curve is attributed to hysteresis of the contact angle as well as how the pores of different shapes and sizes are connected [58]. This capillary pressure curve is one tool that is used to measure the residual saturation in a porous medium, in the quasi-static condition.

Two-phase Darcy's law The two-phase extension of Darcy's law has been used for almost a century to model the co-flow of fluids inside porous media [141][140]. The law arises from simple consideration: during the steady state flow of two fluids, each fluids occupy one part of the porous medium. Usually, the wetting fluid occupies the small pores, while the non-wetting fluid stays in the bigger pores, see Fig. 2.18[28]. To derive this law, we assume that the two fluids do not interact and that the interfaces between them remain stationary [57]. Under these conditions, the single-phase Darcy's law (2.30) is applied separately to each fluid. Since part of the pore space is occupied by the other fluid, each phase can only flow through a subset of the available pores. Consequently, the permeability for each fluid is a fraction of the total permeability of the porous medium. This fraction is known as the relative permeability and is denoted $k_{r,i}$, where $i = [I, II]$ indicates the fluid phase. Then, the two-phase Darcy's law reads as,

$$v_i = \frac{-k_{ri}k}{\mu_i}\nabla P_i, \tag{2.34}$$

v_i is the average velocity of the fluid i, μ_i is its dynamic viscosity, P_i is the pressure in the phase, and k is the intrinsic permeability of the media as defined in the single-phase Darcy's law. The two pressure gradients are related to each other via the gradient of capillary pressure P_c, such as [111],

$$\nabla P_2 - \nabla P_1 = \nabla P_c. \tag{2.35}$$

Relative permeabilities One of the challenges of this law is to find the relative permeability values, which depend on many different parameters and can differ from medium to medium. But under certain conditions, these relative permeabilities are expected to depend on only one value: the fluid saturation, which is the fraction of the pore space occupied by one of the fluids. For this to be the case, the following conditions must be met: the solid matrix is strongly wetted by one fluid, the viscosity of neither fluid is very high, the surface tension is not negligible, and the system is quasi-steady. If all these assumptions are met, then it is generally accepted that each fluid flows in its own part of the porous media, the wetting fluid being in the smallest pore and along the walls, while the non-wetting fluid flows in the center of the biggest pores, as represented in Fig. 2.18(a), and the interfaces behave like rigid walls [57]. In this case, (2.36) is valid and the relative permeabilities depend only on the saturation of the fluids. Computing the relative permeabilities numerically or theoretically is challenging and sometimes inaccurate. The most reliable way to determine them is through experimental measurements, in which two fluids are injected into a sample, and their respective flow rates are recorded. A common procedure is to first perform a primary drainage, reducing the wetting fluid saturation to its minimum, and then carry out a secondary imbibition. This process yields four curves representing the relative permeabilities of both fluids during drainage and imbibition. The issue encountered is the capillary pressure hysteresis. For a fixed saturation, the capillary pressure is not the same during drainage or imbibition. This leads to a range of relative permeabilities existing for a fixed saturation, as seen in Fig. 2.19. The influence of various parameters, such as contact angle, interfacial tension, and flow rate, on relative permeabilities has been extensively investigated in the literature [57]. One interesting parameter is the viscosity ratio between the fluids. If the non-wetting fluid is much more viscous

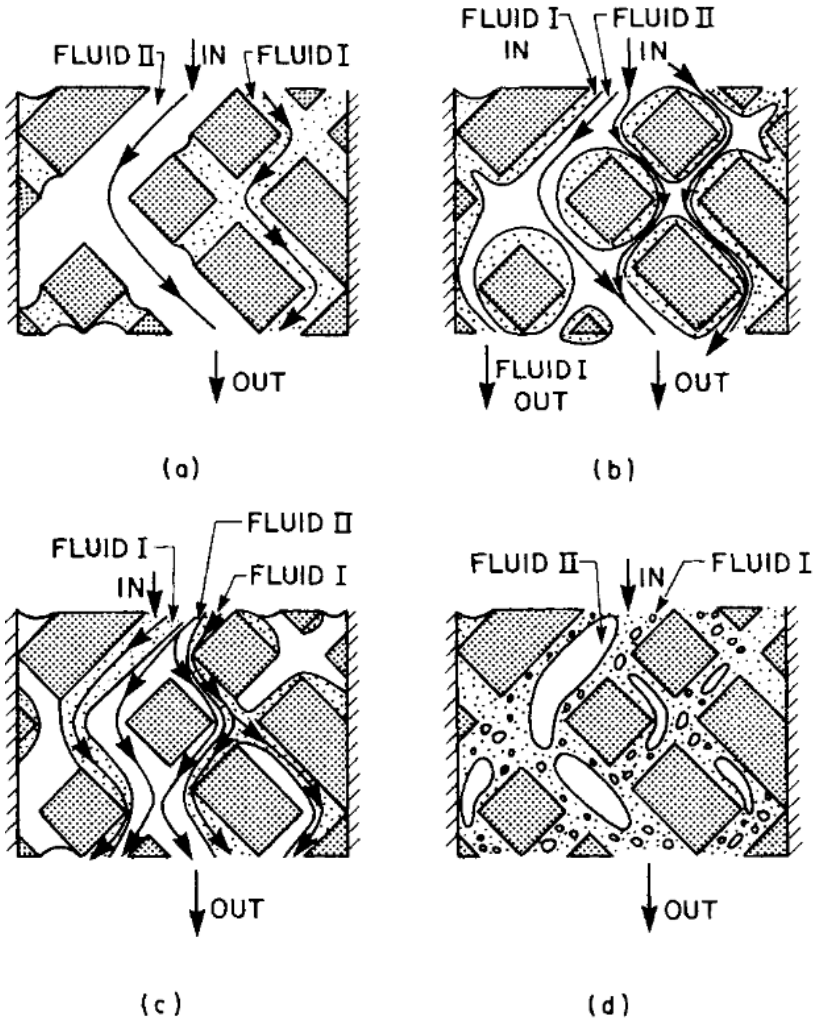

Figure 2.18: Representation of steady state two-phase flow in porous media. (a) Both fluids flow in separate channels, with fluid *I* wetting the uniformly wet solid preferentially. (b) The saturation of fluid *I* has been reduced. Now, both fluids can flow in the same channel. (c) Now the solid is not uniformly wet; each fluid wets different parts of the mixed-wet solid. Both fluids flow in the same channel. (d) One fluid is continuous, and the other is not, with fluid *I* wetting the uniformly wet solid. Figure from Dullien (1988).

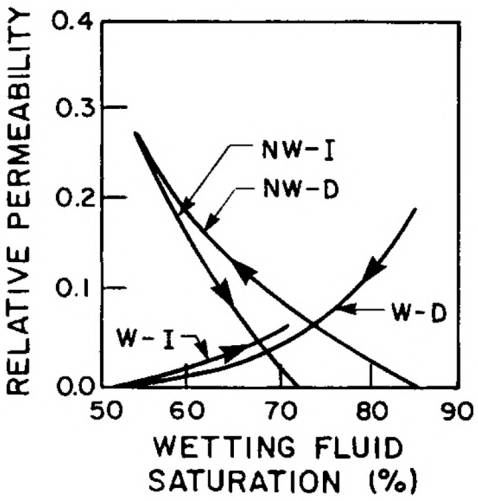

Figure 2.19: Diagram of relative permeabilities, for the drainage (D) and the imbibition (I) for both the wetting (W) and the non-wetting (NW) fluid [58].

than the wetting one, it is possible to reach a relative permeability above one, which is normally impossible! This is visible in Fig. 2.20, where the relative permeability of the non-wetting fluid reaches 180% for low wetting fluid saturation. This behavior is due to the hydraulic coupling between the two fluids. At low wetting fluid saturation, it flows along the walls of the solid matrix, similarly to what is represented in Fig. 2.18(b). Then, the non-wetting fluid flows in the center of the channels. Or, since the flow of both are coupled by the continuity condition, the wetting fluid acts as a lubricant to the flow of the non-wetting fluid, effectively decreasing its apparent viscosity[62]. One can notice that this phenomenon can only increase the relative permeability of the non-wetting fluid, and only when it is more viscous than the wetting fluid. It is also much more visible when the porous sample has a low permeability to start with [146, 49].

Open questions about the validity of the two-phase Darcy equation The validity of Eq. (2.36) has been discussed by numerous researchers, since it relies on very strong assumptions. The existence of a continuous stable flow-path with immobile interfaces, essential for the validity of the law, has been questioned [188][189]. Moreover, the fact that the interface between the fluids behaves like a solid wall is only true for specific situations, where the viscosity ratio of the fluids is far from one, making one fluid almost immobile with respect to the other (like for the co-flow of gas and water). However, when the viscosities of the fluids are comparable, it is known that the viscous coupling at the interface can lead to a transfer of momentum from one fluid to the other[169] [72][94][5]. To take into account this momentum transfer between fluids, an extension to the two-phase Darcy's law has been proposed that introduces cross-permeabilities, or coupling terms, in the two-phase equation [61, 113],

$$v_i = \frac{-k_{i,i}k}{\mu_i}\nabla P_i - \frac{k_{i,j}k}{\mu_j}\nabla P_j, \tag{2.36}$$

where j refers to the second fluid. $k_{i,i}$ refers to the relative permeability of fluid i, while $k_{i,j}$, the cross-permeability, refers to the influence of the pressure gradient of j on the flow of i. These cross-permeabilities are easy to compute for simple situations [18],

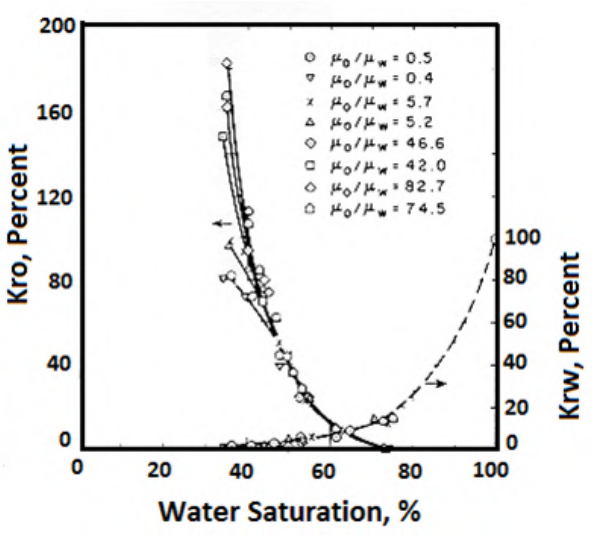

Figure 2.20: Relative permeabilities of oil (o) and water (w) with respect to saturation in a low permeability water-wet sandstone, from Odeh (1959). Several values of the viscosity ratio have been explored.

but for more complex ones, they depend on many different parameters and are hard to predict.

Moreover, this law works only in the Stokes regime, where inertia has no impact. or, more and more studies show that during two-phase flow, inertia can have a significant impact, even for low Reynolds numbers [24, 11, 168, 135].

Chapter 3

Methods for assessing residual trapping in porous media: A review

This chapter aims to systematically identify the physical mechanisms governing residual trapping in porous media and to review the numerical and experimental methods used to quantify its extent, spanning from static to dynamic approaches. We highlight the existing gaps in understanding and modeling residual trapping, particularly in addressing dynamic effects, heterogeneity, and upscaling challenges. Finally, we use these insights to motivate and introduce the specific objectives of this thesis.

3.1 Static estimation of residual trapping

3.1.1 Principle: saturation and capillary pressure relationship

The first approach to estimate the residual saturation of non-wetting fluid is the capillary pressure curve that links the saturation of fluid (S_w) to the capillary pressure (P_c), as we saw in Sec. 2.4.3. By running experiments using rocks from geological reservoirs, one can draw the capillary pressure curve describing the residual saturation, see Fig. 3.1. To correlate these experimental results with other kinds of rocks and fluids, scaling capillary pressures have been introduced, which try to generalize the P_c-S_w curves by taking into account some of the properties of the fluids and the porous media. The first one introduced is the Leverett J function [111, 172] that reads as,

$$J(S_w) = \frac{P_c}{\sigma \cos\theta} \sqrt{\frac{k}{\phi}}, \tag{3.1}$$

with k and ϕ the porosity of the porous media, σ the interfacial tension between the two fluids, and θ the contact angle between the wetting fluid and the solid. The J function is successful at correlating capillary pressure data originating from a specific rock type within the same formation, but fails when the rock type is changed. This is because $\sqrt{\frac{k}{\phi}}$ is an inadequate scaling factor, as it does not take into account how the topology of the pores affects the permeability. The scaled capillary pressure [210] Π_c has been introduced and is defined by taking the characteristic pore or grain size to be

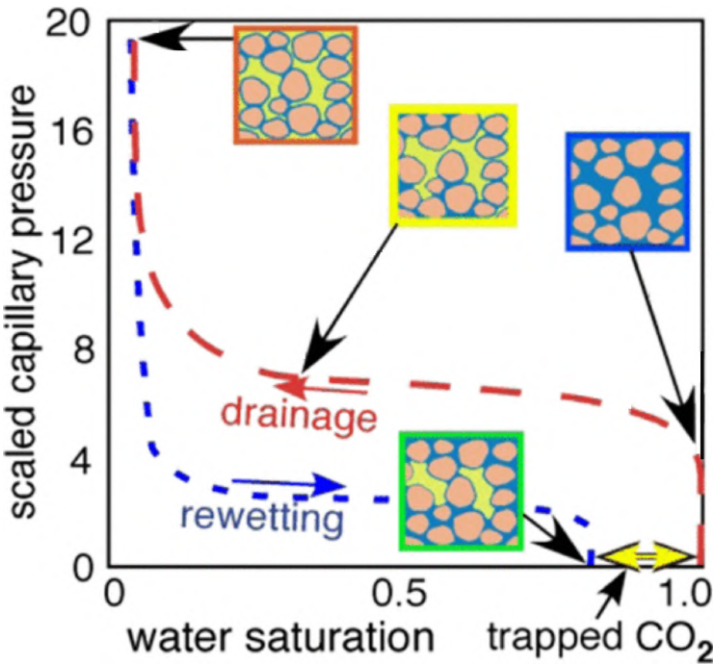

Figure 3.1: Example of capillary pressure-curve relations. The trapped residual saturation of CO_2 is estimated at the end of the secondary imbibition (curve in blue)[210].

the capillary length scale l_c of the porous medium

$$\Pi_c = \frac{l_c P_c}{\sigma}. \tag{3.2}$$

One can also take into account the wettability of the minerals by including a factor $0 \leq w \leq 1$, sometimes assumed to be equivalent to $\cos\theta$, reading as,

$$\Pi_{c,w} = \frac{l_c P_c}{w\sigma}. \tag{3.3}$$

This scaled capillary pressure is used to predict $\Pi_c - S_w$ relationships for geometrically equivalent porous media.

3.1.2 Example of residual CO_2 saturation assessment

Estimation of residual trapping of non-wetting fluid has been done extensively using the relationship between capillary pressure and saturation of the fluid. Measuring the capillary pressure between the fluids gives a range of residual saturation possible, between the drainage and the imbibition curves. A few examples of these studies and their results are found in the Table. 3.1, in which we summarize the type of rocks studied, the fluids used, as well as the resulting residual saturation measured, and the general conclusions of the study.

These studies all show similar conclusions. High aspect ratio in pores leads to more snap-off, which increases the amount of trapped non-wetting fluid. Higher viscosity and density in the CO_2 phase also improve the trapping. Several studies also report alteration of the wettability of the solid by CO_2 at reservoir conditions [210, 199]. They showed the wettability alteration by repeating the experiment with sand aged with $scCO_2$ and brine and finding very different capillary pressure-saturation curves. In

Table 3.1: A few examples of the studies that were done on the residual trapping using the capillary pressure-saturation relationship.

Sample type	Conditions	Residual non-wetting saturation	Key findings	Reference
Limestone and dolomite sands	45 °C, 8.5 MPa-12 MPa $scCO_2$	8%-44%	Higher pressure leads to more trapping, with CO_2 less buoyant and more viscous. Wettability alteration observed, enhancing the trapping.	Wang and Tokunaga (2015)
Berea, Paaratte, Mt. Simon and Tuscallosa sandstones	50 °C, 9 MPa	15%-30%	Trapping increases with initial CO_2 saturation.	Krevor et al. (2012).
Bentheimer and Fontainbleau sandstones	20 °C- 50 °C, 9 MPa-10 MPa. Liquid and supercritical CO_2	16%-32%	Higher viscosity leads to higher trapping. High aspect ratio in the pore leads to more capillary trapping.	Abdoulghafour et al. (2020)
Indiana limestone	50 °C, 4.2 MPa-9 MPa, supercritical and gaseous CO_2	8%-30%	Usage of a sacrificial core upstream to avoid dissolution by the injected fluids. $scCO_2$ is better trapped than gaseous CO_2.	El-Maghraby and Blunt (2013)
Sand	45 °C, 8.5 MPa-12 MPa, $scCO_2$	8%-32%	Wettability alteration of silica surfaces. Better trapping at higher pressure.	Tokunaga et al. (2013)
Unconsolidated sand pack	Ambient conditions, analogue fluids used (n-octane/air and water)	0%-12%	Low residual saturation caused by the homogeneous pore space leading to poor trapping via snap-off.	Mansoori et al. (2009)

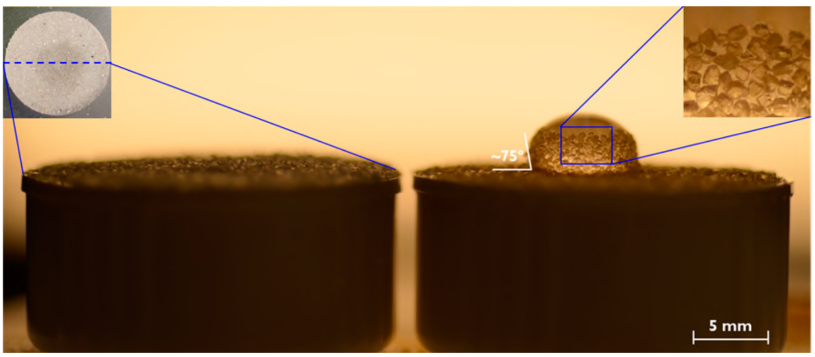

Figure 3.2: Wettability comparison between pre-(left) and post-(righ) experiment limestone sands using DI-water. After exposure to $scCO_2$ and brine at 12 MPa for 6 months, the sand shows wettability alteration toward hydrophobicity [210].

Fig. 3.2, they also performed post-experiment contact angle measurements to verify the wettability alteration

3.1.3 Limitations of static estimation

From Table. 3.1, some researchers reported an alteration of the solid contact angle by the $scCO_2$ and the brine. This wettability alteration changes the shape of the capillary pressure-saturation curves [210, 199]. This was not considered in every studies, as this alteration can occur over a time scale much longer than the experiment duration.

Moreover, for these studies, it is assumed that the entire system is in capillary equilibrium thanks to the quasi-static displacement. This is not always the case, because of the very slow movement of wetting fluid through the films that appear at the surface of the rocks, as discussed in Dullien (1988). This displacement of the wetting phase can alter the wetting saturation at the endpoint of the drainage. However, it is not taken into account in these studies because of the very long time for the drainage to occur.

More generally, quasi-static studies cannot capture the inherently dynamic nature of two-phase flow, which governs fluid trapping through mechanisms such as snap-off and bypass, and gives rise to the hysteresis of capillary pressure–saturation curves. The influence of this dynamic behavior can already be inferred from capillary pressure curve results: several studies have reported that a more viscous non-wetting fluid leads to enhanced CO_2 trapping [210, 2, 124, 199]. Since viscosity is inherently a dynamic parameter (as it characterizes the displacement of the fluid in response to stress), it becomes clear that static approaches are insufficient to fully describe the underlying physics of fluid displacement and trapping.

3.2 Dynamic mechanisms of residual trapping

We have seen in the previous section how to estimate the residual trapping based on static experiments that link residual saturation with capillary pressure, and how it is not enough to have a proper understanding of the two-phase flow displacement. Thus, we need to take a deeper look at the dynamics of the displacement on the pore-scale, where the physics resides.

3.2.1 Displacement of the meniscus

In a fundamental work, Lenormand et al. (1983) described how the meniscus between the two fluids moves inside a porous medium. For this, they designed a 2-D network of capillaries made out of transparent resin completely wetted by one of the fluids ($\theta = 0$). The capillaries were made out of rectangular ducts of constant depth but varying width that would intersect each other. Using this model, they studied both drainage and imbibition.

Drainage In the case of drainage, the non-wetting fluid has only one way of invading a rectangular duct: via piston-like displacement, see Fig. 3.3 (a). When the non-wetting fluid enters the duct, it cannot invade the corners, as its pressure is not high enough, meaning that the corners are still saturated with the wetting fluid. The amount of fluid trapped in these corners depends on the capillary pressure between the fluids. Due to the curvature of the meniscus inside the channel, the pressure of the non-wetting fluid needs to be above a certain threshold to invade a wetting-fluid-filled capillary. This threshold is called the entry capillary pressure and is expressed as,

$$P_{entry} = P_w + 2\sigma\left(\frac{1}{w} + \frac{1}{D}\right), \tag{3.4}$$

where P_w is the pressure in the wetting phase, and w and D are respectively the width and the depth of the rectangular channel. This means that, for a given pressure of the non-wetting fluid, only pores above a certain threshold can be invaded.

Imbibition During imbibition, the meniscus can also move in a piston-like fashion, see Fig. 3.3 (b), but when it reaches an intersection, two other displacement mechanisms can be observed. First, the I_1 imbibition that occurs when the wetting fluid arrives through three adjacent capillaries, see Fig. 3.3 (c), where the successive positions of the meniscus are represented. When position 2 is reached, the menisci no longer touch the walls, and the curvature of the meniscus decreases suddenly. This creates an instability where the meniscus quickly enters the channel filled with non-wetting fluid. The I_2 imbibition occurs when the wetting fluid arrives from two capillaries. When the meniscus reaches the A position, an instability occurs, and the meniscus is separated into two menisci, see Fig. 3.3 (d). At low flow rates, the wetting fluid does not invade the entirety of the pores, but flows along the corners and crevices of the solid, without invading the center of the pores [224]. This is known as corner flow and creates wetting films along the edges of the walls.

3.2.2 Transient event during meniscus movement

During meniscus displacement, two key phenomena can occur, each of which can significantly influence the flow dynamics and the resulting trapping: snap-off and Haines jumps.

Snap-off We already briefly discussed snap-off in Sec. 1.2.2. It was first introduced in the seminal work of Roof (1970). It describes an instability of the front interface, which causes the wetting fluid to accumulate in a constriction and cut, or 'snap', the non-wetting phase in two. This phenomenon can occur both during drainage and imbibition. To explain it, it is important to consider the wetting fluid left in the corners of the channel after drainage or during imbibition via corner flow. Even if the walls are smooth, there is still a layer of wetting fluid after drainage known as Bretherton's layers [30]. These films increase the connectivity of the wetting phase, which can flow

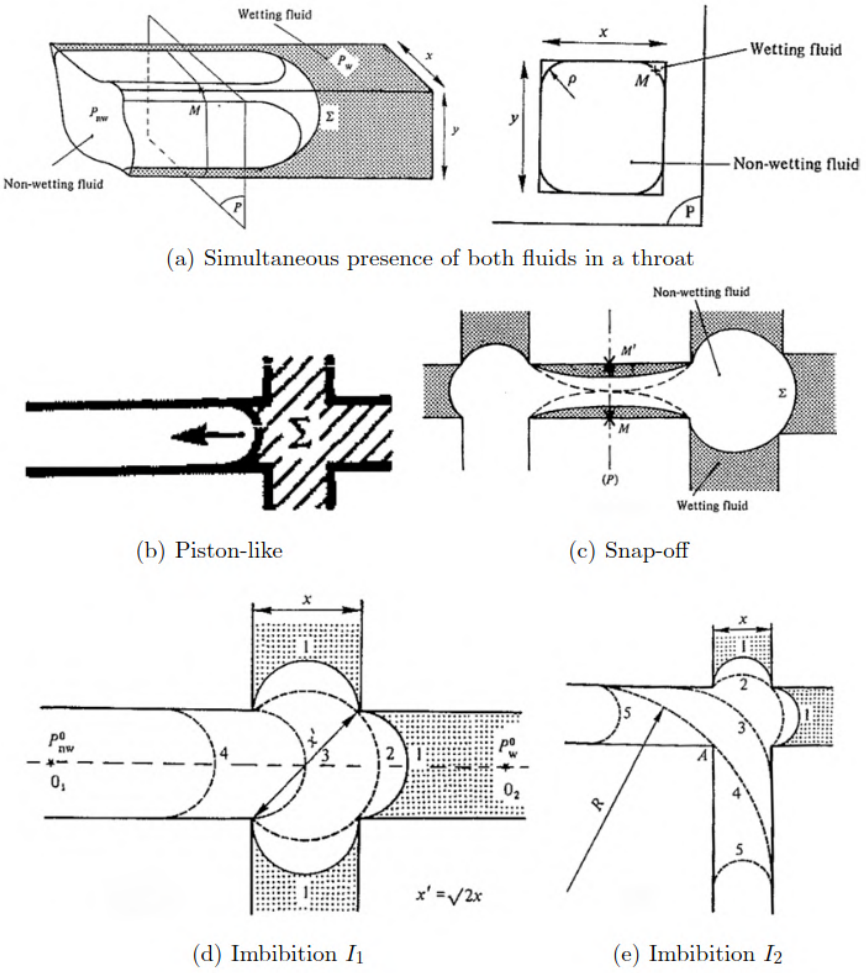

(a) Simultaneous presence of both fluids in a throat

(b) Piston-like

(c) Snap-off

(d) Imbibition I_1

(e) Imbibition I_2

Figure 3.3: Displacement mechanisms of the meniscus at the pore-scale [108]. (a) Piston-like displacement of the meniscus during drainage, leaving films of wetting fluid in the corner. (b) Piston-like displacement during imbibition. The whole section is invaded by the wetting fluid. (c) Representation of the snap-off mechanisms. (d)-(e) Type I_1 and I_2 imbibitions. Figure from Lagree (2014).

through pores that seem occupied by the non-wetting phase. They also result in the formation of an additional interface between the fluids along the channel walls. This creates a local capillary pressure, which is different from the capillary pressure across the front meniscus. These two capillary pressures are the key parameters for snap-off. When the meniscus is in the constriction, or pore-throat, the curvature of the front meniscus is high, leading to a high capillary pressure, see Fig. 3.4. But when the interface enters the following pore, its curvature and thus the capillary pressure across the front meniscus decrease, while the local capillary pressure at the pore throat remains high. When the capillary pressure at the front meniscus decreases below the local capillary pressure at the pore-throat, the difference in pressure between the front meniscus and the constriction leads the wetting phase to flow back into the constriction. The wetting films thicken and eventually become unstable, rejoining at the center of the channel, creating a snap-off event [53, 165]. After the ganglion has been separated from the bulk of the fluids via the snap-off, it can stay trapped inside the porous matrix, but there are also regimes where it reconnects to the bulk, before another snap-off event occurs, see Fig. 3.5. These results show that even when we observe snap-off, we not always have the formation and trapping of fluid ganglia.

Haines jumps During drainage, the interface displacement occurs through two distinct mechanisms: isons and rheons [139]. Isons are reversible displacement of the interface, as we saw with piston-like invasion. But once the pressure in the non-wetting phase is no longer enough to invade new pores (because of the entry capillary pressure), the pressure in the invading phase increases, and so does capillary pressure. According to the Young–Laplace law, this increase in capillary pressure requires an increase in the curvature of the fluid–fluid menisci. The menisci are gradually pushed into the pore throats through slow, quasi-static, and reversible movements [139]. If the capillary pressure continues to rise, the meniscus in the largest pore throat eventually reaches a critical point where it can no longer sustain the pressure. At this stage, the meniscus becomes unstable and rapidly reconfigures into a new metastable state, invading one or more neighboring pores. This abrupt and irreversible event is known as a rheon, or Haines jump [74, 139]. This irreversibility gives rise to the hysteresis observed in drainage/imbibition cycles in porous media [66].

Haines jumps are frequent and significant; it has been reported that over 50% of the pore volume is invaded through these rapid interface movements during drainage [24]. During a jump, the local fluid velocity can reach values one to three orders of magnitude higher than the average front velocity [136, 168, 10]. In capillary-dominated regimes—typically in systems with small characteristic lengths—the speed of the jump is independent of the bulk flow rate. However, when viscous and inertial forces become more prominent, the velocity of the jump begins to depend on the imposed flow [10].

Because of the rapid nature of the jump, the mass flux required to fill the newly invaded pore exceeds what can be delivered by the fixed boundary flow rate during that short time [136, 10]. To compensate, fluid is drawn from neighboring pores, making the jump a cooperative event. While the invading meniscus rapidly advances into one pore, adjacent menisci retreat to supply the necessary fluid volume. As a result, Haines jumps are not purely local phenomena; their influence propagates through the surrounding pore network, see Fig. 3.6 [136, 198]. These jumps occur during drainage, but can also appear during imbibition [66]. This mechanism will be studied in more detail in Chapter. 8.

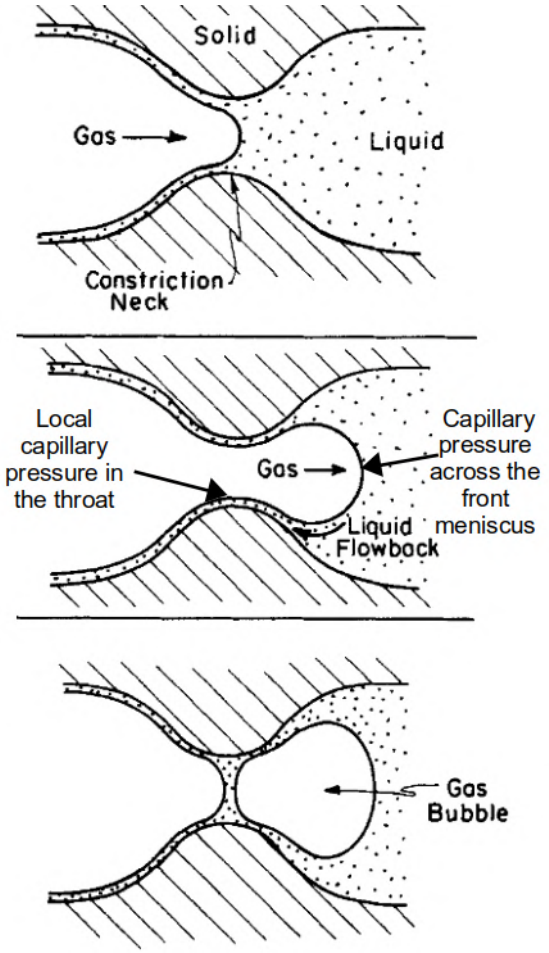

Figure 3.4: Snap-off in a pore-throat, adapted from Ransohoff et al. (1987). As the gas invades the porous medium, it leaves behind a thin liquid film along the pore walls. When the advancing gas meniscus enters a constriction, the capillary pressure increases. Upon passing through the pore throat into the next pore, the meniscus relaxes, leading to a drop in capillary pressure at the front. However, because of the narrow geometry at the constriction, the local capillary pressure there remains high. If the capillary pressure at the front meniscus falls below the interfacial pressure within the pore throat, a snap-off event occurs, resulting in the formation of a gas bubble.

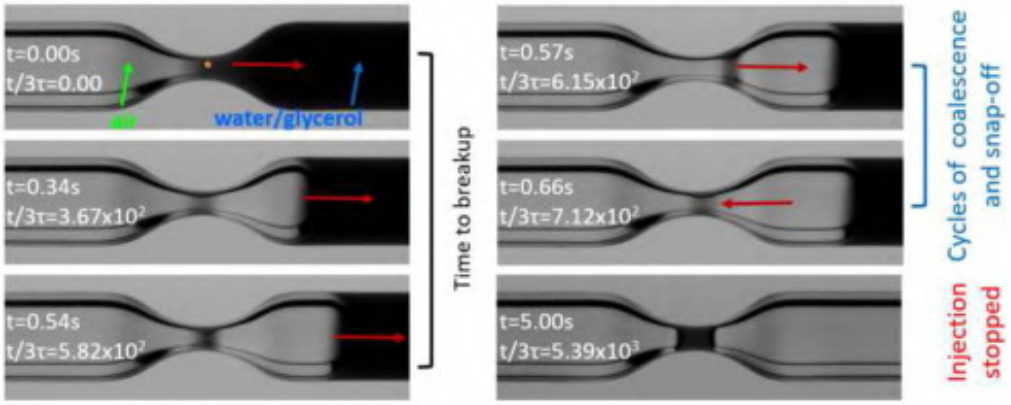

Figure 3.5: Cycle of snap-off and reconnection in a constricted capillary. The red arrow shows the direction of the flow of wetting fluid, from Roman et al. (2017).

3.2.3 Lenormand phase diagram

Following their work on the displacement mechanisms at the pore scale, Lenormand (1990) performed drainage and imbibition experiments using a wide range of fluid and injection speeds. The different fluids used in their studies had a viscosity between 0.32 mPa·s and 1000 mPa·s. To characterize their experiments, they used the capillary number Ca and the viscosity ratio M. Ca is defined through the defending phase and reads as,

$$Ca = \frac{\mu_2 u}{\sigma}, \tag{3.5}$$

where μ_2 is the viscosity of the injected fluid. They performed experiments over a wide range of Ca and M for both imbibition and drainage, and were able to recover general trends in the invasion of the porous media for both.

Drainage In the case of drainage, the meniscus can only move in a piston-like manner, and capillary force prevents spontaneous imbibition. During their experiments, they were able to highlight three main invasion patterns. These three regimes correspond to the limits where two of the three involved forces (capillary forces and the viscous forces in both the defending and invading fluids) are negligible, see Fig. 3.7.

- The stable displacement (for $M > 10$ and $Ca > 10^{-1}$), when the capillary and the viscous forces in the defending fluid are low. In this regime, the invasion pattern presents a flat front, and only very little defending fluid is left behind the interface. This is a regime where we recover most of the defending fluid. According to [152], the limit of this stable regime is characterized by the dimensionless number

  $$I_{sc} = \frac{(\mu_1 - \mu_2) V D^2}{C^* \sigma k} \tag{3.6}$$

  for a cylindrical core, where k is the permeability, D the core diameter, V the velocity of the interface, C^* is a wettability constant such as $C = 2\pi\sqrt{3C^*}$, where C is the Chuoke's constant [43]. If $I_{sc} < \pi^2$, the displacement is stable, whereas it is unstable for higher values.

- The viscous fingering regime (for $M < 10^{-3}$), where it is the viscous forces in the displaced fluid that dominate. This means that the pressure drop in the injected

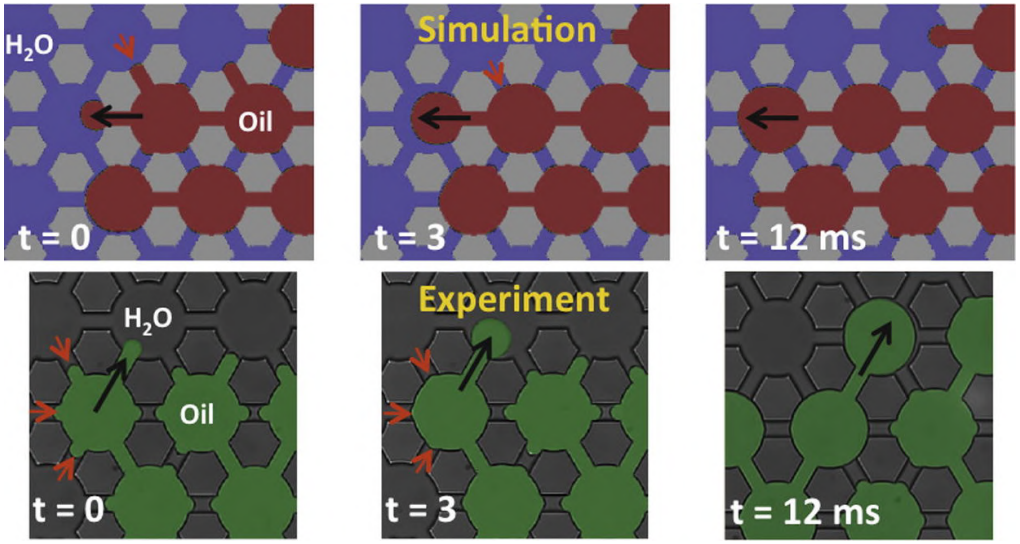

Figure 3.6: Experimental and simulation results displaying the cooperative behavior of the fluids during Haines jumps. The depth of the system is 5 µm, while the width of the pore-troat is 13 µm [10].

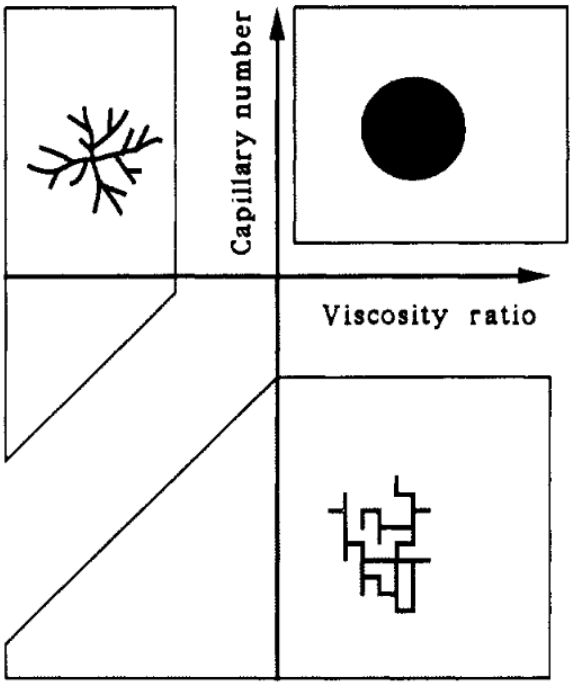

Figure 3.7: The different regimes observed during drainage of a pore network, from Lenormand (1990).

fluid is negligible. This leads to the formation of a finger-like pattern that grows toward the outlet, which only displaces a small fraction of the defending fluid. One finger generally grows faster than the others and inhibits their development. This pattern is a direct consequence of the Saffman-Taylor instability, presented in Appendix. A.

- The capillary fingering (for $M > 10^{-4}$ and $Ca < 10^{-6}$), where the two viscous forces are negligible. This regime creates fingers that randomly invade the porous medium, capable of even growing backward. They form loops, trapping the wetting fluid inside the geometry, leading to poor displacement efficiency. This is caused by the way the menisci can only enter ducts that are above a certain threshold in size defined by (3.4).

These three regimes can be assimilated into three different statistical models, which allows for reproducing the pattern formed during drainage using numerical simulations. The capillary regimes correspond to the invasion-percolation model, while the viscous fingering and the stable regime correspond respectively to the anti-Diffusion Limited Aggregation (anti-DLA) and the DLA models [109]. When the injected fluid reaches the outlet (percolation), it defines a preferential pathway and cannot explore other parts of the geometry.

Since the pioneering work of Lenormand and Zarcone (1985), several studies have expanded our understanding of the three flow regimes [225, 211, 202, 129, 45]. However, the exact limits of these regimes vary greatly from study to study. One reason that was advanced to explain this behavior is that each work used a different pore-network geometry, showing that these regimes are not only functions of Ca and M but are also sensitive to the topology of the pore network. Understanding the pore-scale displacement mechanisms is essential to predict residual trapping under various conditions.

For the CCS process, the viscosity ratio is between 0.03 and 0.2 [143] and the capillary number is between 10^{-5} and 10^{-10}, meaning that the injection of CO_2 underground is in between the viscous and capillary regimes, leading to a poor displacement efficiency.

Imbibition The same study was conducted for imbibition, i.e., the displacement of a non-wetting fluid by a wetting fluid [108]. But here, the situation is more complex, as the fluid can not only move in a piston-like manner, but can also flow along the wall of the channel. Moreover, the size of the ducts also plays a crucial role in the displacement. At high flow rate (high Ca), we still recover a viscous unstable and a viscous stable regime, see Fig. 3.8. When the capillary number is decreased, we first encounter the continuous capillary regime, where the meniscus moves mostly via piston-like displacement and invades the smallest pores preferentially because of spontaneous capillary imbibition. For an even lower capillary number, the invasion no longer occurs via piston-like displacement, but instead by corner flow, meaning that the wetting fluid moves through the corners of the ducts and invades the smallest pores in the geometry by filling them via snap-off. This leads to pores filled with wetting fluid without being connected to each others, also called the discontinuous capillary domain.

3.3 Techniques to investigate residual trapping

Two main approaches are commonly employed to study residual trapping dynamically: experimental investigations and numerical modeling.

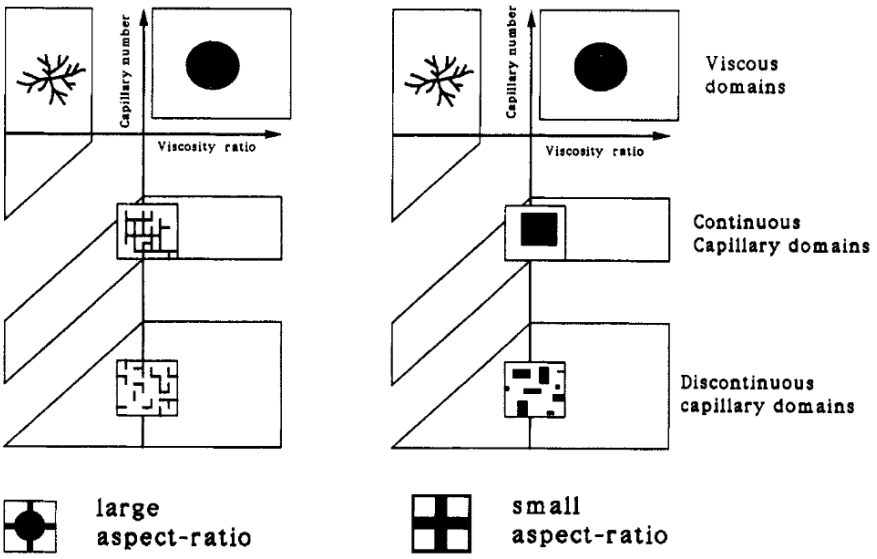

Figure 3.8: Phase diagram in the case of imbibition from Lenormand and Zarcone (1985). Similarly to the drainage diagram, we recover a viscous unstable and a viscous stable regime, as well as a capillary regime. But due to the different displacement mechanisms available to the meniscus in imbibition, the situation is more complex and can lead to disconnected ganglia of wetting fluid because of corner flows.

3.3.1 Experimental approaches

Core flooding approach To investigate the dynamics of fluids during residual trapping, we need to image the fluid inside the porous medium. This has driven the development of specialized imaging techniques for visualizing the fluids inside the cores. Many of those are imported from the medical field, such as X-ray microtomography [24, 185] or Nuclear Magnetic Resonance (NMR) [46].

Microtomography uses X-rays to generate cross-sections of an object, which are then combined to reconstruct a 3D model without destroying the sample. The prefix micro refers to the pixel size of these cross-sections, typically a few micrometers. The principle of microtomography is presented in Fig. 3.9. To image a porous medium, a beam of high-energy photons passes through the sample and reaches a receptor that records the transmitted intensity. The sample is then rotated incrementally, and the process is repeated. From the collected data, the internal structure of the material is reconstructed using advanced software. Recent technological advances have significantly improved both spatial and temporal resolution, making it possible to achieve sub-millisecond time resolution while maintaining a spatial resolution of about 10 µm [198]. Wildenschild et al. (2011) used X-ray tomography to study the impact of interfacial tension, viscosity, and flow rate on capillary trapping. They used the scan to compute the interfacial area between both fluids. They report that a more viscous non-wetting fluid leads to higher residual saturation. Spurin et al. (2019) used X-ray scans to image a carbonate rock during two-phase flow, and highlighted the intermittent nature of the flow. This means that the continuous flow paths assumed for the two-phase Darcy's law to hold are not always true. In a following work, they identified that the intermittency of the flow depends on both the capillary number Ca and the viscosity ratio M [189]. In a recent study, the same group looked at the impact of changing the flow rate on the connected flow path, and also showed that starting the injection at a low flow rate and

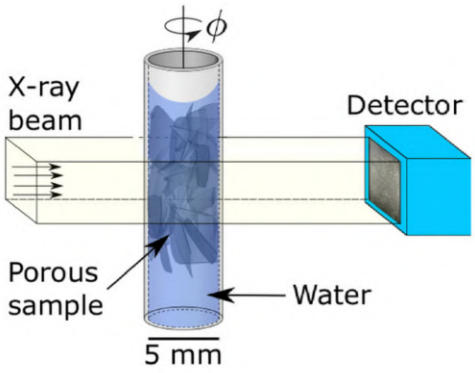

Figure 3.9: Working principle of the X-ray microtomography. The material is bombarded with X-rays, and the transmitted intensity is measured by a receptor. This can then be used to reconstruct the interior of the material [198].

increasing it later increases the residual saturation [190]. Using a column composed of glass beads, Altman et al. (2014) showed that capillary forces can trap between 2% and 15% of the injected CO_2 after secondary imbibition, depending on the wettability of the beads, with a better potential for storage for hydrophilic beads. This indicates that the wettability of the system plays a role in the fluid's trapping.

X-ray tomography, coupled with image processing techniques, also allows for the study of the topology of the porous media. The Euler's number χ is characterized as the integral of the curvature over the entire object. It can also be defined using the genus that we briefly introduced in Sec. 2.4.2 and reads as,

$$\chi = \beta_0 - \beta_1 + \beta_2, \tag{3.7}$$

where β_i is the i-th Betti number. β_0 is the number of objects, β_1 is the genus, and β_2 is the number of voids or loops in the objects. Using Euler's number, Andersson et al. (2018) introduced the notion of morphological aspect ratio and correlated it with residual saturation. A similar approach has been taken by Herring et al. (2013). In Fig. 3.10, after a secondary imbibition, they were able to link the residual saturation of the non-wetting phase to the Euler's number of the non-wetting phase after the first drainage, but it does not apply for any geometry, as the relationship was not found for a glass bead pack. They also studied cyclic injection of water and gas [76]: after the secondary injection, another drainage is performed, followed by a tertiary imbibition. This cycle of drainage and imbibition is repeated up to three times. During each cycle of injection, they followed Euler's number and the residual trapping. In Fig. 3.11, they reported the relationship between initial and residual saturation based on the number of cycles performed. After the first imbibition, between 0% and 27% of the CO_2 present in the porous media before the imbibition was still trapped inside the matrix. But for the second cycle of drainage and imbibition, these values increased to more than 50%. With these experiments, they showed that a cyclic injection of CO_2 could improve the residual trapping of CO_2. A more in-depth description of topology, Euler's number, and Minkowski functionals can be found in Armstrong et al. (2019).

Some studies were also able to image the movements of the fluids inside the porous material at high speed using strong X-rays sources. Berg et al. (2013) were able to image Haines jumps (Fig. 3.12) and snap-off events (Fig. 3.13) at 83 frames per second with a voxel size of 3 µm using high-speed synchrotron-based microtomography, and estimated the amount of energy dissipated during Haines jumps, highlighting their

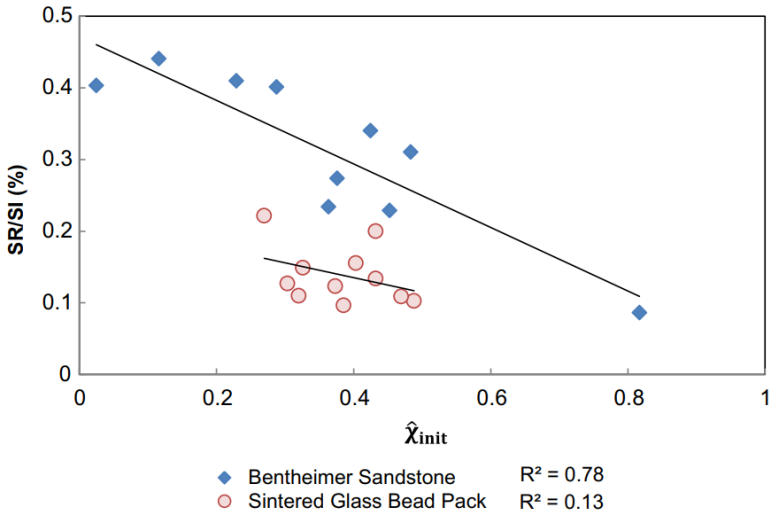

Figure 3.10: Residual saturation (S_r) normalized by initial saturation (S_i) plotted as a function of normalized Euler number at initial saturation (after first drainage) for a sandstone and a glass bead pack. A correlation exists between the Euler number and the residual saturation for the sandstone, but this is not the case for the glass bead pack [77].

role in the hysteresis of two-phase flow in porous media. A similar study was conducted by Tekseth et al. (2024) to observe Haines jumps, reporting on the importance of inertial during these jumps and the nonlocal effects they have on the system. This highlights the importance of Haines jumps and snap-off during the flow, and that a proper understanding of their impact during the invasion is important to accurately assess the capillary trapping.

This work shows the importance of a proper understanding of the impact of snap-off and Haines jumps on two-phase flow.

Microfluidic approach To study snap-off and Haines jumps, small-scale analog models are preferred to microtomography, as they do not require special equipment, are less time-consuming, and allow for very high spatial and temporal resolution without the need for a synchrotron. Moreover, it allows one to isolate a specific phenomenon and remove the constraint on spatial and temporal resolution, as the flow can be imaged using an optical camera. For these reasons, many researchers use these small-scale artificial models, similar to Lenormand and Zarcone (1985), also known as microfluidic devices, to study two-phase flow dynamics and residual saturation [225, 129, 73, 136, 81]. More details on the fabrication and usage of these devices can be found in Chap. 4.

For example, Cottin et al. (2010) studied the competition between the viscous and capillary forces during drainage with a favorable viscosity ratio ($M > 1$). Zhang et al. (2011) followed up on the study of Lenormand and Zarcone (1985) using a porous medium made of cylindrical grains homogeneously distributed. They probed a larger range of capillary number and viscosity ratio, and recovered similar drainage regimes and residual saturation. Their work was continued by Wang et al. (2013), who used $scCO_2$ as a non-wetting phase and water as a wetting fluid to replicate the conditions of underground storage. They observed that the displacement was dominated by either capillary fingering for low Ca or viscous fingering for high Ca with a crossover between capillary and viscous fingering between $\log Ca = -5.91$ to $\log Ca = -5.21$, where they

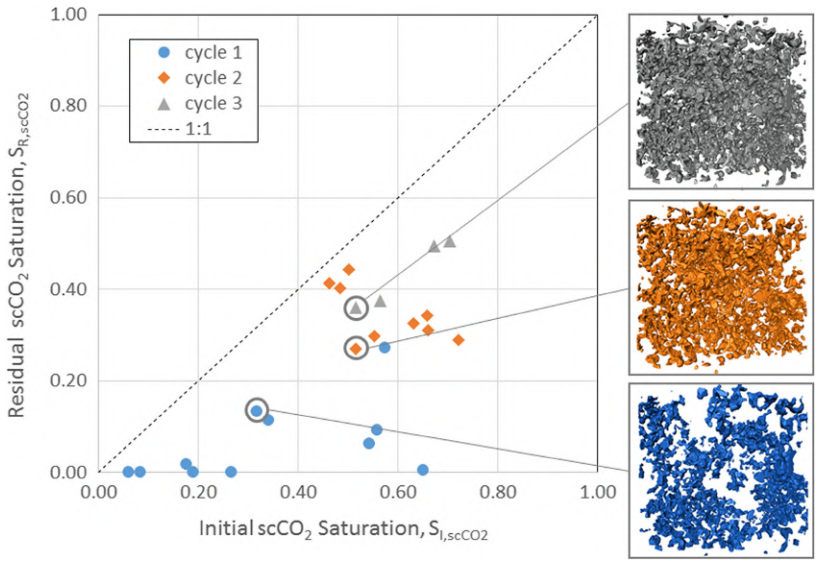

Figure 3.11: Relationship between residual and initial saturation of $scCO_2$, where the values are differentiated based on the number of imbibition-drainage cycles performed. 3D visualizations of the non-wetting phase for different cycles are shown on the right [76].

measured the lowest $scCO_2$ saturation. A study by Rabbani et al. (2018) experimentally showed that a particular design of porous media can be used to inhibit or promote the formation of viscous fingers in a micromodel. All the studies mentioned above report the same three drainage regimes, but the relationship between the final saturation of the invading phase and Ca and M is not agreed upon. Some studies show an increase in the saturation with Ca [33, 45], while others predict nonmonotonic behavior [222]. For example, in Lenormand et al. (1988), the authors reported a decrease in the saturation during the transition between capillary and viscous fingering, a conclusion supported by numerous other studies [211, 39, 114, 162].

Another parameter of importance during two-phase flow is the wettability of the solid. In Fig. 3.14, we present the displacement patterns obtained by Zhao et al. (2016), who systematically varied the capillary number and wettability of the micromodel. They reported that increasing the affinity of the solid to the invading fluid results in a more efficient displacement of the defending fluid (cooperative pore-filling), up to a certain threshold where the injected fluid starts to flow in the corners of the porous media (Fig. 3.3 (a)), leading to a poor displacement. Another example of the influence of wettability on immiscible displacement in porous media is the study of Hu et al. (2017), where they performed experiments using a microfluidic device composed of a periodic and regular arrangement of cylindrical posts, using $scCO_2$ and brine. They used chemical treatment to obtain two wettability states: water-wet and intermediate-wet. They then studied the impact of wettability on the trapping of non-wetting fluid. After a secondary imbibition, they showed that if the solid is less hydrophobic, it increases the CO_2 residual saturation. Indeed, a more hydrophilic material promotes cooperative pore-filling by the injected wetting fluid and reduces the by-pass trapping, which was the main trapping mechanism in this study. Irannezhad et al. (2023) studied two-phase flow in a micromodel presenting a heterogeneous wettability, and showed how water preferentially fills water-wet clusters of pores, but encircles weakly water-wet clusters. This highlights the complexity and non-monotonic impact of the

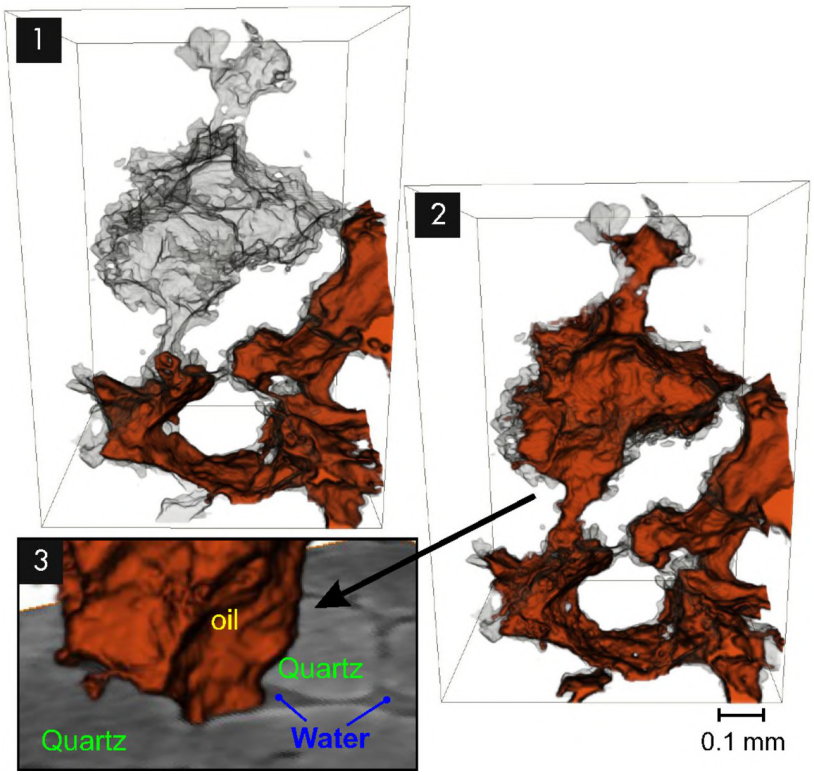

Figure 3.12: (1-2) Oil-filling event of a single pore during drainage. (3) cross-section showing the wetting film along the roughness of the solid [24].

wettability on the two-phase displacement. Li et al. (2021) investigated the flow of liquid CO_2 at the pore scale using Particle Image Velocimetry (PIV) in a micromodel with different wetting properties, and highlighted how the wettability profoundly alters the dynamics of the invasion. When CO_2 is injected in a water-wet micromodel, the invasion occurs in a succession of Haines jumps, while at intermediate wetting conditions, these bursts disappear and a cooperative pore-filling occurs, leading to a more compact displacement pattern.

Other studies have looked at the impact of the Haines jumps on the trapping of fluids, as these jumps lead to high interfacial velocities and can affect the flow several pores away from the local jumps [129, 10, 168, 11]. Moebius and Or (2012) highlighted that these jumps can locally cause inertia to become important and impact the invasion of the media. Armstrong and Berg (2013) showed that Haines jumps impact the surrounding pores because of the redistribution of fluids that occurs. The presence of these jumps in a heterogeneous micromodel has also been highlighted by Roman et al. (2016). All these studies show the presence of Haines jumps and how inertia becomes important during the jumps, but studies on its impact on residual trapping are still scarce.

3.3.2 Numerical modelling

In addition to experimental methods, numerical simulations are widely used to predict residual saturation during two-phase flow in porous media. The two approaches are complementary: experimental data are essential to validate simulation results, while simulations help identify the parameter ranges where the phenomena of interest can be

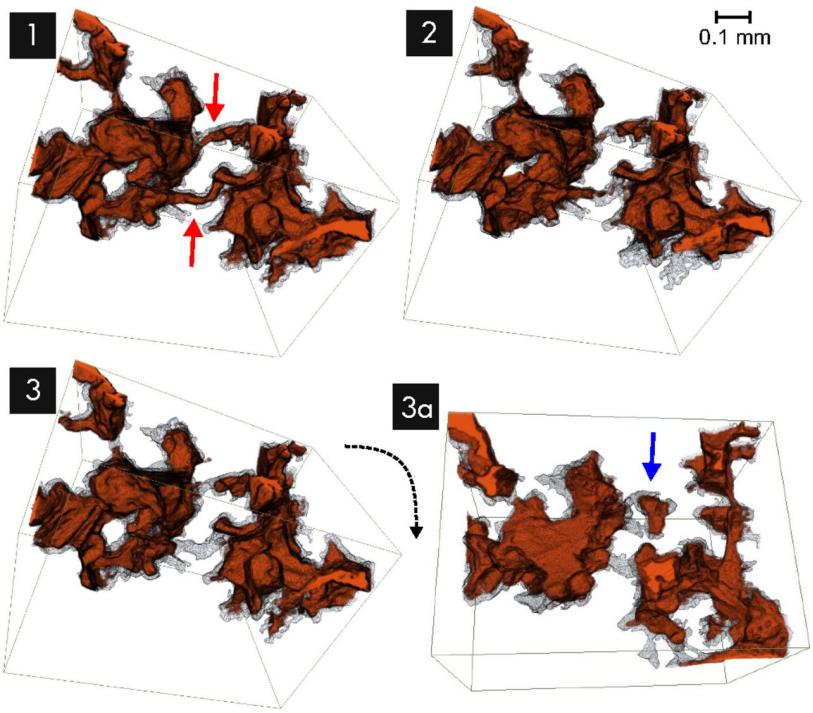

Figure 3.13: (1-3) Sequence of snap-off in the narrowest pore-throats (red arrows) during imbibition, leading to the trapping of an oil ganglion (3a). [24].

observed. Numerical models span multiple scales, from large-scale approaches based on two-phase Darcy's law to predict CO_2 migration in geological formations, down to pore-scale simulations where the Navier–Stokes equations are directly solved to capture the detailed fluid dynamics.

Direct Numerical Simulation (DNS) Direct simulation of the flow in a given pore geometry has greatly improved in recent years, thanks to conjoined progress in hardware and software, and is now able to capture the complex physics of two-phase flow, such as snap-off [165] or Haines jumps [66], but difficulties are still encountered. For example, for low capillary number simulations, the spurious currents that appear at the fluid-fluid interface can lead to important errors in the shape of the interface [184]. Wettability, which plays a crucial role in two-phase flow in porous media, is usually modeled by imposing a contact angle between one fluid and the pore wall. However, this approach is not enough to take into account the change in wettability that can occur with a change of pH, salinity [91], or even the hydrodynamic conditions [47]. This is also an issue when thin films are present in the system, as their impact on the wettability is great, but their small size makes them almost impossible to resolve explicitly, since the mesh used for the simulation is much bigger than the films. Different approaches have been proposed to replace the fixed contact angle model, but they are still in development. One of these approaches is to take into account the very thin film (50 to 300 nm) ahead of the contact line. Using a lubrication model accounting for the intermolecular interactions, it is possible to predict the wettability of the system without any assumptions on the contact angle. It also predicts the wettability changes due to fluid composition changes [145].

Different methods can be used to solve the Navier-Stokes equation: computational

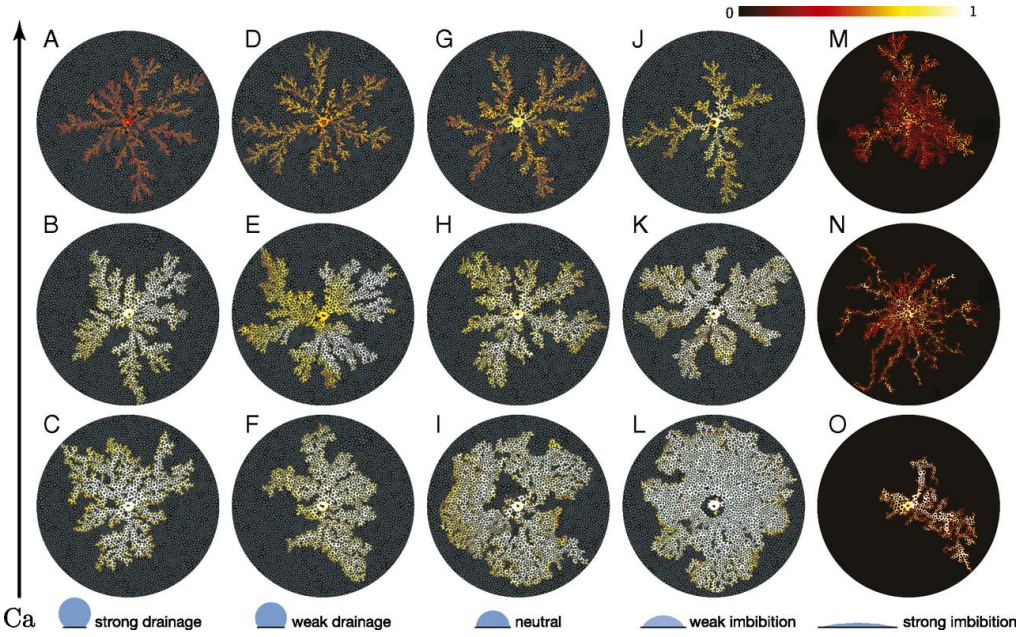

Figure 3.14: Displacement pattern for different capillary numbers (bottom to top: $Ca = 2.9 \times 10^{-3}$, 2.9×10^{-2}, and 2.9×10^{-1}) and contact angle (left to right: $\theta = 150, 120, 90, 60, 7$). The saturation in each pore is color coded: pores in red are only partially filled with invading fluid, while pores in white are fully saturated [224].

fluid dynamics, where an Eulerian grid is used to discretize the spatial differential operator, using methods such as the finite difference method, the finite volume method, or the finite element method [184]. Other methods are available, such as the Lattice Boltzmann Method (LBM), which uses the Lattice Boltzmann equation to find the probability of finding a fluid molecule at a given position. Due to the huge numbers of particles, this statistical approach converges to the solution given by the Navier-Stokes equation. This approach is very common in porous media, and is often used to predict the relative permeabilities [84] and the residual saturation [200]. The modelling of the fluid-fluid interface is challenging using LBM, but recent advancements have improved the predictive capabilities [220]. Another method is the Smooth Particle Hydrodynamics (SPH), which is a mesh-free Lagrangian approach where the fluid is modeled as a set of moving particles [20].

Pore Network Modeling (PNM) DNS is very computationally expensive, which limits its use if one does not have access to powerful computers. Even in this case, performing DNS simulations over an entire core is still out of reach. To upscale and predict the flow on a larger scale, simplifications need to be made. This is the goal of Pore Network Modeling. The porous medium is described as a network of pores connected by throats of ideal geometries, see Fig. 3.16, neglecting the complex structures of the pore; only their connectivity matter. Laws are then chosen to describe the 1-dimensional flow inside the pore throats. Coupled with mass conservation, we reach a system of equations that one can solve to describe the pressure field inside the pore network and model the dynamics of the fluids [27, 70]. This method can be automated, and more and more commercial software can build a pore network using only the microtomography scans of a rock sample. It is also a lot less computationally intensive than DNS, allowing for the modeling of the flow over a much bigger section of the porous media. The scale

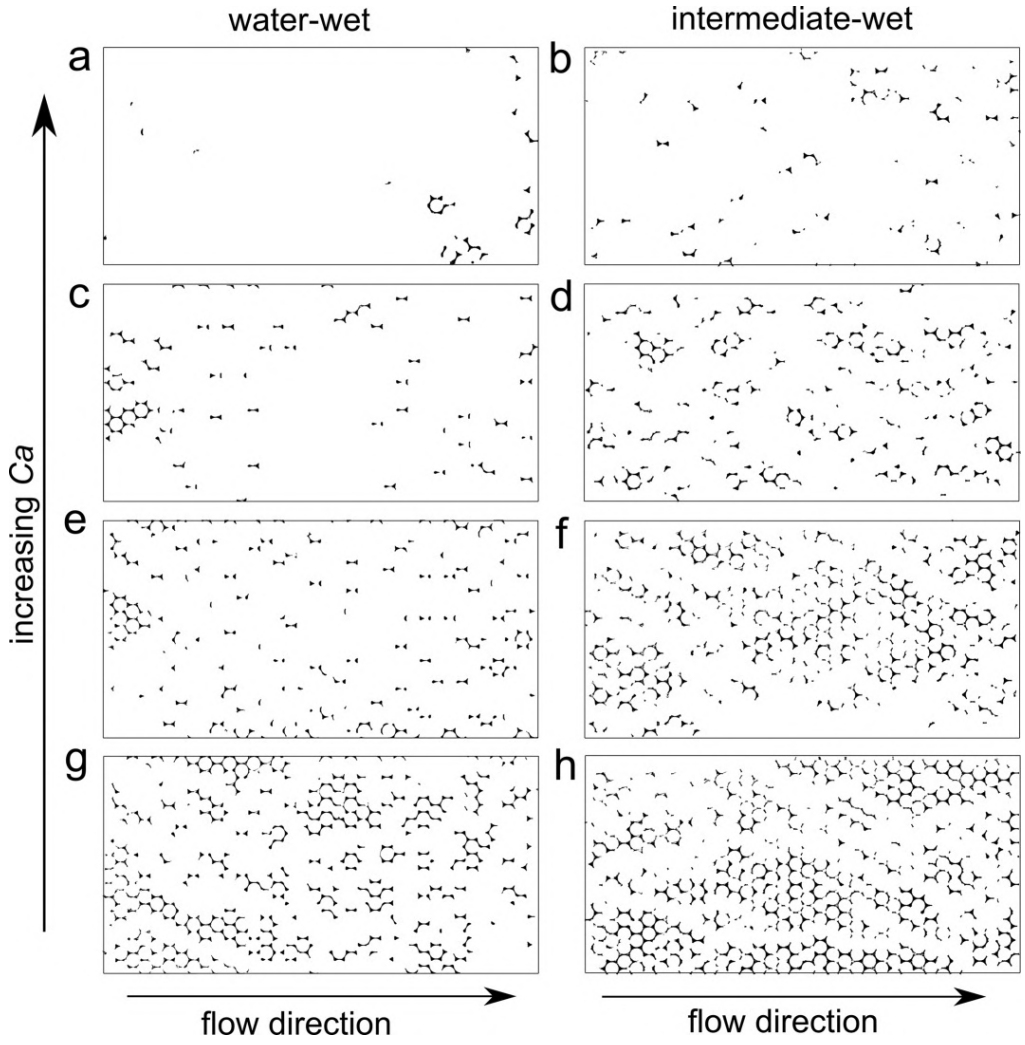

Figure 3.15: Residual $scCO_2$ saturation after brine flooding for different values of Ca and wettability. The micromodel was composed of cylindrical posts regularly arranged. The dark color is the CO_2, while the white is the brine and the grains. (a,b) $Ca = 7.5 \times 10^{-4}$, (c,d) $Ca = 3.6 \times 10^{-4}$, (e,f) $Ca = 1.58 \times 10^{-4}$, and (g,h) $Ca = 9.0 \times 10^{-6}$. The CO_2 saturation in each experimental image is : (a) 2.5%, (c) 7.2%, (e) 14.8%, (g) 27.6%, (b) 4.6%, (d) 14.7%, (f) 27.2% and (h) 41.5%, from Hu et al. (2017).

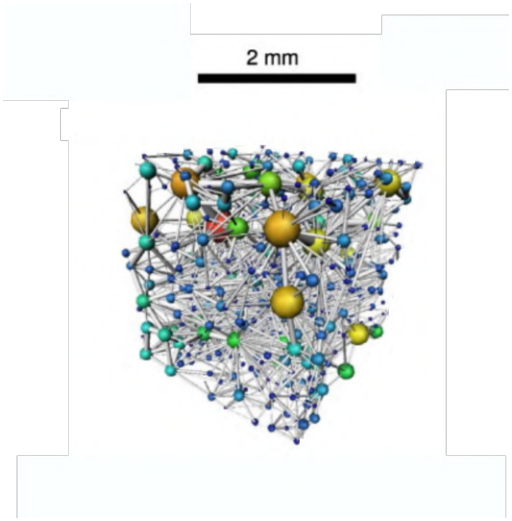

Figure 3.16: Pore network extracted from a microtomography scan of a carbonate stone. The pore space is represented as a lattice of wide pores (shown as spheres) connected by narrower throats (shown as cylinders) [29].

of this model is still limited, as it is typically used to model flow over a small fraction of a core. Moreover, it greatly simplifies the geometry of the media, which can lead to errors, and the laws describing the flow need to be chosen adequately to model the phenomenon of interest.

The laws used for the motion of the fluid can be very simple, taking only into account the piston-like displacement, like the model of Washburn (1921), while more advanced models can model corner flow and snap-off [226], or add another phenomenon, like inertia [135]. In their work, Moebius and Or (2014) developed a model for the displacement of the meniscus in a channel taking into account inertia. They consider a simplified pore-network draining by gravity, and found a residual saturation of wetting fluid of 0.36 with inertia and 0.34 without, showing very little effect of inertia (more on that in Chapter. 8).

In Fig. 3.17, we present the PNM model developed by Reis et al. (2023). The authors take into account the flow of wetting fluid in the film remaining in the corners of the geometry, even after drainage of the pores, and compared their results with experiments. Their PNM represented a porous medium composed of glass beads of 1 mm sandwiched in a Hele-Shaw cell. Their experimental apparatus was first saturated with a wetting fluid composed of a mix of glycerol and water, which was drained at a constant flow rate. They studied the residual saturation after primary drainage depending on the inclinations of the Hele-Shaw cell. Their results show that gravity tends to stabilize the front and decreases the amount of wetting fluid trapped inside the network.

The PNM approach is a compromise between continuous and numerical approaches: it combines the physical pore-scale phenomenon within the law used for modeling the flow of the fluid inside the channel, and also uses a simple description of the pore volume, which allows for describing the flow at a larger scale.

Large scale simulation (Darcy's law) These simulations take a continuous approach to the porous media, where it is characterized by its permeability and porosity defined using the notion of REV introduced in Chapter. 2. To simulate the drainage and imbi-

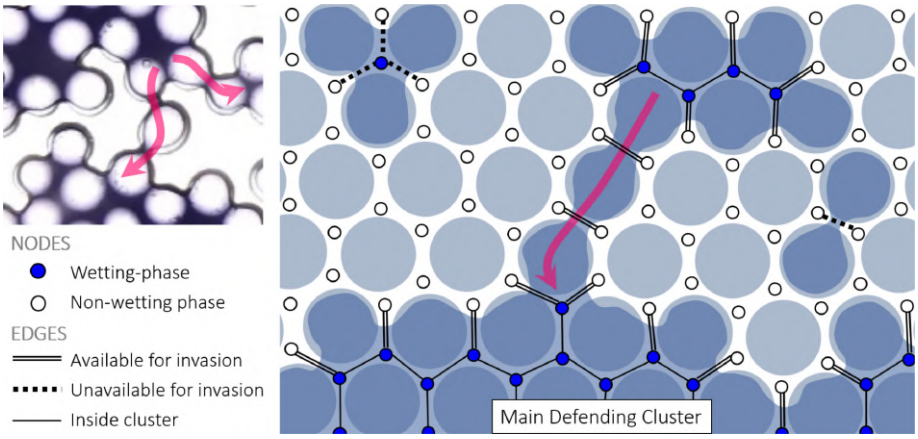

Figure 3.17: Example of a PNM representing the drainage by gravity of a porous medium composed of glass beads sandwiched between two glass plates. The particularity of this model is that it takes into account the flow of fluid through the films left at the surface of the glass beads [163].

bition, the two-phase Darcy's law is used.

Li and Benson (2015) studied the injection of $scCO_2$ at the column scale at fixed pressure, and showed that the small-scale heterogeneities in permeability inside the porous media can significantly speed up the invasion of the core by the non-wetting phase. Simulations of the underground reservoir showed that between 15% to 40% of the injected CO_2 can be immobilized by the capillary forces, with a high porosity and permeability reservoir leading to higher residual trapping [79, 196, 78]. This wide variation is explained by the different properties of the porous medium used in the study (porosity, permeability, wettability, connectivity,...) as well as the flow rate [217]. This approach relies on the validity of the two-phase Darcy's law, which is true only over a limited range of parameters, as we saw in Chapter. 2

3.4 Open questions

We have seen the different ways to measure the residual saturation at the core-scale or using microfluidics, but besides general trends, it is hard to correlate precisely residual saturation with flow parameters. DNS at the pore scale gives an accurate description of the two-phase flow, but due to the limitation in computing power, the results are hard to upscale. This leaves us with models derived from the two-phase Darcy's law or obtained via PNM to predict residual saturation. The two-phase Darcy's law requires significant assumptions and is accurate only over a restricted range of parameters. PNM significantly simplifies the geometry of the pores, and all of the physics is hidden inside the laws used for the flow of fluids. Or, these laws are often simplified as well for convenience, neglecting, for example, the existence of wetting film on the pore-wall or the impact of inertia that arises from the Haines jumps. They also hardly ever take into account the snap-off, which is a crucial trapping mechanism.

The drainage stability diagram introduced by Lenormand (1990) gives us some indications on the behavior of the flow, but similar studies do not always predict the same residual saturation. More concerningly, the boundaries between the different regimes are not always the same from study to study, highlighting the role of the pore geometry/ topology in the flow of the two fluids.

Finally, we have seen multiple experimental examples of wettability alteration. Given that the contact angle between the fluids and the solid is a crucial parameter for capillary trapping, the alteration of the wettability is a phenomenon that needs to be investigated more in depth.

3.5 Objectives and methodology of the study

Throughout our introduction and the state of the art, we have seen that residual trapping is a crucial parameter for the storage of CO_2 underground. We have seen that the static methods to estimate residual trapping are not enough, as they lack the dynamic aspect of the two-phase flow. The dynamic models used for the prediction lack accuracy as they are simplified and sometimes do not take into account phenomena that can have an effect on the flow. All of this raises a question: How to quantify residual trapping by integrating dynamic effect and heterogeneities for CO_2 sequestration?

3.5.1 Objectives

The objective of this thesis is two-fold:

- First, to gain a deeper understanding of the local hydrodynamic processes that lead to residual trapping in porous media, and to identify the key parameters governing this phenomenon. In particular, we aim to elucidate the roles of wetting films and inertia effects during pore invasion in shaping residual trapping.
- Second, to investigate the mechanisms of wettability alteration when rocks are exposed to a supercritical CO_2/brine mixture.

Ultimately, we expect these insights to provide a more predictive framework for assessing and optimizing CO_2 storage efficiency in geological formations.

3.5.2 Methods

To achieve this objective, we investigate the two-phase flow at the pore scale using microfluidics experiments and numerical models. We study in particular the phenomena that occur at the pore scale but impact the flow on a large scale, such as the Haines jump and the wetting films.

We first use a heterogeneous microfluidic device replicating real rocks to highlight the importance of wetting films and Haines jumps during drainage. Then, we use a simpler object, known as a pore doublet, to isolate and analyse the impact of wetting films and inertia on the two-phase flow stability. Finally, to better understand how long-term storage of CO_2 in geological formation can alter the wettability, we investigate the wettability alteration of calcite during its exposure to brine and CO_2 at reservoir conditions.

Chapter 4

Pore-scale investigation of residual trapping using Microfluidics

In the previous section, we discussed how a deeper understanding of residual trapping could contribute to safer and more efficient CO_2 storage. In the following section, we introduce the methodology used in this study —microfluidics- as a tool to investigate residual trapping at the pore scale.

4.1 Microfluidics for geosciences: principles

Microfluidics involves the manipulation of small volumes of fluids, typically in the micro to atto (10^{-18}!) liter, using channels with sizes of ten to hundreds of micrometers. It is used to perform chemical analysis, biological studies, medical diagnostics, or fluid mechanics experiments. Their small size means that surface tension is one of the dominant forces, and the Reynolds number of the flow is typically below one, resulting in a creeping flow regime in most conditions. To handle these very small volumes, it uses microfluidic systems, also known as micromodels or lab-on-chip, see Fig. 4.1, coupled with pumps, connectors, and tubing. Micromodels share a lot of their fabrication process with microelectronics, the technology that inspired microfluidics. They are made out of a network of small capillaries with inlets and outlets, allowing for the injection and transport of fluids. They have two main advantages: first, the fabrication methods

Figure 4.1: Example of micromodel used in the NanoμLab, from *Pour la Science* N° 535, Soulaine and Roman.

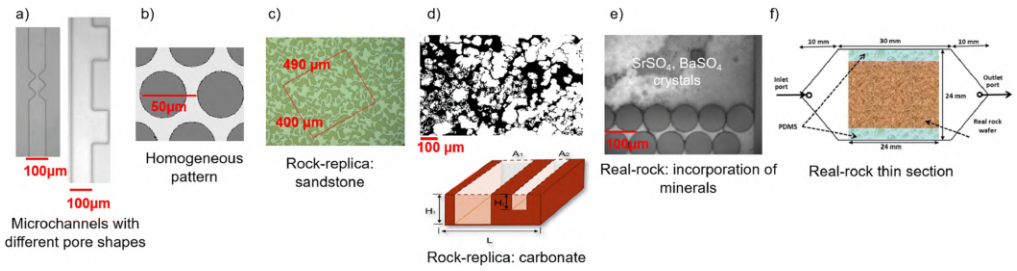

Figure 4.2: Diversity and complexity of micromodels in geosciences. They range from channels with simple geometry, all the way to micromodels made out of real rock thin section, from Roman et al. (2025).

used allow for a great variety in the shape, structure, and properties of the micromodel. Second, their small size and transparent nature enable the direct visualization of the flow under a microscope, and they are much easier to produce and utilize than larger-scale experiments. Moreover, the fabrication techniques used allow for the design of micromodels that replicate flow in porous media at the small scale, from very simple geometries (a single channel) to geometries that replicate the pore space of real-life rocks, see Fig. 4.2 [168].

Thanks to these qualities, microfluidics spread to geoscience as early as 1961 with the work of Mattax and Kyte (1961), where an image of the experimental micromodel that they used for their experiments can be seen in Fig. 4.3. It offers an alternative to large-scale experiments and is a powerful tool for studying flow at the pore scale, especially when used in tandem with numerical simulations. Their transparent nature allows for direct visualization, but also a range of other analyses, such as particle image tracking, interface tracking, as well as more complex techniques, such as microRaman. Raman spectroscopy uses a visible laser to perform chemical analysis of a sample, and coupling of this analysis with microfluidics allows for the in-situ analysis of chemical reactions, such as the dissolution of minerals. Recently, microfluidics experiments have been coupled with geo-physical conductivity measurement [164]. Micromodels able to handle pressure and temperature similar to those of potential CCS sites have been developed, allowing for a direct study of supercritical CO_2 injection [82].

Microfluidics has established itself as a crucial technique in the study of the flow in porous media, and the current improvement of the fabrication and experimental techniques will only accelerate its development in the porous media community.

4.2 Fabrication techniques for microfluidics

Different materials are used for the fabrication of micromodels, each with its advantages and drawbacks. A table resuming the characteristics of these materials can be found in Tab. 4.1. The most commonly used materials are:

- **Silicon**: Silicon microchips are made out of a silicon wafer (the same used for standard microelectronics), where the pattern of interest is etched. Two main methods are used in the creation of the geometry: wet and dry etching. Both technique starts with the design of a mask to protect the parts that need to stay intact. A thin layer (1 to 2 µm) of positive photosensitive resin is then uniformly spread on the wafer. The resin is then covered with the mask before being exposed to UV light. The photosensitive resin reacts to ultraviolet (UV) exposure by either hardening (in the case of a negative resin) or degrading (in the case of a

Ever see a water flood?

A capillary micromodel has been used to study fluid distributions under various wettability conditions, and to find the effects of wettability on water-oil displacement. This article gives the results of these studies, with detailed photographs of the events occurring within the model.

BY C. C. MATTAX AND J. R. KYTE
Jersey Production Research Co., Tulsa

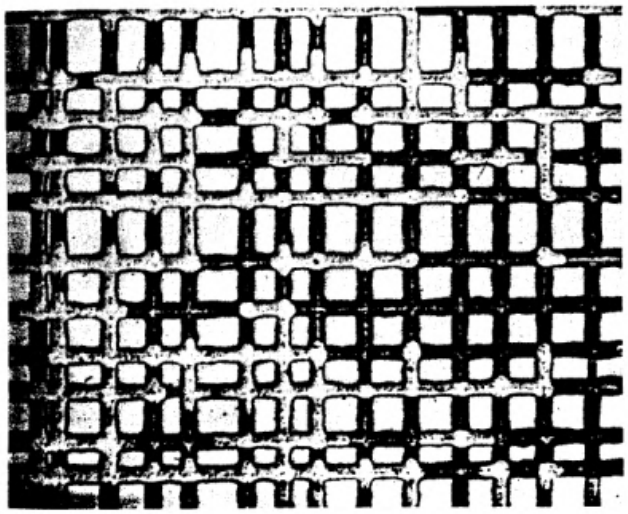

CAPILLARY network in a portion of a micromodel. Fig. 1.

WHAT WE KNOW about multiphase flow through a porous medium is based in part on what we have seen in simple systems such as single capillaries and capillary doublets.[1 2 3 4]

Visual studies in systems of more complex geometry have been made by Chatenever and coworkers.[5 6] They used synthetic flow models consisting of single layers of glass beads between two transparent plates. But it is hard to make detailed observations of interface movements.

To improve on these observations, a capillary micromodel was developed in which fluid movement can be seen in detail. The model possesses many of the over-all characteristics of a reservoir rock, and permits observation of fluid movement from pore to pore.

The capillary micromodel is a

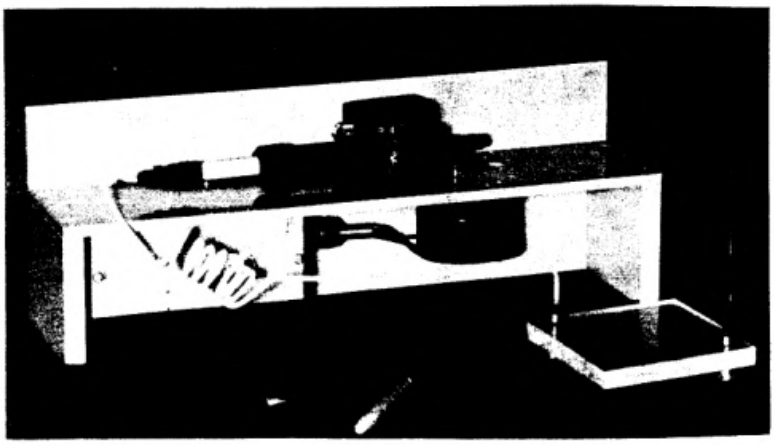

MICROMODEL and auxiliary equipment, including a microburet. Fig. 2.

Figure 4.3: First page of the article of Mattax and Kyte (1961), the first usage of a micromodel in a peer-reviewed article.

Table 4.1: Table describing properties of commonly used materials for microfluidics.

Materials	Silicon	Glass	Thermoplastics	PDMS	NOA81
Accuracy of the geometry	High	High (nm)	Depends on the mold	High	High
Max pressure	100 GPa	10 GPa	1 GPa	1 MPa	1 GPa
Max temperature	> 1000 °C	600 °C	300 °C	300 °C	300 °C
Compatibility with solvents	High	High	Poor with organics solvents	Low with organic solvents	Good
Price	High	Medium	Low	Low	Low
Time for a new geometry	High	High	Requires a mold	Medium	Medium

positive resin). A developer solution is then applied to remove the softened resin; this corresponds to the regions shielded by the mask for negative resins, or the exposed areas for positive resins. After development, the remaining resin shares the same pattern as the mask. This process of using a photosensitive resin to transfer a pattern onto a surface, typically a silicon wafer, is known as photolithography. For silicon etching, the resin serves as a protective layer, shielding the underlying material during the process. For wet etching, a solution of hydrofluoric acid or potassium hydroxide is then used to etch the solid to the desired depth. This technique leads to rounded edges. For the dry etching technique, the silicon wafer is connected to a negative potential and is bombarded with ions, which etch the surface of the silicon not covered by the mask. This technique allows for sharper corners than the wet-etching method.

Once the geometry is ready, the wafer is bonded to a flat glass plate with an inlet and an outlet drilled into it, creating a closed system ready to be used for experiments. The bonding is done by heating the two layers to above 250 °C and imposing a potential of several hundred volts between the plates, in a technique known as anodic bonding. The advantage of this setup is that the materials and the bonding are very resistant, allowing it to be used at high pressure, but the drawback is that silicon is opaque, and the microscope used to image the experiment must be used in reflection mode.

- **Glass**: glass chips are made by etching the geometry of interested in one or two plates of glass, before gluing them together using thermal bonding by heating them above 600 °C. Glass can be etched similarly as silicon, using wet and dry etching [138], but another technique can be used for glass, laser ablation, where a laser is used to remove material from the glass plate, which can lead to sub micrometer resolution [71, 177]. These chips present a high resistance to pressure and chemicals, making them ideal for experiments at high pressure.

- **Thermoplastic**, such as Polymethyl methacrylate (PMMA), also known as Plexiglass, or Cyclic olefin copolymer (COC). These polymers are initially in the form of pellets and can then be melted and cast into a mold to form the desired micromodel. Combined with their low cost and transparency, they are easy and cheap to produce, ideal for large-scale production.

- **PolyDiMethylSiloxane (PDMS)**. This is the most common way to produce micromodels. First, a master with the desired geometry is produced, and PDMS is

then cast on it and cured before being peeled off to produce the micromodel, in a process known as soft-lithography. Usually, the master is initially a flat silicon wafer on which the geometry of interest is imprinted using photolithography. For this, the silicon wafer is spin-coated with a negative photoresist resin, typically SU-8. Then, a photomask that defines the features to be patterned is used to cover the resin, before exposing it to UV light. All of the resin exposed to the UV is cured, while the unexposed photoresist (the one under the mask) is removed using a developer solution. This leaves the master silicon wafer with a positive image of the final pattern. Other materials can be used to produce the master, such as resin or even PDMS itself, if it is treated with the appropriate chemicals first (such as Trichloro(1H,1H,2H,2Hperfluorooctyl), for example).

PDMS is then used to mold the micromodel. PDMS is supplied in two components: the PDMS and a curing agent, both liquid at room temperature. The two are mixed using a 10/1 mass ratio of PDMS/curing agent, and the mix is then poured over the master and baked in an oven at 65°C for 2 hours to cure it. The resulting elastomer is then peeled off the wafer, the individual geometries are cut out, since many micromodels are made with a single master wafer, and holes are punched at the inlet and the outlet. After cleaning with an ultrasonic bath in a solution of water and ethanol, the micromodel is sealed with a flat piece of PDMS, produced similarly, but by using a flat wafer as a master. For bonding the two pieces of PDMS together, plasma treatment is used. The pieces are placed in a plasma chamber and exposed to an air plasma for 50 seconds at 70 W. Immediately after the treatment, the two pieces are pressed together to form the final micromodel, which is then ready for experiments, see Fig. 4.4.

PDMS is inexpensive, non-toxic, transparent, and the soft lithography technique does not require a clean room or any complex equipment, making it an ideal choice for many microfluidics applications. Some of the drawbacks of PDMS are that it is permeable to gas (which is an advantage to biologists trying to cultivate bacteria), and it is not compatible with all solvents [106], as the polymer can absorb some of them, such as silicon oil, which makes it swell. Moreover, PDMS is soft and not rigid like other materials, so it can deform when pressure is applied to it. This method of production is the one chosen for this study, and all the microfluidics devices presented in this work will be produced according to the above description.

- **Photocurable polymers** The most common of these polymers is the thiolene-based resin NOA81 (Nordland optical adhesive). This is a UV-curable polymer that can be used similarly to PDMS. It also uses a master, often made out of PDMS, where the photo-polymer is cast and cured, and then peeled away (soft-lithography). But instead of using heat, UV radiation is used for curing the polymer. The produced patterned thiolene layer can be bonded to PDMS, glass, or another layer of thiolene using plasma treatment to form a closed micromodel. Due to having a Young's modulus three orders of magnitude higher than PDMS, the injection holes are much harder to punch manually. The inlet and the outlet of the NOA81 micromodel need to be made using a needle post that is embedded into the polymer before curing it, and is then removed to form the inlet/outlet. The resulting micromodel can be treated similarly to PDMS to alter its wetting properties [21, 86].

  NOA81 presents a few differences with PDMS: it has a much higher resistance to swelling caused by organic solvents. Its higher elastic modulus makes it much less deformable, making it more suited for the flow of high viscosity or complex fluids, where the pressure in the micromodel can reach several bars. Since it

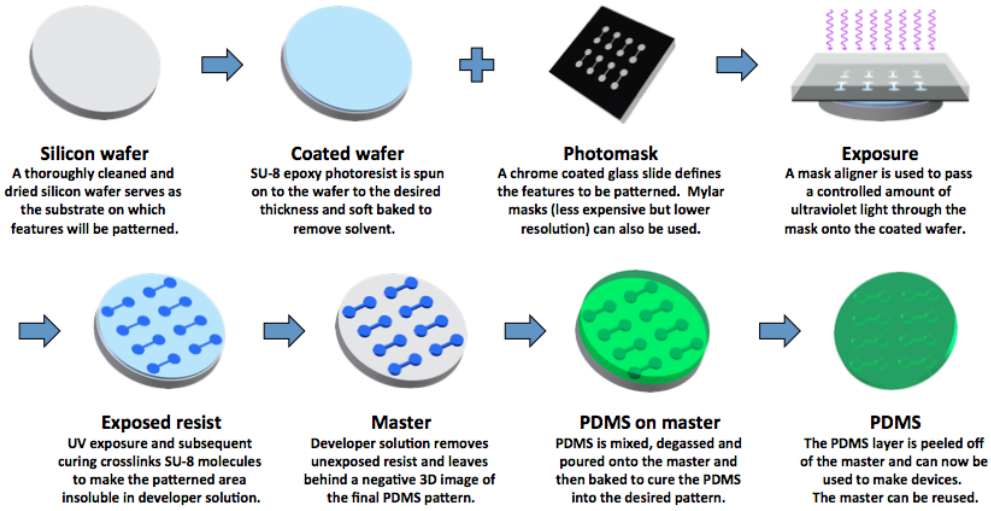

Figure 4.4: Photolithography and soft lithography processes for the fabrication of PDMS micromodel [149].

is less deformable, we also observe that NOA81 has a shorter relaxation time, meaning that it reacts faster to changes in pressure/ flow conditions. It is also impermeable to air and still allows for a very precise geometry [207]. However, this material is much less common than PDMS and is not used in many labs.

4.3 Experimental procedure

Now that we have selected PDMS as the material of choice for our micromodel, we go over the treatment of these chips and the experimental procedure we use for two-phase flow experiments.

4.3.1 Wettability treatment of micromodels

The produced PDMS micromodels exhibit a heterogeneous hydrophobic behavior, meaning that their wetting properties are neither uniform nor constant over time [95]. Or, since capillary pressure is of utmost importance in our study, a precise and durable mastery of the wettability of our micromodel is required. For this, we do a chemical treatment of the walls of the channel. Two main treatments are used: Polyvinyl alcohol (PVA) deposition [201] and silanization [95]. They ensure, respectively, consistent hydrophilic or hydrophobic behavior of the channels.

Hydrophilic treatment The process of PVA deposition is simple and fast: after bonding the micromodel, it is put back in the plasma oven at 100 W for 5 minutes. The micromodel is then taken out of the oven, and a water solution of 1 wt% polyvinyl alcohol is immediately injected. Great care is taken that all of the pore space is saturated with it. The solution is left to react for 10 minutes before using pressured air to dry the micromodel. It is then put on a hot plate for 10 minutes at 110 °C to remove any remaining trace of humidity, see Fig. 4.5. To prepare the PVA solution, we mix 87-90% hydrolysis PVA, which initially presents itself as a white powder, with DI-water,

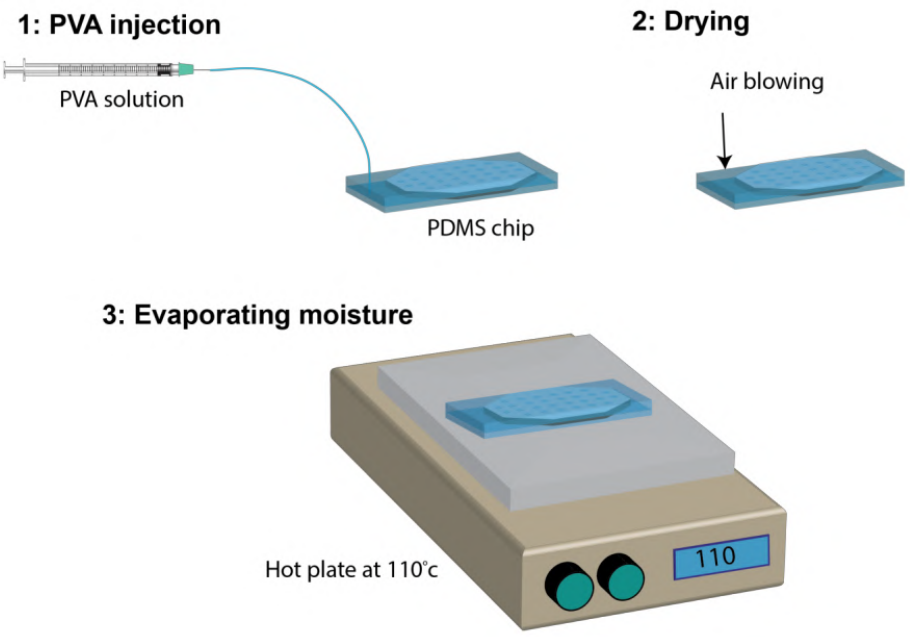

Figure 4.5: PVA treatment of a PDMS chip to make it uniformly hydrophilic, from Mansouri-Boroujeni (2022).

to reach a 1 wt% mix. To help the PVA dissolve, the solution is stirred for 40 minutes. The temperature of the solution is then raised to 100 °C using a hot plate while stirring continues for another 40 minutes. To finish the dissolution, the temperature is lowered to 65 °C, and the solution is left to stir overnight. The following day, the water loss that occurred via evaporation is compensated to keep the solution at 1 wt%, and the solution is now ready to be used. After the PVA deposition, the micromodel becomes hydrophilic with a measured contact angle of about 25° between the solid and water in the presence of air, see Fig. 4.6 and stays hydrophilic for a long period (no change after 30 days) [201]. PVA presents no particular risk for human health and is cheap, making this process easy to perform.

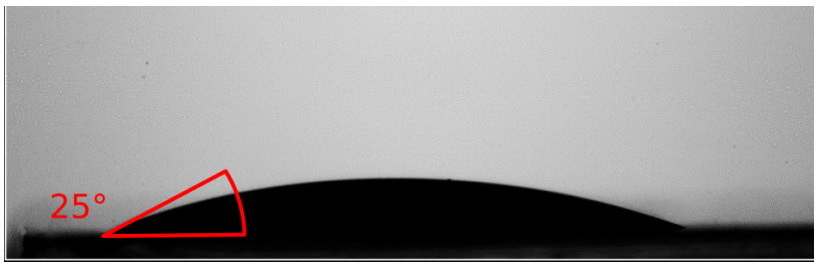

Figure 4.6: Measure of the contact angle between DI water and PVA-treated PDMS. The measure is done using the tensiometer of the NanoμLab. A value of around 25° is measured, highlighting the hydrophilic nature of the PDMS after treatment.

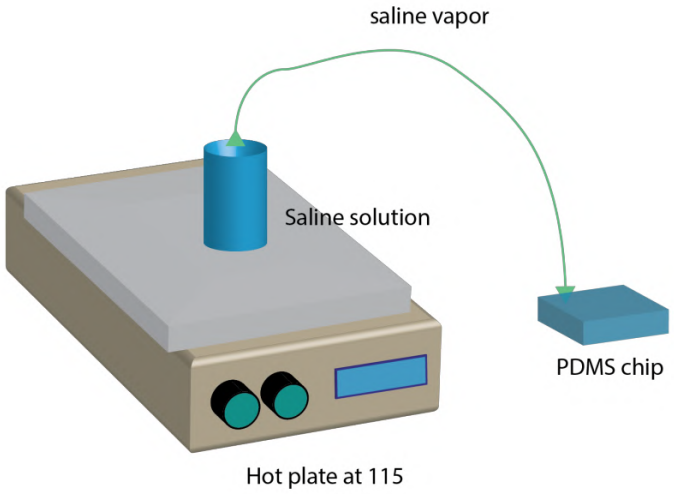

Figure 4.7: Deposition of TCP to make a PDMS micromodel uniformly hydrophobic, from Mansouri-Boroujeni (2022).

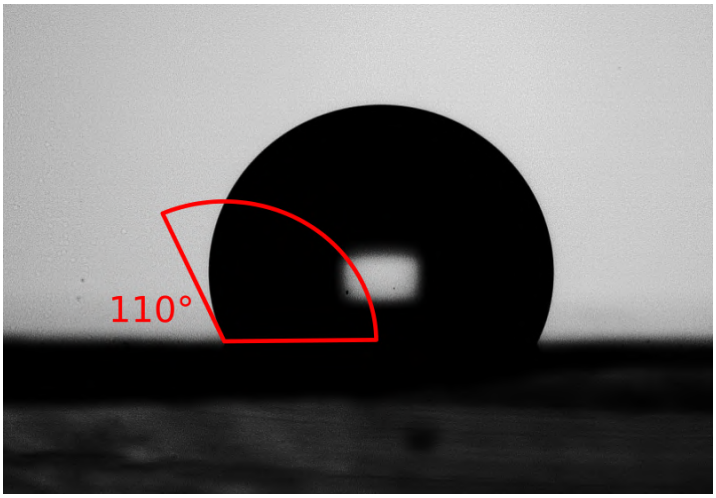

Figure 4.8: Measure of the contact angle between DI water and TCP-treated PDMS. A value of around 110° is measured, showing the hydrophobic nature of the TCP-treated PDMS.

Hydrophobic treatment The deposition of silane uses Trichloro(1H,1H,2H,2Hperfluorooctyl), or TCP, to create a uniformly hydrophobic behavior of the PDMS. The TCP is first dissolved in ethanol to reach an 18% volume ratio. Any contact of this solution with water needs to be avoided, as its reaction with the solution results in the production of heat and solid silicon, which might clog the micromodel. Before injecting the solution, the fluid is filtered using a 0.45 µm pore size Millex filter. The microfluidic chip is then connected to the flask containing the solution, which is then heated up to 115 °C. The resulting vapors are conducted through the micromodel for half an hour, and the chip is then placed in an oven at 110 °C to dry, see Fig. 4.7. The resulting micromodel has a hydrophobic behavior, with a contact angle of 176° between the treated PDMS and water in the presence of Fluorinert, a fluorine-based inert liquid, as reported by Karadimitriou et al. (2013). Our experimental measurements revealed a contact angle of 110° to 120° between DI-water and the TCP-treated PDMS in the presence of air, as seen in Fig. 4.8.

Other treatment Another example of wettability treatment in microfluidics is the use of low-temperature and low-pressure plasma. The plasma is created by passing a high voltage through air or a noble gas, creating a high-energy plasma that alters the surface properties, changing its wettability. This is caused by a combination of surface decontamination, modification of the channel roughness, and/or functionalization of the surface. This treatment is fast (between 10 seconds and a few minutes) and studies show a change in contact angle of up to 100° [55]. Moreover, the same plasma that is used for the bonding of PDMS microchips can also be used to perform the plasma treatment, making it convenient.

One issue with this technique is wettability aging, a phenomenon where the newly created wettability slowly reverts to its initial state. The time-scale for this reversal depends on the material of the microchip, experimental and storage conditions, and ranges from a few hours to a few days. This instability of the wettability is a huge problem for two-phase flow experiments, as a strict control of the contact angle is required, meaning that more stable chemical treatments are often preferred. However, recent work from Gredicak et al. (2025) has introduced a novel technique using atmospheric pressure plasma for the treatment of micromodels. They reported treatment effects lasting between 1 and 70 days, depending on the storage conditions.

UV-ozone treatment is another technique used for wettability alteration. It is less common than chemical and plasma treatment. It consists of exposing the micromodel to UV-radiation that interacts with the oxygen inside the air of the channels to produce ozone. The ozone, combined with the UV radiation, reacts with the PDMS molecules to form a layer of oxidized material (SiOx), with a much more hydrophilic behavior than PDMS. This procedure is slower than plasma treatment, which can allow tuning the contact angle to the desired value [23]. This technique still suffers from wettability aging.

4.3.2 Experimental setup

All of our microfluidic experiments are performed in the NanoµLab platform, the nano-microfluidic laboratory of the Earth Science Institute of Orléans. It is equipped with all the necessary tools to produce PDMS micromodels, perform microfluidic experiments, and conduct complex analysis of these experiments. This includes syringes and pressure pumps, connectors and tubing, microscopes and cameras, a plasma oven, and the fluids used to perform the experiments, such as silicon oils.

Syringe pumps These pumps are used to inject or withdraw fluids at a fixed flow rate by mechanically displacing the plunger of the syringe containing the fluid. They are accurate, but take some time to reach the prescribed flow rate value. There are two syringe pumps commonly used in the platform: a LEGATO 110 syringe pump from kdScientific and a Pump 11 Pico Plus Elite from Harvard Apparatus.

Pressure pumps They take a pressure as an input (around 10 bars) and output a smaller pressure dictated by the user. They create a constant pressure in the injected fluid, but this does not automatically translate to a constant flow rate (we need a single fluid phase and a constant micromodel geometry to reach a constant flow rate with a constant pressure difference). The pressure pumps available in the NanoμLab are an OB1 MK4 microfluidic flow controller from Elveflow and a LineUp Flow EZ from Fluigent.

Sensors These pumps can be coupled with flow and pressure sensors to measure pressure drop, permeability changes, and/or fluctuations in the flow of the fluids. As flow sensors, the laboratory is equipped with a mini Cori-flow from Bronkhorst and Microfluidic flow rate sensors from Evelflow. The Evelflow pressure controller can be coupled with the flow sensors of the same brand to impose a flow rate based on a feedback loop with the sensors. For pressure sensors, we have several pressure unit sensors from Fluigent.

Tensiometer Contact angles and surface/interfacial tensions are measured in the laboratory using a One Attension Theta Flex, from Biolin Scientific. This apparatus allows for quick and accurate measurements.

Once the micromodels are treated and ready for experiments, the inlet is connected to a 4-way valve using a needle. One of the ports of the valve is closed, and the two remaining ports are connected to syringes of non-wetting and wetting fluid. The valve allows for switching which fluid is injected, without the risk of letting a bubble of air inside of the system, which would ruin the experiments. One of the two fluids is occasionally dyed or injected with tracer particles. This is done to better visualize the flow, both with the naked eye and with the microscope. The addition of dye or particles does not alter the properties of the fluids. A syringe pump is then used to inject one of the fluids at a time at a fixed flow rate, see Fig. 4.9.

The micromodel is placed under an inverted microscope (Eclipse Ti2-U, from Nikon), and a fast camera (HS7 high-speed camera, from Fastec) is used to visualize and record the flow. This camera allows the user to record image sequences at a framerate of up to 35,168 fps, allowing us to precisely image all of the dynamics that occur in our micromodel. It is equipped with an image-trigger system that automatically starts recording when a pixel intensity changes within a predefined area—i.e., when an object enters a specific region of the image. In the case of two-phase flow, this object would be the meniscus entering the inlet channel. This setup allows us to capture the invasion process in the micromodel without requiring any manual intervention.

4.4 Image analysis to capture the invasion dynamics

After completing the experiment, our resulting data is a series of grayscale .tiff images that show the invasion of the micromodel by the injected fluid. To extract useful data, such as residual saturation and fluid velocity, we utilize image analysis. This treatment can be done using the ImageJ software or the Image Processing Toolbox of MATLAB,

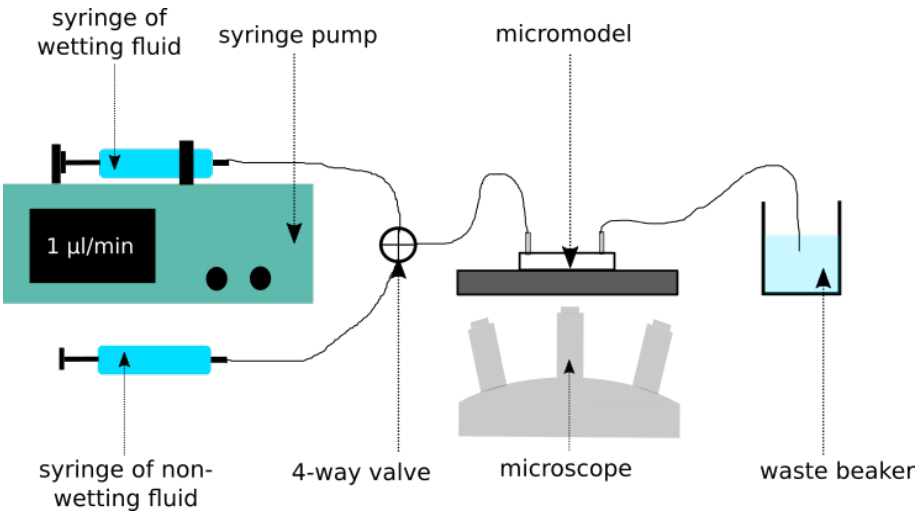

Figure 4.9: Experimental setup. To inject another fluid, the syringe on the syringe pump is replaced by the one containing the other fluid, and the 4-way valve is switched to allow for the injection. Only one fluid is injected at a time.

which is better at automating the process. The first step is to correct the slow drift in illumination that often occurs during long-duration experiments. This is done by defining a reference zone where no flow is present—such as the interior of a grain or a region outside the channel—and calculating its mean pixel intensity in every frame. Whenever a frame's mean differs from the overall average, we uniformly adjust that frame's pixel values so all frames share the same baseline brightness. Once the images are corrected, the treatment applied to them depends on what kind of data we want to obtain.

4.4.1 Residual saturation measurements

Residual saturation is the main focus of our work; it is thus crucial to be able to measure it during our experiments, at any time, and more particularly at the end of the invasion. On an experimental image, the key to determining the residual saturation is to count the number of pixels occupied by the defending fluid leftover in the micromodel and compare it with the total number of pixels of fluid space. This means that we need to remove the space occupied by grains and the portion outside of the channel, where there is no fluid. This gives us a percentage of residual saturation as a result.

For this, we use a morphological opening operation (see Appendix. B) to delete all objects from the picture, leaving only the background. Using the first image of the sequence, where only the defending fluid is present, we record the outlines of the walls and grains. Subtracting this static background from each subsequent frame (background subtraction) eliminates everything that does not move, so only the injected fluid and the fluid-fluid interfaces remain over a black background. We can then fill all the space between the interfaces and the grains with white pixels, giving us the space occupied by the injected fluid. This can then be compared with the total number of pixels in the pore-space, which can be obtained using the first image of the sequence, after we removed the grains and the outside of the channel. An example of this is given in Chapter. 5.

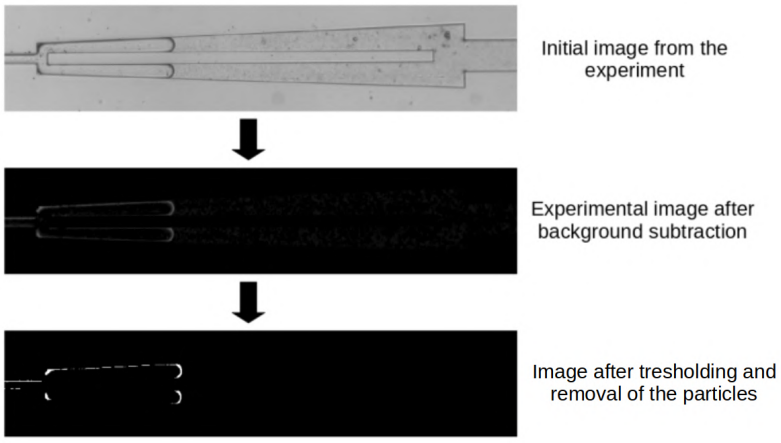

Figure 4.10: Example of the image analysis process for the tracking of interfaces on an experimental picture. The experiment involves the drainage of water by silicon oil. If one pays close attention, particles can be seen in the original and intermediate images, but they were removed by morphological opening in the last image, leaving only the menisci.

4.4.2 Tracking of the fluid-fluid interfaces

We might also like to track the dynamics of the menisci during the experiments. For this, we need to remove everything but the menisci in the micromodel. Then, we track the pixels of the menisci from one image to the other. Knowing the frame-rate of the recording and the size of each pixel in meters, this allows us to measure the velocity of each interface.

The workflow for this treatment is very similar to the residual saturation one. We use a morphological opening as well as background subtraction. The cleaned images are then thresholded so the menisci appear as white features on a black background. After that, another morphological opening is used to remove potential tracer particles or other artifacts present on the images. The complete processing workflow and typical results are illustrated in Fig. 4.10.

Once we have isolated the menisci, we want to follow their position in time. For this, the pixels composing the meniscus are tracked along the x-axis to reconstruct their position in time. We can then, knowing the framerate of the experiments, compute their velocities. The result of this treatment can be seen in Fig. 4.11. In this figure, the positions of two menisci are represented on the y-axis, and time is plotted on the x-axis, with both parameters made dimensionless. For this particular drainage experiment, one of the menisci was lagging behind the other, meaning that some of the wetting phase was trapped in the channel. The experimental data obtained this way can then be confronted with our theoretical results.

These image analysis workflows have been implemented in MATLAB with in-house codes. Other codes have been made to rotate images, crop them, or analyse the concentration of dye inside a fluid in a channel. These codes were designed collaboratively by the author and Sophie Roman. They will be available online at a later date.

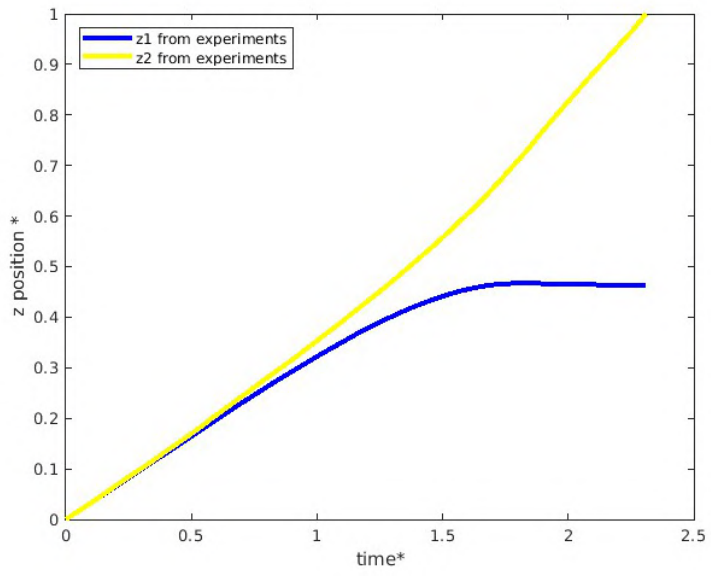

Figure 4.11: Meniscus dynamics in a diverging pore-doublet (see Chapter. 7) during the drainage of water by air. One meniscus is lagging behind the other and does not fully invade the channel. The experimental image corresponding to the time $t^* = 1.5$ can be seen in Fig. 4.12.

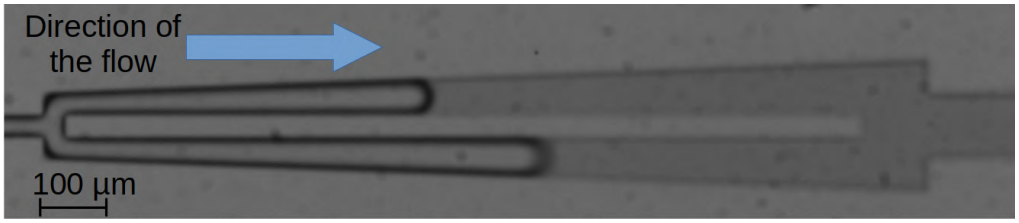

Figure 4.12: Experimental image of the displacement of water from a diverging pore doublet by air. One of the menisci takes the lead over the other, leading to residual trapping at the end of the invasion.

Chapter 5

Residual trapping during drainage in heterogeneous micromodel

In this chapter, we use microfluidic experiments to study two-phase flow in a complex porous medium, representative of geological porous media. These preliminary experiments highlight the complexity of the physics of the two-phase flow and emphasize the presence of wetting films left behind and the existence of local inertia effects even at slow flow rates.

5.1 Introduction

In Sec. 3.3.1 we discussed residual trapping in micromodels and how it has already been the subject of extensive studies [110, 222, 45, 211, 33, 82, 10]. The geometries used in these studies range from homogeneous and periodic patterns of cylindrical posts to complex, heterogeneous geometries that replicate the structures of geological porous media, with pores of varying size and pore throats of irregular shapes.

We have seen previously (Chapter. 3) that Haines jumps are very common during drainage and have a significant impact on the flow during column-scale experiments [24, 198]. However, the study of these jumps in micromodels featuring realistic porous geometries is scarce, as most studies have used homogeneous, regular porous media [136, 10, 209]. We hypothesize that using only a regular geometry is insufficient to properly understand the influence of Haines jumps and inertia on residual saturation. Moebius and Or (2014) used a PNM to compare a drainage of a glass bead pack by air with and without inertia during the Haines jumps. They showed that with inertia, 36% of the wetting fluid was trapped in the geometry, while without inertia, 34% of the wetting fluid was trapped. Despite seeing a different dynamic of invasion when inertia was accounted for (smaller pores were more likely to be drained), the amount of trapped wetting fluid stayed close to constant over the range of parameters that they studied. This result is surprising to us, leading us to also look at inertia during Haines jumps and its potential impact on residual trapping.

In this chapter, we look at two-phase flow using a complex micromodel as an introductory study of residual trapping. For this, we perform drainage in a geometry that replicates the non-homogeneous nature of geological porous media. We focus on the occurrence of Haines jumps and on the presence of wetting layers along the pore walls.

5.2 Materials and methods

In this section, we describe the micromodel as well as the experimental procedure used.

5.2.1 Fabrication of the micromodels

The geometry of the micromodel is hand-drawn by Pauline Etienne, a PhD student from the lab. It is designed to replicate the appearance of sandstone and is illustrated in Fig. 5.1. It has a porosity of 53%. The same pattern is repeated 10 times along the length of the micromodel. The permeability of the micromodel has been measured using the OpenFOAM software by running steady-state flow simulations in the geometry. We recovered a permeability of $k = 4 \times 10^{-12}$ m^2. At the top and bottom of the

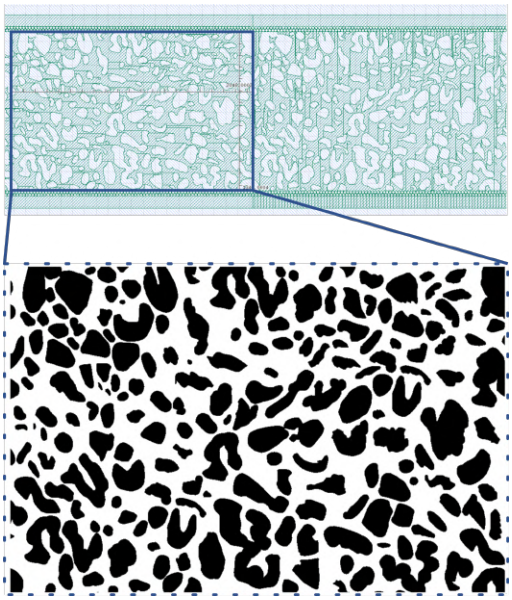

Figure 5.1: Portion of the micromodel designed by Pauline Etienne, with a zoom on the repeating pattern. This pattern is 1346 µm wide and 2048 µm long, with a porosity of 53%. At the top and bottom, we can observe the two layers of cylindrical posts as well as the other channels.

repeating pattern, there are two lines of cylindrical posts separated from each other by 1.5 µm. These cylindrical posts have a diameter of 25 µm and separate the center of the micromodel from two channels (each 100 µm in width), at the top and bottom of the geometry. The two layers of cylindrical posts act as a wall for the non-wetting phase because of their high capillary entry pressure, much higher than that of any other pore throat of the geometry. The average pore size and pore-throat size have been measured using MATLAB software. The average pore radius is 29 µm, and the average pore throat is 20.5 µm in width. The distribution in pore radius and pore-throat size is found in Fig. 5.2. One important phenomenon to note is that the layers of cylindrical posts stop the flow of non-wetting fluid, but the wetting fluid can freely flow through them. This will impact our measure of the wetting phase residual saturation, as it drains through the cylinders and joins the channel, decreasing the amount of trapped wetting phases.

The silicon wafer mold containing the geometry of the micromodel is produced using a photolithography method. PDMS soft lithography is then performed to fabricate

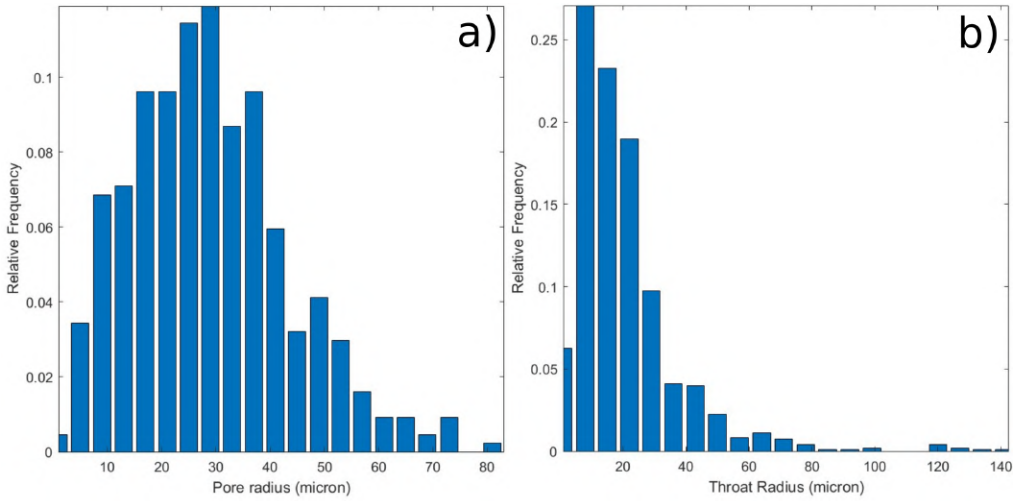

Figure 5.2: Pores (a) and throats (b) size distributions of the pattern used in the micromodel. The pores and throats have been determined using an image processing software [158, 157].

the layer of PDMS containing the geometry. An inlet and an outlet are punched before bonding with a flat piece of PDMS using plasma to form the final micromodel used for the experiments. The depth of the micromodel is 15 µm. Before the experiments, the micromodels are treated with PVA to make them hydrophilic, leading to a contact angle of 25° between the solid and the water in the presence of air. A more in-depth description of this process is found in Sec. 4.2

5.2.2 Fluids properties

For these experiments, the fluids used are: DI-water, with a viscosity of 1 mPa·s and air, with a viscosity of 1.81×10^{-2} mPa·s. Water is the wetting fluid, and air is the injected phase displacing water. This leads to a viscosity ratio of $M = 1.8 \times 10^{-2}$. The interfacial tension between water and air is 73 mN·m^{-1}.

5.2.3 Experimental procedure

For this experiment, we operate slightly differently from what was described in Sec. 4.3.2; the non-wetting fluid is not directly injected into the micromodel. Instead, we withdraw water from the porous medium using the withdrawal mode for the syringe pump. The other side of the micromodel is open to the atmosphere. By withdrawing fluid from the micromodel, we create an underpressure (relative to atmospheric pressure) inside the system, as opposed to the overpressure generated during injection. This underpressure helps prevent issues related to the compressibility of air, which could affect the injected flow rate. This also helps to decrease the stress on the micromodel, limiting the risk of it failing and unbonding during experiments (this happened on multiple occasions in experiments involving very viscous fluids, and usually led to water and silicon oils being projected everywhere in the room).

The water is withdrawn at low flow rate, between 0.1 µL·min^{-1} and 25 µL·min^{-1}. This assures a low capillary number flow, similar to what is seen in CCS. This flow rate leads to a capillary number between 2×10^{-6} and 5×10^{-4}. All the experiments made can be found in Table. 5.1

Table 5.1: Flow rates and corresponding capillary numbers of the experiments. The viscosity ratio in this chapter is kept constant at $M = 1.8 \times 10^{-2}$.

Flow rate imposed	Corresponding capillary number
$0.3\ \mu L \cdot min^{-1}$	6.0×10^{-6}
$0.4\ \mu L \cdot min^{-1}$	8.0×10^{-6}
$1.5\ \mu L \cdot min^{-1}$	3.0×10^{-5}

5.2.4 Image analysis

After conducting experiments, we recovered a series of .tiff images showing the invasion of the porous medium by air. From these experiments, we can measure non-wetting fluid saturation after drainage, and discuss two different phenomena: Haines jumps and wetting layers.

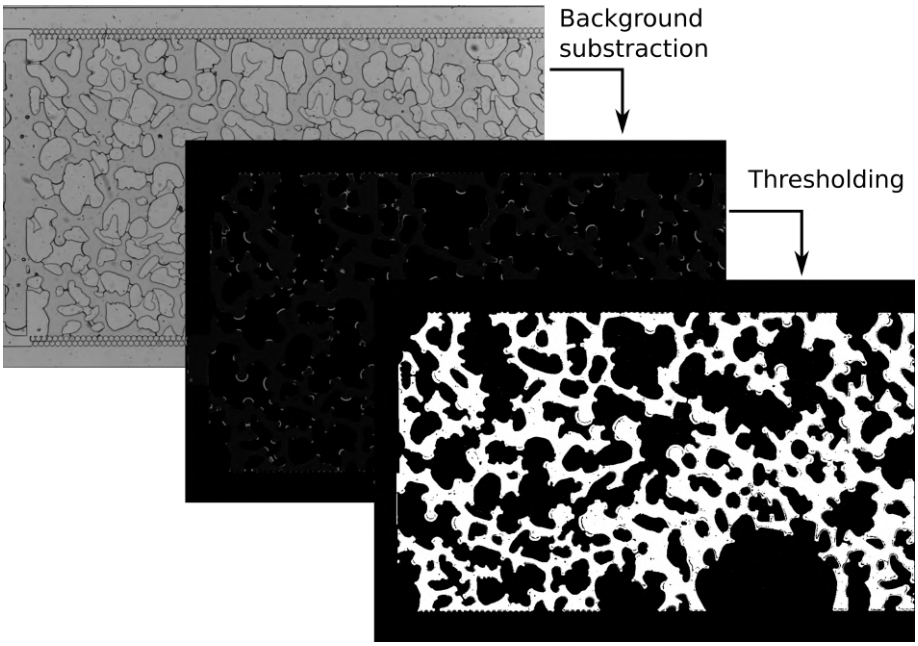

Figure 5.3: Process of isolating the non-wetting fluid from the experimental pictures. From the starting image, we correct the light fluctuation and perform a background removal operation (see Appendix. 4.4) that removes everything but the non-wetting fluid, leading to the intermediate image. Binarizing this image using the correct threshold gives us the final image, where the fluid is in white.

To find the area invaded by the wetting fluid, we use an image analysis pipeline (automated on MATLAB), represented in Fig. 5.3. We first correct the illumination of the figure before removing the background of the picture, leaving only the fluid. This image is then binarized so that all the non-wetting fluid is in white. By doing this process for two images at different time steps, we get the number of pixels 'invaded' (that switched from white to black). This can then be correlated to a displaced volume.

To compute the residual saturation, we also need to know the fraction of the image where the fluid can flow. For this, we need an image where the grains and outside of the channels are in white, and one at the end of the drainage where the non-wetting fluid is made out of white pixels, see Fig. 5.3. By counting the black pixels in the first

image, we can compute the pore volume, while the second image gives us the volume occupied by the non-wetting fluid. The image containing the grains is obtained using the pipeline presented in Fig. 5.4, where we binarize the starting image to keep only the edges of the grains. We then manually close the grains that are not surrounded by white pixels, as well as the outside of the channel, before finally filling all regions of the figure surrounded by white pixels.

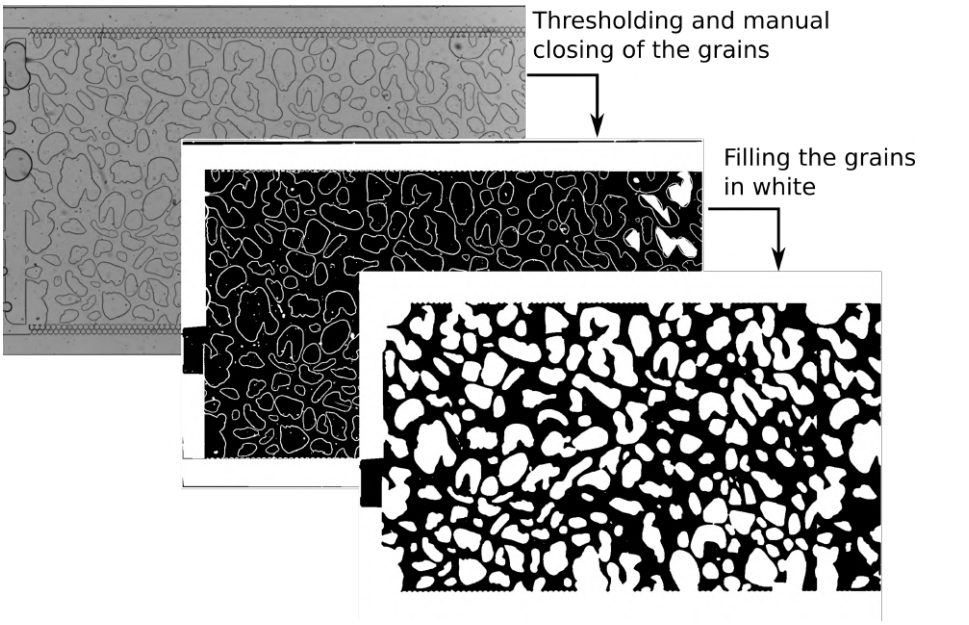

Figure 5.4: Process of filling the grains and the outside of the channels with white pixels. From the starting image, we perform a thresholding operation to remove the fluids. Then, grains that are not properly closed and the outside of the channel are manually filled with white pixels, before finally coloring in all regions of the image surrounded by white pixels, giving us a picture with all the grains in white.

5.3 Results

5.3.1 Drainage pattern

In Fig. 5.5, we present images of the micromodel before and after drainage at a flow rate of 6.6×10^{-12} m$^3 \cdot$s^{-1}, corresponding to $Ca = 8 \times 10^{-6}$. We show pictures close to the inlet, as they are easier to capture with the image trigger of the camera. Water and grains are represented in light gray, while air is depicted in a darker shade. The observed region (composed of 1.1 times the pattern) is completely invaded in 60.1 s. At the end of the drainage, the smallest pores in the geometry remain uninvaded, and the invading air even completely bypasses a large region, leading to a residual saturation of water of 23.9%. We also observe the formation of capillary fingers, showing that we are indeed in the capillary regime, as we discussed in Sec. 3. These fingers invaded all the pores below a certain size threshold, meaning the smallest pores are not drained by air, leaving a residual saturation of wetting fluid. Between 26.3 s and 30.8 s, we observe the quick invasion of several pores, at a calculated flow rate of 8.2×10^{-12} m$^3 \cdot$s^{-1}. This invasion flow rate is only marginally above the average flow rate of 6.6×10^{-12} m$^3 \cdot$s^{-1}. This event is thus not fast enough to be a Haines jump.

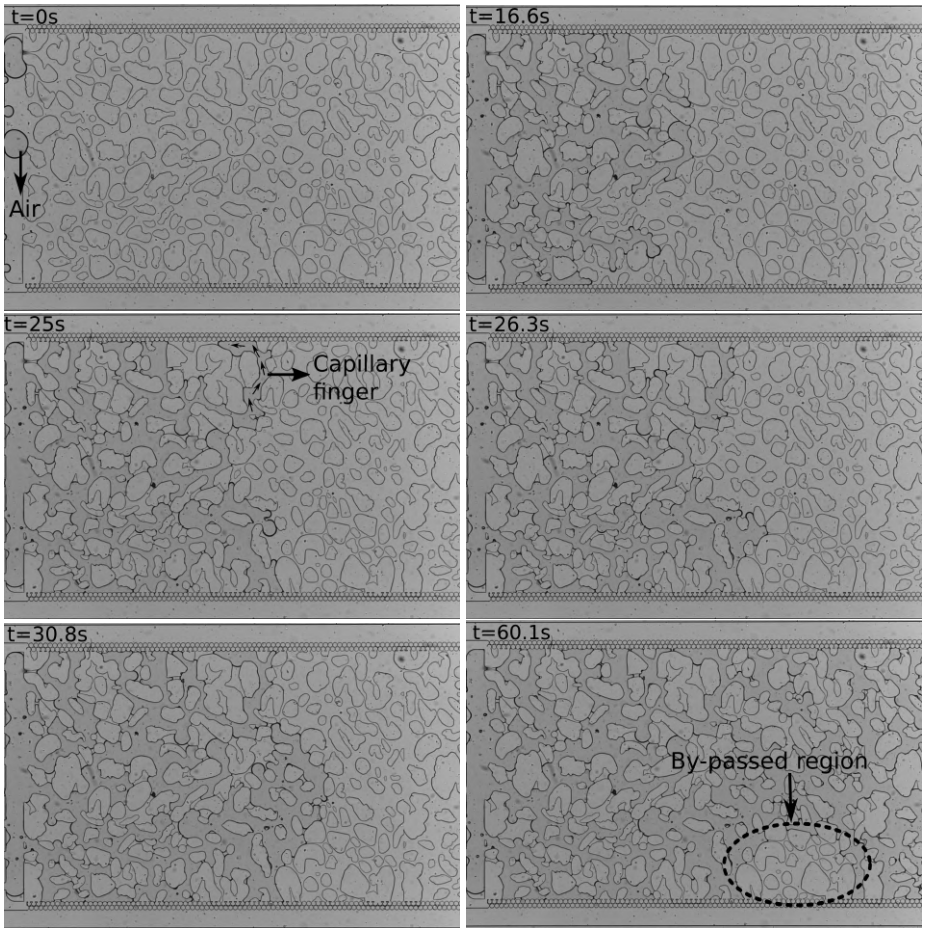

Figure 5.5: Drainage of the micromodel at $Ca = 8 \times 10^{-6}$, the injection direction is from the left to the right. At t=0 s, air enters the micromodel. After percolation, at t=60.1 s, we observe residual water trapped in many different pores. We measure the residual saturation of water to be 23.9%. In particular, there is a significant portion of the porous media bypassed. Indeed, only narrow pore throats lead to this region and cannot be invaded by the non-wetting fluid. During the drainage, capillary fingers form (at t=25 s, for example), with some of them propagating backward (as indicated by the arrow). This is a clear sign that the invasion is dominated by the capillary forces [110]. We also observe that several menisci are moving simultaneously in the micromodel, and we observe a quick invasion of the geometry by the air. For example, between t=26.3 s and t=30.8 s, a volume of 3.7×10^{-11} m^3 of water was drained in 4.5 s, leading to a flow rate of 8.2×10^{-12} m$^3 \cdot$s^{-1}, slightly faster than the average flow rate during the experiment. This event was not a Haines jump, since the velocity is close to the average invasion speed, and Haines jumps are known to be at least an order of magnitude above the average displacement flow rate [24, 168].

In Fig. 5.6, we present the same experiment, done at a higher capillary number, with $Ca = 3 \times 10^{-5}$. The micromodel is drained faster, but the same behavior is observed. We measured a residual saturation of water after percolation of 21.6%. In Fig. 5.7, we represent the evolution of the water saturation in time for the three experiments presented here. For the two experiments that went to completion, we reached around 20% of residual water saturation. We are close to reaching the horizontal asymptotes for the lowest residual saturation of wetting fluid, even though we have not yet reached equilibrium, as there is still a small displacement of the menisci. It is also clear that a higher flow rate leads to a faster decrease in the residual saturation, as expected.

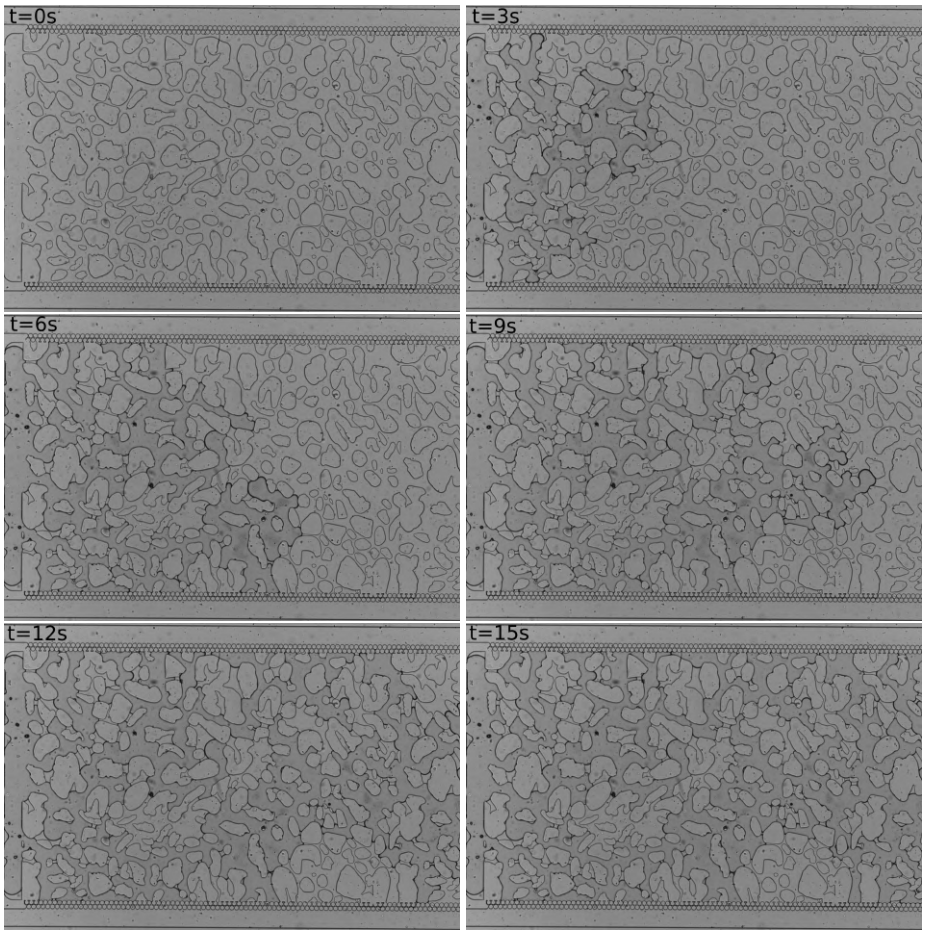

Figure 5.6: Drainage of the micromodel at $Ca = 3 \times 10^{-5}$, the injection direction is from the left to the right. At t=0 s, air enters the micromodel. After percolation, at t=60.1 s, we observe residual water trapped in many different pores. We measure the residual saturation of water to be 21.6%. We still observe the same region to be bypassed by the air.

During those two experiments, at $Ca = 8 \times 10^{-6}$ and $Ca = 3 \times 10^{-5}$, we observe that several pores are invaded simultaneously. If we were in a regime where the viscous forces were negligible in both fluids, only one pore (the biggest) would be invaded at a time.

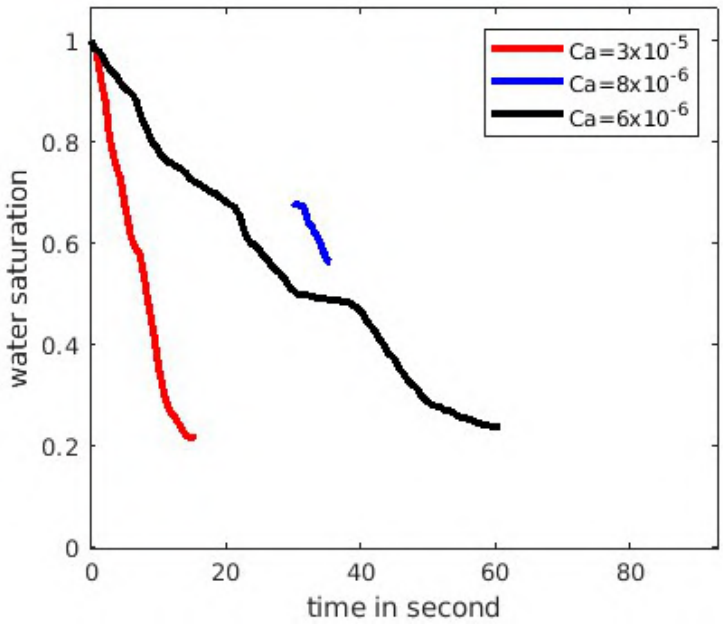

Figure 5.7: Evolution of the water saturation during the drainage for three different capillary numbers. $Ca = 8 \times 10^{-6}$ corresponds to the drainage presented in Fig. 5.5, $Ca = 3 \times 10^{-5}$ correspond to Fig. 5.6 and finally $Ca = 6 \times 10^{-6}$ correspond to the jump presented in Fig. 5.8. The curve for $Ca = 6 \times 10^{-6}$ is incomplete, as the recording began when the fluid was already inside the micromodel and stopped before percolation, due to the use of a higher frame rate for this specific recording.

5.3.2 Haines jumps

To observe Haines jumps, which are present in capillary-dominated regimes, the flow rate is decreased to reach 6.0×10^{-6}. During this drainage experiment, we observe that a large portion of the invasion occurs via Haines jumps, which are quick interfacial movements resulting from interfacial instabilities after the pinning of the menisci at the pore throat. In Fig. 5.8(a), we see menisci in pore throats: because of the imposed flow rate, they are slowly sucked further into those constrictions. Suddenly, one of the menisci can no longer increase its curvature and becomes unstable (red arrow), causing it to jump. This leads to a quick interfacial motion, where the meniscus reaches speeds an order of magnitude above the average invasion speed, see Fig. 5.8.

Interestingly, during this invasion, the meniscus invaded several pores at once without stopping at the pore throats. This behavior is reminiscent of the work of Moebius and Or (2012), where they showed that because of inertia, a Haines jump could 'push' the interface through the next pore throat, leading to a cascading invasion of the porous media. Nevertheless, we did not observe oscillations of the meniscus as they reported during their study. This leads us to wonder under which conditions this cascading invasion of the porous media occurs, and how the cascade of jumps alters the dynamics of the two-phase flow and the residual saturation in non-wetting fluid.

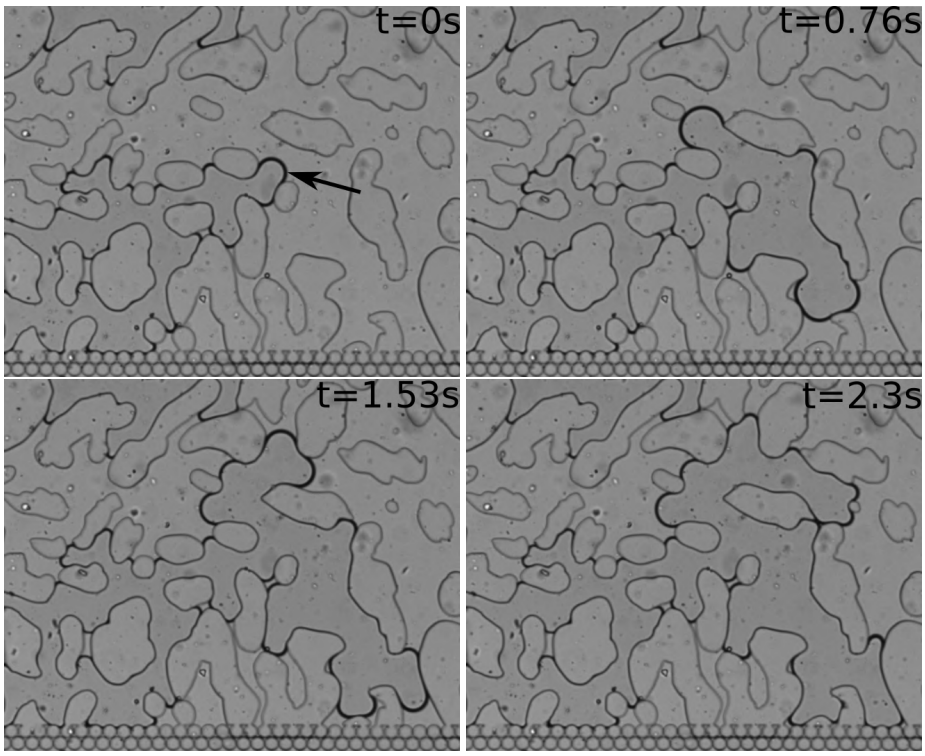

Figure 5.8: Successions of Haines jumps in an experiment at $Ca = 6\times10^{-6}$. (t=0 s)After being stuck in the pore throat, one of the menisci becomes unstable and quickly invades the following pore (the one indicated by the arrow). (t=0.76 s) The jumping meniscus divides into several menisci, invading different pores. This jump leads to a cascading invasion, where the non-wetting fluid quickly invades several pores without stopping. (t=2.3 s) After the jump, a significant portion of the pore space was invaded in a short amount of time. During the jump, we observe (by manual tracking) that the meniscus moves at 4.2×10^{-3} $\mu m\cdot s^{-1}$, an order of magnitude above the average speed of the fluid inside of the micromodel, which based on the imposed flow rate is around 4.7×10^{-4} $\mu m\cdot s^{-1}$, showing the quick burst during Haines jumps.

5.3.3 Wetting layers

In all of our experiments, we observe a thick black line along the walls of the porous media, see Fig. 5.5. This is caused by the presence of a water-air interface along the walls, clearly showing residual water along the wall of the porous medium. These films are a consequence of the balance of viscous and capillary forces close to the walls, and have been described by Taylor (1961) and Bretherton (1961). They have shown that during drainage, a film of wetting fluid is left along the wall behind the invading meniscus. Bretherton showed that the film thickness scales with the capillary number as $Ca^{2/3}$. When the channel is angular, more wetting fluid is left over in the channel, and tends to pool inside the corners [219]. In Fig. 5.9, we represent typical organizations of the wetting films after drainage in a geometry presenting corners. It was obtained by Reis et al. (2023) using Surface Evolver, a software designed to compute equilibrium fluid-fluid interfaces in complex geometries [1].

[1] The program represents the interface as a triangulated surface and evolves it to minimize interfacial energy under constraints such as fixed fluid volumes and prescribed contact angles. This procedure yields equilibrium shapes consistent with the Young-Laplace equation [193].

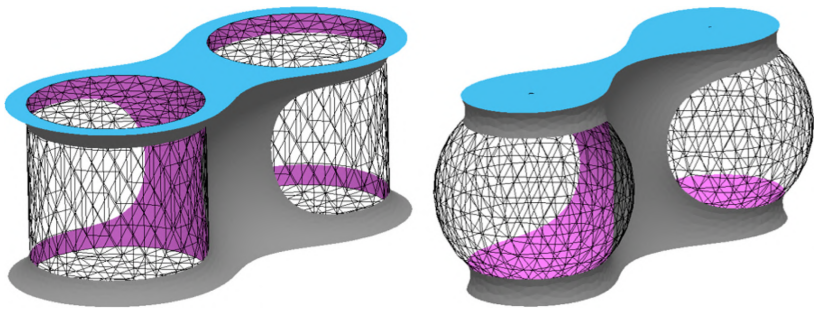

Figure 5.9: Examples of wetting films configurations around a pair of cylinders and spheres. Both pairs are contained between parallel planes, similarly to the situation in our micromodel. Blue, magenta, and gray surfaces represent the portion of the fluid in contact with the planes, the grains, and the non-wetting fluid, respectively, from Reis et al. (2023).

The presence of these films of water along the walls alters how the air flows: indeed, both of them are hydrodynamically connected via the boundary conditions that we introduced in Sec. 2.2.2. Since water is much more viscous than air, the presence of wetting layers reduces the space available for the air to move in the pores and increases the viscous pressure drop. The opposite would occur if the wetting fluid were less viscous than the invading fluid. Then, instead of increasing the viscous drop, these layers would act as a lubricant for the invasion of the injected fluid. This is what we discussed in Sec. 2.4.3, where we saw that these wetting layers acting as a lubricant increase the flow of non-wetting fluid, leading to a relative permeability above 100%.

5.4 Conclusion

Using a complex water-wet micromodel, we performed drainage of water by air in the capillary fingering regime (low Ca). These experiments highlighted the omnipresence of Haines jumps during the drainage of water by air for the regime investigated. During the interfacial jumps, we saw how several pores are invaded in quick succession following a singular interfacial jump. We manually measured the speed of the meniscus to be one order of magnitude above the average invasion speed during this cascading event. This led us to wonder what the impact of inertia during the jumps is and how it affects the saturation in wetting fluid.

We also observed wetting films remaining on the walls of the porous media after displacement by air, caused by the balance between the capillary and viscous forces. Since we have both fluids present in the same channel simultaneously, we have viscous coupling between both of them, meaning that the flow of one impacts the other. These films are rarely taken into account, and we wonder how they impact two-phase flow.

Due to the complexity of the geometry, it is hard to study individual phenomena. An alternative way of investigation is to design specific geometry to isolate and study these phenomena. In the next chapter, we introduce the concept of pore doublet, a simple configuration that focuses on the bifurcation between two pore throats, and present how they are used to isolate phenomena and study their impact on residual saturation.

Chapter 6

Pore doublet: a powerful tool for investigating porous media flow stability.

In the previous section, we introduced microfluidics and highlighted the complexity of two-phase flow within heterogeneous microfluidic systems. We concluded that pore-scale investigation is essential for a proper understanding of residual trapping. This chapter presents a simple but powerful tool to investigate residual saturation and flow stability: the pore doublet.

6.1 General concept

Pore doublets are a simplified representation of a porous medium, composed of capillaries that allow for the flow of fluids: an entry channel that separates into two daughter channels, which can be of various sizes, lengths, and shapes, before they reconnect to create an outlet channel, see Fig. 6.1. They can be seen as two capillaries connecting two pore bodies. The simple geometry of pore doublets allows researchers to analytically derive the set of equations controlling the flow of fluids in the pore doublet, while still retaining the complex physics of two-phase flow. Originally, they were designed to estimate residual saturation during oil recovery [138, 173, 37, 38, 62]. For this, researchers considered the displacement of oil by water from a pore doublet with one channel smaller than the other, and studied how much oil would be trapped after the breakthrough of water, see Fig. 6.2. Indeed, if one capillary is invaded first and water reaches the outlet channel before the other capillary is fully invaded, the residual oil present in the pore doublet would be unable to escape due to the immiscible nature of both fluids. Based on theoretical considerations (that we will develop later), it is possible to predict the relative position of the menisci during the invasion, and thus the amount of oil trapped in the system. The pore-doublet model assumes that the calculated amount of trapped oil can provide an estimate of residual saturation in a larger porous medium.

More recently, other usages of pore doublet include investigation of water infiltration in soil [136, 135], as well as the modeling of liquid composite molding, where a resin is injected in a matrix of fibers and then cured to form composite materials [1]. During this process, any bubbles of air remaining in the initial matrix can cause a significant weakening of the end material [118].

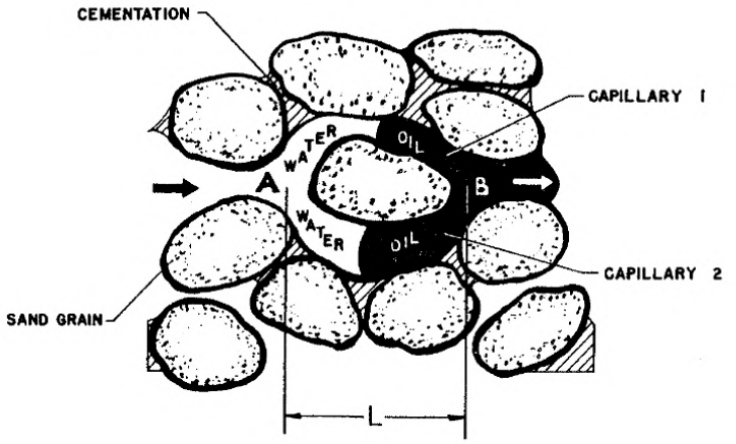

Figure 6.1: Example of a pore doublet in a porous medium, from Moore and Slobod (1955).

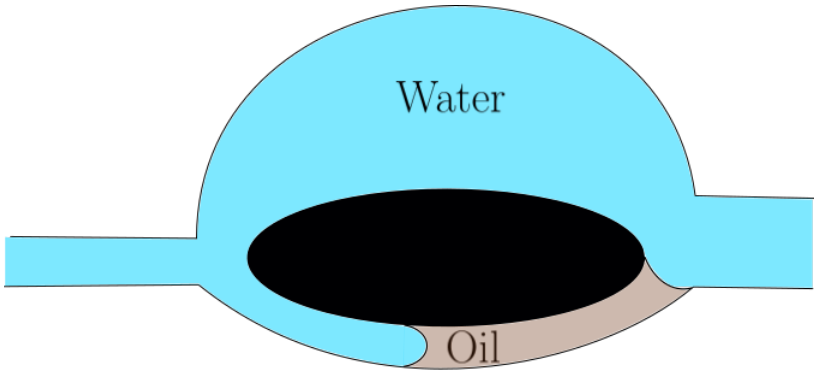

Figure 6.2: Example of a pore doublet used for estimation of residual oil saturation. The big channel was invaded first, trapping the oil in the smaller channel.

Pore doublets with two symmetrical capillaries of various shapes have also been used to investigate the stability of two-phase flow and the different displacement regimes during drainage [121, 80, 129], as we will see in Chapter. 7 and Chapter. 8.

6.2 Main principles to derive pore-doublet equations

To simulate the two-phase flow through a pore doublet, initial characterization of the system and the fluids involved is required. In this work, we assume both channels have the same length L, with z denoting the coordinate along the middle of the channel's length. The upper daughter capillary is indicated by the subscript 1, and the lower one by the subscript 2. The cross-section of each channel is written as $A_i(z)$, $i = [1, 2]$.

Initially, the entire pore doublet is filled with a fluid noted I, and from the left-hand side of the pore doublet, an immiscible fluid, noted II, is injected from the left. The static contact angle between fluid I and the walls of the pore doublet is taken as θ and stays constant in the entire system. Fluid II enters one or both daughter branches, leading to the formation of a meniscus between the fluids in potentially both branches. The position of these menisci is noted as z_i. A pore doublet with the corresponding

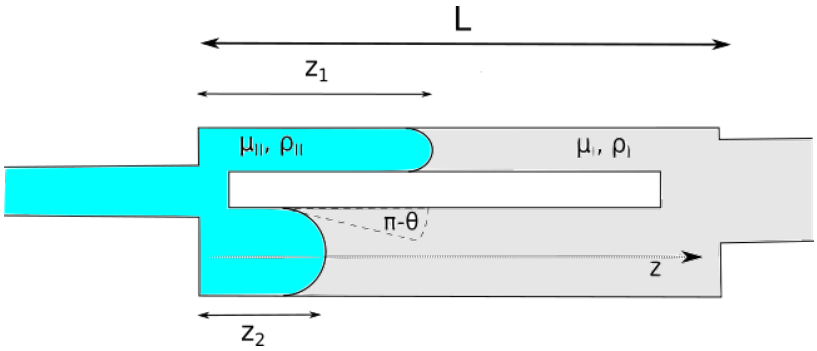

Figure 6.3: Schematic of a standard pore doublet and its parametrization during a drainage. If one of the menisci reaches the outlet before the other, the remaining wetting fluid (in blue) will be trapped in the model. μ_i and ρ_i represent, respectively, the dynamic viscosity and the density of fluid i.

parametrization is represented in Fig. 6.3 during a drainage.

To derive the controlling equations, we must first establish the boundary conditions. There are two main possibilities: fixed pressure drop over the entire pore doublet without any constraints on the flow, or fixed flow rate with no constraints on the pressure. These two conditions lead to two very different behaviors of the fluids.

In the fixed pressure conditions, there is an infinite supply of fluid II at a fixed pressure P_p (the subscript p stands for the parent channel), while the pressure at the outlet is kept constant at P_0. This leads both channels to be invaded individually at a rate that depends only on the geometry and the wettability properties of each channel [173], obeying Washburn's law [212].

At a fixed flow rate Q_p, the pressure drop over the channels fluctuates over time, and the channels are no longer invaded individually. Rather, the speed of each meniscus is influenced by the position of the other, resulting in intricate coupled dynamics, where one meniscus might even retract towards the inlet in the channel [37, 138]. The difference between fixed flow rate and fixed pressure is illustrated in Fig. 6.4.

This led to a debate among researchers between the 60s and the 80s, as the outcomes resulting from selecting different boundary conditions contradict one another: the fixed pressure boundary conditions lead Rose and Witherspoon (1956) to conclude that during imbibition in a pore doublet similar to the one of Fig. 6.2, the biggest capillary would be the first one to be invaded. This was in direct contradiction with the experimental and theoretical work of Chatzis and Dullien (1983), who showed that under the fixed flow rate condition, the smaller channel would be invaded first. In the same work, they suggested that the fixed pressure boundary condition is not realistic for porous media, as it represents a scenario where viscous forces dominate, which occurs only at high and unrealistic capillary numbers. This conclusion was also reached by Sorbie et al. (1995). In the rest of the development, we choose to use the fixed flow rate boundary condition, as it more closely resembles the flow conditions in the underground reservoirs.

Another controversy emerged among researchers at that time. During imbibition, some argued that non-wetting fluid could not be trapped, while others stated that wetting fluid could be trapped if one of the daughter channels was bigger than the other. They advanced that during imbibition, the smallest channel is invaded first, as the capillary pressure driving the imbibition is stronger in this channel. Then, when the meniscus in the smallest channel reaches the ends of the channel, it enters the outlet channel and prevents the non-wetting fluid in the biggest capillary from escaping.

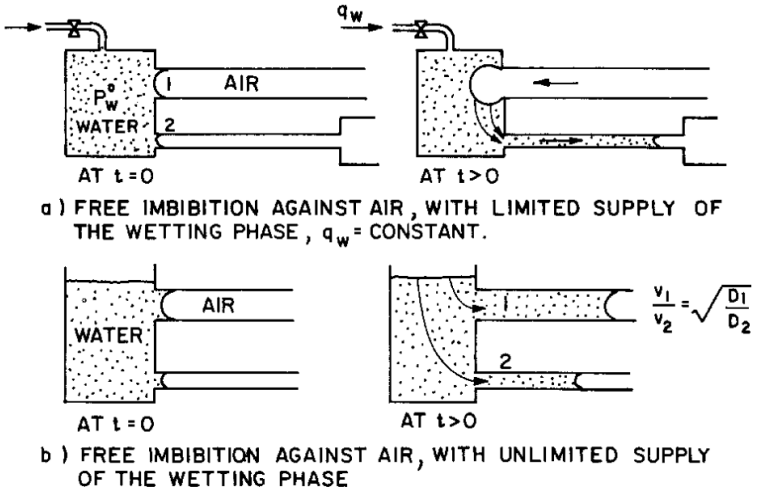

Figure 6.4: Comparison between (a) Fixed flow boundary condition, where the dynamics of the menisci depend on each other's positions, and (b) Fixed pressure boundary condition, where the speed of the individual menisci is independent of each other, from Chatzis and Dullien (1983).

What they did not take into account, as highlighted experimentally by Chatzis and Dullien (1983), is that after the invasion of the smallest channel, the meniscus in the smallest channel is stuck at point B, (see in Fig. 6.5) and cannot enter the outlet channel, as the bigger daughter channel is invaded before the outlet. This means that the invading fluid imbibes the bigger channel before it enters the outlet. Thus, no trapping is possible during imbibition, as shown experimentally during the imbibition of air displacing mercury in Fig. 6.6. This led to the Pore-Doublet Model (PDM) being mostly used in the study of fluid flow during drainage.

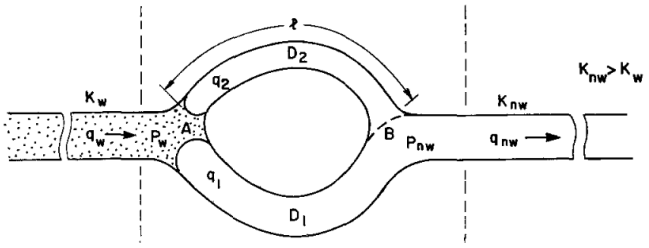

Figure 6.5: Pore-doublet model during imbibition, from Chatzis and Dullien (1983).

Using the fixed flow boundary condition and assuming that both fluids are incompressible, the conservation of mass reads as,

$$Q_p = Q_1(t) + Q_2(t), \tag{6.1}$$

where $Q_i(t)$ is the flow rate in channel i. Since there is no accumulation of fluid in the capillaries, the flow rate of fluid in channel i can be written as, $Q_i(t) = A_i(z)u_i(z)$, $\forall z \in [0, L]$ where $u_i(z)$ is the velocity of the fluid in channel i at position z. Since this is true at any point in the channel, it is also true at the meniscus position, and we write

$$Q_i(t) = A_i(z)u_i(z) = A(z_i)\dot{z}_i, \ \forall z \in [0, L], \tag{6.2}$$

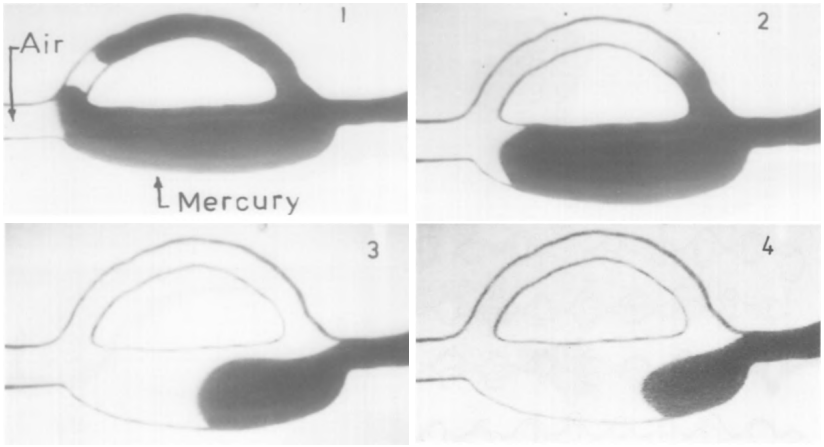

Figure 6.6: Experimental results of an imbibition of air in a glass pore doublet initially filled with mercury. It shows that the small channel is invaded first, but no residual trapping occurs because the big channel is also invaded, figure from Chatzis and Dullien (1983).

where $\dot{z}_i$ is the velocity of the meniscus in channel i. Moreover, since the two channels share the same inlet and outlet, it is immediate that the total pressure drop in each channel is the same as in the other one,

$$\Delta P_1(t) = \Delta P_2(t), \tag{6.3}$$

where $\Delta P_i(t)$, $i = [1, 2]$ is the total pressure drop over channel i. According to Washburn (1921), the total pressure consists of three different pressures: the pressure drop in fluid II ($\Delta P_{i,fluid\ II}$), upstream of the meniscus, the capillary pressure caused by the curvature of the interface (ΔP_{cap}), and finally the pressure in fluid I ($\Delta P_{i,fluid\ I}$), downstream of the meniscus,

$$\Delta P_i(t) = \Delta P_{i,fluid\ II} + \Delta P_{cap} + \Delta P_{i,fluid\ I}. \tag{6.4}$$

In general, to compute the pressure drop in each fluid, we use Stokes equations (2.11), which take into account the viscous forces, and the capillary pressure is given by the Young-Laplace law (2.15).

This set of principles allows for the derivation of Ordinary Differential Equations (ODEs) that give us the meniscus positions in time, and thus the amount of fluid trapped in the pore doublet.

6.3 Limitations of current approaches

The first limit of the pore-doublet model that all researchers are aware of is the use of Hagen-Poiseuille and Young-Laplace laws for the expression of, respectively, the viscous and capillary forces. Hagen-Poiseuille law assumes a fully developed, laminar flow in the capillaries, which is unlikely to be true [37, 80]. The use of the Young-Laplace law with a fixed contact angle in the whole pore doublet also assumes that no hysteresis exists, and that the hydrodynamics of the flow has no impact on the value of θ. Moebius and Or (2012) introduces a dynamic contact angle that obeys Voinov's law [205] to take into account the hydrodynamics of water being displaced by air. Their results show that it has a minimal impact on the flow in their system, but this is a

rare example of a pore-doublet model where the contact angle was not assumed to be constant.

Should we neglect inertia? Another limitation of the classical pore-doublet model is that only viscous, capillary, and sometimes gravitational forces are accounted for. At first glance, this assumption is correct, since for most porous media applications, the Reynolds number is below one, so no impact of inertia is expected. But more and more researchers [182, 136, 135, 66, 11] show that this assumption is not always correct. Indeed, during an interfacial jump, the speed of the fluid can be 2 to 3 orders of magnitude above the average displacement speed, which leads to events where inertia becomes important and alters the meniscus dynamics. An example of Haines jumps in a complex micromodel can be seen in Fig.6.7 [168]. Another work taking into account inertia is the theoretical work of Sorbie et al. (1995), where the authors derived the equation controlling the dynamics of the interface during capillary rise in a tube, taking into account the impact of inertia at the beginning of the invasion, where it is important. This is known as the extended Washburn's law. In a pore doublet, the question of inertia was only tackled by Moebius and Or (2012), and later in a bigger geometry using Pore Network Modelling (PNM) by the same authors [135]. They showed that after an interfacial jump, oscillation of the meniscus around its new equilibrium position appears for certain conditions. These oscillations are a signature of inertia effects and can alter the order in which the pores are invaded.

Should we neglect wetting layers? In the theoretical model describing the flow of fluid in the pore doublet, it is assumed that the flow of fluids occurs only via piston-like displacement, meaning that the invading fluid invades the channel completely, and that no defending fluid is left behind. Or, it has been shown that during imbibition at low capillary number, the invasion of the porous media occurs via corner flow [224], meaning that the middle of the channel is not invaded, and the wetting fluid progresses in the corners and the fracture of the porous media[203, 103]. This can lead to snap-off and further trapping of the non-wetting phase. During drainage, the assumption of a piston-like displacement leads researchers to neglect the existence of wetting layers [30, 197, 15, 19]. These films appear along the solid wall after the moving interface displaced the wetting fluid from the channel center, and can increase the connectivity of the wetting phase, create snap-off, as well as impact the flow of the non-wetting fluid. An example of these films can be seen in Fig. 6.8. On this experimental figure of a drainage, we can see an accumulation of wetting fluid in the pore bodies of the channel caused by the presence of wetting films along the walls of the channel. These wetting layers can also be seen in Fig. 6.6. The impact of the layers can be two-fold: by reducing the available space for the flow of the displacing fluid, as well as by viscous coupling at the boundary between the fluid and the film. In Chapter. 7 and Chapter. 8, we will see how some of these assumptions lead to significant errors for certain flow parameters.

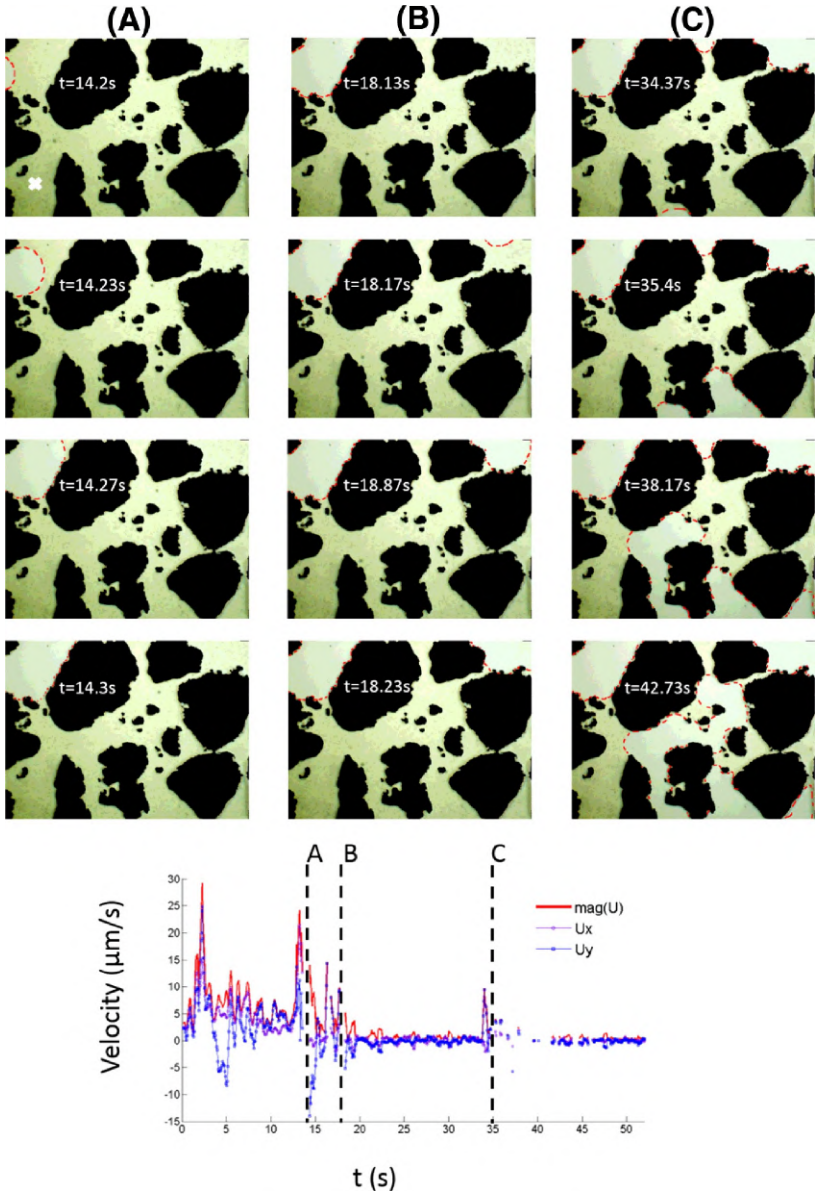

Figure 6.7: Haines jumps in a complex micromodel replicating real-life rock structure. During the experiment, three individual Haines jumps were recorded, from Roman et al. (2016).

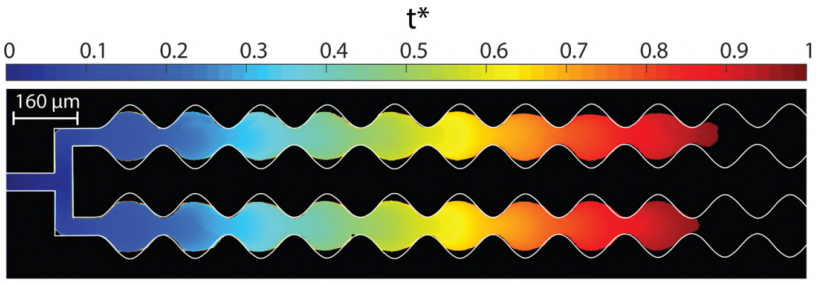

Figure 6.8: Image of a drainage of water by air in the viscous-dominated regime. The presence of water in the pore bodies shows the wetting layers along the walls of the channel. Image taken from Mansouri-Boroujeni et al. (2023).

Chapter 7

Impact of wetting films on the stability of two-phase flow in porous media: a pore-doublet perspective

In this chapter[1], we examine the instability produced by two-phase flow, both experimentally and numerically, and how Bretherton's films influence the flow regimes through viscous coupling.

7.1 Introduction

As we saw in previous sections, multiphase flow in porous media is of utmost importance for CCS. Still, it is also very relevant in many industrial applications, including distillation columns [183], soil remediation [52], enhanced oil recovery [138], or liquid composite molding [121]. Two-phase flows rely on complex coupled interactions between the two immiscible fluids and the porous matrix. The wettability of the solid plays an important role in the fluid distribution: the wetting fluid tends to flow in contact with the solid, along the walls of the pore or in the roughness of the porous matrix while the non-wetting fluid flows in the pore center, minimizing the surface of contact with the solid [28, 73]. Understanding the fluids' behavior is essential for predicting the residual saturation after injection, and thus the efficiency of the displacement.

In porous media, two-phase flow is inherently complex, primarily due to capillary effects [145] and viscous coupling between the phases [169, 113]. This complex system exhibits a non-linear behavior from which instabilities arise and significantly alter the fluid flow. A typical example is the Saffman-Taylor instability [174, 194], which appears when a more viscous fluid is displaced by a less viscous one, leading to the formation of the well-known viscous fingering patterns. In porous media and neglecting gravity effects, Lenormand et al. (1988) identified three regimes of drainage depending on two dimensionless numbers, namely the capillary number, Ca (the ratio of viscous forces and capillary forces), and the viscosity ratio, M (viscosity of the injected phase over the viscosity of the defending phase). For $M > 10$ and $Ca > 10^{-1}$, the viscous forces in the injected fluid dominate the other forces, and the displacement is stable. In this

[1] Parts of this chapter have been published in Advances in Water Resources, Bernard et al. (2025)

regime, the invasion pattern presents a uniform front, and the displacement efficiency is high, meaning that only very little wetting fluid is trapped behind the interface. For $M < 10^{-3}$ and $Ca > 10^{-8}$, the viscous forces in the displaced fluid dominate, leading to a finger-like pattern, due to Saffman-Taylor instability [174]. This regime has poor displacement efficiency, and an important volume of wetting fluid is left behind the invasion front. For $M > 10^{-4}$ and $Ca < 10^{-6}$, the capillary forces dominate, leading to capillary instability [110] in which the pores with the lower capillary entry pressure are invaded preferentially, resulting in a seemingly random invasion pattern and a high residual saturation.

These three regimes – stable front, viscous fingering, and capillary fingering – have been studied extensively at the pore scale [57]. The two-phase flow patterns have been observed experimentally using microfluidic devices that replicate the structure of pores [110, 109, 107, 222, 224, 41] or using core experiments combined with micro-tomography imaging [40]. Pore-scale simulations have been proposed to investigate the conditions leading to the emergence of flow instabilities. Some of them rely on regular pore-network modeling [109, 45]. With the continuous improvement of computational resources, more recent studies directly track the fluid-fluid interface in the pore-space by solving the Navier-Stokes equations [66]. More recent studies simulate a drainage in a 3D reconstruction of the rock pore structure obtained with micro-tomography [202]. All these studies recover the three different flow regimes. The regime boundaries, however, vary from study to study and depend strongly on the pore structure.

Recently Al-Housseiny et al. (2014) and Mansouri-Boroujeni et al. (2023) used pore doublets to investigate the stability of two-phase flow in porous media. Pore doublets represent the most basic constitutive element of porous media, i.e., a solid grain sandwiched between two parallel pores [138]. This theoretical tool was initially designed to assess the oil recovery mechanisms in a petroleum reservoir during waterflooding [173, 37]. Dynamic pore-doublet models are made of coupled ordinary differential equations solving for the fluid-fluid interface position in the two parallel pores that can be of various sizes, shapes, and lengths [57, 155]. Some models also account for inertia effects [129, 135, 182]. Modern usage includes the investigation of water infiltration in soils [136], the assessment of CO_2 storage capacity in aquifers [129], and the modeling of liquid composite molding [1].

The knowledge of the meniscus positions informs on the two-phase flow stability in the pore doublet. In principle and by extrapolation, it should inform on the stability of larger-scale porous media as well. Al-Housseiny et al. (2014) studied drainage in a symmetrical pore doublet. They demonstrated that for two identical straight channels, the system stability depends only on the viscosity ratio, in agreement with Saffman-Taylor instability. They managed to recover a transition between stable and unstable flow that depends on the viscosity ratio and the capillary number by using channels whose radius increases linearly with the distance to the inlet. The dependency in Ca is due to the cross-section variations of the channels, as it changes the interface curvature when the meniscus moves, thus making the interfacial tension play a role in the pore-doublet invasion, according to Young-Laplace's law. Nevertheless, the phase diagram that they derived shows some discrepancies with the regime observed by Lenormand and others.

We posit that the transition between stable front, viscous fingering and capillary fingering can be properly captured by pore doublets if the wetting layers are considered. Wetting films are a crucial aspect of two-phase flow in porous media, yet they are often not included in pore-doublet models for the sake of simplification [28, 57, 184]. During drainage, they deposit behind the front meniscus along the solid walls [197]. Their thickness depends on the balance of viscous and capillary forces [30, 15, 223, 19].

Those layers play a role in the fluid dynamics via increased phase connectivity [203] and snap-off [165]. During drainage, they also act as lubricants via viscous coupling at the fluid-fluid interface [72, 113, 220, 171, 169, 153]. Shams et al. (2018) calculated the flow conductance in channels of various shapes including the effect of wetting layers in corners for various viscosity ratios. The resulting conductance is reminiscent of flow with partial slip conditions at the wall [148], in which the slip length depends on the repartition of the fluids inside the channel (i.e. Ca) and the mutual shear stress (i.e. M). In this work, we develop a new pore-doublet model that accounts for the film effects at the wall via an effective slip length. We use the model to investigate two-phase flow stability in symmetrical pore doublets before confronting the results with microfluidic experiments.

The chapter is organized as follows. First (Sec. 7.2), we introduce a new theory of pore doublet for drainage and imbibition, including wetting layers at the solid surface. Then, in Sec. 7.3, we describe the microfluidic experiments used to probe emerging flow patterns during drainage and to verify the theory. Finally (Sec. 7.4), we discuss the role played by wetting films on the development of instabilities in porous media. We close with conclusions and perspectives (Sec. 7.5).

7.2 Theory of dynamic pore doublets with wetting films

In this section, we describe the mathematics of two-phase flow in pore doublets and show how they are used to assess stability criteria. In particular, we introduce the equations controlling the interface dynamics when wetting layers are involved in both circular and rectangular sections.

7.2.1 Fundamental principles of pore doublets

As we saw in Chapter. 6, pore doublets offer a simplified geometrical representation of the main features of porous media. Fig. 7.1 illustrates a pore doublet with identical branches. In this particular example introduced by Al-Housseiny et al. (2014), the branch radius varies linearly along the channel mid-axis. The cross-section of each branch, noted A_i, with $i = (1, 2)$ is thus a function of z, the distance along the channel. We have,

$$A_i = f(z), \tag{7.1}$$

where f depends on the geometry of the channels.

During drainage in pore doublets, a non-wetting fluid, hereafter noted II is injected in a system saturated with a wetting fluid, denoted I. A meniscus is formed and moves from the injection channel to the bifurcation. According to the flow conditions, the meniscus splits into two menisci that invade the child branches simultaneously or at different rates, or invade only one of the two branches [129]. The position of the menisci, $z_i(t)$ are considered at the center of the channel, see Fig. 7.1 [80, 135]. The knowledge of the meniscus position to the inlet, $z_i(t)$ with $i = 1, 2$, in both branches and particularly the position difference, $\Delta z = z_1(t) - z_2(t)$, characterizes the interface front stability at larger scales. The case $\Delta z \to 0$, corresponds to a stable regime, while a divergence of Δz is characteristic of an unstable regime.

Flow in pore doublets is ruled by two fundamental principles as described in Chapter. 6:

- The flow rate is conserved throughout the system,

$$Q_p = Q_1(t) + Q_2(t), \tag{7.2}$$

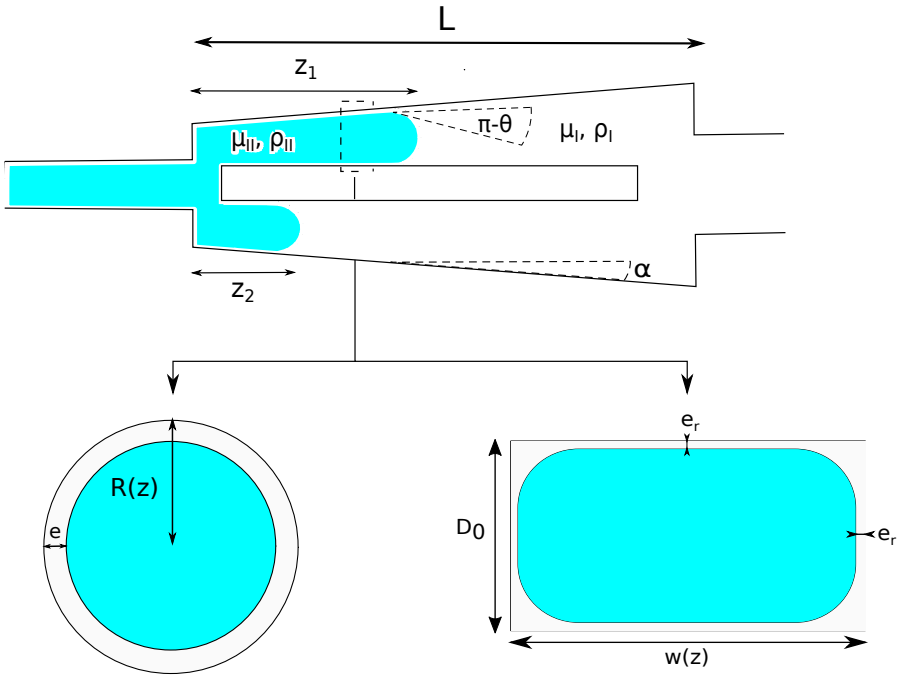

Figure 7.1: Schematic of the pore doublet used in this study. The channels are either cylindrical or rectangular. For this particular example, α is taken to be positive (diverging channels), but α can also be negative, representing converging channels.

where Q_p is the flow rate of the injected fluid in the parent channel, considered as constant in time, and Q_i ($i = 1, 2$) are the flow rates in the two child branches,

- The total pressure difference between the inlet and outlet is the same in the two branches,

$$\Delta P(t) = \Delta P_1(t) = \Delta P_2(t), \tag{7.3}$$

where $\Delta P_i(t)$ is the pressure drop in branch $i = 1, 2$.

These two principles allow the derivation of coupled ordinary differential equations (ODEs) for the evolution of the meniscus positions in both branches.

In each branch, $i = 1, 2$, the flow rate of fluid II is the same at any points upstream of the meniscus, with

$$Q_{i,II}(t) = A_{i,II}(t, z) u_{i,II}(t, z), \tag{7.4}$$

where $A_{i,II}(t, z)$ is the surface area occupied by the fluid II in a cross-section, and $u_{i,II}(t, z)$ is the speed of fluid II averaged on the section $A_{i,II}$ of channel i. Because of the wetting films left behind during the drainage of the channel or ahead of the meniscus during imbibition, $A_{i,j}(t, z_i)$ is not necessarily equal to the area of the channel cross-section. During a drainage, $A_{i,II}(t, z)$ is smaller than the channel cross-section due to wetting layers (see Fig. 7.1). $A_{i,j}(t, z_i)$ is also considered to be time-dependent to account for thickening or thinning of the films, based on the evolution of the capillary numbers in each channel. One of the two differences between ours and the other dynamic pore-doublet models proposed in the literature is the differentiation between the surface area upstream and downstream of the meniscus due to the existence of wetting films[155, 136, 80, 129].

The section-averaged flow velocity, $u_{i,j}(t,z)$ is driven by the pressure gradient, $\partial_z P_{i,II}$, upstream of the meniscus, and by $\partial_z P_{i,I}$ downstream of the meniscus. It is obtained by averaging the Stokes momentum equation over a channel cross-section considering either a no-slip condition if there is no film (i.e. if $z \in]z_i(t);L]$ for a drainage) or a partial slip condition in the presence of wetting layers (i.e., if $z \in [0;z_i(t)[$ for a drainage). The partial slip condition results from the viscous shear stress between the wetting film and the non-wetting fluid. A general formulation reads [18],

$$u_{i,II}(z) = -\frac{g_{i,II}(z)A_{i,II}(t,z)}{\mu_{II}}\frac{\partial P_{i,II}}{\partial z} \text{ if } z \in [0;z_i(t)[, \tag{7.5}$$

$$u_{i,I}(z) = -\frac{g_{i,I}(z)A_{i,I}(t,z)}{\mu_{I}}\frac{\partial P_{i,I}}{\partial z}, \text{ if } z \in]z_i(t);L], \tag{7.6}$$

where $g_{i,j}(z) = k_{i,j}(z)/A_{i,j}(t,z)$ is the channel conductance, and $k_{i,j}(z)$ is the channel apparent permeability. μ_I and μ_{II} are respectively the dynamic viscosity of fluid I and fluid II. Unlike other dynamic pore-doublet models [138, 136, 81, 129], (7.5) and (7.6) account for the impact of the wetting films at the wall if they are present. Indeed, the apparent permeability and conductance not only depend on the section shape but are a function of the film thickness and viscosity ratio as well. It constitutes the second main difference with other models. We will see in the next sections different conductances for various cross-section shapes in the presence of wetting films.

In pore-doublet models, the section-averaged velocity of the bulk of the fluid j is estimated using the speed of the meniscus, $\frac{dz_i}{dt}$. We have,

$$u_{i,j}(t,z_i) = U_i(t) = \frac{dz_i(t)}{dt}. \tag{7.7}$$

The pressure drop in each branch is obtained using,

$$\Delta P_i(t) = \Delta P_{visc,II}(z_i(t)) + \Delta P_{\text{cap}}(z_i(t)) + \Delta P_{visc,I}(z_i(t)), \tag{7.8}$$

where $\Delta P_{visc,II}(z_i(t))$ and $\Delta P_{visc,I}(z_i(t))$ are respectively the viscous pressure drop between the inlet and the meniscus location and between the meniscus and the outlet. $\Delta P_{i,\text{cap}}(z_i(t))$ is the pressure drop due to the curvature of the meniscus. The capillary pressure in channel i, $\Delta P_{i,\text{cap}}$, is due to the meniscus curvature and is estimated by Young-Laplace's law. We neglect the dynamic aspect of the curvature in this study, as we restrict ourselves to low capillary numbers. We then have,

$$\Delta P_{visc,I}(z_i) = \int_{z_i(t)}^{L} \frac{\mu_I u_{i,I}(z)}{g_{i,I}(z)A_{i,I}(t,z)}dz = \mu_I A_{i,I}(t,z_i)\frac{dz_i}{dt}\int_{z_i(t)}^{L}\frac{1}{g_{i,I}(z)A_{i,I}(t,z)^2}dz, \tag{7.9}$$

$$\Delta P_{visc,II}(z_i) = \int_{0}^{z_i(t)} \frac{\mu_{II} u_{i,II}(z)}{g_{i,II}(z)A_{i,II}(t,z)}dz = \mu_{II} A_{i,II}(t,z_i)\frac{dz_i}{dt}\int_{0}^{z_i(t)}\frac{1}{g_{i,II}(z)A_{i,II}(t,z)^2}dz, \tag{7.10}$$

$$\Delta P_{\text{cap}} = \sigma\cos(\theta_i)\kappa_i(t,z_i), \tag{7.11}$$

where $\kappa(t,z_i)$ is the curvature of the interface in channel i, σ is the surface tension, and θ_i is the contact angle between fluid II and the channel's walls. The viscous pressure drops are obtained using (7.5) and (7.6) that relate the pressure gradient to the mean velocity, and because, $U_i(t) = Q_i(t)/A_{i,j}(t,z_i)$ and Q_i being constant along the branch

length at a time t, it can be pulled out the integral. Finally, we have,

$$\Delta P_i(t) = \frac{dz_i}{dt}\left(\mu_{II} A_{i,II}(t,z_i)\int_0^{z_i(t)} \frac{dz}{A_{i,II}^2(t,z)g_{i,II}(z)} + \mu_I A_{i,I}(t,z_i)\int_{z_i(t)}^{L} \frac{dz}{A_{i,I}^2(t,z)g_{i,I}(z)}\right) + \sigma\cos(\theta_i)\kappa_i(z_i). \quad (7.12)$$

The ODEs governing the evolution of the meniscus location in both branches are obtained by combining (7.4)-(7.7)-(7.12) with the two pore-doublet fundamental principles (i.e., conservation of the flow rate at the bifurcation, and same pressure drop in both branches). Hereafter, we form non-dimensionalized ODEs using $z' = z/L$, $t' = t/t_c$, $P_i' = P_i/P_c$, $A_{i,j}' = A_{i,j}/A_c$, $k_{i,j}' = k_{i,j}/k_c$, $g_{i,j}' = g_{i,j}A_c/k_c$, $A_{i,j}' = A_{i,j}/A_c$, $\kappa_i' = \kappa_i/\kappa_c$. The reference variables are noted with subscript c. A_c, k_c, and κ_c depend on the channel geometry and are given in the following sections for cylindrical and rectangular channels. We define the characteristic time as $t_c = A_c L/Q_p$, the reference pressure as $P_c = L\mu_I Q_p/A_c k_c$, the viscosity ratio as $M = \mu_{II}/\mu_I$, and the capillary number as $Ca^* = \frac{\mu_I L Q_p}{\sigma k_c A_c \kappa_c} = Ca\,\zeta^{-1}$ with $Ca = \frac{\mu_I Q_p}{\sigma A_c}$ and $\zeta^{-1} = \frac{L}{k_c\kappa_c}$ a geometrical factor. The dimensionless conservation of the injected flow rate reads,

$$1 = A_{1,II}'\frac{dz_1'}{dt'} + A_{2,II}'\frac{dz_2'}{dt'}. \quad (7.13)$$

Because the two channels share the same inlet and outlet (see Fig. 7.1), the total pressure difference in channel 1 is the same as in channel 2. That means that from (7.12), we have that

$$\frac{dz_1'}{dt'} = \frac{\phi(z_2') + \frac{\zeta}{Ca}\left(\cos(\theta_2)\kappa'(t',z_2') - \cos(\theta_1)\kappa'(t',z_1')\right)}{A_{1,II}'(t',z_2')(\phi(z_1') + \phi(z_2'))}, \quad (7.14)$$

$$\frac{dz_2'}{dt'} = \frac{\phi(z_1') - \frac{\zeta}{Ca}\left(\cos(\theta_2)\kappa'(t',z_2') - \cos(\theta_1)\kappa'(t',z_1')\right)}{A_{2,II}'(t',z_1')(\phi(z_1') + \phi(z_2'))}, \quad (7.15)$$

with

$$\phi(t',z_i') = M\int_0^{z_i'(t')} \frac{dz}{A_{i,II}'(t',z)^2 g_{i,II}'(z)} + \frac{A_{i,I}'(t',z_i')}{A_{i,II}'(t',z_i')}\int_{z_i'(t')}^{1} \frac{dz}{A_{i,I}'(t',z)^2 g_{i,I}'(z)}. \quad (7.16)$$

Equations (7.14) and (7.15) form a generic system of coupled ODEs that solves for the meniscus location in both branches regardless of length and channel geometry, as long as the channels fall within the realm of pore-doublet theory. In the next two parts, we calculate the conductance $g_{i,j}$, the functions $\phi(z)$, the section area $A_{i,j}(z)$, and the meniscus curvature, $\kappa(z)$ for a drainage ($\theta < 90°$) with wetting films for cylindrical and rectangular channels as illustrated in Fig. 7.1.

7.2.2 Converging/diverging cylindrical channel with wetting layers

In this section, we derive the ϕ_i functions, the conductance $g_{i,j}$, and the surface area $A_{i,j}$ in the case of drainage in converging or diverging cylindrical channels. The channels are identical, and their radius is described by $r(z) = r_0 + \alpha z$ (see Fig. 7.1). No assumption is made on the sign of α, as long as it is small enough to fit in the lubrication theory, which is the case for $|\alpha| << 1$ [80]. The reference variables for this geometry are $A_c =$

πr_0^2, $k_c = r_0^2/8$, $g_c = 1/8\pi$, and $\kappa_c = 1/r_0$. The capillary number is, therefore, defined as $Ca^* = \frac{8\mu_I L Q_p}{\sigma \pi r_0^3} = Ca\zeta^{-1}$, with $\zeta^{-1} = \frac{8L}{\pi r_0}$.

In non-dimensionalized form, the channel radius reads,

$$r'(z') = 1 + z'\alpha', \tag{7.17}$$

where $\alpha' = \alpha \frac{L}{r_0}$. The cross-section is,

$$A_i'(z') = r'(z')^2, \tag{7.18}$$

and the conductance reads,

$$g_i' = 1. \tag{7.19}$$

The latter is obtained from the permeability of the cylindrical channel $k(z) = r^2(z)/8$.

The wetting fluid layer, also known as Bretherton film [30, 197] has a thickness $e_i(z)$ that can be approximated using the results of Balestra et al. (2018),

$$\frac{e_i'(t', z')}{r'(z')} \approx \frac{P(M)(3Ca_i(t'))^{2/3}}{1 + P(M)Q(M)(3Ca_i(t'))^{2/3}}, \tag{7.20}$$

where $P(M)$ and $Q(M)$ are given in Appendix. C, and $Ca_i(t') = Ca\frac{U_i(t')}{U_1(t')+U_2(t')}$ is the capillary number of channel i. (7.20) is a generalization of the law derived by Aussillous and Quéré (2000), which assumes the non-wetting fluid to be inviscid. It agrees with the equation of Aussillous and Quéré (2000) for $M < 1$, and predicts an increase of the film's thickness with the viscosity ratio until it reaches a plateau for $M > 10^3$ where the film is $2^{2/3}$ the thickness of the film in the inviscid case. This law is valid for capillary numbers below 1. In practice, e_i is small compared with the channel radius (e.g. if $Ca_i = 10^{-3}$, then $\frac{e_i}{r_0} \approx 10^{-2}$).

The wetting films reduce the space available for the flow of fluid II in the channel. We introduce $\chi_i(z_i)$, as the fraction of the cross-section occupied by the non-wetting fluid in the center of the channel. For drainage, we have

$$\chi_i(t, z) = \begin{cases} \frac{A_{i,II}'}{A_i'} = \left(1 - \frac{e_i'(t,z)}{r'(z)}\right)^2 & \text{for } z \in \left[0; z_i'\right], \\ 0 & \text{for } z \in \left]z_i'; 1\right]. \end{cases} \tag{7.21}$$

The wetted area is then defined as $1 - \chi_i(t, z)$. The surface area and conductance downstream of the meniscus read,

$$A_{i,I}' = A_i' \text{ and } g_{i,I}' = g_i', \tag{7.22}$$

while in the presence of wetting films upstream of the meniscus we have,

$$A_{i,II}' = \chi_i A_i' \text{ and } g_{i,II}' \approx g_{i,I}'\left(1 + 4\frac{\lambda_i(t', z')}{r'(z')}\right), \tag{7.23}$$

with $\lambda_i = e_i'(t', z')M$. A derivation of this equation is described in Appendix. D. The equation for $g_{i,II}'$ is obtained by averaging the velocity profile obtained by solving Stokes equations in a cylindrical channel with a uniform wetting film that is only driven by mutual shear stress [18] and assuming that the film thickness is small compared to the cylinder radius. Mathematically, (7.23) can also be obtained by considering a partial slip condition at the fluid-fluid interface with the effective slip length λ_i (see Appendix. E) describing the lubrication caused by the wetting film.

(7.23) shows that the surface area of contact between the two fluids, as well as the viscosity ratio, play a role in the dynamics of the non-wetting fluid, highlighting the viscous coupling between the two fluids [61, 113]. When M is very small, the wetting layers behave like a wall, and the partial slip becomes a no-slip condition at the interface between the fluid. On the opposite, when M is very high, the wetting layer behaves like a lubricant, decreasing the viscous drop. This notion of slip is used later on to build the conductance in a rectangular wetted channel by analogy with the cylinder.

The curvature of the meniscus reads,

$$\kappa'(z_i') = \frac{2}{r'(z_i') - e_i'(t', z')}. \tag{7.24}$$

Finally after integration (see Appendix. F), we obtain, to the first order in e_i,

$$\begin{aligned}\phi(t', z_i') = &\frac{r'(z_i')^2}{(r'(z_i') - e_i'(t'))^2} \times \frac{1 - \frac{r'(z_i')^3}{r'(1)^3}}{3\alpha' r'(z_i')^3} \\ &+ \frac{M}{\alpha' K^3}\left(-\ln r'(z_i') - K\left(1 - \frac{1}{r'(z_i')}\right) - \frac{K^2}{2}\left(1 - \frac{1}{r'\left(z_i'\right)^2}\right) + \ln\left|\frac{r'(z_i') + 2\lambda_i}{1 + 2\lambda_i}\right|\right),\end{aligned} \tag{7.25}$$

with $K = -4(M-1)e_i'(t', z')$.

7.2.3 Converging/diverging rectangular channel with wetting layers

In the last section, we saw how the wetting layers act as lubricants in cylindrical channels. Porous media and microfluidics devices, however, rarely have cylindrical cross-sections and often present corners and crevices in which fluid accumulates, leading to thicker wetting layers in the corners. In this section, we consider the drainage in rectangular channels whose width varies linearly from the inlet to the outlet. The two channels are identical: their width is described by $w(z) = w_0 + \alpha z$ (see Fig. 7.1), and their depth is constant $D(z) = D_0$. The aspect ratio between the channel length and width is $\epsilon(z) = w(z)/D(z)$, and the reference variables are $w_c = w_0$, $D_c = D_0$, $A_c = w_0 D_0$, $k_c = w_0^2/12$, $g_c = \frac{w_0}{6D_0}$, and $\kappa_c = 2/w_0$. The capillary number is defined as $Ca^* = \frac{6\mu_I L Q_p}{\sigma D_0 w_0^2} = Ca\,\zeta^{-1}$ with $\zeta^{-1} = 6L/w_0$. In our pore doublet, the cross-section at the inlet of the channel is square and $D_0 = w_0$. Because our channel depth is constant, $D' = 1$. In non-dimensionalized form, the channel width reads,

$$w'(z') = 1 + z'\alpha', \tag{7.26}$$

where $\alpha' = \alpha\frac{L}{w_0}$. The cross-section is,

$$A_i'(z) = w'(z')D', \tag{7.27}$$

and the conductance reads,

$$g_i'(z) = \frac{1}{w'(z)}\left(1 - \frac{\beta}{w'(z)}\right). \tag{7.28}$$

The latter is obtained because the permeability of a rectangular channel is $k(z) \approx \frac{D_0^2}{12}\left(1 - \beta\frac{D_0}{w(z)}\right)$ with $\beta = 6\,(2/\pi)^5$. This equation comes from the first term of the Fourier series giving

the solution for the velocity profile. This approximation is valid for $D_0 < w(z)$, and leads to a deviation from the exact solution of less than 10% for $D_0/w(z) < 0.7$ [80].

In rectangular cross-sections, the wetting film is no longer axisymmetric. It is thin along the walls and gets thicker near the corners, as illustrated in Fig. 7.1. At the center of the walls, the thickness is given by [125],

$$\frac{e'_{r,i}(t',z')}{R'_h(z')} = \frac{0.7Ca_i^{2/3}(t')}{1+3.35Ca_i^{2/3}(t')}, \tag{7.29}$$

where $R'_h(z') = \frac{w'(z')D'}{w'(z')+D'}$ is the hydraulic radius. This estimation of the film thickness is no longer true at the corners, where a much larger volume of fluid accumulates [28, 57]. We assess the reduction in the cross-section occupied by the non-wetting fluid by considering an effective uniform film whose mean thickness is given by

$$\frac{e'_{avr,i}(t',z')}{R'_h(z')} = \frac{(1-\chi_i(t',z'))}{2}, \tag{7.30}$$

where $1-\chi(t',z')$ is the cross-sectional fraction occupied by the wetting fluid. Magnini et al. (2022) used numerical simulations to propose the semi-analytical law,

$$\chi_i(t',z) = \begin{cases} \frac{A'_{i,II}}{A'_i} = 1-\psi(z)\left(1-(1-\chi_\infty)\exp\left(a_1\left(Ca_i(t')\left(1+\frac{\epsilon(z')^2}{\epsilon_t^2}\right)^{a_2}\right)\right)\right) & \text{for } z\in\left[0;z'_i\right], \\ 0 & \text{for } z\in\left]z'_i;1\right], \end{cases} \tag{7.31}$$

where $\psi(z)$ is the wet fraction in the asymptotic case $Ca\to 0$, given in C, from Wong et al. (1995), with $\epsilon_t = 5.5$, $\chi_\infty = 0.37$, $a_1 = -0.24$ and $a_2 = -0.5$. Note that the influence of the viscosity ratio is neglected in the calculation of $e_{r,i}$, e_{avr}, and $\chi_i(t',z')$.

The surface area and the conductance downstream of the meniscus read,

$$A'_{i,I}(z') = A'_i(z') \text{ and } g'_{i,I}(z') = g'_i(z'). \tag{7.32}$$

By analogy with the cylindrical case, the surface area and the conductance in the presence of wetting films upstream of the meniscus we have,

$$A'_{i,II}(t',z') = \chi_i(t',z')A_i(z')' \text{ and } g'_{i,II}(z') = g'_i(z')\left(1+c\frac{\lambda_i(t',z')}{R'_h(z'_i)}\right). \tag{7.33}$$

In (7.33), c is a numerical constant that weakly changes with the aspect ratio. For a rectangular shape Ebert and Sparrow (1965) computed $c\approx 6$. At first approach, we take the effective slip length as equal to the effective mean film thickness,

$$\lambda_i(t',z') = e'_{avr,i}(t',z')M. \tag{7.34}$$

This is a significant assumption, but this allows us to find a value for ϕ in the rectangular case while keeping the calculations relatively simple. The mean curvature of the meniscus is approximated using [125]

$$\kappa'_i(t',z') = 2\left(\frac{1}{w'(z')-2e'_{r,i}(t',z')}+\frac{1}{D'-2e'_{r,i}(t',z')}\right), \tag{7.35}$$

where $e_{r,i}(t',z)$ is the thickness of the films at the center of the walls as shown in Fig. 7.1.

Finally, after a first-order Taylor expansion in e and some manipulation, we obtain (see the details in Appendix. F),

$$\begin{aligned}\phi(t',z') = &\frac{M}{2\chi_i^2\alpha'(1+c\lambda)}\left(\ln\left(\frac{(w'(z_i)-\beta)(w'(z_i)(1+c\lambda)+c\lambda)}{(1-\beta)(1+2c\lambda)}\right)\right.\\ &\left.-\frac{c\lambda-\beta(1+c\lambda)}{A}\ln\left(\frac{(w'(z_i)-\beta)(1+2c\lambda)}{(w'(z_i)(1+c\lambda)+c\lambda)(1-\beta)}\right)\right)+\frac{1}{\alpha'\chi_i}\ln\left(\frac{w'(l)-\beta}{w'(z_i)-\beta}\right),\end{aligned} \tag{7.36}$$

with $A = (c\lambda+\beta(1+c\lambda))$.

7.2.4 Numerical implementation

To implement the equations derived in the previous section, we use Matlab with an ODE solver to compute the movement of the menisci in a pore doublet with and without the presence of wetting layers. We choose the ode45 function of Matlab with its default options, as it provides the best compromise of accuracy and computational speed for non-stiff problems [54]. This solver is based on an explicit fourth-order Runge-Kutta method.

To solve these equations, we impose that the interfaces cannot move backward in the channel. This is crucial to preserve the stability of the numerical solutions [80]. To create the perturbation leading to the instability, the initial positions of the interfaces are set differently: $z_1(t=0) = 0$ but $z_2(t=0) = \tau' = 10^{-2}$. The only effect of this parameter is to accelerate or delay the onset of the instability. For a smaller τ, if the system is unstable, the instability will appear later during the invasion, whereas for a larger τ, it will become visible earlier. However, changing the value of τ does not affect the overall stability of the invasion. To find the values of the wet area and the film thickness, we compute the capillary number of each channel defined as $Ca_i(t) = Ca\frac{U_i(t)A_c}{Q_p}$, where $U_i(t)$ and Q_p are calculated from the time-averaged speed of the menisci in the previous time-steps. When one of the interfaces reaches the outlet (when $z_i' = 1$), the speed of the menisci is set to zero to signify the end of the invasion.

7.2.5 Stability criteria

The system stability analysis on the experiments and the simulations is done by looking at the difference in the menisci positions, $\Delta z'$, once one interface reaches the outlet. We consider three different regimes:

- Stable: $\Delta z' < \tau'$, both interfaces arrive at the outlet almost simultaneously.
- Strongly unstable: $\Delta z' > 0.99$, one of the two menisci remains stuck at the inlet.
- Weakly unstable: $\tau' < \Delta z' < 0.99$, both channels are invaded, but only one of the interfaces reaches the outlet.

Alternatively, Al-Housseiny et al. (2014) derived a theoretical condition to predict whether the system is stable or unstable. In their derivation, they look at the sign of the growth rate $\frac{1}{\Delta z'}\frac{d\Delta z'}{dt'}$. On the one hand, if it is negative, any difference in the position decreases with time, and the invasion is stable. On the other hand, if it is positive, the perturbation grows in time until it diverges, leading to an unstable invasion. For a pore doublet with rectangular channels, they show that:

$$\frac{1-M}{1-\beta}+\frac{2\zeta\alpha\cos\theta}{Ca}-\ln\frac{w(l)-\beta}{1-\beta}\geq 0. \tag{7.37}$$

This relation, however, neither informs about the weakly unstable regime nor accounts for the wetting layers. This is further discussed in Section. 7.4.

Table 7.1: Dimensions of the micromodels used in the experiments.

L (µm)	α	D_0 (µm)	w_0 (µm)	w_f (µm)
1800	0.037	45	45	112
3400	0.037	90	90	216

7.3 Experimental material and methods

In this section, we describe the experimental procedure to investigate the two-phase flow stability conditions in porous media. It includes the microfabrication of pore doublets in microfluidic devices, the fluid properties, and the image analysis used to interpret the results.

7.3.1 Fabrication of microfluidic pore doublets

A photolithography method is used to create silicon wafer molds with the desired geometry. Then, PDMS (PolyDiMethylSiloxane) soft lithography is used to produce the microfluidic chips containing the pore doublet [166] (the procedure is described in more detail in Chapter. 4). The pore-doublet length, L, from the bifurcation to the point where the child branches reconnect, the etching depth, D_0, the initial and final channel width, w_0 and w_f (corresponding to $\alpha = (w_f - w_o)/L$) are found in Tab. 8.1 and can be seen on Fig. 7.1. Since the produced PDMS chips have a heterogeneous hydrophobic behavior, we use either Polyvinyl alcohol (PVA) deposition or silanization techniques to get a uniformly hydrophilic or hydrophobic behavior of the channels. These two approaches are described in Chapter. 4. After the PVA deposition, the micromodel becomes hydrophilic with $\theta \approx 25°$ and stays hydrophilic for a long period (no change after 30 days) [201]. The silanization process, on the other hand, creates a strongly and uniformly hydrophobic PDMS surface, with a contact angle of 120° between the air-water interface and the solid. Using these two methods enables a wider range of viscosity ratios by choosing proper fluid pairs for which water is either the wetting or the non-wetting fluid.

7.3.2 Fluid properties

Different fluids are picked to investigate the stability of the invasion: water with a viscosity of 1.005×10^{-3} Pa·s at room temperature, air with a viscosity of 1.85×10^{-5} Pa·s, and silicon oils with a viscosity of 5.0×10^{-3} Pa·s and 1.0×10^{-2} Pa·s. Water is used as a wetting fluid in PVA-treated micromodels and is displaced by air (viscosity ratio of $M = 1.84 \times 10^{-2}$) or by silicon oils ($M = 5$ or $M = 10$). Silicon oils are used as wetting fluids for hydrophobic micromodels and are displaced by water, leading to viscosity ratios of $M = 2.0 \times 10^{-1}$ or $M = 1.0 \times 10^{-1}$. The air-water interfacial tension is 73 mN·m^{-1} at 20°C [204]. The interfacial tensions between the silicon oils and water were measured using the OneAttention Theta Flex tensiometer from Biolin Scientific present in the Nanoµlab, and are both around 47 mN·m^{-1}. During the experiments, dye (Royal Blue) or tracer particles are added to the water for an easier distinction of the fluids. We also performed experiments with untreated PDMS, where silicon oil is used as a wetting fluid, and the non-wetting fluid is a mix of glycerol and DI water. In this case, the contact angle of the silicon oil with PDMS is close to zero. Glycerol and water can be mixed in different proportions to reach different values of viscosity, from 1 mPa·s (pure water) to 1410 mPa·s (pure glycerol) at 20 °C. The silicon oil chosen

as the wetting fluid has a viscosity of 5 mPa·s. The experiments in Sec. 7.4 were done with a mix containing $80wt\%$ glycerol and $20wt\%$ DI water. The mix has a viscosity of 60.1×10^{-3} Pa·s [176] and the measured interfacial tension between the mix and the silicon oil is 33 mN·m^{-1} at room temperature.

7.3.3 Experimental procedure and image analysis

The micromodel inlet is connected to a 4-way valve using a needle. One of the ports of the valve is closed. The two remaining ports are connected to syringes of non-wetting and wetting fluids, and A LEGATO 110 syringe pump from kdScientific is used to inject the fluids. The micromodel is placed under an inverted microscope (Eclipse Ti2-U, from Nikon), and a fast camera (HS7 high-speed camera, from Fastec) is used to visualize and record the flow, see schematic of the experimental setup in Fig. 4.9.

To proceed with the experiment, the micromodel is first saturated with the wetting fluid, then the valve is switched and the non-wetting fluid is injected at a fixed flow rate (between 10^{-4} mL·min^{-1} and 1 mL·min^{-1}). When the interface approaches the pore doublet, the recording is started. After the invasion, the pore doublet is again saturated with the wetting fluid before starting the procedure again with another flow rate.

The image sequences are then processed to isolate the interfaces on each frame, see Chapter. 4 for a more in-depth description of the image analysis procedure. Then, using an in-house Matlab code, we track the position of the three interfaces (one in the inlet channel and one in each channel) frame by frame to deduce their velocities. Using this information, we can then find the capillary number of the invasion. This is necessary because the flow rate imposed by the syringe pump is not always accurate during experiments. In fact, the measured flow rate can differ from the nominal value set on the pump by up to an order of magnitude. This discrepancy is largely due to capillary effects. As the fluid interface enters the pore doublet, its curvature increases due to the smaller dimensions, which in turn raises the capillary pressure between the fluids. To maintain a constant flow rate, the pump must exert a higher pressure on the syringe. Additionally, as mentioned in Sec. 4.3.2, the syringe pump requires some time to stabilize at the target flow rate, further contributing to deviations from the expected value. As a result, we always use the measured flow rate to compute the capillary number, and this value is used consistently throughout our analysis.

7.4 Results and discussion

In this section, we investigate the role of wetting layers in pore doublets using the models introduced in Section 7.2 and the microfluidics experiments of Section 7.3. First, we present experimental evidence of stable and unstable flow regimes in rectangular pore doublets. Then, we highlight the role of wetting films in both rectangular and cylindrical channels using our numerical model coupled with experimental results in the rectangular channels case.

7.4.1 Stable, weakly unstable and unstable regimes

We conduct pore-doublet experiments that cover capillary number and viscosity ratio ranging from $Ca \in \left[1.2 \times 10^{-6}; 4 \times 10^{-2}\right]$ and $M \in \left[1.84 \times 10^{-2}; 1.2 \times 10^{1}\right]$. In all experiments, the non-wetting fluid drains the main channel and then splits into two menisci at the bifurcation to invade the two daughter channels. Typical invasions are shown in Fig. 7.2. We observe three different invasion patterns: *i)* viscous stable invasions,

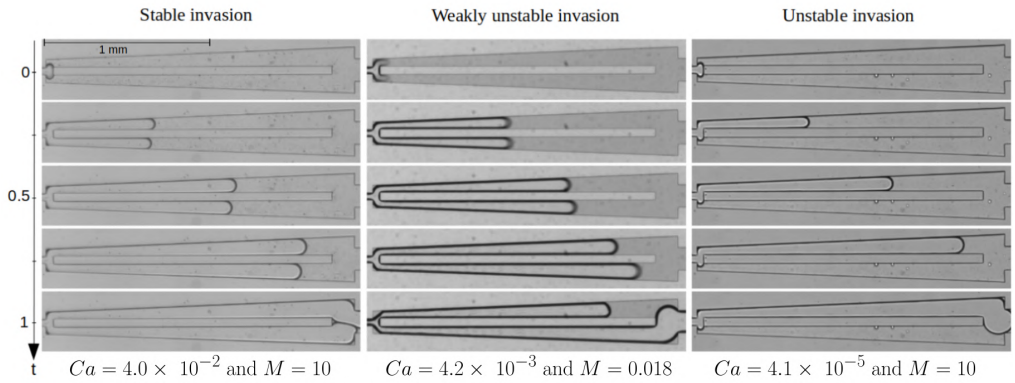

Figure 7.2: Experimental images of the displacement of water from the pore doublet. The experiments are rescaled with $t = 0$ at the beginning of the invasion and $t = 1$ at the end of the invasion. The injection occurs from the left to the right.

if both daughter channels are invaded simultaneously at the same rate, *ii)* weakly unstable drainage, if one channel is only partially invaded, and *iii)* capillary unstable invasions, if only one channel is invaded by the non-wetting fluid, see Fig. 7.2.

Viscous stable invasion occurs if the viscosity of the injected fluid is larger than the defending fluid ($M > 1$) and if viscous forces dominate capillary forces ($Ca > 10^{-2}$). In these conditions, both channels are invaded at the same time, and the menisci have the same velocity. Eventually, they rejoin each other at the end of the pore doublet. All the wetting fluid is recovered. This regime, observed here in a pore doublet, corresponds to the viscous stable front propagation in porous media [109].

Weakly unstable invasion occurs at intermediate capillary numbers ($10^{-4} < Ca < 10^{-2}$) and low viscosity ratio ($M < 1$), for which both capillary and viscous forces are of similar intensity [129]. Viscous forces are strong enough for the injected fluid to enter both daughter branches. The displacement rate of the two menisci, however, is not equal. As a consequence, one meniscus reaches the pore-doublet outlet before the other one, stopping the progression of the delayed meniscus, and leaving residual saturation in the partially invaded channel [57]. This unstable regime is reminiscent of the viscous fingering introduced by Saffman and Taylor (1958) that leads to the trapping of fluid ganglia in an ensemble of adjacent pores [122].

Unstable invasion occurs at low capillary numbers ($Ca < 10^{-4}$) for which surface-tension forces dominate. In this case, only one of the child branches is invaded, the other remains completely saturated with the initial fluid. This instability appears because the path of least resistance is the channel with the lower capillary pressure, which is also the channel with the leading meniscus. Unlike the weakly unstable regime for which one of the branches is partially drained, the residual trapping in this regime is greater as one of the channels is still fully saturated with the wetting fluid when the meniscus reaches the outlet. This regime is the capillary instability highlighted by Lenormand and Zarcone (1985).

The experimental results are summarized in figure 7.3 using a $Ca - M$ diagram where a square represents an unstable invasion, a circle a stable one, and a triangle corresponds to a weakly unstable experiment. The theoretical frontier between stable and unstable regimes proposed by Al-Housseiny et al. (2014) is added for comparison (see (7.37)). Some experiments are not correctly predicted by the theoretical criteria, especially for $M \geq 10$, where we observe unstable experiments in the stable domain. We posit that this contraction between our experiments and the regime boundary is

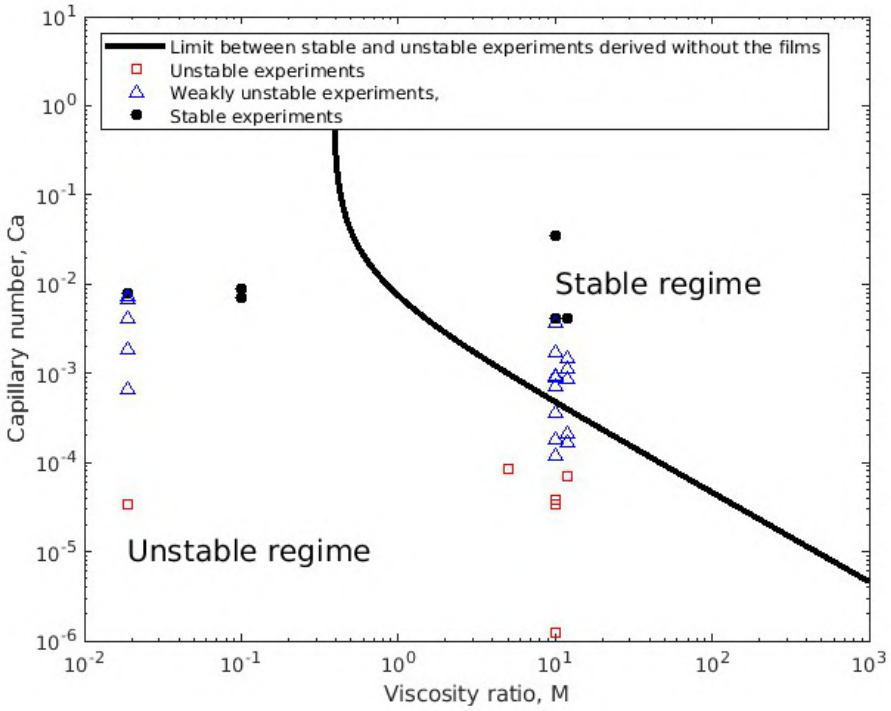

Figure 7.3: Experimental results compared with the theoretical stability curve without films. We observe unstable experiments in the stable domain, suggesting that wetting layers impact the flow stability.

due to the impact of the wetting layers on the flow, which is not considered in the theoretical criteria. Indeed, in our experiments, we observe a wetting layer left behind the meniscus [129]. In the following sections, we study the impact of these films and how they alter the stability criteria

7.4.2 Impact of wetting layers on two-phase flow in cylindrical channels

We look at the impact of the wetting layers in pore doublets with cylindrical channels. The channel geometry is set to $\alpha = 0.05$, $L = 1.8 \times 10^{-3}$ m and $r_0 = 4.5 \times 10^{-5}$ m. We run two kinds of simulations: with and without the films. In Fig. 7.4, we compare the evolution of the meniscus positions for four (Ca, M) couples. In all cases, we see an impact of the wetting layer on the meniscus dynamics. This is expected as the wetting layers change both capillary and viscous forces. For small viscosity ratios ($M < 1$), the films tend to stabilize the invasion, as the difference in meniscus position predicted by the model with films is smaller than the prediction of the model without films (see Figs. 7.4a and 7.4b). For large viscosity ratios ($M > 1$), the opposite occurs. In Fig. 7.4d, the model without the film predicts a stable invasion, as the meniscus positions follow the same curve, while the model with films predicts a weakly unstable invasion. This shows the impact of the viscous coupling between the two fluids inside the channel. If the wetting fluid is less viscous than the invading fluid ($M > 1$), the invasion is more unstable, while if the wetting fluid is more viscous ($M < 1$), the invasion is stabilized by the viscous coupling.

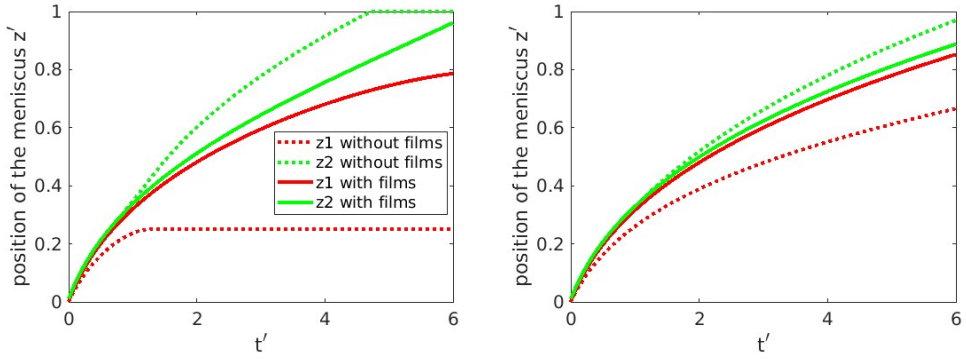

(a) $Ca = 0.08$ and $M = 0.1$

(b) $Ca = 0.05$ and $M = 0.5$

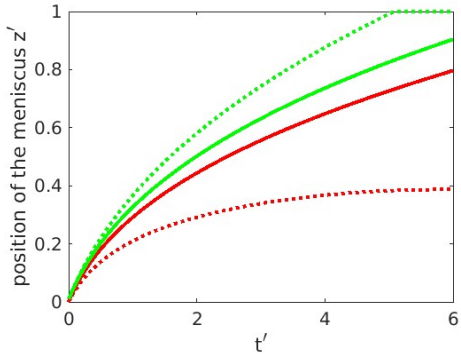

(c) $Ca = 0.015$ and $M = 2$

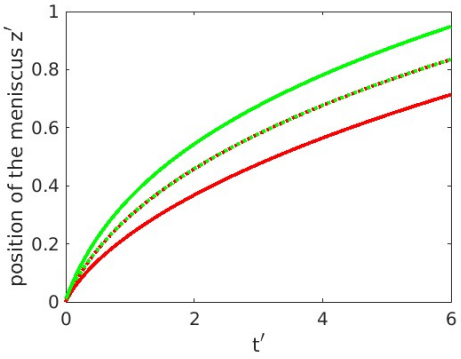

(d) $Ca = 2 \times 10^{-3}$ and $M = 100$

Figure 7.4: Simulations with and without wetting layers for cylindrical channels. The channel geometry is $\alpha = 0.05$, $L = 1.8 \times 10^{-3}$ m and $r_0 = 4.5 \times 10^{-5}$ m. The two models do not always predict the same stability regime.

To see the impact of the films on a wider range of parameters, we draw the M–Ca phase diagram similar to Lenormand et al. (1988). We run 500×500 simulations to cover values logarithmically distributed over the ranges $M \in \left[10^{-3}; 10^{3}\right]$ and $Ca \in \left[10^{-6}; 10^{-1}\right]$. Each simulation is then identified as either stable, unstable, or weakly unstable. The results are presented in Fig. 7.5. The colored regions correspond to the invasion regimes obtained using the model with films. In dashed and plain lines, we draw the boundaries between the domains without films. We observe an important difference for $M > 100$, where a horizontal asymptote bounds the stable regime including wetting layers at $Ca \approx 10^{-2}$. This is also the case for the strongly unstable domain that plateaus at $Ca \approx 10^{-3}$. Our predictions with films for large viscosity ratio are in very good agreement with the prediction of Lenormand et al. (1988), which considered drainage in a network of pores.

For $M < 1$, we observe that the boundary of the stable regime with the film shifts slightly toward smaller M and Ca compared to the prediction of the model without films. This is due in part to the viscous coupling between the fluids, where the more viscous wetting layers increase the viscous dissipation, and also the reduction of the available space for the flow of the non-wetting fluid because of the presence of the wetting films, which occupy a significant portion of the channel at high Ca, increasing the viscous pressure drop. Both of these phenomena increase the relative strength of the viscous forces and thus stabilize the invasion.

Our results highlight the differences between the models with and without films, and in the next section, we will compare them to microfluidics experiments to see which one better describes the invasion.

7.4.3 Impact of wetting layers on two-phase flow in rectangular channels

In this section, we use the experimental data obtained in Sec. 7.4.1 to check the accuracy of the model developed in Sec. 7.2 for rectangular channels. For that, we use the Matlab code introduced in Sec. 7.3 to extract the menisci positions in time and compare them with the theoretical models, see Fig. 7.6. In blue and yellow are the experimental curves, and in green and red are the meniscus positions predicted by the model without the films (dashed lines) and with the films (full lines). On Fig. 7.6(a), the experimental curves show a weakly unstable behavior, with one meniscus lagging behind the other, as predicted by our model with films. For the same parameters, the model without the wetting layers predicts a stable invasion, which does not fit with the experiment. Fig. 7.6(b), the experimental curves show a strong instability, with one of the meniscus not being invaded at all, which is coherent with the prediction of the model with the wetting layers, while the model without the films presents significant errors. This shows that our model developed in Sec. 7.2 is in good agreement with experiments and can be used to predict the invasion regimes.

We discretize the $Ca - M$ phase diagram into a grid of 500×500 points, with values logarithmically distributed over the ranges $M \in \left[10^{-3}; 10^{3}\right]$ and $Ca \in \left[10^{-6}; 10^{-1}\right]$ to observe the impact of the films for a wider range of parameters for channel with rectangular sections. We then run two simulations for each point: one excluding the films and one including them. Based on the position difference between the two menisci, each simulation is classified as stable (when $\Delta z_{final} < \Delta z_{initial}$), unstable (when $\Delta z > 0.99L$), or weakly unstable. We then draw the borders between each regime using the models with and without films. Finally, the experimental points are added for comparison.

As can be seen in Fig. 7.7, the model with films leads to an unstable regime dominating at low capillary numbers, a stable domain at high Ca and $M > 1$, and finally a

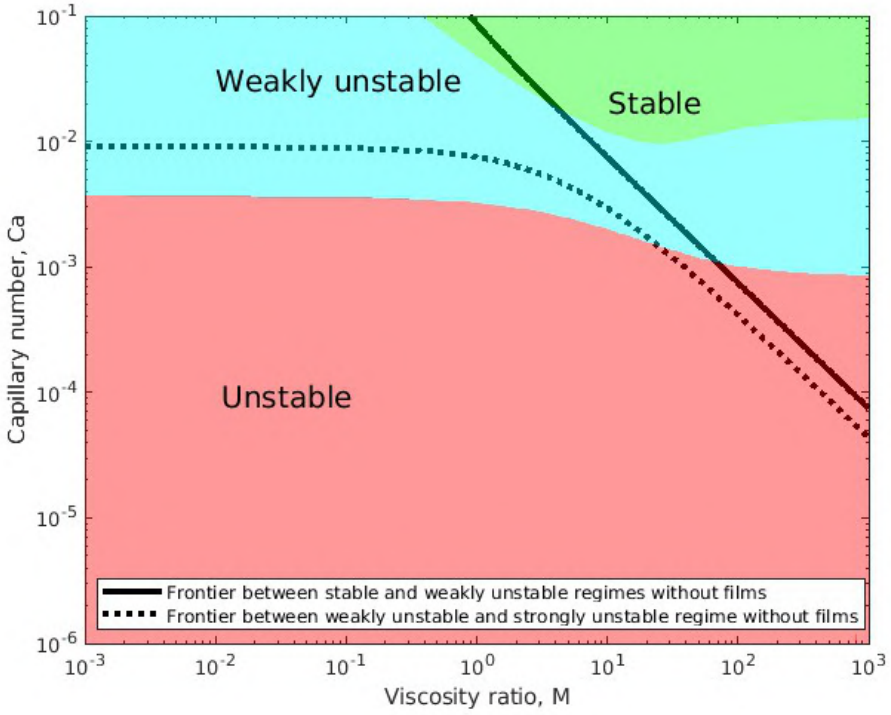

Figure 7.5: $Ca-M$ phase diagram of a pore doublet with cylindrical channels with $\alpha = 0.05$, $L = 1.8\times10^{-3}$ m and $r_0 = 4.5\times10^{-5}$ m. The three regimes, stable (green), weakly unstable (blue), and unstable (red), are determined using the model with the wetting layers. Without the wetting layers, the limit between stable and weakly unstable is shown in black lines, and the dotted line is the limit between weakly unstable and unstable.

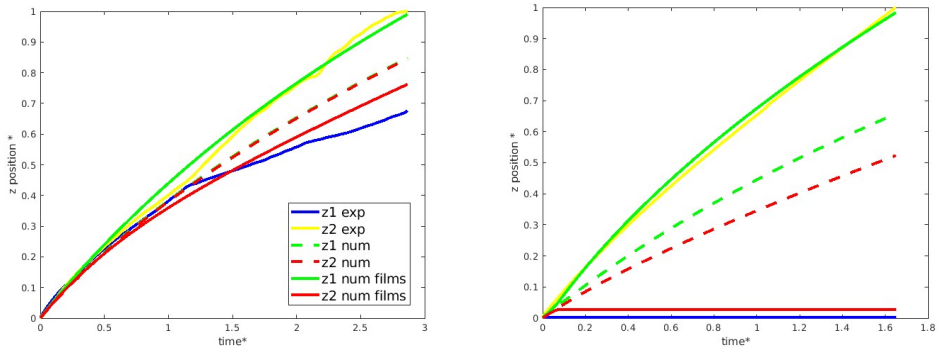

(a) $Ca = 3.1\times10^{-4}$ and $M = 10$ (b) $Ca = 7.9\times10^{-5}$ and $M = 12$

Figure 7.6: Comparisons between experimental curves and the two models for, (a) silicon oil displacing water in a PVA-treated pore doublet, and (b) a mix of $80w\%$ glycerol and $20w\%$ DI water displacing silicon oil. The blue and yellow curves correspond to the experimental menisci position. The dotted and continuous red and green curves correspond to the numerical prediction of the model without and with the wetting layers, respectively.

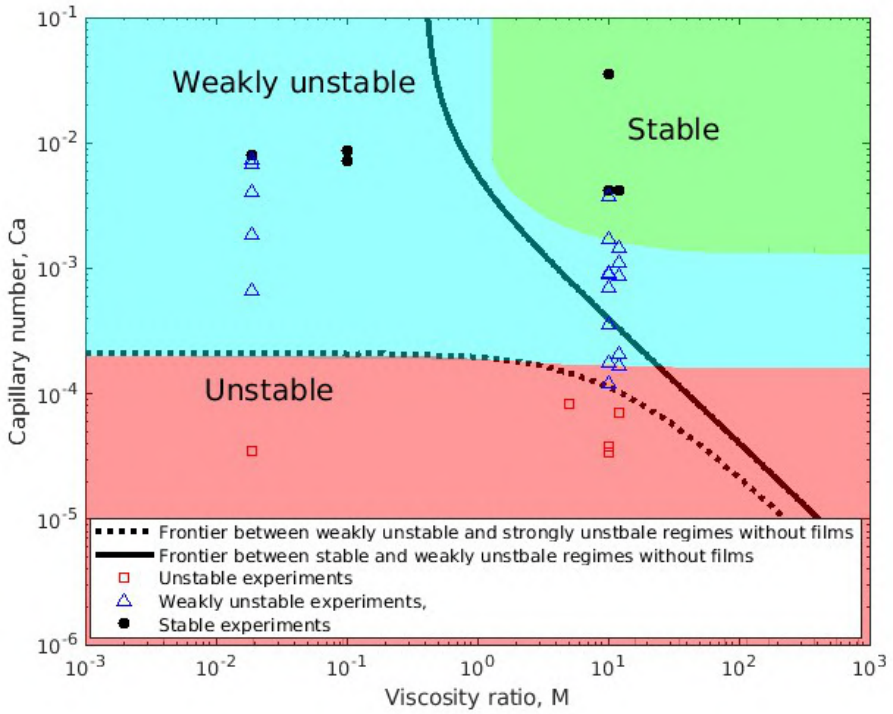

Figure 7.7: $Ca - M$ phase diagram for a pore doublet with rectangular channels, with the different regimes determined using the model with wetting layers. The stability limit determined using the model without the wetting layer model is shown, as well as the experimental points. Significant differences between the two models can be seen, especially when $M > 10$.

weakly unstable regime in between them. Similar to the classic phase diagram first introduced by Lenormand [110], we recover a stable displacement for $M > 1$ and $Ca > 10^{-3}$, an unstable regime for $Ca < 10^{-4}$, associated with capillary fingering that arises when capillary forces are dominant, and the weakly unstable regime for $M < 1$ and $Ca > 10^{-4}$, dominated by the destabilizing effect of the unfavorable displacement.

Similarly to Fig. 7.5, the difference between the two models is higher when the viscosity ratio is far from 1. But in the rectangular case, the effects of the films are more pronounced, as more wetting fluid stays behind the meniscus, thus increasing the impact of the wetting layers, see Sec. 7.4.2. The impact of the wetting films is complex and non-linear. On the one hand, these layers reduce the available surface area for the flow of the non-wetting fluid and change the flow condition via viscous coupling, as can be seen in Eq. (7.23). For $M > 1$, the viscous coupling leads to a slip-length larger than the flow surface reduction, thus decreasing the viscous drop. For $M < 1$, the slip-length is smaller than the surface reduction, increasing the viscous drop and stabilizing the invasion. On the other hand, the wetting layers also increase the curvature of the menisci, see Eq. (7.24), which increases the capillary force, leading to a more unstable invasion.

We see this effect for $M > 10$, where the viscous coupling and the increased menisci curvature destabilize the flow and shift the lower border of the stable regime to a higher capillary number compared to the model without films. This explains the weakly unstable experiments observed in that region, see Fig. 7.7. This lower border reaches a plateau at $Ca = 10^{-3}$, where increasing the viscosity ratio further does not increase the stability of the invasion, as reported by Gong et al. (2023).

For $0.3 < M < 1$ and $10^{-2} < Ca < 1$, the presence of the wetting layers also decreases the range of parameters for which the invasion is stable. Indeed, the model without the film allows stable invasion for $M < 1$ if the capillary number is high enough, see the continuous black line in Fig. 7.7. For these values of M, the slip-length leads to a viscous coupling that compensates for the reduction in flow surface area, meaning that the viscous forces are roughly unchanged compared to the model without films, but the capillary forces are increased by the curvature increase, which destabilizes the invasion.

This complex effect of the films means that there should also be a regime for $M << 1$ and a high Ca where the invasion would be stable. Indeed, the meniscus curvatures increases with the thickness of the film $\left(\Delta P_{i,cap} \propto \frac{1}{w'(z_i)-2e'_{i,r}}\right)$ but not as quickly as the viscous drop caused by the decrease of the available surface for the flow of the non-wetting fluid $\left(\Delta P_{visc,II} \propto \frac{1}{(w'(z_i)-2e'_{i,avr})^2}\right)$. This means that for a capillary number high enough, we should have a stable regime despite a very unfavorable displacement. We do not observe this behavior in Fig. 7.7 because it appears for $Ca > 0.1$, which is a range of capillary numbers where the hypotheses taken for the derivation of our model are no longer valid. This could partially explain the stable experiments that we observed for $M < 1$, even though some other phenomena are needed to explain these experimental results.

In Fig. 7.7, we observe that, while the model with films demonstrates good agreement at high viscosity ratios, some discrepancies remain in predicting certain experimental points. This could be attributed to the approximations made during the derivation of the slip length in rectangular channels (see Section. 7.2.3) or to the assumption of steady flow, which becomes less accurate at the relatively high flow rates considered.

The different regimes predicted by the model with films exhibit significant similarities with the phase diagram obtained for a complex porous structure by Lenormand et al. (1988). In their work, a stable regime is observed only when both Ca and M exceed certain thresholds ($Ca > 0.1$ and $M > 10$). Similarly, our model with films predicts

a stable regime only when α, Ca, and M are above specific thresholds. In contrast, the model without the wetting layers predicts a stable regime at a low capillary number when the viscosity ratio is sufficiently high, which contradicts the conclusions of Lenormand et al. (1988).

7.5 Conclusion and perspectives

Immiscible two-phase flow in porous media remains one of the most challenging research topics in fluid mechanics. Complex flow patterns and fluid distributions arise from the intricate interplay between surface tension and viscous forces. During drainage, residual wetting layers are often deposited after the passage of the fluid-fluid interface and lie in corners and crevices. These films are ubiquitous in porous media. In this paper, we investigate their impact on flow stability using a pore-scale analysis.

We demonstrated that state-of-the-art pore-doublet models are unable to reproduce the transition between the stable, viscous, and capillary fingering regimes observed in complex pore networks. We proposed a novel type of dynamic pore-doublet model that accounts for the presence of a wetting film using an effective slip condition, which characterizes the mean film thickness and the mutual shear stress at the interface between the two fluids. The slip length is a non-linear function of the capillary number and the viscosity ratio. We proposed models for pore doublets of identical channels with circular or rectangular cross-sections.

Our model, supported by microfluidic experiments, highlights the role of the films in the flow stability, especially if the viscosity ratio is larger than one. The film acts as a lubricant for the invading non-wetting fluid. On the one hand, it decreases the viscous pressure drop if the wetting fluid has a lower viscosity. On the other hand, the viscous drop increases if the wetting fluid is more viscous than the invading fluid. This effect is amplified in rectangular geometries because the films form thicker layers in the corners, inducing stronger viscous coupling between the two fluids. We obtained phase diagrams that are similar to Lenormand diagrams built using complex pore networks. In particular, we recover a similar regime transition for high viscosity ratios, which is not the case for pore-doublet models that neglect the effect of the films.

We demonstrated that despite its simplicity, pore-doublet models reconcile the complex non-linear two-phase flow behavior in heterogeneous porous media if the wetting films are considered. Because film thickness strongly depends on the pore geometry, the impact observed here in straight and smooth channels is expected to amplify in geometries more representative of porous systems.

Chapter 8

Inertia during Haines jumps in porous media: a pore-doublet approach

In this chapter, we examine the influence of inertial effects on drainage in porous media. Using both experimental and numerical pore doublets, we highlight how inertia governs flow stability during abrupt pore invasion events.

8.1 Introduction

At the Darcy scale (*cm* to *m*), the drainage of a cylindrical core appears smooth, with the interface between two immiscible fluids advancing steadily at a rate determined by the imposed flow rate and cross-sectional area. But when zooming in at the pore-scale (μm to *mm*), the pore space can be subdivided into individual pores of varying shapes and sizes, separated by narrow constrictions known as pore throats. At this scale, the invasion process is much more complex. The displacement of the wetting phase occurs through two distinct mechanisms: isons and Haines jumps [139].

As the pressure in the invading phase increases, so does the capillary pressure. According to the Young–Laplace law, this increase in capillary pressure requires an increase in the curvature of the fluid–fluid menisci. The menisci are gradually pushed into the pore throats through slow, quasi-static, and reversible movements known as isons [139]. If the capillary pressure continues to rise, the meniscus in the largest pore throat eventually reaches a critical point where it can no longer sustain the pressure. At this stage, the meniscus becomes unstable and rapidly reconfigures into a new metastable state, invading one or more neighboring pores. This abrupt and irreversible event is known as a rheon, or Haines jump [74, 139]. This irreversibility gives rise to the hysteresis observed in drainage/imbibition cycles in porous media [66].

Haines jumps are frequent and significant; it has been reported that over 50% of the pore volume is invaded through these rapid interface movements [24]. During a jump, the local fluid velocity can reach values one to three orders of magnitude higher than the average front velocity [136, 168, 10]. In capillary-dominated regimes—typically in systems with small characteristic lengths—the speed of the jump is independent of the bulk flow rate. However, when viscous and inertial forces become more prominent, the velocity of the jump begins to depend on the imposed flow [10].

During the rapid reorganization of the interface, the flow rate of non-wetting fluid can temporarily exceed what is injected at the inlet [136, 10]. To compensate, fluid

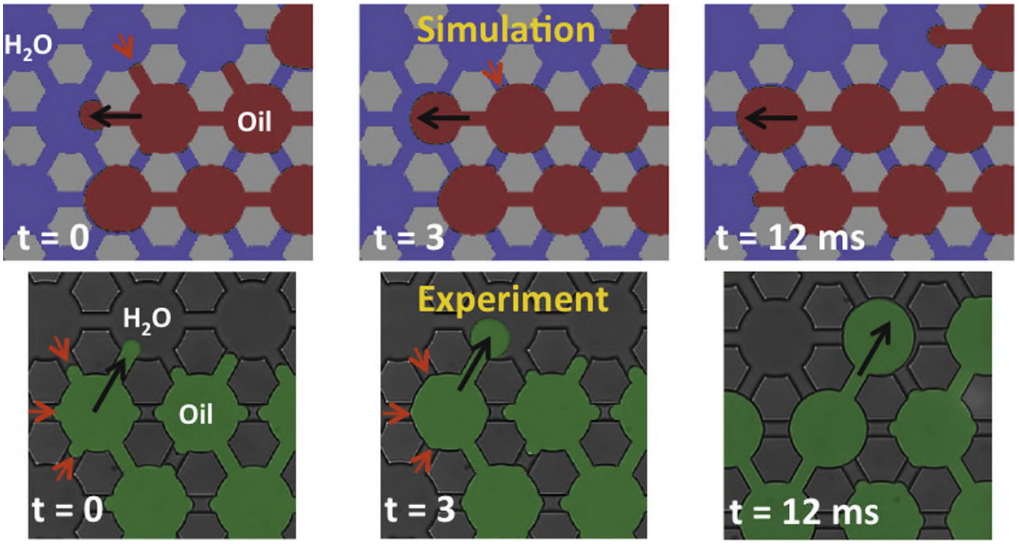

Figure 8.1: Experimental and simulation results displaying the cooperative behavior of the fluids during Haines jumps. The depth of the system is 5 μm, while the width of the pore-throat is 13 μm [10].

is drawn from neighboring pores, making the jump a cooperative event. While the invading meniscus rapidly advances into one pore, adjacent menisci retreat to supply the necessary fluid volume. As a result, Haines jumps are not purely local phenomena; their influence propagates through the surrounding pore network[136, 198]. In Fig. 8.1, we observe the jump of one interface inside a pore. During this event, the flow going into the newly invaded pore is very high, and draws oil from neighbouring pore throats. One can explain this cooperative pore filling by looking at the menisci: in the pore throats, their curvature is high, while the meniscus that just entered the pore has a lower curvature since it is not constrained by the walls anymore. This creates a gradient of capillary pressure inside the oil, leading to the flow from high capillary pressure to low capillary pressure, in a phenomenon known as Ostwald ripening [206].

Due to the high invasion velocities during Haines jumps, inertial effects can no longer be neglected. The Reynolds number (Re), which compares inertial forces to viscous dissipation, can locally reach significant values. Armstrong et al. (2015) reported Reynolds numbers close to unity in micromodels with a depth of 5 μm and a width of 10 μm, where inertia would typically be considered negligible. For larger geometries, Moebius and Or (2012) observed Reynolds numbers approaching 1000, near the onset of turbulence. In these cases, oscillations of the fluid interface were observed during and after the jumps, indicating the presence of inertial effects, see Fig. 8.2. Since the influence of the jumps spreads to the surrounding pores, these oscillations are not restricted to the local throat but spread throughout the pore network. These inertial oscillations are critical, as they may influence which meniscus jumps next if not sufficiently damped between events [66]. This can, in turn, affect the final residual saturation of the wetting phase after invasion [135, 129], a key parameter in many industrial applications. Despite these works, most models of the underground flows assume a creeping flow everywhere ($Re < 1$). Knowing whether or not inertia plays a role is key to better model the underground flows.

In this chapter, we investigate the impact of inertia on two-phase flow in porous media using pore-scale modelling and experiments. We propose a section-averaged mathematical model to take into account the effects of inertia in a pore doublet, and

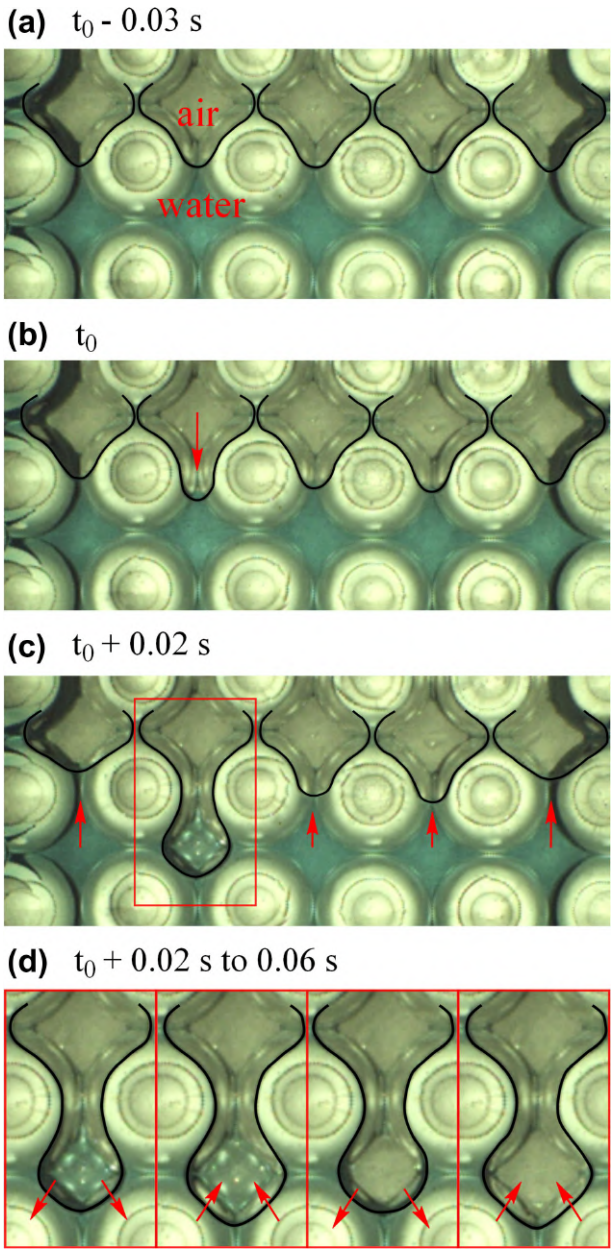

Figure 8.2: Experimental meniscus dynamics during drainage of glass bead packing. (a) Before the jump, the menisci are pinned at the pore throat. (b) The jump occurs at the pore-throat with the lowest entry capillary pressure. (c) The flow rate reached during the jump surpasses the imposed flow rate of the system. This forces a redistribution of the fluids toward the neighboring menisci. (d) Zoom of the section highlighted in red in (c). Inertial oscillations of the interface after the Haines jump [136].

present a novel method to solve it that improves the speed and stability of the solver. We validate our approach using microfluidic experiments. Then, we examine the conditions under which inertial effects become significant and how they influence residual saturation.

8.2 Theory of pore doublets with inertia

In this section, we introduce pore-doublet equations that account for inertial effects. While similar models have been proposed in the literature [135, 129], existing derivations and numerical implementations exhibit several flaws, which will be discussed in the results section. Here, we revisit the derivation of the pore-doublet model with inertia and propose a new numerical approach.

8.2.1 System of study: sinusoidal pore doublet

We employ pore doublets with sinusoidal channels to study the dynamics of Haines jumps (see Fig.8.3). These sinusoidal channels consist of alternating pore bodies and pore throats, where menisci become pinned before rapidly invading the next pore body.

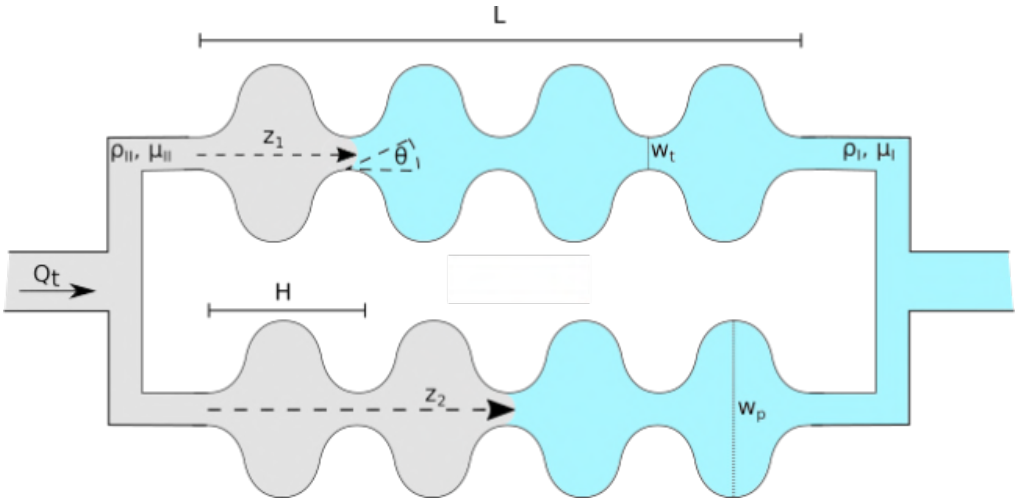

Figure 8.3: Sinusoidal pore doublet

The pore doublet is composed of two rectangular channels (channel 1 and channel 2) of uniform depth D_0, and a sinusoidal width $w_i(z)$, $(i = 1, 2)$, given as,

$$w_i(z) = \frac{w_p + w_{t,i}}{2} + \frac{w_{t,i} - w_p}{2} \cos\left(\frac{2\pi z}{H}\right), \tag{8.1}$$

where w_p is the width of the largest portion of the channel, $w_{t,i}$ is the throat's width of channel i, and H is the length of one pore, see Fig. 8.3. The total length of the pore doublet is L. We note

$$A_i(z) = D_0 w_i(z) \tag{8.2}$$

the cross-section of channel i at the position z.

This pore doublet is initially filled with a wetting fluid (noted fluid I), and a non-wetting fluid (fluid II) is injected at a constant flow rate Q_p from left to right, which creates a meniscus in each of the channels (see Fig. 8.3). The relative position of the menisci provides information about the stability of the drainage: if both menisci invade

the channels at the same rate, the invasion is stable; whereas if one meniscus takes the lead and a channel gets invaded preferentially, the drainage is unstable. This allows us to differentiate between the various drainage regimes and estimate the amount of residual trapping at larger scales.

8.2.2 Mathematical descriptions of pore doublet with inertia

In this section, we adapt the approach proposed by Moebius and Or (2012) for modeling meniscus dynamics in the pore-doublet system described above, with a focus on how inertia has been accounted for. Then, we introduce a novel approach that offers an improved description of inertial effects within the pore-doublet framework.

The two derivations share the same fundamental principles: conservation of mass flow rate and the same pressure drop in both channels. Because both fluids are incompressible, the conservation of the flow rate reads,

$$Q_p = Q_1(t) + Q_2(t), \tag{8.3}$$

where $Q_i(t) = A_i(z)v_i(z), \forall z \in [0, L]$ is the flow rate of non-wetting fluid inside channel $i = 1, 2$. The cross-section averaged speed of the fluid is denoted $v_i(z)$. Since this is true at any point of the channel, it is also true at the meniscus position, and we can write

$$Q_i(t) = A_i(z_i)\dot{z}_i, \tag{8.4}$$

where $\dot{z}_i$ is the meniscus velocity in channel i.

Since both channels share the same inlet and outlet, the total pressure drop in each channel is the same,

$$\Delta P_1(t) = \Delta P_2(t). \tag{8.5}$$

The two derivations introduced in this section differ in the method used to compute the pressure difference in each channel.

8.2.2.1 Derivation of Moebius and Or

This derivation was first done by Moebius and Or (2012) to study the impact of inertia in a pore doublet. They looked at the drainage of water by air, neglecting the density and viscosity of air. The cross-section of their channels was cylindrical. They were able to numerically solve for the position of the menisci in time, considering the influence of inertia; however, their derivation of the equations raises some questions. Indeed, their method of deriving the controlling equation presents some significant assumptions in the expression of the pressure drop over the channels.

Derivation of the total pressure drop according to Moebius and Or We derive the equations describing the system presented in Fig. 8.3, adapting the method employed by Moebius and Or (2012) with two viscous fluids and rectangular channels. The total pressure drop across the channel can be expressed as

$$\Delta P(t) = \Delta p_{viscous} + \Delta p_{capillary} + \Delta p_{inertia}. \tag{8.6}$$

which accounts for contributions from viscous dissipation, capillary effects, and inertial losses. Each term is derived individually.

The viscous pressure drop is given by the Hagen-Poiseuille law. However, instead of taking into account the variation in the channel width, they compute the value of the viscous drop as if the entire channel were a tube of constant width and depth equal to the smallest length scale. They consider that the smallest length scales in the

channel (depth or width) would dominate and control the flow. According to Hele-Shaw's equation, the viscous drop reads as,

$$\Delta p_{viscous}(z_i) = \frac{12\dot{z}_i}{\min[D_0, w_t]^2}\left(z_i\mu_{II} + (L - z_i)\mu_I\right). \tag{8.7}$$

For sinusoidal and rectangular channels, this approximation leads to a significant overestimation of the viscous drop compared to the real value.

The capillary pressure is expressed using Young-Laplace's law. In a sinusoidal geometry, the slope of the wall needs to be considered, as it impacts the curvature of the meniscus. This was neglected in the previous Chapter. 7, as the variation of the channel width was very slow. The capillary forces are written as,

$$\Delta p_{capillary}(z_i) = -2\sigma\left(\frac{\cos(\theta + \alpha(z_i))}{w_i(z_i)} + \frac{\cos(\theta)}{D_0}\right), \tag{8.8}$$

where σ is the interfacial tension between the two fluids, and θ is the static contact angle, measured through the wetting phase, and $\alpha(z) = \arctan\left(\frac{dw}{dz}\right)$ is the slope of the wall.

Finally, for the inertia part of the total pressure drop, they consider it to be the resistance of the column of liquid to any change in motion and is written, in terms of pressure, as,

$$\Delta p_{inertia}(z_i) = \frac{d}{dt}\left(\dot{z}_i\left(\rho_{II}z_i + \rho_I(L - z_i)\right)\right) = \ddot{z}_i\left(z_i(\rho_{II} - \rho_I) + L\rho_I\right) + \dot{z}_i^2(\rho_{II} - \rho_I). \tag{8.9}$$

To obtain this expression, it looks like the authors assumed that the channel was of constant cross-section. Moreover, the inertia force is converted to a pressure simply by dividing it by the cross-section of the channel, but it is never made clear which one.

Non-dimensionalization The following characteristic variables are used to make the system dimensionless: $w_c = \frac{w_p + w_{t,1}}{2} \equiv a$, $\mu_c = \mu_I$, $\rho_c = \rho_I$, $D_c = D_0$, $z_c = L$, $t_c = \frac{LD_0a_1}{Q_p}$, and $P_c = \frac{12\mu LQ_p}{aD_0^3}$. The dimensionless viscous, inertial, and capillary pressure read,

$$\Delta p'_{viscous}(z_i) = \dot{z}_i\left(1 + z_i(M - 1)\right)k, \tag{8.10}$$

with $M = \frac{\mu_{II}}{\mu_I}$ the viscosity ratio and $k = 1$ if $D_0 < w_t$ or $k = \frac{w_t^2a^2}{D_0^2}$ if $D_0 > w_t$,

$$\Delta p'_{capillary}(z_i) = \frac{1}{Ca^*}\left(\frac{\cos(\theta + \alpha(z))}{w_i(z_i)} + \frac{a\cos(\theta)}{D_0}\right), \tag{8.11}$$

with $Ca^* = \frac{6\mu_I Q_p L}{\sigma D_0^3} = Ca * \zeta$ where $\zeta = \frac{6aL}{D_0^2}$ is a geometrical factor, Ca the capillary number of the system, and

$$\Delta p'_{inertia}(z_i) = Re^*\left[\ddot{z}_i\left(z_i(\Gamma - 1) + 1\right) + \dot{z}_i^2(\Gamma - 1)\right], \tag{8.12}$$

with $Re^* = \frac{\rho_I D_0 Q_p}{12\mu_I a_1 L} = Re * \eta$, $\eta = \frac{1}{2\zeta}$ a geometrical factor and Re the Reynolds number. $\Gamma = \frac{\rho_{II}}{\rho_I}$ is the density ratio between the fluids.

Finally, the dimensionless total pressure loss is,

$$\Delta P'_i(t) = Re^*\left[\ddot{z}_i\left(z_i(\Gamma - 1) + 1\right) + \dot{z}_i^2(\Gamma - 1)\right] + \dot{z}_i\left(1 + z_i(M - 1)\right) + \frac{1}{Ca^*}\left(\frac{\cos(\theta + \alpha(z))}{w_i(z_i)} + \frac{a\cos(\theta)}{D_0}\right), \tag{8.13}$$

and the dimensionless conservation of the flow rate is,

$$\dot{z}_1 A_1(z_1) + \dot{z}_2 A_2(z_2) = 1. \tag{8.14}$$

(8.13) and (8.14) give us a system that can be solved for the position of the menisci in time.

8.2.2.2 A section-averaged derivation for the governing equations of pore doublets with inertia

The derivation of Moebius and Or (2012) is not correct because their force balance only applies on the meniscus, and the expressions for inertia and viscous dissipation present significant approximations. Here, we derive the model using a rigorous approach by decomposing a channel into 3 domains: a first zone occupied by the invading fluid, the meniscus, and a last region occupied by the defending fluid. We assumed a fully-developed Poiseuille flow in each fluid and each channel, as well as a constant contact angle between the solid and the wetting fluid, neglecting the dynamic aspect of the contact angle [205]. The Navier-Stokes equation is first averaged over the cross-section of the channel to form a one-dimensional equation and then integrated over the region. A similar approach has been adopted by Al-Housseiny et al. (2014) Protière et al. (2010) for viscous flow and by Mansouri-Boroujeni et al. (2023) for pore doublet with inertia.

Derivation of the pressure loss including inertia The total pressure drop consists of three different pressures [212]: the pressure drop in fluid II, upstream of the meniscus, the pressure drop in fluid I, downstream of the meniscus, and finally the capillary pressure caused by the curvature of the interface.

$$\Delta P_1(t) = \Delta P_{fluid\,II} + \Delta P_{cap} + \Delta P_{fluid\,I}. \tag{8.15}$$

The capillary pressure is expressed using Young-Laplace's law, and similarly to (8.8), we have

$$\Delta P_{cap}(z_i) = -2\sigma\left(\frac{\cos(\theta + \alpha(z_i))}{w_i(z_i)} + \frac{\cos(\theta)}{D_0}\right). \tag{8.16}$$

The pressure drop in each of the fluids is obtained by integration of the section-averaged Navier-Stokes equation along the length of the channel. The section-averaged Navier-Stokes equation in fluid j is given by[129]:

$$\rho_j \frac{\partial v(z)}{\partial t} = -\frac{dP}{dz} - \mu_j \frac{v(z)}{k(z)}, \tag{8.17}$$

with $v(z)$ the average speed of the fluid at position z, and $k(z)$ the permeability of the channel at position z. In this equation, the fluid is assumed to only move in the z direction, and the speed of the fluid in the x and y directions is neglected. The term on the left-hand side of (8.17) is due to the inertia and is neglected in most applications in porous media. When this term is removed, Darcy's law is recovered. After integration along the channel, we recover the pressure drop caused by fluid II in channel i,

$$\Delta P_{fluid\,II} = \rho_{II} \int_0^{z_i} \frac{\partial v(z)}{\partial t} dz + \mu_{II} \int_0^{z_i} \frac{v(z)}{k(z)} dz, \tag{8.18}$$

and the pressure drop in channel i caused by the fluid I is given by,

$$\Delta P_{fluid\,I} = \rho_I \int_{z_i}^{L} \frac{\partial v(z)}{\partial t} dz + \mu_I \int_{z_i}^{L} \frac{v(z)}{k(z)} dz. \tag{8.19}$$

Summing up (8.8), (8.18), and (8.19) gives the total pressure drop over the two channels. We can now use (8.4) to take the mass flow rate $Q_i(t)$ out of the integrals, as it is constant along the entire channel. Then, the total pressure drop reads:

$$\Delta P_i(t) = \frac{\partial}{\partial t}\left(\rho_I A(z_i)\dot{z}_i \psi(z_i,\Gamma)\right) + \mu_I A(z_i)\dot{z}_i \phi(z_i,M) + 2\sigma\left(\frac{\cos(\theta+\alpha(z_i))}{w_i(z_i)} + \frac{\cos(\theta)}{D_0}\right), \quad (8.20)$$

with

$$\psi(z_i,\Gamma) = \Gamma\int_0^{z_i}\frac{dz}{A_i(z)} + \int_{z_i}^{L}\frac{dz}{A_i(z)}, \quad (8.21)$$

$$\phi(z_i,M) = M\int_0^{z_i}\frac{dz}{A_i(z)k_i(z)} + \int_{z_i}^{L}\frac{dz}{A_i(z)k_i(z)}. \quad (8.22)$$

For a rectangular channel, the permeability is given by [192],

$$k_i(z) = \begin{cases} \frac{D_0^2}{12}\left(1-\beta\frac{D_0}{w_i(z)}\right) & \text{when } D_0 < w(z), \\ \frac{w_i(z)^2}{12}\left(1-\beta\frac{w_i(z)}{D_0}\right) & \text{when } w(z) < D_0, \end{cases} \quad (8.23)$$

with $\beta = \left(\frac{192}{\pi^5}\right)$. This equation is a simplification of the exact solution given in Spiga and Morino (1994). (8.23) leads to less than 10% of error as long as the ratio of the smaller lengthscale over the larger lengthscale is below 0.7 [80]. Both $\phi(z_i,M)$ and $\psi(z_i,\Gamma)$ depends on the relative value of w_p, w_t, and D_0 and are given in the Appendix F.

Non-dimensionalization Our system of equations is made dimensionless using the same characteristic variables as in Sec. 8.2.2.1. This will allow us to compare both models later. All the equations in the following development are dimensionless, unless stated otherwise. The dimensionless cross-section is given by,

$$A_i(z) = w_i(z) = \left(\frac{a_i}{a_1} + \frac{b_i}{a_1}\cos\left(\frac{2\pi z L}{H}\right)\right), \quad (8.24)$$

and the conservation of mass now reads as,

$$\dot{z}_1 A_1(z_1) + \dot{z}_2 A_2(z_2) = 1. \quad (8.25)$$

The permeability is now expressed as,

$$k(z) = \begin{cases} \left(1-\beta\frac{D_0}{w(z)a}\right) & \text{when } D_0 < Hw(z), \\ \frac{a^2 w(z)^2}{D_0^2}\left(1-\beta\frac{aw(z)}{D_0}\right) & \text{when } Hw(z) < D_0, \end{cases} \quad (8.26)$$

And finally, the total dimensionless pressure difference over one channel is,

$$\begin{aligned} \Delta P_i(t) = \quad & Re^*\left(\dot{z}_i^2\left(\Gamma - 1 + \psi(z_i,\Gamma)\frac{dw_i(z)}{dz}\right) + \ddot{z}_i w_i(z_i)\psi(z_i,\Gamma)\right. \\ + \quad & \left. w_i(z_i)\dot{z}_i\phi_i(z_i,M) + \frac{1}{Ca^*}\left(\frac{\cos(\theta+\alpha(z))}{w_i(z_i)} + \frac{a\cos(\theta)}{D_0}\right)\right). \end{aligned} \quad (8.27)$$

Note that the dimensionless numbers Ca^* and Re^* are the same in both derivations.

8.3 Numerical solution of pore-doublet equations

In this section, we present the numerical strategy to solve the pore-doublet equations derived in Sec. 8.2.2 using MATLAB. We use two different strategies: the one proposed by Moebius and Or (2012) and Mansouri-Boroujeni et al. (2023), and a new, more robust one.

8.3.1 Numerical strategy by Moebius and Or

The system of equations derived by Moebius and Or (2012) was implemented using MATLAB. They expressed their equations in matrix form to facilitate numerical integration. In our case, the corresponding matrix takes the following form:

$$\begin{bmatrix} 1 & 0 & 0 & 0 \\ 0 & 1 & 0 & 0 \\ w_1(z_1) & w_2(z_2) & 0 & 0 \\ 0 & 0 & Re^*(1+z_1(\Gamma-1)) & -Re^*(1+z_2(\Gamma-1)) \end{bmatrix} \frac{d}{dt}\begin{bmatrix} z_1 \\ z_2 \\ \dot{z}_1 \\ \dot{z}_2 \end{bmatrix} = \begin{bmatrix} \dot{z}_1 \\ \dot{z}_2 \\ 1 \\ \Omega \end{bmatrix}, \tag{8.28}$$

with

$$\Omega = \frac{1}{Ca^*}\left(\frac{\cos(\theta+\alpha(z_2))}{w(z_2)} - \frac{\cos(\theta+\alpha(z_1))}{w(z_1)}\right) + \dot{z}_2\,(1+z_2(M-1)) - \dot{z}_1\,(1+z_1(M-1)) + Re^*\,(\Gamma-1)\left(\dot{z}_2^2 - \dot{z}_1^2\right). \tag{8.29}$$

This system is a Differential Algebraic Equation (DAE) with a non-constant, non-invertible mass matrix. These kinds of systems are computationally heavy to resolve and require a guess of the initial value (here on z_1, z_2, $\dot{z}_1$, and $\dot{z}_2$). If this guess is not good enough, the numerical solution can not be computed. This matrix system is implemented in MATLAB using the ode15s solver, as it is capable of handling a stiff algebraic system while still retaining good accuracy [178]. This numerical method will be referred to as the DAE numerical approach in the rest of the chapter.

Mansouri-Boroujeni et al. (2023) have adopted the same numerical strategy to solve the system formed by (8.27), (8.25), and (8.5). It turns out, however, that the term Ω is treated explicitly, which requires very small time steps and long simulation times. In many cases, the simulations simply crashed. It was then difficult to perform sensitivity analysis for a wide range of parameters.

8.3.2 A more robust implementation of pore-doublet equations

We propose an alternative approach to solve the system formed by (8.27), (8.25), and (8.5). We look for an expression for $\ddot{z}_i$, which would allow us to rewrite the problem as an ODE. This expression is obtained by taking the derivative of the conservation of flow rate (8.25) with respect to time:

$$\dot{z}_1^2\frac{dw(z_1)}{dz_1} + \dot{z}_2^2\frac{dw(z_2)}{dz_2} + w(z_1)\ddot{z}_1 + w(z_2)\ddot{z}_2 = 0. \tag{8.30}$$

This leads us to a second-order nonlinear differential equation,

$$\ddot{z}_2 = \frac{-\dot{z}_2^2\Big(w_z(z_2)\left(\psi(z_2,\Gamma)+\psi(z_1,\Gamma)\right)\Big)+(\dot{z}_1^2-\dot{z}_2^2)(\Gamma-1)}{w(z_2)\Big(\psi(z_1,\Gamma)+\psi(z_2,\Gamma)\Big)} + \frac{w(z_1)\dot{z}_1\phi(z_1,M)-w(z_2)\dot{z}_2\phi(z_2,M)}{Re\,w(z_2)\Big(\psi(z_1,\Gamma)+\psi(z_2,\Gamma)\Big)} + \frac{1}{Ca\,Re\,w(z_2)\Big(\psi(z_1,\Gamma)+\psi(z_2,\Gamma)\Big)}\left(\frac{\cos(\theta+\alpha(z_1))}{w(z_1)}-\frac{\cos(\theta+\alpha(z_2))}{w(z_2)}\right). \quad (8.31)$$

The equation for $\ddot{z}_1$ is found by simply switching the indices of (8.31). To numerically solve this second-order differential equation, we need to reduce the order of the equation using a matrix expression, similarly to (8.28). It reads simply as,

$$\frac{d}{dt}\begin{bmatrix} z_1 \\ z_2 \\ \dot{z}_1 \\ \dot{z}_2 \end{bmatrix} = \begin{bmatrix} \dot{z}_1 \\ \dot{z}_2 \\ \ddot{z}_1 \\ \ddot{z}_2 \end{bmatrix}, \quad (8.32)$$

where $\ddot{z}_1$ and $\ddot{z}_2$ are given by (8.31).

As interfacial jumps create a stiff behavior in the problems, the equation is solved using MATLAB's solver ode15s, which is designed for stiff problems, [178].

The difficulty of this formulation is that it does not explicitly conserve the flow rate of fluid II, since (8.30) only imposes the flow rate to be constant. To enforce the desired flow, the initial velocity of each meniscus needs to be chosen appropriately to reach a dimensionless flow rate of 1. This is a much easier task than finding accurate initial conditions for (8.28), as any guess that enforces the correct flow rate will yield results. Moreover, it is easier for the solver to handle and leads to a solution much quicker (around one order of magnitude faster than with the DAE formulation). From a more general point of view, it is also much easier to implement in other software. This approach will be referred to as the ODE numerical approach in the rest of this chapter.

8.3.3 Parameters for the resolution

The throat of channel 2 is set to be slightly bigger than that of channel 1, $w_{t,2} = 1.01 w_{t,1}$. This means that during capillary-dominated regimes, only the channel with the bigger pore throat will be invaded, creating the asymmetry necessary to have a numerically unstable flow. For the initial conditions, we take both menisci at the same position $z_i(0) = H * 1.1/L$, already inside the two channels. Indeed, during Haines jump there is a redistribution of the fluid, which causes the non-jumping meniscus to recede in the pore-throat [136, 10]. This initial condition allows for one of the menisci to recede without reaching a negative value of z_i. As we saw, (8.28) requires a 'good guess' of the initial conditions to perform the calculation. For our system, we take the initial speeds of the menisci to be:

$$\begin{aligned} \dot{z}_1(0) &= \frac{1}{2w(z_1(0))}, \\ \dot{z}_2(0) &= \frac{1}{2w(z_2(0))}. \end{aligned} \quad (8.33)$$

Table 8.1: Dimensions of the micromodel used in the experiments, see Fig. 8.3.

Name of micromodel	L (µm)	H (µm)	D_0 (µm)	w_t (µm)	w_p (µm)
A	3600	120	90	20	60
B	3600	90	90	9	45
C	3200	160	40	40	160

According to (8.25), this assures a dimensionless flow rate equal to 1. This boundary condition is used for both models.

Due to the unstable nature of the problem, the error tolerance of the solver needs to be strict. In MATLAB, we chose an absolute tolerance of 10^{-12} and a relative tolerance of 10^{-10}. Combined with the initial conditions described above, this stringent error tolerance allows our solver to compute the correct solution.

To avoid any issue with the meniscus positions being negative, the simulation is stopped as soon as one of the menisci reaches the value zero, or when it reaches 1 (end of the invasion). Once a solution is produced, the number of oscillations in the position of z_1 is counted. If it is above the number of pore bodies in channel 1, it means that oscillations linked to inertia took place, which potentially impact the flow in the pore doublet.

Overall, both numerical implementations of this system of equations are challenging to solve numerically due to their complexity and nonlinearity. Additionally, maintaining a constant flow rate over time imposes strict tolerance requirements. For certain parameter sets, the solver fails to accurately capture the full invasion dynamics, causing the simulation to terminate prematurely—before the invasion process is completed.

8.4 Material and methods for microfluidic experiments

In this section, we quickly go over the materials and methods used to perform microfluidic experiments.

8.4.1 Fabrication of microfluidic pore doublets

A photolithography method is used to create silicon wafer molds with the geometry of interest. Then, PDMS (PolyDiMethylSiloxane) soft lithography is used to produce the microfluidic chips containing the pore doublet [166]. The pore-doublet length, L, the etching depth, D_0, the pore throats and pore body width, w_p and w_t are found in table 8.1. We use polyvinyl alcohol (PVA) deposition to obtain a uniform hydrophilic behavior in the chips. More details on the fabrication techniques and the surface treatment can be found in Chap. 4.

8.4.2 Fluid properties

Different fluids are picked to perform experiments: water with a viscosity of 1.005×10^{-3} Pa·s and density of 997 kg·m^{-3} at room temperature, air with a viscosity of 1.85×10^{-5} Pa·s and a density of 1.2 kg·m^{-3}. Two silicon oils are used with a viscosity of 5.0×10^{-3} Pa·s (s-oil 1) and 1.0×10^{-2} Pa·s (s-oil 2), and density of respectively 970 kg·m^{-3} and 930 kg·m^{-3}. Finally, to reach high viscosity, a water solution of glycerine (containing 80 wt% of glycerine) is used as a non-wetting fluid. Its viscosity and

Table 8.2: Properties of the flow for different pairs of fluids at 20°C. s-oil 1: silicon oil with a viscosity of 5 mPa·s, s-oil 2: silicon oil with a viscosity of 10 mPa·s.

Wetting fluid	Non-wetting fluid	σ(mN/m)	M	Γ	θ
s-oil 1	DI water	47	0.2	1.03	<10°
s-oil 2	DI water	47	0.1	1.08	<10°
s-oil 1	glycerine(80wt%)-water	33	12	1.25	<10°
s-oil 2	glycerine(80wt%)-water	33	6	1.29	<10°
DI water	air	73	0.018	0.001	40° (PVA treated)
s-oil 1	air	20	0.0036	0.001	0°
s-oil 2	air	20	0.0018	0.001	0°

density are respectively 60.1×10^{-3} Pa·s and 1208 kg·m^{-3}[176][195]. Water is used as a wetting fluid in PVA-treated micromodels, and silicon oils are used as wetting fluids for untreated micromodels due to their strong affinity with PDMS. The superficial and interfacial tensions of the different fluids are measured using a OneAttention Theta Flex tensiometer from Biolin Scientific. Static contact angles between the PDMS and the fluid pairs were also measured using the same tensiometer to find θ (measured through the wetting fluid). The results of these measurements and the values of M and Γ can be found in Table. 8.2.

8.5 Results

In this section, we compare the two models introduced in Sec. 8.2 to investigate the impact of inertia in pore doublets.

8.5.1 Comparison between the two pore-doublet models

General comparisons For the comparison, we fix the geometry of the pore doublet as well as the properties of the fluids: $M = 5$, $\Gamma = 10$, $\sigma = 47$ mN·m^{-1}, $\rho_I = 1000$ kg·m^{-3}, and $\mu_I = 1.0$ mPa·s. For the geometry, we set $D_0 = 200$ µm, $w_t = 150$ µm, $w_p = 300$ µm, $H = 300$ µm, and $L = 10H$. This choice of parameters is an intermediate choice between experiments and parameters that the model of Moebius and Or, using the DAE solver, is able to resolve. Indeed, the system presented in Eq. (8.28) does not work with all parameters. The chosen parameters were found by slowly changing one parameter at a time to find which ones worked.

From the simulations that were run, it is evident that the system using the ODE equation that we developed is much more stable than the DAE system. The stringent conditions of the initial conditions for the meniscus velocities required for the DAE system make it hard to solve, and it is common for the solver to crash.

One simulation at $Ca = 4.3 \times 10^{-7}$ and $Re = 5.0 \times 10^{-3}$ is shown in Fig. 8.4, where the two continuous lines represent the meniscus dynamics computed using the section-averaged model, solved with the new ODE approach, and the dotted lines represent the results computed with the model of Moebius and Or solved with the DAE approach. Both follow the trend of a capillary-dominated invasion: the biggest channel, channel 2, is invaded because of its bigger pore throat, while the meniscus of channel 1 stays in the same pore body during the entire invasion. During each Haines jump, we can see the withdrawal of the other menisci to provide the fluid necessary for the jump to occur. The speed of this withdrawal varies between both models, with the model of

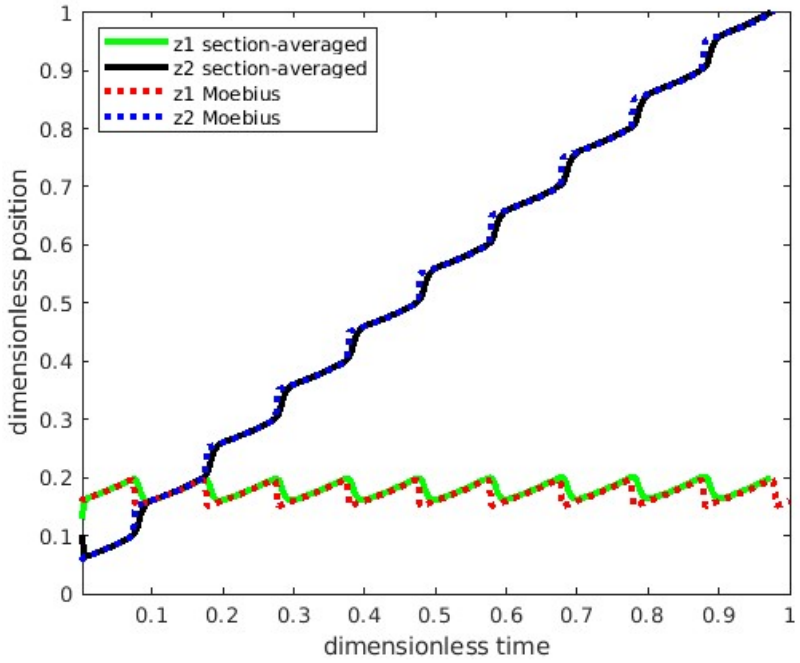

Figure 8.4: Comparison between both models with $Ca = 4.3 \times 10^{-7}$ and $Re = 5.0 \times 10^{-3}$. Both models follow the same trend of a capillary-dominated invasion, with small differences in the relaxation of the interface after a jump.

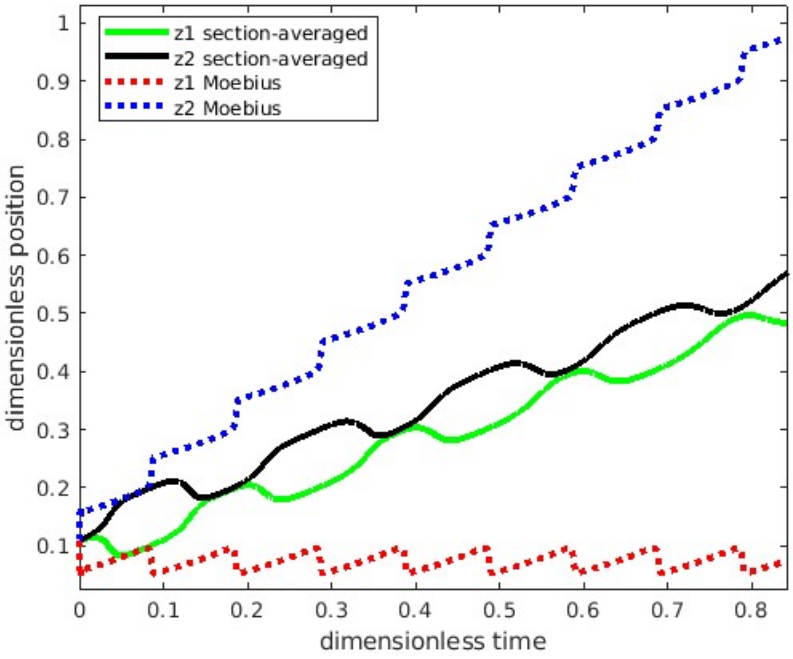

Figure 8.5: Comparison between the two models at $Ca = 4.3 \times 10^{-6}$ and $Re = 5.0 \times 10^{-2}$. The predictions of the two models are completely different from each other. The model of Moebius and Or still follows a capillary-dominated regime, while the section-averaged model predicts a regime where the viscous forces have more impact.

Moebius and Or predicting a very sharp, abrupt motion, while the section-averaged model produces a slightly smoother motion of the interfaces during the Haines jumps.

Increasing the flow rate leads to a change in the meniscus dynamics, as can be seen in Fig. 8.5, where $Ca = 4.3 \times 10^{-6}$ and $Re = 5.0 \times 10^{-2}$. Here, the predictions of both models differ, with the DAE approach predicting a capillary-dominated regime, as seen previously on Fig. 8.4. The section-averaged model predicts a succession of jumps, one in capillary 2, then one in capillary 1, before another jump in capillary 2, etc. This means that the menisci are never more than one pore body away from each other, leading to a stable invasion with very little residual saturation. This is a sign of a cross-over regime where both capillary and viscous forces are important [129]. While in the case of the model of Moebius and Or, the residual saturation in the pore doublet is high, since capillary 1 is still saturated with the defending fluid after percolation.

This difference is due to how the viscous drop is accounted for in the model of Moebius and Or. It creates an unrealistic viscous drop that keeps the model in a capillary-dominated regime. This is even more evident when we raise the capillary and Reynolds numbers to $Ca = 4.3 \times 10^{-5}$ and $Re = 5.0 \times 10^{-1}$, see Fig. 8.6, where the section-averaged model predicts a viscous-dominated regime, where the favorable viscosity ratio ($M = 10$) leads to a stable displacement and all of the defending fluid is recovered. On the contrary, the model of Moebius and Or still predicts a capillary-dominated regime.

Both models predict similar results again when we reach $Ca = 4.3 \times 10^{-3}$ and $Re = 50$, see Fig. 8.7, where we are in a viscous-dominated regime: both channels are invaded simultaneously, with no pinning of the interfaces at the pore throats. This leads

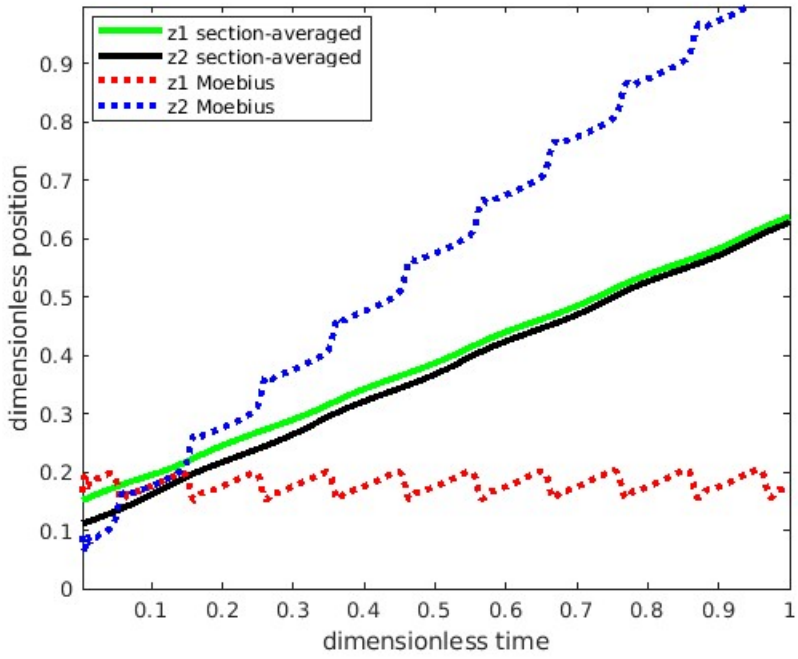

Figure 8.6: Comparison between the two models at $Ca = 4.3 \times 10^{-5}$ and $Re = 5.0 \times 10^{-1}$. The predictions of the two models are completely different from each other. The model of Moebius and Or still follows a capillary-dominated regime, while the section-averaged model predicts a stable viscous regime.

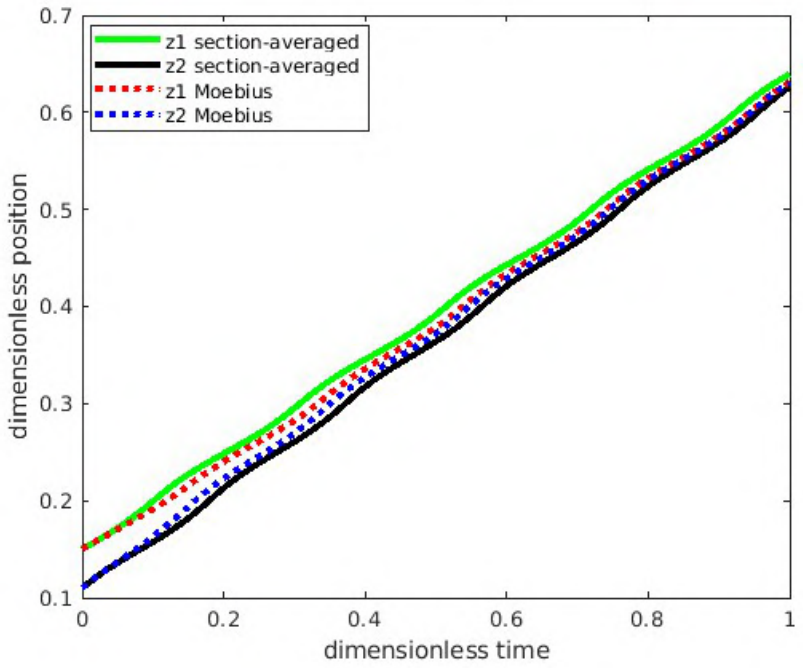

Figure 8.7: Comparison between the two models at $Ca = 4.3 \times 10^{-3}$ and $Re = 50$. The predictions of both models finally agree on a viscous-dominated invasion.

to a stable displacement and no trapping of the wetting fluids, since we are in a stable invasion regime($M = 10$).

We have seen that for low capillary number ($Ca \lessapprox 10^{6}$), both models agree on a capillary-dominated invasion and predict almost the same meniscus dynamics. But when the capillary number is increased ($10^{-6} \lessapprox Ca \lessapprox 10^{-3}$), both implementations predict very different regimes: the DAE model keep predicting a capillary-dominated regime, while the section-averaged model switches from a cross-over regime for $Ca \approx 5\times10^{-6}$, to a viscous-dominated one for $Ca = 5\times10^{-5}$. Finally, both models agree again for $Ca > 10^{-3}$, where they both predict a viscous-dominated regime. One can note that the model of Moebius and Or never predicts the cross-over regime and switches directly from capillary to viscous-dominated regimes.

8.5.1.1 Inertial oscillations

For now, we have not seen any impact of inertia in the interface dynamics. For this, we need to increase a bit the depth of the channel for the simulations, from 200 µm to 300 µm. We also increased the density of fluid I, from 1000 $\mathrm{kg\cdot m^{-3}}$ to 5000 $\mathrm{kg\cdot m^{-3}}$. A bigger depth means that a larger volume of fluid jumps during the Haines jumps. Combined with the higher density, this greatly increases inertia during the jumps.

As we can see in Fig. 8.8 for $Ca = 3.2 \times 10^{-6}$ and $Re = 3.3 \times 10^{-2}$, oscillations can be seen in the positions of both menisci after each Haines jump. These oscillations are a signature of inertial effects, which are present despite the Reynolds number being lower than 1. In this case, the DAE approach crashed at $t = 0.5$, which is why the rest of the invasion is not represented. This is another argument for our model being more stable. When we zoom in on an interfacial jump, the oscillation period differs between

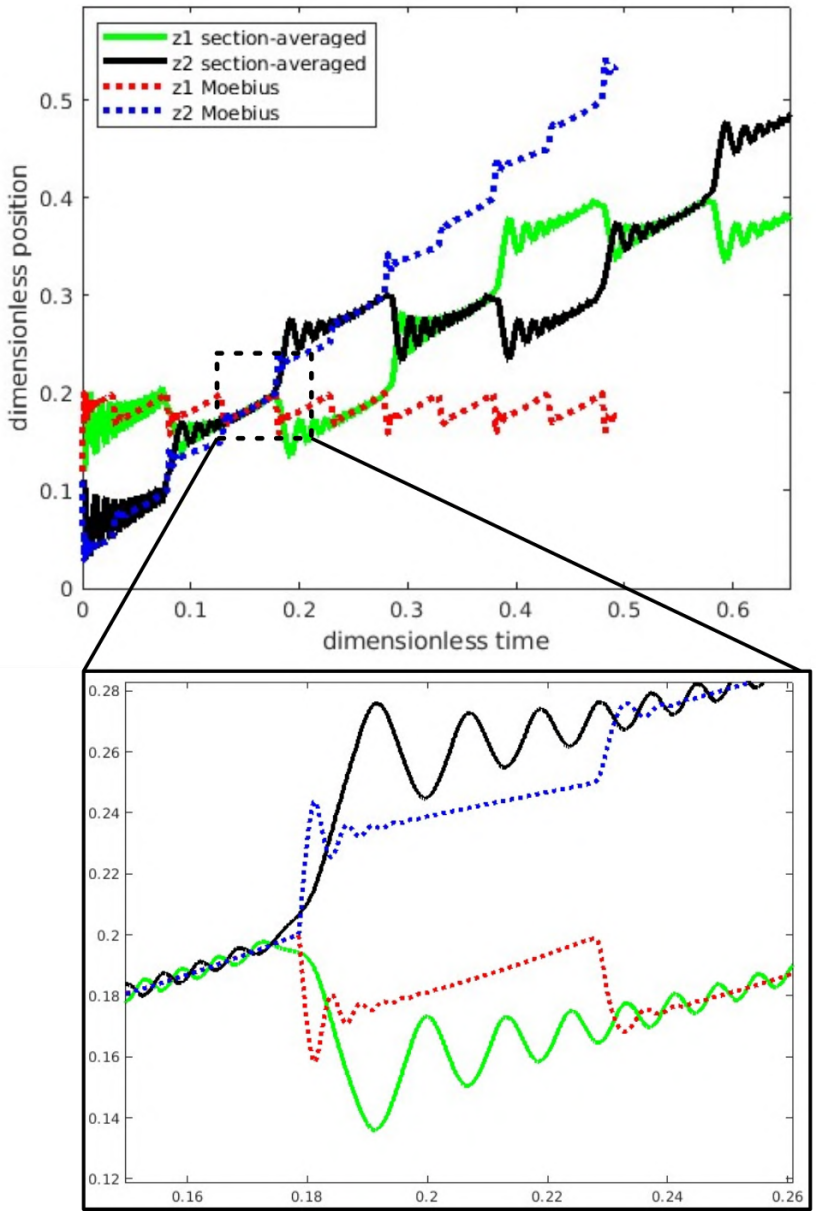

Figure 8.8: Comparison between both models with $Ca = 3.2 \times 10^{-6}$ and $Re = 3.3 \times 10^{-2}$. Both models follow the same trend and show oscillations after a Haines jump. Zooming in on one of the jumps, we can see that the section-averaged model dissipates the oscillations much slower than the model of Moebius and Or.

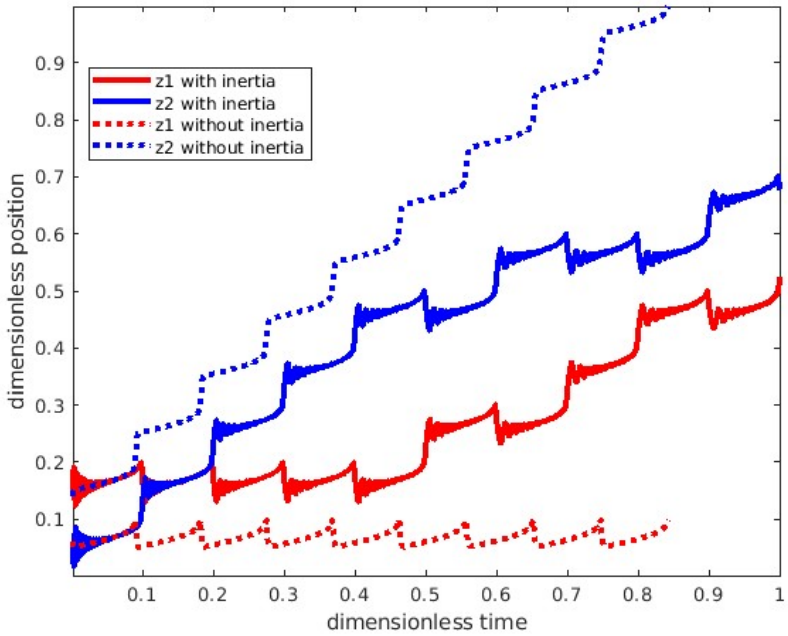

Figure 8.9: Numerical simulation of the dynamics of the menisci using the section-averaged model with $Ca = 1 \times 10^{-6}$, $M = 10$. Two pairs of curves are shown: the continuous lines are for $Re = 0.1$, and the dotted lines are for $Re = 0$, where we turned off the effect of inertia. The two situations predict different results: without inertia, we predict a classic capillary-dominated regime, where the invasion occurs only in the capillary 2, since it has a larger pore throat. If we take into account inertia, the invasion is much more complex, with jumps in both channels. At the end of the invasion, we have much less residual trapping than in the case without inertia.

models. The model of Moebius predicts rapid oscillations with a short period that are quickly damped by viscous forces. In contrast, the section-averaged model produces slower, longer-lasting oscillations that last until the next jump. These differences arise partly from an overestimation of viscous pressure drops in the earlier model, but also from inaccuracies in its treatment of inertial effects, which contribute to the discrepancy in the predicted dynamics.

In their initial paper, Moebius and Or (2012) proposed a characteristic decay time of inertial oscillations that reads as,

$$\tau_d = \frac{\rho_I w_t^2}{4\mu_I}. \tag{8.34}$$

However, as the simulations show us, this decay time is underestimated, as it seems that oscillations last longer than predicted by this equation, around 10 times longer. This is, again, due to the overestimation of the viscous drop in the channels due to the simplifying assumptions taken at the beginning. This is of significant importance, as if the inertial oscillations are not dampened before the next jump, residual oscillations may assist in overcoming the capillary entry pressure, changing the order in which the pore bodies are invaded. In Fig. 8.9, we present numerical simulations done with our section-averaged model and the ODE numerical approach. For one of the simulations, the Reynolds number was set to be zero (no inertia), and for the other,

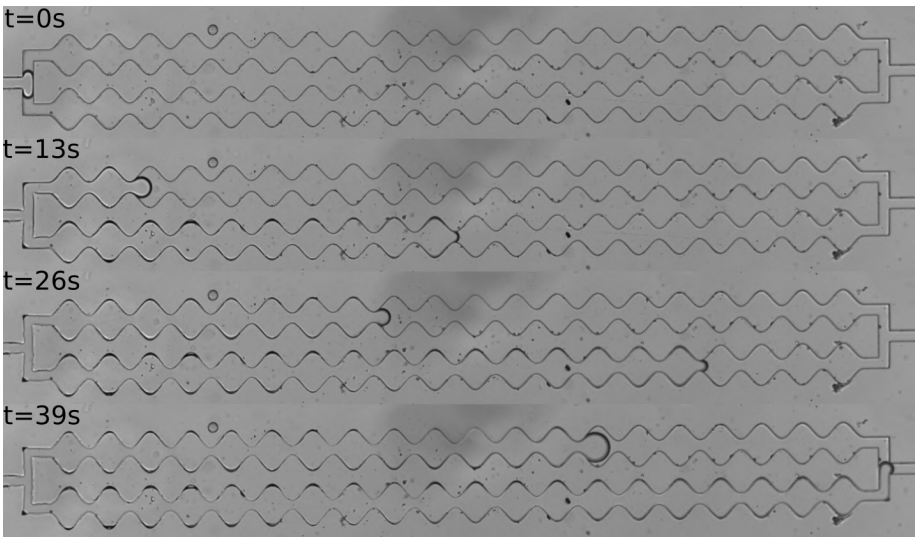

Figure 8.10: Drainage of water by silicon oil in micromodel C, with $Ca = 4.1\times10^{-6}$, $M = 5$, and $Re = 1.47\times10^{-4}$. The injection occurs from left to right. During the experiment, we observe pinning of the interface, followed by a Haines jump. The next pore invaded is dictated by the small imperfections that occurred during the fabrication process.

the Reynolds number was $Re = 0.1$. We see that without inertia, we predict a classic capillary-dominated invasion, where the fluid invades the channel with the biggest pore throat. If we take inertia into account (continuous lines), we observe a very different situation, where the oscillations caused by the inertia are enough to force the other meniscus to jump, leading to a much more complex behavior. At the end of the invasion, the model predicts a lower residual saturation with inertia than without. A proper understanding of this mechanism is important to predict residual saturation in systems where inertia plays a role. Our updated model provides a significant improvement in our capacity to predict these events in a pore doublet.

8.6 Experimental results

Using the experimental setup described in Sec. 8.4, we performed experiments in sinusoidal pore doublets for different values of the viscosity ratio and Reynolds number. In Fig. 8.10, we present a drainage experiment at $Ca = 4.1\times10^{-6}$, $M = 5$, and $Re = 1.47\times10^{-4}$. We are in the capillary regime, as we do observe that the invasion of the pore body occurs in a quick interfacial jump, before pinning of the interface at the pore throats. We are also able to recover the viscous-dominated regime, as seen in Fig. 8.11. In this experiment at $Ca = 1.2\times10^{-2}$, $M = 5$, $Re = 20$, there is no pinning of the interfaces, the menisci continuously invade the channels, without pinning at the pore throats. At the end of the experiment, because of the favorable viscosity ratio ($M = 5$), all of the wetting fluid is recovered, and the residual trapping is very low.

However, for this experiment and all of the others performed, we never observed oscillations caused by inertia in any of our three micromodels. This was confirmed by our numerical model: after reproducing the experimental conditions inside our model, no oscillations of the menisci were observed numerically. This means that the geometries of our models are inappropriate to study the impact of inertia using standard fluids (using mercury, we could have seen some oscillations, but for obvious safety rea-

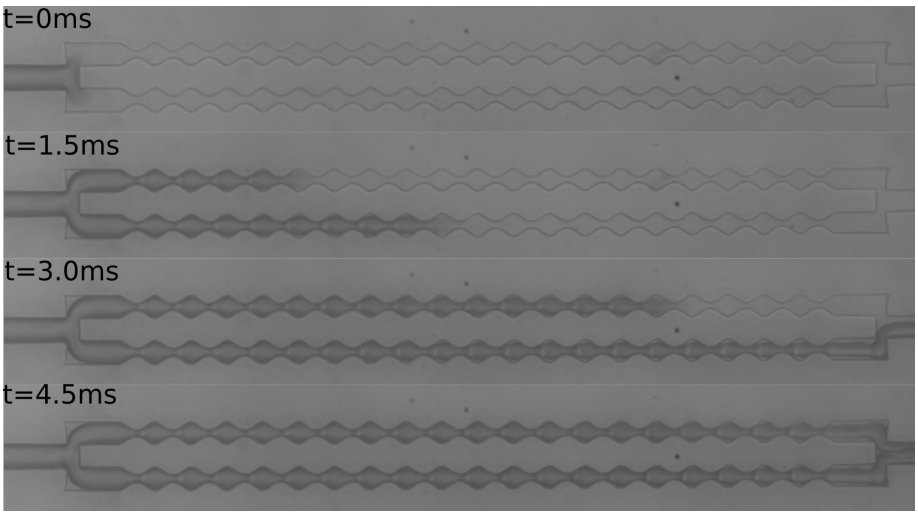

Figure 8.11: Drainage of water by silicon oil in micromodel A, at $Ca = 1.2 \times 10^{-2}$, $M = 5$, $Re = 20$, recorded at 5500 frames per second. We observe no pinning of the interfaces; the non-wetting fluid continuously invades the pore doublet. This is a sign of a viscous regime. Even after the first interface reaches the outlet, the wetting fluid is still able to exit the pore doublet via the thick wetting films along the walls, allowing the second interface to keep moving forward. At the end of the invasion, no wetting fluid is trapped.

sons, we decided not to use mercury in our experiments). This leads us to conclude that if the pores are below a certain size, inertia will not come into play. This makes sense, as the smallest volumes of pore, the smallest volume of water jumping, leading to less inertia.

We do still want to experimentally see these oscillations to check the accuracy of our section-averaged model. For that, we designed a new set of pore doublets with larger and deeper pores, in which our model predicts that oscillations will occur. Sadly, the master wafer has not yet been produced, and no experiments with this new design have been made for now.

8.7 Conclusion and perspectives

In this chapter, we presented a mathematical model describing the two-phase flow in a pore doublet while taking into account the effect of inertia. We proposed a new numerical method to solve the set of equations describing the menisci positions. After its implementation in MATLAB, we were able to show that this novel method improves the stability and speed of the solver. Using this numerical model, we emphasized the role of inertia in pore doublets during interfacial jumps, also known as Haines jumps. We showed that the high interface velocities reached during these events can induce oscillations driven by inertial effects - oscillations that may, in turn, influence subsequent jumps within the system. Experiments were made, but we were not able to highlight oscillations caused by inertia, simply because the micromodels used were too small to create these oscillations with the usual fluids. Nevertheless, using our model as a guide, we designed a new set of pore doublets that will allow us to recreate these oscillations, but experiments have not yet been performed with these new micromodels.

Our next step is to perform experiments in the new geometry and compare it with

our numerical model, before performing numerical simulations for a wider range of parameters, and identifying the scenarios in which inertia can alter the amount of fluid trapped.

Chapter 9

Wettability alteration during CO_2 underground storage

In this final chapter, we go over the phenomenon of wettability alteration, and we design a protocol to experimentally study how the surface properties of calcite change when exposed to both brine and CO_2 at reservoir conditions.

9.1 Introduction

As we have seen throughout this manuscript, the contact angle between the fluids and the porous media plays a crucial role in the different mechanisms that we have discussed (capillary pressure, Haines' jumps, wetting layers, etc). Variations in the contact angle can profoundly alter the nature of the flow by turning the invasion from a drainage to an imbibition or vice versa. For a safe storage of the carbon, it is generally accepted that we need the brine to be as wetting as possible [31], to facilitate the residual and the structural trapping of CO_2. Indeed, if wettability reversal occurs in the storage formation, meaning if CO_2 becomes the wetting fluid instead of water, we expect to see remobilization of the ganglia of CO_2 trapped in the porous matrix. If wettability reversal occurs in the caprock, capillary suction may drive migration of CO_2 upward through the barrier, thereby reducing structural trapping.

In the controlled environment of the lab, we undergo extensive work (see Section. 4.3.1) to ensure that the wettability of the micromodels is properly controlled. In geological formations, however, the system is far more complex. Constitutive rocks are composed of various minerals, each with distinct surface properties, resulting in porous media with heterogeneous wettability. Moreover, these surfaces are far from perfect; they present significant chemical heterogeneity and roughness, leading to high contact angle hysteresis, see Sec. 2.3.

The depth of the storage formation also means that the temperature and the pressure are high, above 100 bars and 50 °C [100]. This also impacts the interfacial tensions between the fluids and the solid. Studies suggest that the increase in CO_2 pressure leads to an increase in its superficial tensions [8, 9, 92, 175]. Indeed, an increase in CO_2 pressure raises its density, thereby reducing the average intermolecular distance and strengthening cohesive interactions. The largest increase in density occurs when CO_2 reaches its supercritical state, at 73 bars and 31 °C. Beyond this point, the density still increases with pressure, but at a much lower rate. On the contrary, an increase in temperature tends to dilate the gas, increasing the average distance between molecules and reducing the cohesive forces. It has also been reported that the concentration of ionic

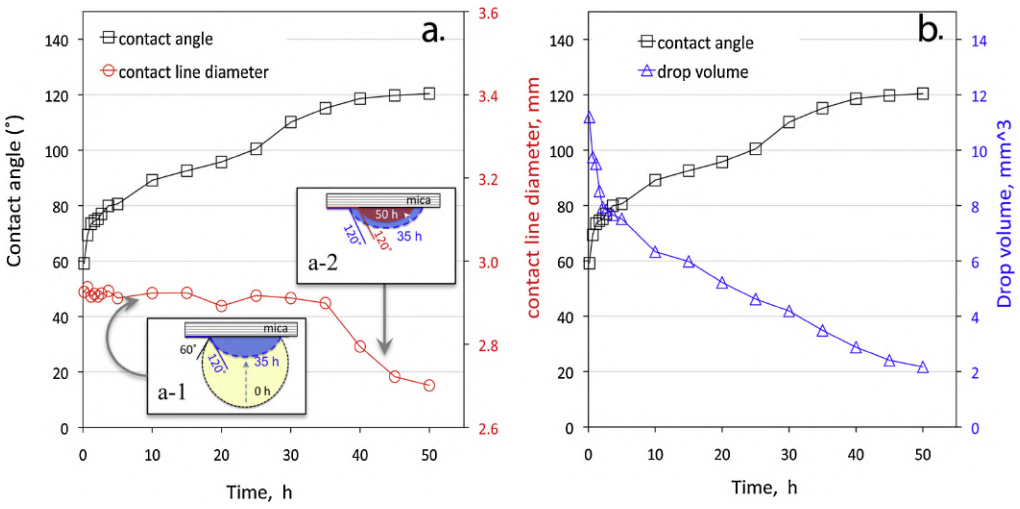

Figure 9.1: Example of a CO_2 droplet dissolving in brine right after an increase of the system's pressure. The curves show the evolution of the contact angle with time as well as (a) the contact line diameter and (b) the drop volume. We see that while the volume of the drop decreased, the contact line was pinned, and the contact angle increased from 60° to 120°, showing a wettability reversal. The contact line moved 35 hours after the pressure increased, once the contact angle had reached a plateau [208].

species in brine increases the interfacial tension between CO_2 and brine. According to the Young-Dupré equation, an increase in CO_2-brine interfacial tension decreases the brine-mineral contact angle, potentially leading to wettability reversal. However, not all studies report consistent trends: some observe no increase in contact angle with pressure, while others even report a decrease with temperature [31, 65, 64]. These ambiguities in the measurements can be explained in a few different ways:

- The substrate used in the experiments is not always the same. The preparation methods, from mineral cleavage to cleaning procedures, can introduce imperfections or leave contaminants on the solid surface, significantly affecting the wettability measurement [208, 88]. For example, calcite, which is naturally hydrophilic, becomes oil-wet after adsorption of organic compounds [96].

- If the fluids are not perfectly equilibrated before the measurement, CO_2 dissolves into brine. This dissolution leads to a decrease in the droplet volume, which can impact the contact angle, as seen in Fig. 9.1. In this figure, we see the dissolution of a CO_2 bubble inside the brine, just after a change in pressure. Even after 50 hours, the drop was still dissolving inside the brine, showing that the equilibrium was still not reached. During dissolution, the contact angle increased, from 60° to 120° over 40 hours, leading to significant errors if the measurement is taken too early.

- It has been shown that repeated contact angle measurements at the same location on mica using $scCO_2$ and brine lead to different contact angle measurements, even when all the parameters were the same [208]. This suggests that CO_2 alters surface properties of the minerals, either by reaction or sorption at its surface. This surface property alteration was also reported in many other studies [120, 83, 98, 150, 42]. A majority of these studies show that CO_2 alters the surface of the minerals and makes them more hydrophobic.

Given the importance of the wettability properties of the solid matrix in the flow of fluids in porous media, a proper understanding of the alteration of the contact angle by CO_2 is essential. Different mechanisms have been proposed to explain the observed wettability alteration. Some studies suggest that the increased acidity of the brine due to the presence of CO_2 starts to dissolve the minerals and increase their roughness, altering the contact angle according to Cassie-Baxter or Wenzel models, see Sec. 2.3 [208]. Others believe that this is due to the alteration of certain chemical groups on the surface of the minerals, changing the interfacial tension between CO_2 and the minerals [98, 123]. In this chapter, we investigate how $scCO_2$ can alter the wettability of calcite, one of the most abundant minerals in the geological reservoirs. For this, we present an experiment using a vertical autoclave to expose a crystal of calcite as well as brine and CO_2 at temperatures and pressures characteristic of geological formation. This allows us to measure the surface properties of the calcite after the contact with the brine and CO_2 mixture, and compare them with their values before the reaction.

9.2 Materials and Methods

In this section, we go over the methods used to perform and analyze the wettability alteration experiments.

9.2.1 Experimental procedure

Preparation of the calcite sample A calcite sample is prepared by cleaving a block of pure calcite. The cleavage is done using a razor blade cleaned with DI water, ethanol, and acetone, which is placed on one of the edges of the crystal, parallel to the cleavage plane. Water and ethanol are used to remove most of the pollutants, while acetone is necessary to get rid of the organic compounds that could be adsorbed on the surface, altering surface properties [96]. All equipment used to handle or store the calcite samples before and after the reaction is cleaned using the same procedure. The razor blade is then gently hit with a hammer, breaking a part of the crystal and exposing two new surfaces. The smaller crystal that is separated from the bulk of the material is used for the experiments. It has a rhombohedral shape, measuring approximately 10 mm in length, 5 mm in width, and 1 mm in depth. Because of the production method, each sample exhibits slight variations and is not identical to the others. The cleaved face is identified by scratching the opposite side with a razor blade, ensuring that all contact angle measurements after reaction are performed on the same face.

Autoclave experiments Immediately after cleavage, the crystal is weighed and inserted into the autoclave using a pair of tweezers, which were cleaned similarly using water, ethanol, and acetone. The interior of the autoclave used is lined with Teflon to prevent the contamination of the solution by the autoclave itself. The autoclave's internal volume is around 33 mL. For the experiments, the autoclave is filled with 16.5 mL of DI-water, closed, and placed in an oven at 65 °C. It is then connected to a compressor, and CO_2 is injected until the desired pressure is reached (this pressure is chosen based on the desired partial pressure of CO_2). The initial CO_2 pressure ranges from 0 bar (control experiments) to 10 bar. After the initial injection of CO_2, the system is allowed to equilibrate for 4 hours. Once the pressure stabilizes (indicating thermal equilibrium of the gas), argon is injected to reach 100 bars. Following this final injection, the autoclave is closed, and calcite dissolution begins. A schematic of the setup is found in Fig. 9.2. A summary of the experimental conditions used in the experiment can be found in Table. 9.1.

Table 9.1: Table presenting the different experimental conditions. The experiments done using brine showed no difference from the experiments done using DI-water.

Type of experiments	Fluid used	Partial pressure of CO_2
Control experiment	DI water	$P_{CO2} = 0$ bar
Control experiment	Brine with NaCl at one molar	$P_{CO2} = 0$ bar
CO_2 experiment	DI water	$P_{CO2} = [0;10]$ bar
CO_2 experiment	Brine with NaCl at one molar	$P_{CO2} = [0;10]$ bar

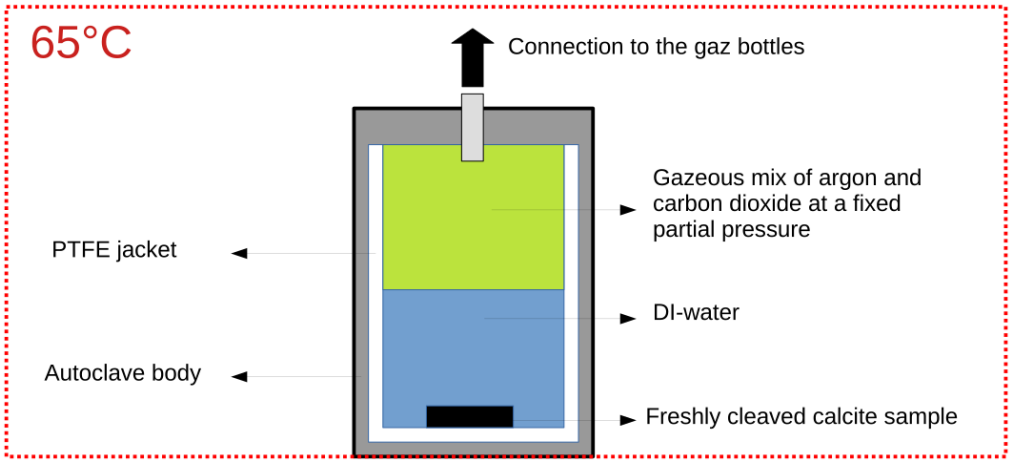

Figure 9.2: Schematic of the experimental setup used to perform the wettability alteration of calcite samples.

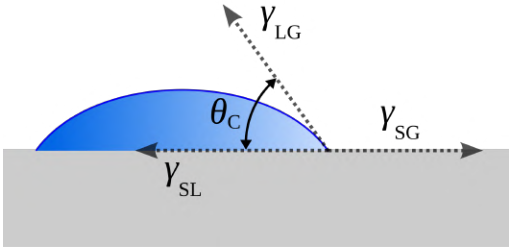

Figure 9.3: Sessile drop measurement.

Once the reaction is complete, heating is stopped, the pressure is rapidly released, and the crystal is recovered along with the water. The calcite sample is then rinsed with a minimal amount of DI water, and excess water is removed using absorbent paper. Great care is taken to avoid contamination of the sample, and the paper towel is never brought into contact with the cleaved face. Finally, the crystal is dried using a flux of clean air to remove the last traces of humidity. The calcite crystal is then weighed to determine the mass lost during the reaction.

Experiment duration assessment using PHREEQC calculations We use PHREEQC to estimate the time required for the calcite to reach equilibrium with water and CO_2. PHREEQC is a software used to perform aqueous geochemical calculations. This allows us to estimate both the dissolved mass of calcite and the dissolution kinetics, given the temperature, CO_2 partial pressure, calcite mass, and fluid volume. The simulation uses the same parameters as the experiments, with the gas quantity in the autoclave calculated from the ideal gas law, and the calcite mass and surface area measured beforehand. The initial pH of the water is set to be 8, as determined experimentally. For all the partial pressures tested (between 0 and 10 bars), the equilibrium is reached in less than a day. Based on these calculations, the system is left to react between two and five days to ensure that equilibrium is reached. PHREEQC simulations with brine at one molar of NaCl showed no difference in the dissolution rate and the equilibrium conditions compared to simulations using DI water. An example of the code used to perform the simulation can be found in Appendix G.

9.2.2 Analysis of the surface

The calcite surface is analyzed using three complementary techniques before and after the experiment. First, the contact angle is measured with a pendant drop apparatus. Next, the surface topography is characterized using atomic force microscopy (AFM). Finally, the chemical composition of the surface is examined with Raman spectroscopy.

Contact angles measurements Contact angle measurements are carried out using the tensiometer available in the NanoμLab, see Fig. 9.4. These measurements are made with water that has been previously equilibrated with calcite to avoid any dissolution of the sample during measurement. To perform the analysis, the sessile drop method is used, in which a droplet is placed on the surface of the sample while the surrounding fluid is air, see Fig. 9.3. Supercritical CO_2 is not used, as we lack the equipment to perform measurements under high-pressure and high-temperature conditions. Nevertheless, this approach still provides valuable insight into the trends of wettability alteration.

Figure 9.4: One Attension Theta Flex tensiometer from Biolin Scientific used to perform the contact angle measurements.

For each sample, the contact angle was measured twice: one right after the experiment and one after annealing. To perform a contact angle measurement, we do two to three sessile drop experiments on the sample, one after the other, but on different locations each time, so that the previous drop of water does not alter the following experiments. The first measurement is performed directly after the experiments, less than 10 minutes after removing the crystal from the autoclave. After this measure, the sample is carefully placed in glassware previously cleaned with water, ethanol, and acetone and is then left in an oven at 120°C. The glassware is closed with aluminium foil to prevent contamination from the oven. This step is done to dry the sample and remove the hydrated calcite that may have formed. Indeed, it is known that a newly cleaved surface of calcite will react with atmospheric water to form a layer of hydrated calcite at the surface of the sample, forming hillocks and trenches [218, 151]. The presence of a hydrated calcite layer also alters the water contact angle on the sample. However, the formation of this layer is reversible: placing the sample in a very dry environment (relative humidity below 1.5%) removes most of the layer and restores the initial wettability. After 24 hours, the sample is taken out (using cleaned tweezers and without touching the cleaved face), and the contact angle is measured. The final measurement after annealing is not relevant for studying wettability alteration during CCS, since dehydrated calcite will not be encountered in practice. However, this analysis helps interpret the history of the mineral surface during experiments.

Atomic Force Microscopy (AFM) Atomic Force Microscopy (AFM) imaging was performed at the CBM (Centre de Biologie Moléculaire) and the CEMHTI (Conditions Extrêmes et Matériaux: Haute Température et Irradiation) in Orléans. AFM is a technique used to image surfaces at extremely small scales, down to the ångström (10^{-10} m). It works by "feeling" the surface with a nanometric tip mounted on a flexible cantilever. This mechanical probe is brought into interaction with the sample surface, while piezoelectric elements control the fine positioning of the cantilever, enabling high-resolution

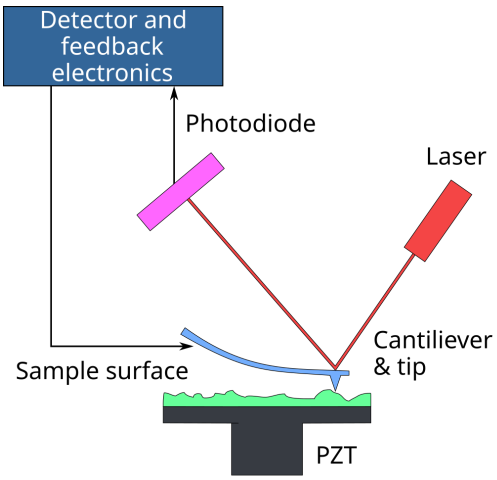

Figure 9.5: Schematic of the Atomic Force Microscopy. The probe is in contact with the surface, and any vertical movement of the tip is measured using a laser reflected on the top of the cantilever [14].

surface scanning [26]. There are two main modes of operation for the AFM: contact and tapping mode.

In contact mode, the tip maintains continuous contact with the surface. To measure its vertical displacements, a laser is directed at the back of the cantilever and reflected toward a photodiode. Any vertical deflection of the cantilever alters the reflection angle of the laser, which is then detected by the photodiode, providing the vertical displacement of the probe (see Fig. 9.5). Combining these deflections with the controlled lateral movement of the probe enables a high-resolution reconstruction of the surface topography.

In tapping mode, the probe oscillates near its resonant frequency with a given amplitude and is then approached to the surface. When the tip intermittently touches the surface, the oscillation amplitude decreases. This reduction is monitored and correlated with the surface features, allowing the topography to be mapped. Tapping mode reduces the contact time between the tip and the sample, thereby minimizing wear of both the probe and the surface. This technique can perform measurements in vacuum, air, or underwater, with a resolution down to a fraction of a nanometer. It is highly sensitive, so excessively rough surfaces cannot be measured; the maximum allowable surface roughness is approximately 5 μm.

Several measurements were made on calcite samples cleaved a few minutes before the analysis. One measurement was done on the sample resulting from a control experiment, on the same day that the sample was taken out of the autoclave. We tried to perform measurements on CO_2-reacted samples with a partial pressure of CO_2 between 1 and 10 bars, but none of the samples yielded any results. The calcite crystals were transported using plastic sample holders that were thoroughly cleaned beforehand. To prevent the sample from moving during transportation, they were held in place using a weak adhesive on the side opposite of the cleaved face.

Raman spectroscopy Another technique used to analyze the surface composition is Raman spectroscopy. This technique is used to determine the vibrational modes of molecules to identify chemical species. It is done by exciting the sample's molecules with a visible-light laser. The photons, after interacting with the laser, are scattered in all directions. Most photons typically retain their original wavelength and return with

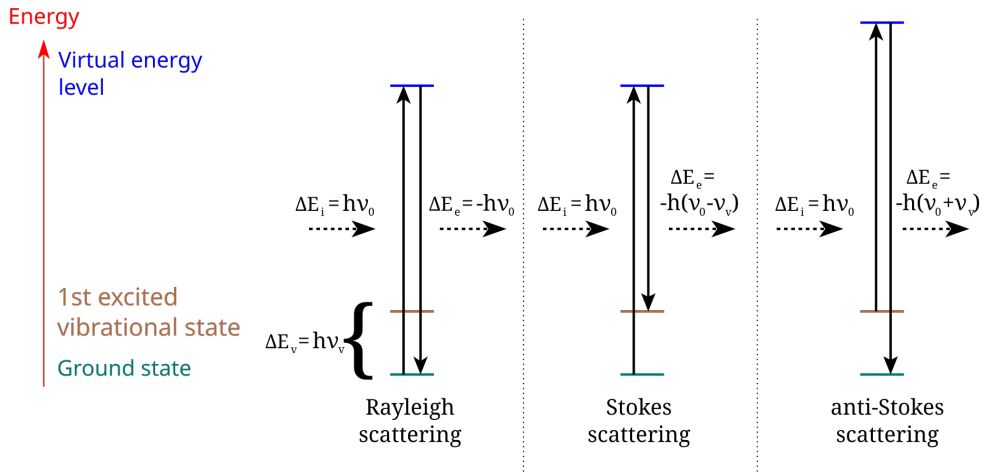

Figure 9.6: Schematic of the different light scattering possibilities. Rayleigh, or elastic scattering, where both incident and emitted photon share the same wavelength, Stokes scattering, where the emitted photon has less energy than the incident photon, and the anti-Stokes scattering, where the emitted photon has more energy than the incident one [160].

the same energy they had initially, in a process known as Rayleigh, or elastic, scattering. A small percentage of these scatter inelastically, gaining or losing energy in the process. By energy conservation, the molecules in the material correspondingly lose or gain the same amount of energy. There are two cases: normal Stokes and anti-Stokes scattering, see Fig. 9.6. In Stokes scattering, the photon loses energy when interacting with the molecules, which is transferred to the molecules as vibrational energy or a phonon. Anti-Stokes scattering occurs more rarely and is when the photon gains energy after being scattered by the molecule. This means that the material loses vibrational energy or a phonon. The shift in the photon energy (in cm^{-1}) and the magnitude of the peaks are correlated to the chemical bonds present in the molecule, and based on these shifts, a fingerprint of the molecule is recovered, which is then used to determine the exact molecule being investigated (different analyses might be required for complete identification of the molecule). For our analysis, we perform a Raman mapping of the sample. A surface is selected, and a set of points is defined for spectroscopy. Each point provides a Raman signal, which is then used to identify the chemical composition at the location.

We performed one analysis on one sample reacted with NaCl brine at $P_{CO2} = 10$ bar. It was carried out at CEMHTI, two days after the end of the experiment.

9.3 Results

All of the analyses presented here are made using samples from experiments made with DI-water, except the Raman spectroscopy, which was performed using a sample from an experiment using brine.

9.3.1 Calcite surface before the experiment

Before the reaction, the contact angle between the calcite-saturated water and the freshly cleaved sample was measured to be zero. Indeed, the water spreads at the surface of the sample, covering it entirely, see Fig. 9.8. The fresh calcite surface is thus strongly hydrophilic, as it has been reported in the literature [3, 102]. The surface of calcite is so reactive that a few hours after cleavage, it is known to rearrange itself (aging) to lower its energy state, decreasing its wettability to reach contact angles between 60° and 80°, a weakly hydrophilic behavior, by reacting with water in the atmosphere and adsorbing different atmospheric pollutants. We measured the contact angle of an aged surface of calcite after exposure to ambient air for several months, see Fig. 9.8. AFM measurement of the surface can be seen in Fig. 9.7. We see that initially, the samples are clean and extremely flat. The surface is composed of atomically flat terraces, separated by molecular steps.

9.3.2 Calcite surface after the control experiment

We perform two blank experiments, without any CO_2 injected inside the autoclave. For both of them, we measured an average contact angle of 31°, see Fig. 9.8. All of the contact angle measures on reacted calcite samples are summarized in Fig. 9.9. The AFM measurement performed on this sample showed reorganization of the surface. Indeed, the molecular steps present just after the cleavage have been smoothed out during the experiments and replaced by hillocks. This shows that a small fraction of the calcite dissolved in the DI-water

This topographic change and the increase in the contact angle showed reorganization of the surface, even during the control experiment using only argon.

9.3.3 Calcite surface after exposure to CO_2-water mixture

For the experiments with CO_2, all samples show a strongly hydrophilic behavior for all of CO_2 partial pressures imposed, see Fig 9.9. The measured contact angles are all between 0° and 10°, see Fig. 9.8. Higher concentration of CO_2 appears to decrease the contact angle between the calcite and water. We also tried to analyze the surface of calcite samples that reacted with CO_2 using AFM, but we were unable to image them. AFM is very sensitive to changes in topology, which also means that if the roughness of the surface is above ≈ 5 µm, the AFM cannot analyze the sample. This means that CO_2 reacted samples have a roughness above 5 µm, way above the roughness of the freshly cleaved calcite or the blank experiments. This effect is also evident when the sample is removed from the experimental vessel. After the reaction, the calcite appears opaque, in contrast to its initial transparency, suggesting an increase in surface roughness.

Raman spectroscopy was used to analyze the calcite surface after reaction with $P_{CO2} = 10$ bars, a few hours after ending the reaction. The result can be seen in Fig. 9.10. On this figure, the characteristic signal of calcite was obtained at every analysis point, with different intensity (due to the surface accidents). This indicates that the entire surface of the reacted material is composed of calcite, with no other minerals precipitating. This was expected, as the brine only contained NaCl and none of the other salts that compose the real-life brine of the geological reservoir. This means that the surface roughness observed previously is calcite that precipitated on the sample, and that the alteration on wettability properties is caused by topological changes and not chemical changes.

The second contact angle measurement takes place after the sample was put in an oven for 24 hours at 120 °C. This step serves to dehydrate the calcite surface. The results of these measurements highlight different behaviors. For a partial pressure of

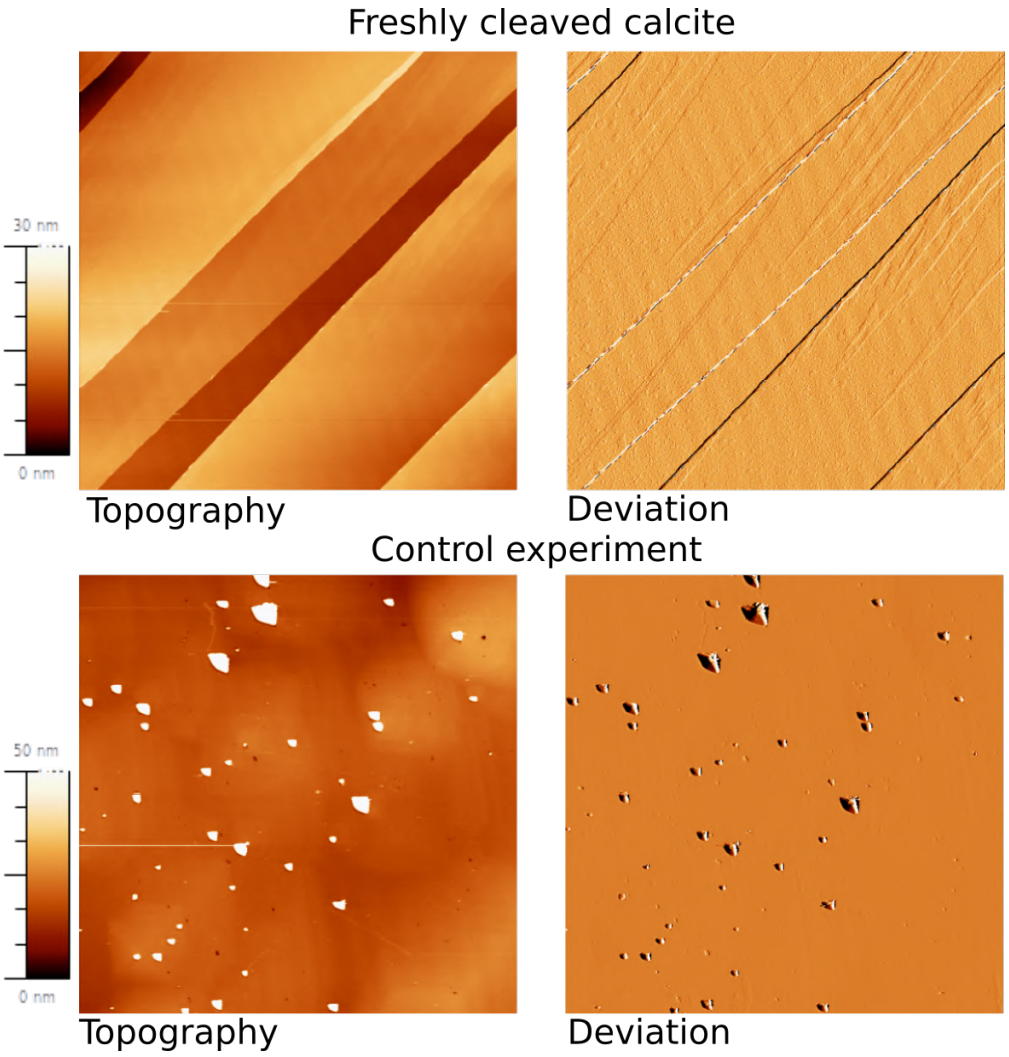

Figure 9.7: AFM images of the freshly cleaved surface of calcite (top) and the control experiment surface (bottom). The images on the right are the deflection of the probe recorded by the AFM, and on the left are the reconstructed images from the deflection. Both measures were done in contact mode. For the freshly cleaved surface, several terraces are present, with no roughness on them. They are separated by steps that are several molecular layers thick. For the surface after the control experiment, these terraces and the molecular steps have been smoothed out, and periodic shapes resembling hillocks have taken their place. The size of the scans is 15 µm × 15 µm Credits: F. Foucher.

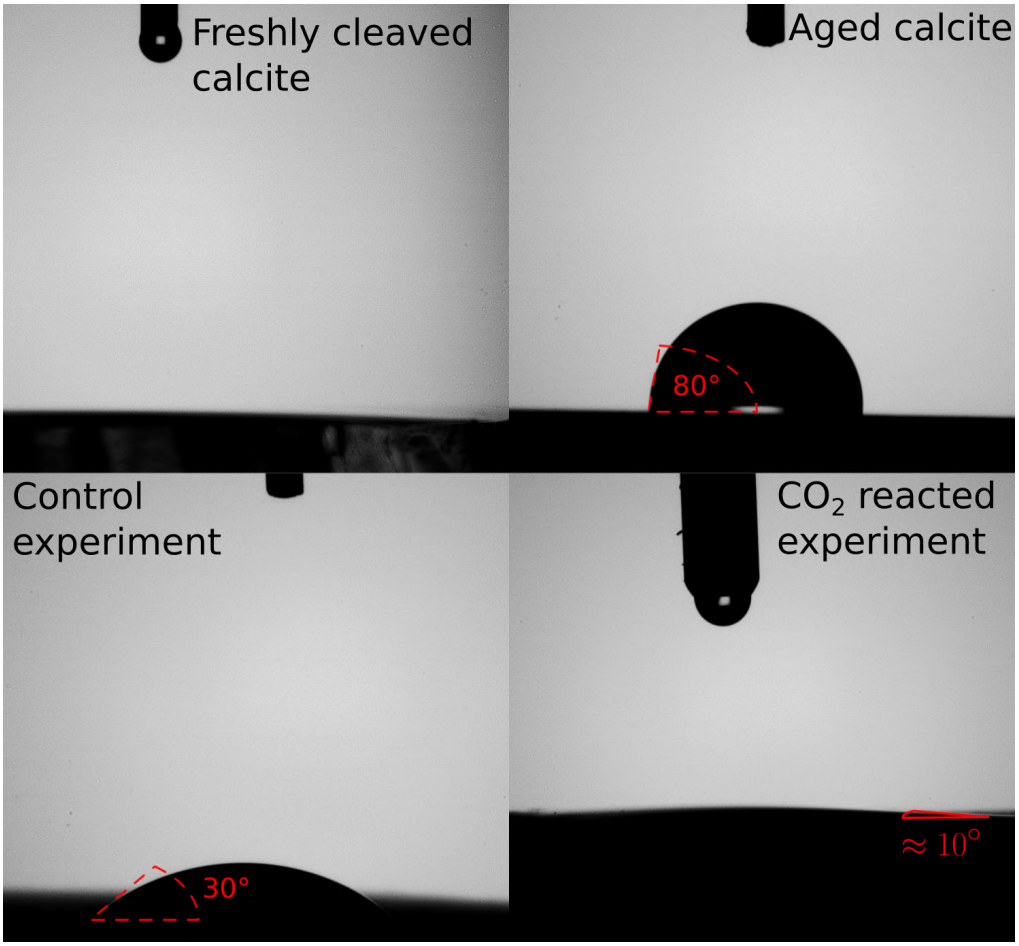

Figure 9.8: Sessile drop experiment done on freshly cleaved calcite, aged calcite (several months at ambient conditions), calcite from the control experiment, and CO_2-reacted calcite at P_{CO2} = 5 bar. We observe, respectively, a contact angle of 0°, 80°, 30° and 10°. This highlights the hydrophilic behavior of the freshly cleaved calcite, which turns to a more intermediate wettability after aging. After experiments, we also measure a higher contact angle compared to the freshly cleaved calcite. The control experiment shows a higher contact angle than the CO_2-reacted calcite.

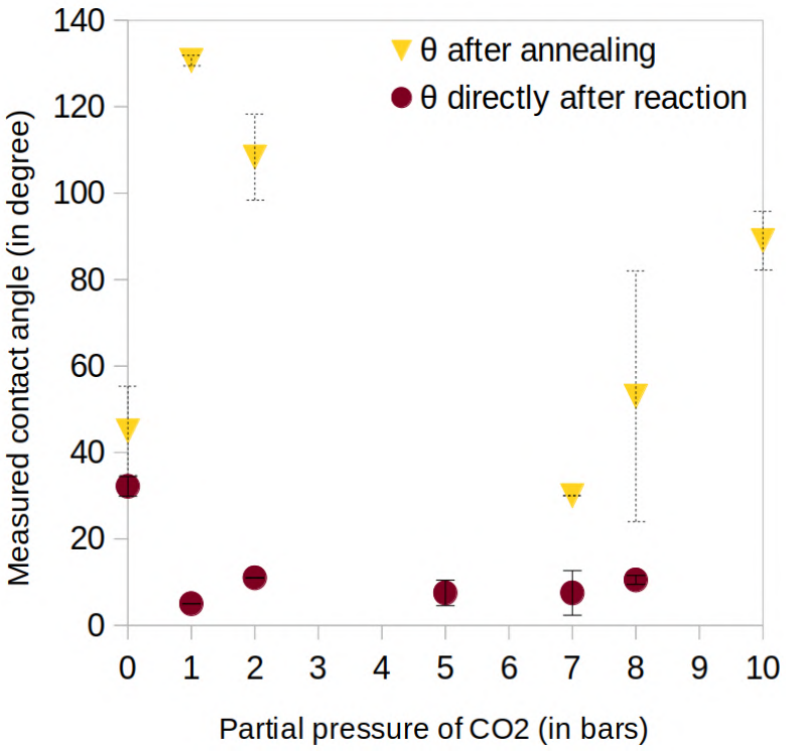

Figure 9.9: Experimentally measured contact angle between calcite saturated water and the calcite sample after reaction. The x-axis represents the partial pressure of CO_2 present in the autoclave during the reaction. The blank experiment sits at $P_{CO2} = 0$. For each partial pressure condition, two measurements were done: one right after the experiments (purple circles) and one after 24 hours of annealing (yellow triangles). The error margin is calculated using a 95% confidence interval and is obtained by doing several sessile drop experiments on the same sample. For some experiments, one of the measurements was not made due to accidental contamination of the surface.

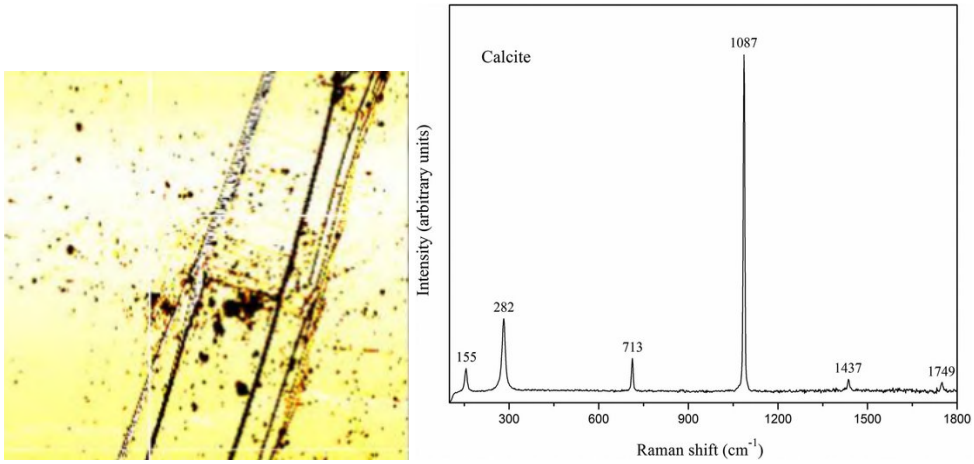

Figure 9.10: Raman cartography of a CO_2 reacted calcite surface. On the left is the intensity of the signal over the analyzed surface, with white being high intensity and black low intensity. The right is the Raman signal of calcite. For our sample, the signal of the calcite was obtained at every point of the cartography, with different intensities. The surface accidents can be seen in black (less intense). Credits: A. Canizares.

CO_2 of 1 bar, we measure an astonishing contact angle of 130°, a sign of a hydrophobic surface, meaning that annealing the sample turned it hydrophobic by increasing the contact angle by 125°! Similar behavior is observed for a partial pressure of 2 bar and 10 bars, albeit with lower contact angles, but still in the hydrophobic range.

But for other partial pressures of CO_2, such as 3, 7, and 8 bars, we do not observe this impressive wettability reversal. There is still an increase in the contact angle, but not as significant. This is also the case for the blank experiments.

9.4 Discussion

We have seen that right after cleaving the calcite, the surface created is strongly hydrophilic, but after exposure to air and water, the surface ages, and this strong hydrophilicity turns to weak hydrophilicity. This is what we see for the blank experiment, where only argon was injected during the experiment, as highlighted by the contact angle measurements done right after the reaction. This can also be seen via the AFM images. During the reaction, the roughness increases slightly, and the molecular steps were dissolved to form hillocks on the surface, see Fig. 9.7. This is a sign that dissolution and precipitation of the calcite occurred, aging the calcite. We do still measure a hydrophilic behavior of the sample.

When we start to add CO_2 to the autoclave, we observe an increase in the wettability of the sample, with the contact angle decreasing from 30 in the blank experiment to 10 for P_{CO2} = 8 bar and for P_{CO2} = 2 bar, and even lower for the other partial pressure tested. This shows that the presence of CO_2, no matter the quantity (over the range tested), increases the wettability of the surface. This behavior is explained by the increased roughness of these samples. Indeed, we saw in Sec. 9.3 that CO_2 reacted samples were too rough to be analyzed using the AFM, showing that their roughness is above 5 µm. According to Wenzel's law, we have that,

$$\cos\theta^* = r\cos\theta, \tag{9.1}$$

where θ^* is the apparent (large-scale) contact angle, r is the roughness defined as the

real surface area divided by the apparent surface, and θ is the contact angle defined by the Young-Dupré equation and is obeyed locally by the contact line, see Sec. 2.3. This means that the increased roughness of CO_2 reacted samples explains the increased wettability of the samples. By taking an average apparent contact angle of $\theta^* = 10°$ for CO_2-reacted samples, and we suppose that the blank experiment is close to a flat surface with no roughness, giving us the Young contact angle: $\theta = 30°$. With these data and Wenzel's law, we can compute the roughness of the calcite surface that reacted with CO_2. We find a roughness of $r = 1.137$.

The roughness of these samples is clearly caused by the presence of CO_2 in the mixture. It diffuses inside the water, lowering its pH, which causes the dissolution of calcite. The dissolution occurs preferentially at steps and defects, where the surface energy is the highest. This leads to the steps retreating (as we saw occurring for the blank experiment) and the formation of dissolution pits of rhombic shape [117, 227]. Once equilibrium is reached, dissolution slows down and is compensated by precipitation of newly formed calcite crystals on the surface, which can also increase the roughness.

The increased hydrophilicity of calcite can be attributed to the roughness enhancement induced by CO_2 and is consistent with Wenzel's law. However, this result contrasts with much of the literature, where the presence of CO_2 is generally reported to increase minerals' hydrophobicity [120, 83, 98, 150, 42], but none of these studies looked at the influence of CO_2 on calcite wettability. One possible reason why we do not observe an increase in the hydrophobic character of the calcite after reaction is that calcite does not have Si-OH chemical bonds. The modification of these atomic bonds is one of the mechanisms advanced to explain how CO_2 makes silica minerals more hydrophobic [120, 123, 98]. Moreover, due to its crystalline structure, it is also harder for CO_2 to enter the calcite sample and swell, as proposed in Wan et al. (2014). Another possible explanation lies in the simplicity of our experimental setup: we used only deionized water or a simple NaCl brine, which prevented the precipitation of secondary mineral phases, as confirmed by Raman spectroscopy.

We observe wettability alteration on the freshly reacted sample, but no wettability reversal. This leads us to expect no wettability reversal for calcite in the presence of CO_2. In the context of CCS, this decrease of the contact angle with water could lead to corner flow during secondary imbibition, which has a poor displacement efficiency [224]. This would lead to a higher residual trapping of CO_2 after secondary imbibition, favoring CO_2 storage. Moreover, the increase in surface roughness promotes the formation of wetting films at the solid surface, favoring snap-off and the trapping of the non-wetting phase. It has been shown that even for small changes in contact angles (from 50° to 20°), we observe a significant increase in the residual trapping and in the dissolution of CO_2 inside of the brine.

For the contact angle measured after annealing, the wettability reversal observed for certain partial pressures of CO_2 is unexpected. One possible explanation is the trapping of air in the roughness of the surface, as we have discussed in Sec. 2.3. Or, according to the simplified model that we derived there, the trapping of air is only possible for intrinsically hydrophobic materials, which is not the case for our calcite. But when we look at a shape a bit more complex, we see that even if we have a contact angle below $\frac{\pi}{2}$, it is possible to trap air below the drop. This is the case, for example, when we add an overhang slope to the well-defined, idealized crevices that we introduced [75]. Then, air can be trapped below the drop, increasing the contact angle as we have seen with the experiment of Shibuichi et al. (1996), see Fig. 9.11. To verify this hypothesis, imaging of the surface is required to observe if small structures with overhang developed on the surface of the calcite. This could be done via digital microscopy, which is similar to optic microscopy, but the use of an LCD camera to image the sample allows for a deeper field of view.

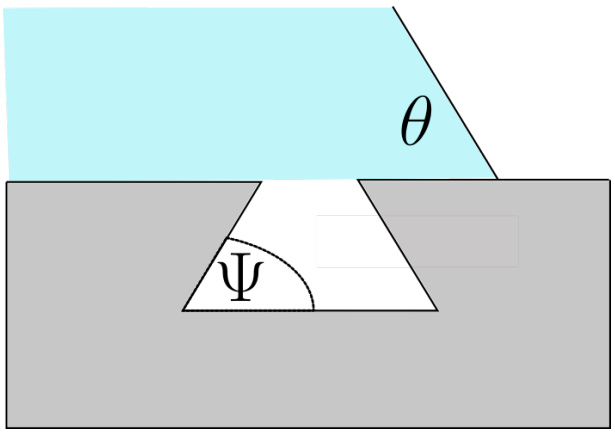

Figure 9.11: Crevices with an overhang slope. Even if the fluid is wetting ($\theta < \frac{\pi}{2}$) it cannot enter the crevices as long as $\theta + \Psi > \frac{\pi}{2}$. This causes air to be trapped under the drop, increasing the apparent contact angle θ^*.

9.5 Conclusion

In this chapter, we conducted experiments at 100 bar and 65 °C to investigate the alteration of freshly cleaved calcite surfaces in the presence of water and CO_2 under reservoir conditions. Our results show that the presence of CO_2 leads to an increasing surface roughness of the calcite surface and thereby enhances its hydrophilicity in accordance with Wenzel's law. This conclusion contrasts with much of the existing literature, which reports that mineral alteration by CO_2 typically promotes hydrophobicity. We attribute this discrepancy to our use of pure calcite, which has no Si-OH bonds for CO_2 to alter. Moreover, our use of DI water or brine containing only NaCl prevents the precipitation of secondary minerals during the reaction.

Complementary measurements are also performed after annealing. Although this is not directly relevant to CCS, it helps us to understand the impact of CO_2 on the calcite surface. We hypothesize that the increase in surface roughness caused by CO_2 could create dissolution pits with an overhang slope, which could trap air and explain the dramatic rise in contact angle. However, further analysis is required to confirm this. To validate our hypothesis, post-reaction imaging of the calcite surface, using, for example, a digital microscope, is necessary in order to quantify roughness and directly compare it to the values inferred from contact angle measurements.

A good understanding of how roughness and surface topology alter wettability could be used in the design of micromodels with heterogeneous wettability.

Chapter 10

Conclusions and perspectives of the work

This thesis has examined the fundamental mechanisms driving two-phase flow in porous media, with particular emphasis on the processes controlling the residual trapping of CO_2 in geological reservoirs. Residual trapping is a key mechanism that ensures the long-term security of underground CO_2 storage. Traditionally, it is investigated through static models and experiments that link residual saturation to capillary pressure. However, such static approaches fail to capture the inherently dynamic phenomena, such as Haines jumps, inertial effects, snap-off, or Bretherton films, that play a critical role in determining residual saturation, often leading to inaccurate estimations of trapping efficiency. To address this limitation, this work focused on the dynamics of two-phase flow, especially at the pore scale, where the physical mechanisms originate and ultimately dictate large-scale behavior.

By combining experimental and numerical approaches, we investigated three aspects that significantly influence the fate of CO_2 in the subsurface: the role of wetting films in flow stability, inertial effects during Haines jumps, and wettability alteration of minerals under reservoir conditions.

First, we introduced an extended pore-doublet model that incorporates the presence of wetting films, a ubiquitous feature in porous systems. Our results revealed that these films can either act as lubricants or resistive layers, depending on the viscosity contrasts between the fluids. This dual role significantly modifies the stability of the invasion front and reconciles experimental observations with theoretical predictions. These insights underscore the importance of considering wetting films in any predictive model of multiphase flow, particularly when scaling up from the pore to the Darcy scale.

Second, we showed that inertial effects, often neglected in porous media studies, can play a non-trivial role during interfacial jumps. Using pore-doublet models and microfluidic experiments, we demonstrated that the rapid interface velocities reached during Haines jumps may induce oscillations, which in turn influence subsequent displacements and the amount of fluid trapped. This finding challenges the traditional assumption that inertia is negligible at the pore scale, highlighting the need to account for transient events when assessing capillary trapping efficiency.

Third, we investigated how CO_2 injection alters the wettability of underground rocks, a crucial parameter for storage security. Our experiments on calcite surfaces at reservoir conditions revealed that CO_2 exposure increases surface roughness and enhances hydrophilicity, in contrast with much of the existing literature that reports hydrophobic trends. We attribute this discrepancy to our use of pure calcite and sim-

plified aqueous chemistries, which prevented secondary mineral precipitation. While limited in scope, these findings suggest that mineral-specific and environment-specific responses must be carefully considered when evaluating long-term wettability evolution in storage sites.

Altogether, this work contributes to a more nuanced understanding of the complex interplay between capillarity, viscosity, inertia, and surface wettability in porous media. It emphasizes that residual trapping is not governed by a single mechanism, but rather by the collective action of transient interfacial dynamics, film-mediated flow pathways, and evolving surface properties.

Looking forward, several perspectives arise. First, more experiments on Haines jumps are required to validate the model that was developed. Second, a deeper look at wettability alteration is required by conducting a more in-depth surface analysis. More experiments need to be done, using different minerals and brine combinations.

An aspect of two-phase flow that was only briefly glanced over in this work is the snap-off mechanism, which plays an important role in residual trapping. We have seen that cycles of snap-off and reconnection appear during drainage in a single capillary, but is it still the case in a pore doublet? We have seen the static conditions for snap-off, but is it still valid when accounting for flow dynamics?

Once a better understanding of snap-off and wettability alteration is reached, one of our objectives is to combine all of our work on pore doublets in a single code. It should be able to predict the displacement and the residual saturation in a multitude of different geometries, taking into account inertia, wetting films, and wettability alteration of the solid. Such a model would help us understand two-phase flow in different geometries and the role played by the different parameters and phenomena. It could then be used in pore-network modeling, to take into account the wetting layers and inertia.

Using this deeper understanding of the two-phase flow, we aim to couple pore-scale insights with larger-scale models, bridging the gap between microfluidic observations and reservoir-scale predictions. In particular, the influence of heterogeneity, mineral diversity, and chemical reactivity in natural systems must be incorporated to assess the robustness of residual trapping in real geological formations. Experimentally, advances in high-resolution imaging, such as fast X-ray microtomography, could provide direct evidence of the pore-scale processes inferred in this work.

In conclusion, by dissecting the pore-scale physics of immiscible two-phase flow, this thesis advances our understanding of residual trapping and contributes to the broader effort of making carbon capture and storage a reliable solution for mitigating climate change.

Nomenclature

α	Growth rate of the channel width or radius.
α_0	Thermal dilation coefficient
β	Numerical constant for the calculation of the rectangular channel permeability
β_i	i-th Betti number
$\boldsymbol{\sigma}$	The total stress tensor
$\boldsymbol{\tau}$	Shear stress tensor
χ	Euler's number
χ_i	Dry area in channel i
ΔP_i	Pressure difference between the beginning and the end of channel i
ΔP_{cap}	Capillary pressure between fluid I and II.
$\Delta P_{visc,j}$	Viscous drop in fluid j
Δz	Position difference between the two menisci
ϵ	Aspect ratio of the rectangular channels
η	Geometrical factor
Γ	Density ratio between the invading and defending fluid
κ_i	Curvature of the interface in channel i
κ_T	Isothermal compressibility coefficient
λ_i	Slip length in channel i
μ_I	Viscosity of the wetting fluid
μ_{II}	Viscosity of the non-wetting fluid
$\nabla P_{i,j}$	Pressure gradient in fluid j for channel i
ϕ	Porosity
$\phi_i(t,z)$	Parameter related to the viscous drop in channel i
$\Pi_{c,w}$	Scaled capillary pressure
ψ_i	Wet fraction in the asymptotic case $Ca \to 0$

$\psi_i(z,t)$ Parameter related to inertia in channel i

ρ_i Density of fluid i

σ Interfacial tension

τ Initial difference in the menisci position imposed for the simulations

τ_d Characteristic time for the decay of the oscillations caused by inertia

θ^* Apparent contact angle

θ_i Contact angle measure through the wetting phase in channel i

ζ Dimensionless geometrical factor

ζ Geometrical factor

A Cross-section

a Average width of a sinusoidal channel

A_i Total cross section of channel i

$A_{i,j}$ Cross section of the channel i occupied by fluid j

c Numerical constant used for the conductance in rectangular channel

Ca Capillary number of the whole system

Ca^* Capillary number used in the equations, connected to classic capillary number by ζ

Ca_i Local capillary number defined in channel i

d Diameter of a pore

D_0 Constant depth of the rectangular channel

e_i Film thickness in the channel i for the cylindrical channel

$e_{avr,i}$ Average thickness of the film in the rectangular case, calculated from the wetted area in the channel i

$e_{r,i}$ Thickness of the films at the center of the walls for the rectangular channel i

f_l Fraction of the surface occupied by liquids, for the Cassie-Baxter model of wettability.

$g_{i,j}$ Conductance of the channel i to the fluid j.

H Length of one pore for sinusoidal pore doublet

k Permeability of a porous media

$k_{i,j}$ Permeability of the channel i to the fluid j

$k_{r,i}$ Relative permeability of fluid phase i

L Total length of the channel

l_c Capillary length scale of the porous media, used for scaled capillary pressure calculation

M	Viscosity ratio
$P(M)$	Functions used to compute the thickness of the wetting films in a cylindrical channel
P_{CO2}	partial pressure of CO_2 for the wettability alteration experiments
$Q(M)$	Functions used to compute the thickness of the wetting films in a cylindrical channel
Q_i	Flow rate of non-wetting fluid in channel i.
Q_p	Total flow rate of non-wetting fluid injected in the inlet.
r	Roughness, determined as the ratio of true surface area over apparent surface area.
$r(z)$	Radius of the cylindrical channel
r_0	Initial radius of the cylindrical channel
$R_{h,i}$	Hydraulic radius of the rectangular channel
Re	Reynolds number
RE^*	Reynolds number used in the equations, connected to classic Reynolds number by η
S_w	Saturation of wetting fluid
S_{nw}	Saturation of non-wetting fluid
SEF	Storage Efficiency Factor
T	Temperature of the system
t'	Dimensionless time
t_c	Characteristic time of the system
t'_{end}	Dimensionless simulated time
$U_i(t)$	Average velocity of fluid II in channel i
$u_{i,j}$	Velocity of fluid j inside of channel i at a given position.
w	Width of the channel
w_0	Initial width of the channel
w_f	Width at the end of the channel in the rectangular case
w_p	width of the largest portion of a sinusoidal channel
$w_{t,i}$	width of the narrowest portion of the channel i of a sinusoidal pore doublet
z_i	Distance from the inlet to the position of the meniscus in channel i
$J(S_w)$	Leverett J function

References

[1] B. Aaboud, A. Saouab, and C. H. Park. "Modeling of air bubble dynamics during resin transfer molding by pore doublet model". In: *The International Journal of Advanced Manufacturing Technology* 105.5 (Dec. 1, 2019), pp. 2343–2355. DOI: 10.1007/s00170-019-04435-1.

[2] H. Abdoulghafour, M. Sarmadivaleh, L. P. Hauge, M. Fernø, and S. Iglauer. "Capillary pressure characteristics of CO2-brine-sandstone systems". In: *International Journal of Greenhouse Gas Control* 94 (Mar. 1, 2020), p. 102876. DOI: 10.1016/j.ijggc.2019.102876.

[3] M. Aboushanab, A. Isah, M. Mahmoud, D. H. Anjum, and M. Arif. "Surface wettability of quartz and calcite: Impact of cleavage, exposure time, and scale of measurement". In: *Petroleum Research* (Apr. 4, 2025). DOI: 10.1016/j.ptlrs.2025.04.001.

[4] S. J. Altman, B. Aminzadeh, M. T. Balhoff, P. C. Bennett, S. L. Bryant, M. B. Cardenas, K. Chaudhary, R. T. Cygan, W. Deng, T. Dewers, D. A. DiCarlo, P. Eichhubl, M. A. Hesse, C. Huh, E. N. Matteo, Y. Mehmani, C. M. Tenney, and H. Yoon. "Chemical and Hydrodynamic Mechanisms for Long-Term Geological Carbon Storage". In: *The Journal of Physical Chemistry C* 118.28 (July 17, 2014), pp. 15103–15113. DOI: 10.1021/jp5006764.

[5] P. Ø. Andersen, E. K. Nesvik, and D. C. Standnes. "Analytical solutions for forced and spontaneous imbibition accounting for viscous coupling". In: *Journal of Petroleum Science and Engineering* 186 (Mar. 1, 2020), p. 106717. DOI: 10.1016/j.petrol.2019.106717.

[6] L. Andersson, A. Herring, S. Schlüter, and D. Wildenschild. "Defining a novel pore-body to pore-throat "Morphological Aspect Ratio" that scales with residual non-wetting phase capillary trapping in porous media". In: *Advances in Water Resources* 122 (Dec. 1, 2018), pp. 251–262. DOI: 10.1016/j.advwatres.2018.10.009.

[7] *AR6 Synthesis Report: Climate Change 2023*. URL: https://www.ipcc.ch/report/ar6/syr/.

[8] M. Arif, M. Lebedev, A. Barifcani, and S. Iglauer. "CO2 storage in carbonates: Wettability of calcite". In: *International Journal of Greenhouse Gas Control* 62 (July 1, 2017), pp. 113–121. DOI: 10.1016/j.ijggc.2017.04.014.

[9] M. Arif, A. Z. Al-Yaseri, A. Barifcani, M. Lebedev, and S. Iglauer. "Impact of pressure and temperature on CO2–brine–mica contact angles and CO2–brine interfacial tension: Implications for carbon geo-sequestration". In: *Journal of Colloid and Interface Science* 462 (Jan. 15, 2016), pp. 208–215. DOI: 10.1016/j.jcis.2015.09.076.

[10] R. T. Armstrong and S. Berg. “Interfacial velocities and capillary pressure gradients during Haines jumps”. In: *Physical Review E* 88.4 (Oct. 22, 2013), p. 043010. DOI: 10.1103/PhysRevE.88.043010.

[11] R. T. Armstrong, N. Evseev, D. Koroteev, and S. Berg. “Modeling the velocity field during Haines jumps in porous media”. In: *Advances in Water Resources* 77 (Mar. 1, 2015), pp. 57–68. DOI: 10.1016/j.advwatres.2015.01.008.

[12] R. T. Armstrong, J. E. McClure, V. Robins, Z. Liu, C. H. Arns, S. Schlüter, and S. Berg. “Porous Media Characterization Using Minkowski Functionals: Theories, Applications and Future Directions”. In: *Transport in Porous Media* 130.1 (Oct. 1, 2019), pp. 305–335. DOI: 10.1007/s11242-018-1201-4.

[13] *Assessment of the CO2 Storage Potential in Europe (CO2Stop) - European Commission*. URL: https://energy.ec.europa.eu/publications/assessment-co2-storage-potential-europe-co2stop_en.

[14] *Atomic force microscopy*. In: *Wikipedia*. May 22, 2025.

[15] P. Aussillous and D. Quéré. “Quick deposition of a fluid on the wall of a tube”. In: *Physics of Fluids* 12.10 (Oct. 2000), pp. 2367–2371. DOI: 10.1063/1.1289396.

[16] B.Metz, O.Davidson, H. Coninck, M.Loos, and L.Meyer. *Carbon Dioxide Capture and Storage — IPCC*. 2005. URL: https://www.ipcc.ch/report/carbon-dioxide-capture-and-storage/.

[17] S. Bachu, D. Bonijoly, J. Bradshaw, R. Burruss, S. Holloway, N. P. Christensen, and O. M. Mathiassen. “CO2 storage capacity estimation: Methodology and gaps”. In: *International Journal of Greenhouse Gas Control* 1.4 (Oct. 1, 2007), pp. 430–443. DOI: 10.1016/S1750-5836(07)00086-2.

[18] J.-C. Bacri, M. Chaouche, and D. Salin. “Modèle simple de perméabilités relatives croisées. (Modelling cross relative permeabilities)”. In: *Comptes Rendus de l’Académie des Sciences. Série II* 311 (Jan. 1, 1990).

[19] G. Balestra, L. Zhu, and F. Gallaire. “Viscous Taylor droplets in axisymmetric and planar tubes: from Bretherton’s theory to empirical models”. In: *Microfluidics and Nanofluidics* 22.6 (June 12, 2018), p. 67. DOI: 10.1007/s10404-018-2084-y.

[20] U. C. Bandara, A. M. Tartakovsky, and B. J. Palmer. “Pore-scale study of capillary trapping mechanism during CO2 injection in geological formations”. In: *International Journal of Greenhouse Gas Control* 5.6 (Nov. 1, 2011), pp. 1566–1577. DOI: 10.1016/j.ijggc.2011.08.014.

[21] D. Bartolo, G. Degré, P. Nghe, and V. Studer. “Microfluidic stickers”. In: *Lab on a Chip* 8.2 (Jan. 29, 2008), pp. 274–279. DOI: 10.1039/B712368J.

[22] E. Ben-Jacob and P. Garik. “The formation of patterns in non-equilibrium growth”. en. In: *Nature* 343.6258 (Feb. 1990), pp. 523–530. DOI: 10.1038/343523a0.

[23] Y. Berdichevsky, J. Khandurina, A. Guttman, and Y. .-. Lo. “UV/ozone modification of poly(dimethylsiloxane) microfluidic channels”. In: *Sensors and Actuators B: Chemical* 97.2 (Feb. 1, 2004), pp. 402–408. DOI: 10.1016/j.snb.2003.09.022.

[24] S. Berg, H. Ott, S. A. Klapp, A. Schwing, R. Neiteler, N. Brussee, A. Makurat, L. Leu, F. Enzmann, J.-O. Schwarz, M. Kersten, S. Irvine, and M. Stampanoni. “Real-time 3D imaging of Haines jumps in porous media flow”. In: *Proceedings of the National Academy of Sciences* 110.10 (Mar. 5, 2013), pp. 3755–3759. DOI: 10.1073/pnas.1221373110.

[25] N. Bernard, C. Soulaine, and S. Roman. “Impact of wetting films on the stability of two-phase flow in porous media: A pore-doublet perspective”. In: *Advances in Water Resources* 204 (Oct. 1, 2025), p. 105060. DOI: 10.1016/j.advwatres.2025.105060.

[26] G. Binnig, C. F. Quate, and C. Gerber. “Atomic force microscope”. In: *Physical review letters* 56.9 (Mar. 1, 1986), pp. 930–933. DOI: 10.1103/physrevlett.56.930.

[27] M. J. Blunt. “Flow in porous media — pore-network models and multiphase flow”. In: *Current Opinion in Colloid & Interface Science* 6.3 (June 1, 2001), pp. 197–207. DOI: 10.1016/S1359-0294(01)00084-X.

[28] M. J. Blunt. *Multiphase Flow in Permeable Media: A Pore-Scale Perspective*. Cambridge: Cambridge University Press, 2017. DOI: 10.1017/9781316145098.

[29] M. J. Blunt, B. Bijeljic, H. Dong, O. Gharbi, S. Iglauer, P. Mostaghimi, A. Paluszny, and C. Pentland. “Pore-scale imaging and modelling”. In: *Advances in Water Resources*. 35th Year Anniversary Issue 51 (Jan. 1, 2013), pp. 197–216. DOI: 10.1016/j.advwatres.2012.03.003.

[30] F. P. Bretherton. “The motion of long bubbles in tubes”. In: *Journal of Fluid Mechanics* 10.2 (Mar. 1961), pp. 166–188. DOI: 10.1017/S0022112061000160.

[31] D. Broseta, N. Tonnet, and V. Shah. “Are rocks still water-wet in the presence of dense CO2 or H2S?” In: *Geofluids* 12.4 (2012), pp. 280–294. DOI: 10.1111/j.1468-8123.2012.00369.x.

[32] S. Budinis, S. Krevor, N. Mac Dowell, N. Brandon, and A. Hawkes. “An assessment of CCS costs, barriers and potential”. In: *ENERGY STRATEGY REVIEWS* 22 (2018), p. 61.

[33] S. C. Cao, S. Dai, and J. Jung. “Supercritical CO2 and brine displacement in geological carbon sequestration: Micromodel and pore network simulation studies”. In: *International Journal of Greenhouse Gas Control* 44 (Jan. 1, 2016), pp. 104–114. DOI: 10.1016/j.ijggc.2015.11.026.

[34] A. B. D. Cassie and S. Baxter. “Wettability of porous surfaces”. In: *Transactions of the Faraday Society* 40.0 (Jan. 1, 1944), pp. 546–551. DOI: 10.1039/TF9444000546.

[35] J. A. d. Chalendar, C. Garing, and S. M. Benson. “Pore-scale modelling of Ostwald ripening”. In: *Journal of Fluid Mechanics* 835 (Jan. 2018), pp. 363–392. DOI: 10.1017/jfm.2017.720.

[36] C. Chang, Q. Zhou, T. J. Kneafsey, M. Oostrom, and Y. Ju. “Coupled supercritical CO2 dissolution and water flow in pore-scale micromodels”. In: *Advances in Water Resources* 123 (Jan. 1, 2019), pp. 54–69. DOI: 10.1016/j.advwatres.2018.11.004.

[37] I. Chatzis and F. A. L. Dullien. “Dynamic immiscible displacement mechanisms in pore doublets: Theory versus experiment”. In: *Journal of Colloid and Interface Science* 91.1 (Jan. 1, 1983), pp. 199–222. DOI: 10.1016/0021-9797(83)90326-0.

[38] I. Chatzis, N. R. Morrow, and H. T. Lim. “Magnitude and Detailed Structure of Residual Oil Saturation”. In: *Society of Petroleum Engineers Journal* 23.2 (Apr. 1, 1983), pp. 311–326. DOI: 10.2118/10681-PA.

[39] Y.-F. Chen, S. Fang, D.-S. Wu, and R. Hu. “Visualizing and quantifying the crossover from capillary fingering to viscous fingering in a rough fracture”. In: *Water Resources Research* 53.9 (2017), pp. 7756–7772. DOI: 10.1002/2017WR021051.

[40] Y.-F. Chen, D.-S. Wu, S. Fang, and R. Hu. "Experimental study on two-phase flow in rough fracture: Phase diagram and localized flow channel". In: *International Journal of Heat and Mass Transfer* 122 (July 1, 2018), pp. 1298–1307. DOI: 10.1016/j.ijheatmasstransfer.2018.02.031.

[41] K. Chen, P. Liu, W. Wang, Y. Chen, and B. Bate. "Effects of Capillary and Viscous Forces on Two-Phase Fluid Displacement in the Microfluidic Model". In: *Energy & Fuels* 37.22 (Nov. 16, 2023), pp. 17263–17276. DOI: 10.1021/acs.energyfuels.3c03170.

[42] P. Chiquet, D. Broseta, and S. Thibeau. "Wettability alteration of caprock minerals by carbon dioxide". In: *Geofluids* 7.2 (2007), pp. 112–122. DOI: 10.1111/j.1468-8123.2007.00168.x.

[43] R. Chuoke, P. van Meurs, and C. van der Poel. "The Instability of Slow, Immiscible, Viscous Liquid-Liquid Displacements in Permeable Media". In: *Transactions of the AIME* 216.1 (Dec. 1, 1959), pp. 188–194. DOI: 10.2118/1141-G.

[44] R. Combescot, V. Hakim, T. Dombre, Y. Pomeau, and A. Pumir. "Analytic theory of the Saffman-Taylor fingers". In: *Physical Review A* 37.4 (Feb. 1988), pp. 1270–1283. DOI: 10.1103/PhysRevA.37.1270.

[45] C. Cottin, H. Bodiguel, and A. Colin. "Drainage in two-dimensional porous media: From capillary fingering to viscous flow". In: *Physical Review E* 82.4 (Oct. 28, 2010), p. 046315. DOI: 10.1103/PhysRevE.82.046315.

[46] P. Coussot. "Progress in rheology and hydrodynamics allowed by NMR or MRI techniques". In: *Experiments in Fluids* 61.9 (Sept. 2, 2020), p. 207. DOI: 10.1007/s00348-020-03037-y.

[47] R. G. Cox. "The dynamics of the spreading of liquids on a solid surface. Part 1. Viscous flow". In: *Journal of Fluid Mechanics* 168 (July 1986), pp. 169–194. DOI: 10.1017/S0022112086000332.

[48] *Curvature*. In: *Wikipedia*. July 6, 2025.

[49] M. Danis and C. Jacquin. "Influence du contraste de viscosités sur les perméabilités relatives lors du drainage. Expérimentation et modélisation". In: *Revue de l'Institut Français du Pétrole* 38.6 (Nov. 1, 1983), pp. 723–733. DOI: 10.2516/ogst:1983044.

[50] H. Darcy. *Les fontaines publiques de la ville de Dijon: exposition et application des principes à suivre et des formules à employer dans les questions de distribution d'eau*. Victor Dalmont, 1856. 664 pp.

[51] P. G. De Gennes. "Wetting: statics and dynamics". In: *Reviews of Modern Physics* 57.3 (July 1, 1985), pp. 827–863. DOI: 10.1103/RevModPhys.57.827.

[52] M. Delshad, G. A. Pope, and K. Sepehrnoori. "A compositional simulator for modeling surfactant enhanced aquifer remediation, 1 formulation". In: *Journal of Contaminant Hydrology* 23.4 (Aug. 1, 1996), pp. 303–327. DOI: 10.1016/0169-7722(95)00106-9.

[53] W. Deng, M. B. Cardenas, and P. C. Bennett. "Extended Roof snap-off for a continuous nonwetting fluid and an example case for supercritical CO2". In: *Advances in Water Resources* 64 (Feb. 1, 2014), pp. 34–46. DOI: 10.1016/j.advwatres.2013.12.001.

[54] J. R. Dormand and P. J. Prince. "A family of embedded Runge-Kutta formulae". In: *Journal of Computational and Applied Mathematics* 6.1 (Mar. 1, 1980), pp. 19–26. DOI: 10.1016/0771-050X(80)90013-3.

[55] Y. Dou, F. Li, B. Tang, and G. Zhou. "Surface Wettability Tuning of Acrylic Resin Photoresist and Its Aging Performance". In: *Sensors* 21.14 (Jan. 2021), p. 4866. DOI: 10.3390/s21144866.

[56] F. A. L. Dullien, F. S. Y. Lai, and I. F. MacDonald. "Hydraulic continuity of residual wetting phase in porous media". In: *Journal of Colloid and Interface Science* 109.1 (Jan. 1, 1986), pp. 201–218. DOI: 10.1016/0021-9797(86)90295-X.

[57] F. A. L. Dullien. *Porous Media: Fluid Transport and Pore Structure*. Academic Press, Dec. 2, 2012. 598 pp.

[58] F. A. L. Dullien. "Two-phase flow in porous media". In: *Chemical Engineering & Technology* 11.1 (1988), pp. 407–424. DOI: 10.1002/ceat.270110153.

[59] W. A. Ebert and E. M. Sparrow. "Slip Flow in Rectangular and Annular Ducts". In: *Journal of Basic Engineering* 87.4 (Dec. 1, 1965), pp. 1018–1024. DOI: 10.1115/1.3650793.

[60] R. Edgeworth, B. J. Dalton, and T. Parnell. "The pitch drop experiment". In: *European Journal of Physics* 5.4 (Oct. 1, 1984), p. 198. DOI: 10.1088/0143-0807/5/4/003.

[61] R. Ehrlich. "Viscous coupling in two-phase flow in porous media and its effect on relative permeabilities". In: *Transport in Porous Media* 11.3 (June 1993), pp. 201–218. DOI: 10.1007/BF00614812.

[62] R. Ehrlich and F. Crane. "A Model for Two-Phase Flow in Consolidated Materials". In: *Society of Petroleum Engineers Journal* 9.2 (June 1, 1969), pp. 221–231. DOI: 10.2118/2231-PA.

[63] *Estimation des capacités de stockage géologique de CO2 en France métropolitaine*. La librairie ADEME. URL: https://librairie.ademe.fr/industrie-et-production-durable/7966-estimation-des-capacites-de-stockage-geologique-de-co2-en-france-metropolitaine.html.

[64] R. Farokhpoor, B. J. A. Bjørkvik, E. Lindeberg, and O. Torsæter. "CO2 Wettability Behavior During CO2 Sequestration in Saline Aquifer -An Experimental Study on Minerals Representing Sandstone and Carbonate". In: *Energy Procedia*. GHGT-11 Proceedings of the 11th International Conference on Greenhouse Gas Control Technologies, 18-22 November 2012, Kyoto, Japan 37 (Jan. 1, 2013), pp. 5339–5351. DOI: 10.1016/j.egypro.2013.06.452.

[65] R. Farokhpoor, B. J. A. Bjørkvik, E. Lindeberg, and O. Torsæter. "Wettability behaviour of CO2 at storage conditions". In: *International Journal of Greenhouse Gas Control* 12 (Jan. 1, 2013), pp. 18–25. DOI: 10.1016/j.ijggc.2012.11.003.

[66] A. Ferrari and I. Lunati. "Inertial effects during irreversible meniscus reconfiguration in angular pores". In: *Advances in Water Resources* 74 (Dec. 1, 2014), pp. 1–13. DOI: 10.1016/j.advwatres.2014.07.009.

[67] C. Garing, J. A. de Chalendar, M. Voltolini, J. B. Ajo-Franklin, and S. M. Benson. "Pore-scale capillary pressure analysis using multi-scale X-ray micromotography". In: *Advances in Water Resources* 104 (June 1, 2017), pp. 223–241. DOI: 10.1016/j.advwatres.2017.04.006.

[68] S. R. Gislason and E. H. Oelkers. "Carbon Storage in Basalt". In: *Science* 344.6182 (Apr. 25, 2014), pp. 373–374. DOI: 10.1126/science.1250828.

[69] S. R. Gíslason, H. Sigurdardóttir, E. S. Aradóttir, and E. H. Oelkers. "A brief history of CarbFix: Challenges and victories of the project's pilot phase". In: *Energy Procedia*. Carbon in natural and engineered processes: Selected contributions from the 2018 International Carbon Conference 146 (July 1, 2018), pp. 103–114. DOI: 10.1016/j.egypro.2018.07.014.

[70] L. M. Giudici, A. Qaseminejad Raeini, M. J. Blunt, and B. Bijeljic. "Representation of Fully Three-Dimensional Interfacial Curvature in Pore-Network Models". In: *Water Resources Research* 59.4 (2023), e2022WR033983. DOI: 10.1029/2022WR033983.

[71] D. Gomez, I. Goenaga, I. Lizuain, and M. Ozaita. "Femtosecond laser ablation for microfluidics". In: *Optical Engineering* 44.5 (May 2005), p. 051105. DOI: 10.1117/1.1902783.

[72] W. Gong, Y. Liu, W. Lei, Y. Ju, and M. Wang. "Viscous coupling effect on hydraulic conductance in a square capillary tube". In: *Advances in Water Resources* (Nov. 3, 2023), p. 104568. DOI: 10.1016/j.advwatres.2023.104568.

[73] V. Gredicak, C. Douat, A. Slodczyk, S. Dozias, and S. Roman. "Wettability alteration of closed glass microfluidic devices by in situ plasma". In: *Microfluidics and Nanofluidics* 29.4 (Mar. 21, 2025), p. 22. DOI: 10.1007/s10404-025-02793-9.

[74] W. B. Haines. "Studies in the physical properties of soil. V. The hysteresis effect in capillary properties, and the modes of moisture distribution associated therewith". In: *The Journal of Agricultural Science* 20.1 (Jan. 1930), pp. 97–116. DOI: 10.1017/S002185960008864X.

[75] S. Herminghaus. "Roughness-induced non-wetting". In: *Europhysics Letters* 52.2 (Oct. 15, 2000), p. 165. DOI: 10.1209/ep1/i2000-00418-8.

[76] A. L. Herring, L. Andersson, and D. Wildenschild. "Enhancing residual trapping of supercritical CO2 via cyclic injections". In: *Geophysical Research Letters* 43.18 (2016), pp. 9677–9685. DOI: 10.1002/2016GL070304.

[77] A. L. Herring, E. J. Harper, L. Andersson, A. Sheppard, B. K. Bay, and D. Wildenschild. "Effect of fluid topology on residual nonwetting phase trapping: Implications for geologic CO2 sequestration". In: *Advances in Water Resources* 62 (Dec. 1, 2013), pp. 47–58. DOI: 10.1016/j.advwatres.2013.09.015.

[78] M. A. Hesse, F. M. O. Jr, and H. A. Tchelepi. "Gravity currents with residual trapping". In: *Journal of Fluid Mechanics* 611 (Sept. 2008), pp. 35–60. DOI: 10.1017/S002211200800219X.

[79] M. H. Holtz. "Residual Gas Saturation to Aquifer Influx: A Calculation Method for 3-D Computer Reservoir Model Construction". In: SPE Gas Technology Symposium. OnePetro, Apr. 30, 2002. DOI: 10.2118/75502-MS.

[80] T. T. Al-Housseiny, J. Hernandez, and H. A. Stone. "Preferential flow penetration in a network of identical channels". In: *Physics of Fluids* 26.4 (Apr. 29, 2014), p. 042110. DOI: 10.1063/1.4872275.

[81] T. T. Al-Housseiny and H. A. Stone. "Controlling viscous fingering in tapered Hele-Shaw cells". In: *Physics of Fluids* 25.9 (2013).

[82] R. Hu, J. Wan, Y. Kim, and T. K. Tokunaga. "Wettability impact on supercritical CO2 capillary trapping: Pore-scale visualization and quantification". In: *Water Resources Research* 53.8 (2017), pp. 6377–6394. DOI: 10.1002/2017WR020721.

[83] Y. Hu and Y.-S. Jun. "Biotite Dissolution in Brine at Varied Temperatures and CO2 Pressures: Its Activation Energy and Potential CO2 Intercalation". In: *Langmuir* 28.41 (Oct. 16, 2012), pp. 14633–14641. DOI: 10.1021/la3028995.

[84] H. Huang and X.-y. Lu. "Relative permeabilities and coupling effects in steady-state gas-liquid flow in porous media: A lattice Boltzmann study". In: *Physics of Fluids* 21.9 (Sept. 10, 2009), p. 092104. DOI: 10.1063/1.3225144.

[85] C. Huh and L. E. Scriven. “Hydrodynamic model of steady movement of a solid/liquid/fluid contact line”. In: *Journal of Colloid and Interface Science* 35.1 (Jan. 1, 1971), pp. 85–101. DOI: 10.1016/0021-9797(71)90188-3.

[86] L.-H. Hung, R. Lin, and A. P. Lee. “Rapid microfabrication of solvent-resistant biocompatible microfluidic devices”. In: *Lab on a Chip* 8.6 (May 21, 2008), pp. 983–987. DOI: 10.1039/B717710K.

[87] S. Iglauer, C. H. Pentland, and A. Busch. “CO2 wettability of seal and reservoir rocks and the implications for carbon geo-sequestration”. In: *Water Resources Research* 51.1 (2015), pp. 729–774. DOI: 10.1002/2014WR015553.

[88] S. Iglauer, A. Salamah, M. Sarmadivaleh, K. Liu, and C. Phan. “Contamination of silica surfaces: Impact on water–CO2–quartz and glass contact angle measurements”. In: *International Journal of Greenhouse Gas Control* 22 (Mar. 1, 2014), pp. 325–328. DOI: 10.1016/j.ijggc.2014.01.006.

[89] A. Irannezhad, B. K. Primkulov, R. Juanes, and B. Zhao. “Fluid-fluid displacement in mixed-wet porous media”. In: *Physical Review Fluids* 8.1 (Jan. 11, 2023), p. L012301. DOI: 10.1103/PhysRevFluids.8.L012301.

[90] K. L. J. “The permeability of porous media to liquids and gases”. In: *Am. Petrol. Inst., Drilling and Production Practice* 2 (1941), pp. 200–213.

[91] M. D. Jackson, D. Al-Mahrouqi, and J. Vinogradov. “Zeta potential in oil-water-carbonate systems and its impact on oil recovery during controlled salinity water-flooding”. In: *Scientific Reports* 6.1 (Nov. 23, 2016), p. 37363. DOI: 10.1038/srep37363.

[92] J.-W. Jung and J. Wan. “Supercritical CO2 and Ionic Strength Effects on Wettability of Silica Surfaces: Equilibrium Contact Angle Measurements”. In: *Energy & Fuels* 26.9 (Sept. 20, 2012), pp. 6053–6059. DOI: 10.1021/ef300913t.

[93] L. P. Kadanoff. “Simulating hydrodynamics: A pedestrian model”. en. In: *Journal of Statistical Physics* 39.3 (May 1985), pp. 267–283. DOI: 10.1007/BF01018663.

[94] F. Kalaydjian. “Origin and quantification of coupling between relative permeabilities for two-phase flows in porous media”. In: *Transport in Porous Media* 5.3 (June 1, 1990), pp. 215–229. DOI: 10.1007/BF00140013.

[95] N. K. Karadimitriou, M. Musterd, P. J. Kleingeld, M. T. Kreutzer, S. M. Hassanizadeh, and V. Joekar-Niasar. “On the fabrication of PDMS micromodels by rapid prototyping, and their use in two-phase flow studies”. In: *Water Resources Research* 49.4 (2013), pp. 2056–2067. DOI: 10.1002/wrcr.20196.

[96] O. Karoussi, L. L. Skovbjerg, T. Hassenkam, S. L. S. Stipp, and A. A. Hamouda. “AFM study of calcite surface exposed to stearic and heptanoic acids”. In: *Colloids and Surfaces A: Physicochemical and Engineering Aspects* 325.3 (Aug. 1, 2008), pp. 107–114. DOI: 10.1016/j.colsurfa.2008.04.039.

[97] P. Kelemen, S. M. Benson, H. Pilorgé, P. Psarras, and J. Wilcox. “An Overview of the Status and Challenges of CO2 Storage in Minerals and Geological Formations”. In: *Frontiers in Climate* 1 (Nov. 15, 2019). DOI: 10.3389/fclim.2019.00009.

[98] Y. Kim, J. Wan, T. J. Kneafsey, and T. K. Tokunaga. “Dewetting of Silica Surfaces upon Reactions with Supercritical CO2 and Brine: Pore-Scale Studies in Micromodels”. In: *Environmental Science & Technology* 46.7 (Apr. 3, 2012), pp. 4228–4235. DOI: 10.1021/es204096w.

[99] S. C. M. Krevor, R. Pini, L. Zuo, and S. M. Benson. “Relative permeability and trapping of CO2 and water in sandstone rocks at reservoir conditions”. In: *Water Resources Research* 48.2 (2012). DOI: 10.1029/2011WR010859.

[100] S. Kumar, J. Foroozesh, K. Edlmann, M. G. Rezk, and C. Y. Lim. "A comprehensive review of value-added CO2 sequestration in subsurface saline aquifers". In: *Journal of Natural Gas Science and Engineering* 81 (Sept. 1, 2020), p. 103437. DOI: 10.1016/j.jngse.2020.103437.

[101] B. Lagree. "Modelling of two-phase flow in porous media with volume-of-fluid method". PhD thesis. Université Pierre et Marie Curie - Paris VI, Sept. 17, 2014.

[102] C.-Y. Lai, M. Cozzolino, M. V. Diamanti, S. Al Hassan, and M. Chiesa. "Underlying Mechanism of Time Dependent Surface Properties of Calcite (CaCO3): A Baseline for Investigations of Reservoirs Wettability". In: *The Journal of Physical Chemistry C* 119.52 (Dec. 31, 2015), pp. 29038–29043. DOI: 10.1021/acs.jpcc.5b10595.

[103] T. Lan, R. Hu*, and B. Zhao*. "Impact of pore-scale corner and film flows on macroscopic transport in porous media". In: *Capillarity* 16.1 (June 2, 2025), pp. 1–4.

[104] J. S. Langer. "Dendrites, Viscous Fingers, and the Theory of Pattern Formation". In: *Science* 243.4895 (Mar. 1989), pp. 1150–1156. DOI: 10.1126/science.243.4895.1150.

[105] J. S. Langer. "Instabilities and pattern formation in crystal growth". In: *Reviews of Modern Physics* 52.1 (Jan. 1980), pp. 1–28. DOI: 10.1103/RevModPhys.52.1.

[106] J. N. Lee, C. Park, and G. M. Whitesides. "Solvent Compatibility of Poly(dimethylsiloxane)-Based Microfluidic Devices". In: *Analytical Chemistry* 75.23 (Dec. 1, 2003), pp. 6544–6554. DOI: 10.1021/ac0346712.

[107] R. Lenormand. "Liquids in porous media". In: *Journal of Physics: Condensed Matter* 2 (S Dec. 1990), SA79. DOI: 10.1088/0953-8984/2/S/008.

[108] R. Lenormand, C. Zarcone, and A. Sarr. "Mechanisms of the displacement of one fluid by another in a network of capillary ducts". In: *Journal of Fluid Mechanics* 135 (Oct. 1983), pp. 337–353. DOI: 10.1017/S0022112083003110.

[109] R. Lenormand, E. Touboul, and C. Zarcone. "Numerical models and experiments on immiscible displacements in porous media". In: *Journal of Fluid Mechanics* 189 (Apr. 1988), pp. 165–187. DOI: 10.1017/S0022112088000953.

[110] R. Lenormand and C. Zarcone. "Invasion Percolation in an Etched Network: Measurement of a Fractal Dimension". In: *Physical Review Letters* 54.20 (May 20, 1985), pp. 2226–2229. DOI: 10.1103/PhysRevLett.54.2226.

[111] M. Leverett. "Capillary Behavior in Porous Solids". In: *Transactions of the AIME* 142.1 (Dec. 1, 1941), pp. 152–169. DOI: 10.2118/941152-G.

[112] B. Li and S. M. Benson. "Influence of small-scale heterogeneity on upward CO2 plume migration in storage aquifers". In: *Advances in Water Resources* 83 (Sept. 1, 2015), pp. 389–404. DOI: 10.1016/j.advwatres.2015.07.010.

[113] H. Li, C. Pan, and C. T. Miller. "Pore-scale investigation of viscous coupling effects for two-phase flow in porous media". In: *Physical Review E* 72.2 (Aug. 29, 2005), p. 026705. DOI: 10.1103/PhysRevE.72.026705.

[114] Y. Li, G. Blois, F. Kazemifar, and K. T. Christensen. "High-Speed Quantification of Pore-Scale Multiphase Flow of Water and Supercritical CO2 in 2-D Heterogeneous Porous Micromodels: Flow Regimes and Interface Dynamics". In: *Water Resources Research* 55.5 (2019), pp. 3758–3779. DOI: 10.1029/2018WR024635.

[115] Y. Li, G. Blois, F. Kazemifar, R. S. Molla, and K. T. Christensen. "Pore-Scale Dynamics of Liquid CO2–Water Displacement in 2D Axisymmetric Porous Micromodels Under Strong Drainage and Weak Imbibition Conditions: High-Speed PIV Measurements". In: *Frontiers in Water* 3 (Aug. 16, 2021). DOI: 10.3389/frwa.2021.710370.

[116] S. Liang. "Random-walk simulations of flow in Hele Shaw cells". In: *Physical Review A* 33.4 (Apr. 1986), pp. 2663–2674. DOI: 10.1103/PhysRevA.33.2663.

[117] Y. Liang, D. R. Baer, J. M. McCoy, J. E. Amonette, and J. P. Lafemina. "Dissolution kinetics at the calcite-water interface". In: *Geochimica et Cosmochimica Acta* 60.23 (Dec. 1, 1996), pp. 4883–4887. DOI: 10.1016/S0016-7037(96)00337-7.

[118] L. Liu, B.-M. Zhang, D.-F. Wang, and Z.-J. Wu. "Effects of cure cycles on void content and mechanical properties of composite laminates". In: *Composite Structures* 73.3 (June 1, 2006), pp. 303–309. DOI: 10.1016/j.compstruct.2005.02.001.

[119] *Loi de Jurin*. In: *Wikipédia*. Nov. 29, 2022.

[120] Y. Lu, R. Tian, W. Liu, J. Tang, H. Li, X. Chen, and X. Sun. "Mechanisms of shale water wettability alteration with chemical groups after CO2 injection: Implication for shale gas recovery and CO2 geo-storage". In: *Journal of Natural Gas Science and Engineering* 90 (June 1, 2021), p. 103922. DOI: 10.1016/j.jngse.2021.103922.

[121] T. S. Lundström, L. H. Gustavsson, N. Jēkabsons, and A. Jakovics. "Wetting dynamics in multiscale porous media. Porous pore-doublet model, experiment and theory". In: *AIChE Journal* 54.2 (2008), pp. 372–380. DOI: 10.1002/aic.11387.

[122] M. Lysyy, G. Ersland, and M. Fernø. "Pore-scale dynamics for underground porous media hydrogen storage". In: *Advances in Water Resources* 163 (May 1, 2022), p. 104167. DOI: 10.1016/j.advwatres.2022.104167.

[123] J. Maes and S. Geiger. "Direct pore-scale reactive transport modelling of dynamic wettability changes induced by surface complexation". In: *Advances in Water Resources* 111 (Jan. 1, 2018), pp. 6–19. DOI: 10.1016/j.advwatres.2017.10.032.

[124] R. M. El-Maghraby and M. J. Blunt. "Residual CO2 Trapping in Indiana Limestone". In: *Environmental Science & Technology* 47.1 (Jan. 2, 2013), pp. 227–233. DOI: 10.1021/es304166u.

[125] M. Magnini, F. Municchi, I. El Mellas, and M. Icardi. "Liquid film distribution around long gas bubbles propagating in rectangular capillaries". In: *International Journal of Multiphase Flow* 148 (Mar. 1, 2022), p. 103939. DOI: 10.1016/j.ijmultiphaseflow.2021.103939.

[126] L. Makkonen. "A thermodynamic model of contact angle hysteresis". In: *The Journal of Chemical Physics* 147.6 (Aug. 11, 2017), p. 064703. DOI: 10.1063/1.4996912.

[127] S. A. Mansoori, S. Iglauer, C. H. Pentland, B. Bijeljic, and M. J. Blunt. "Measurements of Non-Wetting Phase Trapping Applied to Carbon Dioxide Storage". In: *Energy Procedia*. Greenhouse Gas Control Technologies 9 1.1 (Feb. 1, 2009), pp. 3173–3180. DOI: 10.1016/j.egypro.2009.02.100.

[128] M. Mansouri-Boroujeni. "A microfluidic study of the physical and chemical mechanisms induced by CO2 injection in deep saline aquifers". These de doctorat. Orléans, May 12, 2022.

[129] M. Mansouri-Boroujeni, C. Soulaine, M. Azaroual, and S. Roman. “How interfacial dynamics controls drainage pore-invasion patterns in porous media”. In: *Advances in Water Resources* 171 (Jan. 1, 2023), p. 104353. DOI: 10.1016/j.advwatres.2022.104353.

[130] C. C. Mattax and J. R. Kyte. “Ever see a water flood”. In: *Oil Gas J* 59.42 (1961), pp. 115–128.

[131] L. Maya Fogouang. “Transport of fine particles. Application to injectivity in geothermal reservoirs”. These de doctorat. Orléans, Oct. 14, 2024.

[132] A. Mazzoldi and T. Hill. “CO2 transportation for carbon capture and storage: Sublimation of carbon dioxide from a dry ice bank”. In: *International Journal of Greenhouse Gas Control* 2 (Apr. 1, 2008), pp. 210–218. DOI: 10.1016/S1750-5836(07)00118-1.

[133] J. W. McLEAN and P. G. Saffman. “The effect of surface tension on the shape of fingers in a Hele Shaw cell”. In: *Dynamics of Curved Fronts*. Ed. by P. Pelcé. San Diego: Academic Press, Jan. 1988, pp. 175–189. DOI: 10.1016/B978-0-08-092523-3.50018-6.

[134] J. C. Melrose. “Characterization of Petroleum Reservoir Rocks by Capillary Pressure Techniques”. In: *Studies in Surface Science and Catalysis*. Ed. by K. K. Unger, J. Rouquerol, K. S. W. Sing, and H. Kral. Vol. 39. Characterization of Porous Solids. Elsevier, Jan. 1, 1988, pp. 253–261. DOI: 10.1016/S0167-2991(09)60749-7.

[135] F. Moebius and D. Or. “Inertial forces affect fluid front displacement dynamics in a pore-throat network model”. In: *Physical Review E* 90.2 (Aug. 28, 2014), p. 023019. DOI: 10.1103/PhysRevE.90.023019.

[136] F. Moebius and D. Or. “Interfacial jumps and pressure bursts during fluid displacement in interacting irregular capillaries”. In: *Journal of Colloid and Interface Science* 377.1 (July 1, 2012), pp. 406–415. DOI: 10.1016/j.jcis.2012.03.070.

[137] *Molecular dynamics*. In: *Wikipedia*. July 30, 2025.

[138] T. F. Moore and R. L. Slobod. “Displacement of Oil by Water-Effect of Wettability, Rate, and Viscosity on Recovery”. In: Fall Meeting of the Petroleum Branch of AIME. OnePetro, Oct. 2, 1955. DOI: 10.2118/502-G.

[139] N. R. Morrow. *Physics and Thermodynamics of Capillary Action in Porous Media*. ACS Publications. June 1, 1970. DOI: 10.1021/ie50726a006. URL: https://pubs.acs.org/doi/pdf/10.1021/ie50726a006.

[140] M. Muskat. “The Flow of Fluids Through Porous Media”. In: *Journal of Applied Physics* 8.4 (Apr. 1, 1937), pp. 274–282. DOI: 10.1063/1.1710292.

[141] M. Muskat and M. W. Meres. “The Flow of Heterogeneous Fluids Through Porous Media”. In: *Physics* 7.9 (Sept. 1, 1936), pp. 346–363. DOI: 10.1063/1.1745403.

[142] *Non-Newtonian fluid*. In: *Wikipedia*. July 21, 2025.

[143] J. M. Nordbotten, M. A. Celia, and S. Bachu. “Injection and Storage of CO2 in Deep Saline Aquifers: Analytical Solution for CO2 Plume Evolution During Injection”. In: *Transport in Porous Media* 58.3 (Mar. 1, 2005), pp. 339–360. DOI: 10.1007/s11242-004-0670-9.

[144] J. M. Nordbotten, M. A. Celia, S. Bachu, and H. K. Dahle. “Semianalytical Solution for CO2 Leakage through an Abandoned Well”. In: *Environmental Science & Technology* 39.2 (Jan. 1, 2005), pp. 602–611. DOI: 10.1021/es035338i.

[145] M. Norouzisadeh, P. Leroy, and C. Soulaine. "A lubrication model with slope-dependent disjoining pressure for modeling wettability alteration". In: *Computer Physics Communications* 298 (May 1, 2024), p. 109114. DOI: 10.1016/j.cpc.2024.109114.

[146] A. Odeh. "Effect of Viscosity Ratio on Relative Permeability (includes associated paper 1496-G)". In: *Transactions of the AIME* 216.1 (Dec. 1, 1959), pp. 346–353. DOI: 10.2118/1189-G.

[147] N. OTSU. "A THRESHOLD SELECTION METHOD FROM GRAY-LEVEL HISTOGRAMS". In: *A THRESHOLD SELECTION METHOD FROM GRAY-LEVEL HISTOGRAMS* (1979).

[148] S. Pasquier, M. Quintard, and Y. Davit. "Modeling flow in porous media with rough surfaces: Effective slip boundary conditions and application to structured packings". In: *Chemical Engineering Science* 165 (June 29, 2017), pp. 131–146. DOI: 10.1016/j.ces.2017.01.063.

[149] *PDMS Microfluidics Fabrication | Nano- and Microscale Fabrication and Characterization*. URL: https://cleanroom.soe.ucsc.edu/microfluidics (visited on 09/14/2025).

[150] J. K. Pearce, G. K. W. Dawson, A. C. K. Law, D. Biddle, and S. D. Golding. "Reactivity of micas and cap-rock in wet supercritical CO2 with SO2 and O2 at CO2 storage conditions". In: *Applied Geochemistry* 72 (Sept. 1, 2016), pp. 59–76. DOI: 10.1016/j.apgeochem.2016.06.010.

[151] T. D. Perry, R. T. Cygan, and R. Mitchell. "Molecular models of a hydrated calcite mineral surface". In: *Geochimica et Cosmochimica Acta* 71.24 (Dec. 15, 2007), pp. 5876–5887. DOI: 10.1016/j.gca.2007.08.030.

[152] E. J. Peters and D. L. Flock. "The Onset of Instability During Two-Phase Immiscible Displacement in Porous Media". In: *Society of Petroleum Engineers Journal* 21.2 (Apr. 1, 1981), pp. 249–258. DOI: 10.2118/8371-PA.

[153] D. Picchi and I. Battiato. "The Impact of Pore-Scale Flow Regimes on Upscaling of Immiscible Two-Phase Flow in Porous Media". In: *Water Resources Research* 54.9 (2018), pp. 6683–6707. DOI: 10.1029/2018WR023172.

[154] *Pitch drop experiment*. In: *Wikipedia*. July 30, 2025.

[155] S. Protière, M. Z. Bazant, D. A. Weitz, and H. A. Stone. "Droplet breakup in flow past an obstacle: A capillary instability due to permeability variations". In: *Europhysics Letters* 92.5 (Dec. 2010), p. 54002. DOI: 10.1209/0295-5075/92/54002.

[156] D. Quéré. "Wetting and Roughness". In: *Annual Review of Materials Research* 38 (Volume 38, 2008 Aug. 4, 2008), pp. 71–99. DOI: 10.1146/annurev.matsci.38.060407.132434.

[157] A. Rabbani, S. Ayatollahi, R. Kharrat, and N. Dashti. "Estimation of 3-D pore network coordination number of rocks from watershed segmentation of a single 2-D image". In: *Advances in Water Resources* 94 (Aug. 1, 2016), pp. 264–277. DOI: 10.1016/j.advwatres.2016.05.020.

[158] A. Rabbani, S. Jamshidi, and S. Salehi. "An automated simple algorithm for realistic pore network extraction from micro-tomography images". In: *Journal of Petroleum Science and Engineering*. Neural network applications to reservoirs: Physics-based models and data models 123 (Nov. 1, 2014), pp. 164–171. DOI: 10.1016/j.petrol.2014.08.020.

[159] H. S. Rabbani, D. Or, Y. Liu, C.-Y. Lai, N. B. Lu, S. S. Datta, H. A. Stone, and N. Shokri. "Suppressing viscous fingering in structured porous media". In: *Proceedings of the National Academy of Sciences* 115.19 (May 8, 2018), pp. 4833–4838. DOI: 10.1073/pnas.1800729115.

[160] *Raman scattering*. In: *Wikipedia*. Aug. 8, 2025.

[161] T. C. Ransohoff, P. A. Gauglitz, and C. J. Radke. "Snap-off of gas bubbles in smoothly constricted noncircular capillaries". In: *AIChE Journal* 33.5 (1987), pp. 753–765. DOI: 10.1002/aic.690330508.

[162] A. Ratanpara, Y. Li, and M. Kim. "A review of microfluidic approaches for carbon capture and storage research". In: *Lab on a Chip* (2025). DOI: 10.1039/D5LC00208G.

[163] P. Reis, M. Moura, G. Linga, P. A. Rikvold, R. Toussaint, E. G. Flekkøy, and K. J. Måløy. "A simplified pore-scale model for slow drainage including film-flow effects". In: *Advances in Water Resources* 182 (Dec. 1, 2023), p. 104580. DOI: 10.1016/j.advwatres.2023.104580.

[164] F. Rembert, A. Stolz, C. Soulaine, and S. Roman. "A microfluidic chip for geoelectrical monitoring of critical zone processes". In: *Lab on a Chip* 23.15 (2023), pp. 3433–3442. DOI: 10.1039/D3LC00377A.

[165] S. Roman, M. O. Abu-Al-Saud, T. Tokunaga, J. Wan, A. R. Kovscek, and H. A. Tchelepi. "Measurements and simulation of liquid films during drainage displacements and snap-off in constricted capillary tubes". In: *Journal of Colloid and Interface Science* 507 (Dec. 1, 2017), pp. 279–289. DOI: 10.1016/j.jcis.2017.07.092.

[166] S. Roman, S. Lorthois, P. Duru, and F. Risso. "Velocimetry of red blood cells in microvessels by the dual-slit method: Effect of velocity gradients". In: *Microvascular Research* 84.3 (2012), pp. 249–261.

[167] S. Roman, F. Rembert, A. R. Kovscek, and J. Poonoosamy. "Microfluidics for geosciences: metrological developments and future challenges". In: *Lab on a Chip* 25.17 (Aug. 19, 2025), pp. 4273–4289. DOI: 10.1039/D5LC00108K.

[168] S. Roman, C. Soulaine, M. A. AlSaud, A. Kovscek, and H. Tchelepi. "Particle velocimetry analysis of immiscible two-phase flow in micromodels". In: *Advances in Water Resources*. Pore scale modeling and experiments 95 (Sept. 1, 2016), pp. 199–211. DOI: 10.1016/j.advwatres.2015.08.015.

[169] S. Roman, C. Soulaine, and A. R. Kovscek. "Pore-scale visualization and characterization of viscous dissipation in porous media". In: *Journal of Colloid and Interface Science* 558 (Jan. 15, 2020), pp. 269–279. DOI: 10.1016/j.jcis.2019.09.072.

[170] J. Roof. "Snap-Off of Oil Droplets in Water-Wet Pores". In: *Society of Petroleum Engineers Journal* 10.1 (Mar. 1, 1970), pp. 85–90. DOI: 10.2118/2504-PA.

[171] W. Rose. "Myths about later-day extensions of Darcy's law". In: *Journal of Petroleum Science and Engineering* 26.1 (May 1, 2000), pp. 187–198. DOI: 10.1016/S0920-4105(00)00033-4.

[172] W. Rose and W. Bruce. "Evaluation Of Capillary Character In Petroleum Reservoir Rock". In: *Journal of Petroleum Technology* 1.5 (May 1, 1949), pp. 127–142. DOI: 10.2118/949127-G.

[173] W. Rose and P. A. Witherspoon. "Studies of waterflood performance II. Trapping oil in a pore doublet". In: *Circular no.244* (1956).

[174] P. Saffman and G. I. Taylor. "The penetration of a fluid into a porous medium or Hele-Shaw cell containing a more viscous liquid". In: *Proceedings of the Royal Society of London. Series A. Mathematical and Physical Sciences* 245.1242 (June 24, 1958), pp. 312–329. DOI: 10.1098/rspa.1958.0085.

[175] M. Sarmadivaleh, A. Z. Al-Yaseri, and S. Iglauer. "Influence of temperature and pressure on quartz–water–CO2 contact angle and CO2–water interfacial tension". In: *Journal of Colloid and Interface Science* 441 (Mar. 1, 2015), pp. 59–64. DOI: 10.1016/j.jcis.2014.11.010.

[176] J. B. Segur and H. E. Oberstar. "Viscosity of Glycerol and Its Aqueous Solutions". In: *Industrial & Engineering Chemistry* 43.9 (Sept. 1, 1951), pp. 2117–2120. DOI: 10.1021/ie50501a040.

[177] S. A. M. Shaegh, A. Pourmand, M. Nabavinia, H. Avci, A. Tamayol, P. Mostafalu, H. B. Ghavifekr, E. N. Aghdam, M. R. Dokmeci, A. Khademhosseini, and Y. S. Zhang. "Rapid prototyping of whole-thermoplastic microfluidics with built-in microvalves using laser ablation and thermal fusion bonding". In: *Sensors and Actuators B: Chemical* 255 (Feb. 1, 2018), pp. 100–109. DOI: 10.1016/j.snb.2017.07.138.

[178] L. Shampine and M. Reichelt. "The MATLAB ODE Suite". In: *SIAM Journal on Scientific Computing* 18.1 (1997).

[179] M. Shams, A. Q. Raeini, M. J. Blunt, and B. Bijeljic. "A study to investigate viscous coupling effects on the hydraulic conductance of fluid layers in two-phase flow at the pore level". In: *Journal of Colloid and Interface Science* 522 (July 15, 2018), pp. 299–310. DOI: 10.1016/j.jcis.2018.03.028.

[180] S. Shibuichi, T. Onda, N. Satoh, and K. Tsujii. "Super Water-Repellent Surfaces Resulting from Fractal Structure". In: *The Journal of Physical Chemistry* 100.50 (Jan. 1, 1996), pp. 19512–19517. DOI: 10.1021/jp9616728.

[181] J. H. Snoeijer and B. Andreotti. "Moving Contact Lines: Scales, Regimes, and Dynamical Transitions". In: *Annual Review of Fluid Mechanics* 45 (Volume 45, 2013 Jan. 3, 2013), pp. 269–292. DOI: 10.1146/annurev-fluid-011212-140734.

[182] K. S. Sorbie, Y. Z. Wu, and S. R. McDougall. "The Extended Washburn Equation and Its Application to the Oil/Water Pore Doublet Problem". In: *Journal of Colloid and Interface Science* 174.2 (Sept. 15, 1995), pp. 289–301. DOI: 10.1006/jcis.1995.1394.

[183] C. Soulaine, P. Horgue, J. Franc, and M. Quintard. "Gas–liquid flow modeling in columns equipped with structured packing". In: *AIChE Journal* 60.10 (Oct. 2014), pp. 3665–3674. DOI: 10.1002/aic.14550.

[184] C. Soulaine, J. Maes, and S. Roman. "Computational Microfluidics for Geosciences". In: *Frontiers in Water* 3 (Mar. 2, 2021). DOI: 10.3389/frwa.2021.643714.

[185] C. Soulaine and H. A. Tchelepi. "Micro-continuum Approach for Pore-Scale Simulation of Subsurface Processes". In: *Transport in Porous Media* 113.3 (July 1, 2016), pp. 431–456. DOI: 10.1007/s11242-016-0701-3.

[186] R. Span and W. Wagner. "A New Equation of State for Carbon Dioxide Covering the Fluid Region from the Triple-Point Temperature to 1100 K at Pressures up to 800 MPa". In: *Journal of Physical and Chemical Reference Data* 25.6 (Nov. 1, 1996), pp. 1509–1596. DOI: 10.1063/1.555991.

[187] M. Spiga and G. L. Morino. “A symmetric solution for velocity profile in laminar flow through rectangular ducts”. In: *International Communications in Heat and Mass Transfer* 21.4 (July 1, 1994), pp. 469–475. DOI: 10.1016/0735-1933(94)90046-9.

[188] C. Spurin, T. Bultreys, B. Bijeljic, M. J. Blunt, and S. Krevor. “Intermittent fluid connectivity during two-phase flow in a heterogeneous carbonate rock”. In: *Physical Review E* 100.4 (Oct. 8, 2019), p. 043103. DOI: 10.1103/PhysRevE.100.043103.

[189] C. Spurin, T. Bultreys, B. Bijeljic, M. J. Blunt, and S. Krevor. “Mechanisms controlling fluid breakup and reconnection during two-phase flow in porous media”. In: *Physical Review E* 100.4 (Oct. 29, 2019), p. 043115. DOI: 10.1103/PhysRevE.100.043115.

[190] C. Spurin, S. Ellman, T. Bultreys, T. Kurotori, S. Benson, and H. A. Tchelepi. “The role of injection method on residual trapping: Insights into bridging scales and heterogeneity”. In: *Advances in Water Resources* 197 (Mar. 1, 2025), p. 104913. DOI: 10.1016/j.advwatres.2025.104913.

[191] *Stokes flow*. In: *Wikipedia*. May 4, 2025.

[192] H. A. Stone, A. D. Stroock, and A. Ajdari. “Engineering Flows in Small Devices: Microfluidics Toward a Lab-on-a-Chip”. In: *Annual Review of Fluid Mechanics* 36 (Volume 36, 2004 Jan. 1, 2004), pp. 381–411. DOI: 10.1146/annurev.fluid.36.050802.122124.

[193] *Surface Evolver*. URL: https://kenbrakke.com/evolver/evolver.html (visited on 09/12/2025).

[194] P. Tabeling, G. Zocchi, and A. Libchaber. “An experimental study of the Saffman-Taylor instability”. In: *Journal of Fluid Mechanics* 177 (Apr. 1987), pp. 67–82. DOI: 10.1017/S0022112087000867.

[195] K. Takamura, H. Fischer, and N. R. Morrow. “Physical properties of aqueous glycerol solutions”. In: *Journal of Petroleum Science and Engineering* 98-99 (Nov. 1, 2012), pp. 50–60. DOI: 10.1016/j.petrol.2012.09.003.

[196] S. Taku Ide, K. Jessen, and F. M. Orr. “Storage of CO2 in saline aquifers: Effects of gravity, viscous, and capillary forces on amount and timing of trapping”. In: *International Journal of Greenhouse Gas Control* 1.4 (Oct. 1, 2007), pp. 481–491. DOI: 10.1016/S1750-5836(07)00091-6.

[197] G. I. Taylor. “Deposition of a viscous fluid on the wall of a tube”. In: *Journal of Fluid Mechanics* 10.2 (Mar. 1961), pp. 161–165. DOI: 10.1017/S0022112061000159.

[198] K. R. Tekseth, F. Mirzaei, B. Lukic, B. Chattopadhyay, and D. W. Breiby. “Multiscale drainage dynamics with Haines jumps monitored by stroboscopic 4D X-ray microscopy”. In: *Proceedings of the National Academy of Sciences* 121.1 (Jan. 2, 2024), e2305890120. DOI: 10.1073/pnas.2305890120.

[199] T. K. Tokunaga, J. Wan, J.-W. Jung, T. W. Kim, Y. Kim, and W. Dong. “Capillary pressure and saturation relations for supercritical CO2 and brine in sand: High-pressure Pc(Sw) controller/meter measurements and capillary scaling predictions”. In: *Water Resources Research* 49.8 (2013), pp. 4566–4579. DOI: 10.1002/wrcr.20316.

[200] T. Torskaya, G. Jin, and C. Torres-Verdín. “Pore-Level Analysis of the Relationship Between Porosity, Irreducible Water Saturation, and Permeability of Clastic Rocks”. In: SPE Annual Technical Conference and Exhibition. OnePetro, Nov. 11, 2007. DOI: 10.2118/109878-MS.

[201] T. Trantidou, Y. Elani, E. Parsons, and O. Ces. "Hydrophilic surface modification of PDMS for droplet microfluidics using a simple, quick, and robust method via PVA deposition". In: *Microsystems & Nanoengineering* 3.1 (Apr. 24, 2017), pp. 1–9. DOI: 10.1038/micronano.2016.91.

[202] T. Tsuji, F. Jiang, and K. T. Christensen. "Characterization of immiscible fluid displacement processes with various capillary numbers and viscosity ratios in 3D natural sandstone". In: *Advances in Water Resources*. Pore scale modeling and experiments 95 (Sept. 1, 2016), pp. 3–15. DOI: 10.1016/j.advwatres.2016.03.005.

[203] M. Tuller and D. Or. "Hydraulic conductivity of variably saturated porous media: Film and corner flow in angular pore space". In: *Water Resources Research* 37.5 (2001), pp. 1257–1276. DOI: 10.1029/2000WR900328.

[204] N. B. Vargaftik, B. N. Volkov, and L. D. Voljak. "International Tables of the Surface Tension of Water". In: *Journal of Physical and Chemical Reference Data* 12.3 (July 1, 1983), pp. 817–820. DOI: 10.1063/1.555688.

[205] O. V. Voinov. "Hydrodynamics of wetting". In: *Fluid Dynamics* 11.5 (Sept. 1, 1976), pp. 714–721. DOI: 10.1007/BF01012963.

[206] P. W. Voorhees. "The theory of Ostwald ripening". In: *Journal of Statistical Physics* 38.1 (Jan. 1, 1985), pp. 231–252. DOI: 10.1007/BF01017860.

[207] P. Wägli, A. Homsy, and N. F. de Rooij. "Norland optical adhesive (NOA81) microchannels with adjustable surface properties and high chemical resistance against IR-transparent organic solvents". In: *Procedia Engineering*. Eurosensor XXIV Conference 5 (Jan. 1, 2010), pp. 460–463. DOI: 10.1016/j.proeng.2010.09.146.

[208] J. Wan, Y. Kim, and T. K. Tokunaga. "Contact angle measurement ambiguity in supercritical CO2–water–mineral systems: Mica as an example". In: *International Journal of Greenhouse Gas Control* 31 (Dec. 1, 2014), pp. 128–137. DOI: 10.1016/j.ijggc.2014.09.029.

[209] K. Wang, S. Matsushita, S. Yamashita, M. Nasir, and T. Suekane. "Energy transfer process during Haines jumps and meniscus reconfiguration with a high-density and viscosity ratio". In: *International Journal of Heat and Mass Transfer* 230 (Sept. 15, 2024), p. 125749. DOI: 10.1016/j.ijheatmasstransfer.2024.125749.

[210] S. Wang and T. K. Tokunaga. "Capillary Pressure–Saturation Relations for Supercritical CO2 and Brine in Limestone/Dolomite Sands: Implications for Geologic Carbon Sequestration in Carbonate Reservoirs". In: *Environmental Science & Technology* 49.12 (June 16, 2015), pp. 7208–7217. DOI: 10.1021/acs.est.5b00826.

[211] Y. Wang, C. Zhang, N. Wei, M. Oostrom, T. W. Wietsma, X. Li, and A. Bonneville. "Experimental Study of Crossover from Capillary to Viscous Fingering for Supercritical CO2–Water Displacement in a Homogeneous Pore Network". In: *Environmental Science & Technology* 47.1 (Jan. 2, 2013), pp. 212–218. DOI: 10.1021/es3014503.

[212] E. W. Washburn. "The Dynamics of Capillary Flow". In: *Physical Review* 17 (Mar. 1, 1921), pp. 273–283. DOI: 10.1103/PhysRev.17.273.

[213] R. N. Wenzel. *Surface Roughness and Contact Angle*. ACS Publications. Sept. 1, 1949. DOI: 10.1021/j150474a015. URL: https://pubs.acs.org/doi/pdf/10.1021/j150474a015 (visited on 06/03/2024).

[214] S. Whitaker. "Flow in Porous Media I: A Theoretical Derivation of Darcy's Law". In: *Transport in Porous Media* 1 (Mar. 1, 1986), pp. 3–25. DOI: 10.1007/BF01036523.

[215] J. White, R. Borja, and J. Fredrich. "Calculating the effective permeability of sandstone with multiscale lattice Boltzmann/finite element simulations". In: *Acta Geotechnica* 1 (Dec. 1, 2006), pp. 195–209. DOI: 10.1007/s11440-006-0018-4.

[216] T. M. L. Wigley. "The pre-industrial carbon dioxide level". In: *Climatic Change* 5.4 (Dec. 1, 1983), pp. 315–320. DOI: 10.1007/BF02423528.

[217] D. Wildenschild, R. T. Armstrong, A. L. Herring, I. M. Young, and J. William Carey. "Exploring capillary trapping efficiency as a function of interfacial tension, viscosity, and flow rate". In: *Energy Procedia*. 10th International Conference on Greenhouse Gas Control Technologies 4 (Jan. 1, 2011), pp. 4945–4952. DOI: 10.1016/j.egypro.2011.02.464.

[218] N. A. Wojas, A. Swerin, V. Wallqvist, M. Järn, J. Schoelkopf, P. A. C. Gane, and P. M. Claesson. "Iceland spar calcite: Humidity and time effects on surface properties and their reversibility". In: *Journal of Colloid and Interface Science* 541 (Apr. 1, 2019), pp. 42–55. DOI: 10.1016/j.jcis.2019.01.047.

[219] H. Wong, C. J. Radke, and S. Morris. "The motion of long bubbles in polygonal capillaries. Part 2. Drag, fluid pressure and fluid flow". In: *Journal of Fluid Mechanics* 292 (June 1995), pp. 95–110. DOI: 10.1017/S0022112095001455.

[220] A. G. Yiotis, J. Psihogios, M. E. Kainourgiakis, A. Papaioannou, and A. K. Stubos. "A lattice Boltzmann study of viscous coupling effects in immiscible two-phase flow in porous media". In: *Colloids and Surfaces A: Physicochemical and Engineering Aspects*. Proceedings of the Fourth International TRI/Princeton Workshop "Characterization of Porous Materials: from Angstroms to Millimeters" 300.1 (June 1, 2007), pp. 35–49. DOI: 10.1016/j.colsurfa.2006.12.045.

[221] T. Young. "An Essay on the Cohesion of Fluids. [Abstract]". In: *Abstracts of the Papers Printed in the Philosophical Transactions of the Royal Society of London* 1 (1800), pp. 171–172.

[222] C. Zhang, M. Oostrom, T. W. Wietsma, J. W. Grate, and M. G. Warner. "Influence of Viscous and Capillary Forces on Immiscible Fluid Displacement: Pore-Scale Experimental Study in a Water-Wet Micromodel Demonstrating Viscous and Capillary Fingering". In: *Energy & Fuels* 25.8 (Aug. 18, 2011), pp. 3493–3505. DOI: 10.1021/ef101732k.

[223] B. Zhao, A. Alizadeh Pahlavan, L. Cueto-Felgueroso, and R. Juanes. "Forced Wetting Transition and Bubble Pinch-Off in a Capillary Tube". In: *Physical Review Letters* 120.8 (Feb. 23, 2018), p. 084501. DOI: 10.1103/PhysRevLett.120.084501.

[224] B. Zhao, C. W. MacMinn, and R. Juanes. "Wettability control on multiphase flow in patterned microfluidics". In: *Proceedings of the National Academy of Sciences* 113.37 (Sept. 13, 2016), pp. 10251–10256. DOI: 10.1073/pnas.1603387113.

[225] C.-X. Zhao and A. P. J. Middelberg. "Two-phase microfluidic flows". In: *Chemical Engineering Science*. Microfluidic Engineering 66.7 (Apr. 1, 2011), pp. 1394–1411. DOI: 10.1016/j.ces.2010.08.038.

[226] J. Zhao, F. Qin, Q. Kang, C. Qin, D. Derome, and J. Carmeliet. "A Dynamic Pore Network Model for Imbibition Simulation Considering Corner Film Flow". In: *Water Resources Research* 58.7 (2022), e2022WR032332. DOI: 10.1029/2022WR032332.

[227] G. Zhu, Z. Wei, W. Li, X. Yang, S. Cao, X. Wu, and Y. Li. “Interface dissolution kinetics and porosity formation of calcite and dolomite (1 1 0) and (1 0 4) planes: An implication to the stability of geologic carbon sequestration”. In: *Journal of Colloid and Interface Science* 650 (Nov. 15, 2023), pp. 1003–1012. DOI: 10.1016/j.jcis.2023.07.035.

Appendix A

Saffman Taylor instability

The viscous fingering invasion introduced in Chapter. 3 is a direct consequence of the well-known Saffman-Taylor instability [174]. Some physical phenomena, such as snowflake formation, crystal growth [105], bacteria colonies formation, or two-phase flow in porous media, exhibit the formation of similar, dendritic patterns during their evolution. This pattern is caused by the interplay of the macroscopic diffusion field, which tends to make the interface between the different phases irregular, and the microscopic effect of surface tension or surface kinetics, which tends to keep the interface smooth and the propagating velocity uniform [22]. These two opposing effects lead to the formation of beautiful dendritic or tip-splitting effects, see Fig. A.1, and a better understanding of how they interact would greatly improve our control of physical and biological systems. In our study of the two-phase flow, the formation of these dendrites is called the Saffman-Taylor instability and was first described in an article by Saffman and Taylor in 1958. They showed how the interface between two moving fluids of different properties can be unstable. Via a linear stability analysis, they showed that under certain conditions, the initially flat interface between the fluids deforms and forms a characteristic shape known as viscous fingers.

A.1 Disturbance of the interface by diffusive process

For their analysis, Saffman and Taylor (1958) took two incompressible and immiscible fluids in a porous medium, assumed Darcy's law, and neglected the interfacial tension between the two fluids. Fluid number 1 was injected above fluid number 2 at a constant flow rate. The interface, initially flat, moves downward at a constant speed V_0. By introducing the streaming potential ϕ such that $\boldsymbol{\nabla}\phi_i = \boldsymbol{u_i}$ with u_i the speed of the fluid i, and combining it with the conservation of mass, we end up with Laplace's equation for the streaming function in each fluid

$$\boldsymbol{\nabla}^2\phi_i = 0. \tag{A.1}$$

To perform the linear stability analysis, they introduced a small perturbation in the shape of the interface. At time t, the position x of the interface was now given as

$$x = V_0 t + \mathrm{e}^{\mathrm{i}(ny+\sigma t)} \tag{A.2}$$

where ϵ, n, and σ are respectively the amplitude, the wave vector, and the growth rate of the perturbation, see Fig. A.2. If the growth rate σ is positive for a certain value of the wave vector, then the perturbation with wavelength $l = \frac{2\pi}{n}$ will grow in time and the interface will be unstable. The velocity of the interface will also be perturbed by

Figure A.1: Snowflake highlighting the dendritic shape of the crystal growth.

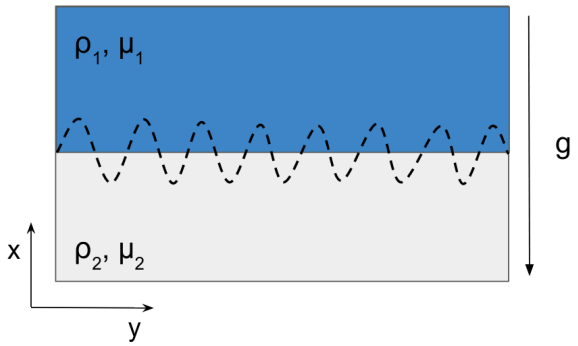

Figure A.2: Situation considered by Saffman and Taylor. They introduced a perturbation in the initially stable interface and studied under which conditions it grows.

the disturbance and can be re-written as the sum of the basic value and a perturbation value

$$V = V_0 + \tilde{V} = V_0 + \epsilon\sigma e^{i(ny+\sigma t)}. \tag{A.3}$$

From the continuity of the velocity at the interface, we can then write,

$$\frac{\partial \phi_1}{\partial x} = \frac{\partial \phi_2}{\partial x} = V + \epsilon\sigma e^{i(ny+\sigma t)}. \tag{A.4}$$

Since the disturbances vanish far from the interface, we have that $\phi_1\big|_{x\to+\infty} = V_0 x$, and $\phi_2\big|_{x\to-\infty} = V_0 x$. With these boundaries condition, Eq. A.1 can be solved and gives us,

$$\phi_1 = V_0 x - \frac{\epsilon\sigma}{n} e^{i(ny-nx+\sigma t)} \tag{A.5}$$

and

$$\phi_2 = V_0 x + \frac{\epsilon\sigma}{n} e^{i(ny+nx+\sigma t)}. \tag{A.6}$$

From Darcy's law, and assuming a different permeability in each phase, the pressure field is given by

$$p_i = \frac{-\mu_i}{k_i}\phi_i - \rho_i g x \tag{A.7}$$

in each phase. Since we have neglected the surface tension, the pressure jump at the interface between the fluid is zero, we can write that

$$\frac{\sigma}{n}\left(\frac{\mu_1}{k_1} + \frac{\mu_2}{k_2}\right) = g(\rho_1 - \rho_2) + V_0\left(\frac{\mu_1}{k_1} - \frac{\mu_2}{k_2}\right). \tag{A.8}$$

From Eq. A.8, we see that the interface is unstable if $(\rho_1 - \rho_2) + V_0\left(\frac{\mu_1}{k_1} - \frac{\mu_2}{k_2}\right) > 0$. If we assume no gravity and the same permeability in both phases, the interface is unstable if $\mu_1 < \mu_2$, which is the classic Saffman-Taylor condition. This derivation, valid for a porous medium, is the same in a Hele-Shaw cell, which can be seen as a porous medium of permeability $k = \frac{h^2}{12}$, where h is the distance between the two plates forming the cell.

A.2 Stabilising effect of the surface tension in a Hele-Shaw cell

We have seen in the previous section how the diffusive process leads to an unstable front displacement. We will now see how surface tension acts as a stabilizing force, and how the interplay between both leads to the growth of a certain perturbation wavelength.
For this derivation, we stay in a Hele-Shaw cell, where the capillary pressure can be calculated with the shape of the interface, which is not the case in a real porous media. This capillary pressure can be expressed as :

$$P_c = T\left(\frac{2}{h} + \frac{d^2x}{dy^2}\right) \tag{A.9}$$

where T is the, for this section only, the interfacial tension between the fluids, $\frac{2}{h}$ is the curvature in the (z-x) plane, and $\frac{d^2x}{dy^2}$ is the curvature in the (x-y) plane.

Since the pressure is not the same in each fluid anymore, the continuity of speed at the interface now reads as,

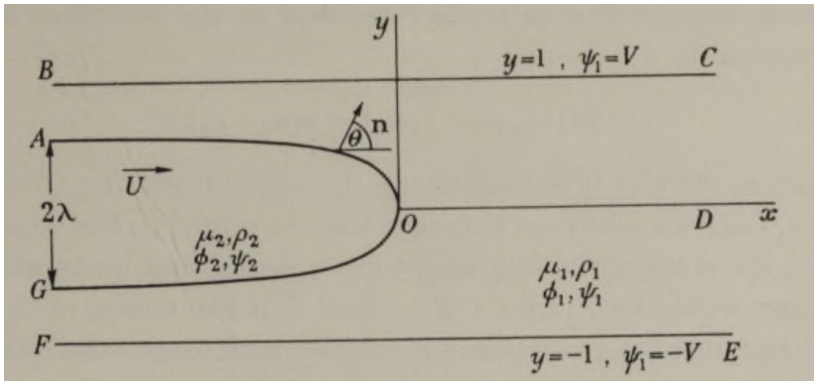

Figure A.3: Finger of fluid moving inside a channel, from Saffman and Taylor [174]

$$\frac{12}{h^2}\sigma(\mu_1+\mu_2) = n\left(\frac{12V_0}{h^2}(\mu_1-\mu_2)+g(\rho_1-\rho_2)\right) - Tn^3. \tag{A.10}$$

We see from Eq. A.10 that the surface tension prevents the perturbations with a wavelength below a certain threshold from being unstable. This threshold is given by

$$l_{crit} = 2\pi h\sqrt{\frac{T}{(12V_0(\mu_1-\mu_2)+h^2g(\rho_1-\rho_2)}}. \tag{A.11}$$

And functional analysis of σ gives us that the fastest growing wavelength is $\sqrt{3}l_{crit}$.

A.3 Stable interface shape

Even though Saffman and Taylor showed that stable flat fronts are unstable, it does not exclude the existence of stable steady interfaces. This can be seen in the Saffman Taylor finger and the parabolic needle growth[104]. In their paper, Saffman and Taylor studied the shape of a single finger during the instability [174]. The system under study is a channel of fixed width with a finger of fluid 2 propagating in a channel of fluid 1. The width at infinity is 2λ, where λ is an unknown, see Fig. A.3. The gravity, the surface tension, and the viscosity of the fluid inside of the finger are supposed negligible.

By conformal mapping, the authors were able to establish that the surface of the finger is given by

$$x = \frac{1-\lambda}{\pi}\ln\frac{1}{2}\left(1+\cos\frac{\pi y}{\lambda}\right). \tag{A.12}$$

However, the value of the parameter λ is still unknown, and of particular interest since it controls the speed of the bubble according to the relationship $V = \lambda U$, where V is the speed of the finger and U is the speed of the fluid at infinity. Experimentally, the authors were able to find a value of $\lambda = 0.5$, valid for certain values of the capillary number. It took 30 years for the scientific community to find that surface tension was the factor selecting the shape of the fingers. They found that the surface tension introduces higher-order terms in the interface equation that could not be taken into account via the linear stability analysis [44, 133]. They showed that, for W the width of the channel, the shape of the interface was controlled by a parameter B, (which is

similar to the inverse of the capillary number)

$$B = \frac{T}{12\mu U}\left(\frac{h^2}{W}\right) \tag{A.13}$$

and that for each value of B, there is a certain set of values λ_n that the width can take. For very small values of B, these values are,

$$\left(\lambda_n - \frac{1}{2}\right) = \frac{1}{8}a_n(16\pi^2 B)^{\frac{2}{3}} \tag{A.14}$$

with $a_n = 2\left(n + \frac{4}{7}\right)^2$. For the growth of a crystal, an equivalent of the surface tension can also be introduced, leading to the same mechanism for the selection of the finger's width [116, 93].

Appendix B

Image processing: general considerations

The section aims at describing the basic operations of image analysis, some of which were used in Sec. 4.3.

To process the experiments, a good understanding of what an image is is required. Images, at their core, are composed of a matrix of pixels, each of which of a certain color. For a color image, each pixel has three values, each of these values coding for a certain intensity of Red, Green, and Blue (RGB). For a grayscale image, each pixel has only one value, which is the gray level. A size $m \times n$ image can then be represented by a $m \times n$ matrix for a grayscale image, or by a $m \times n \times 3$ tensor for a color image. The values of the pixels are between 0 and 256 for a 8bit image ($2^8 = 256$) and between 0 and 65536 for for a 16bit image ($2^{16} = 65536$). To analyse these images, several softwares are available. The two that are used in this study are ImageJ and the Image Processing Toolbox from MATLAB, which allows for the automatic treatment of the numerous experimental images obtained.

For a grayscale image, the histogram is the distribution of the pixel values over the entire picture. It can be used to assess the image quality. Indeed, if all the pixels have values close to each other, the quality of the image is poor. In Fig. B.1, the illumination was not sufficient, leading to a very dark and poorly contrasted picture. Image treatment can improve the picture by spreading the values of the pixels over the entire range, but it cannot create information that is absent from the image because of poor illumination. Too much light is also a problem, causing saturation of the image, meaning that too many pixels reach the maximum intensity value, which erases some of the

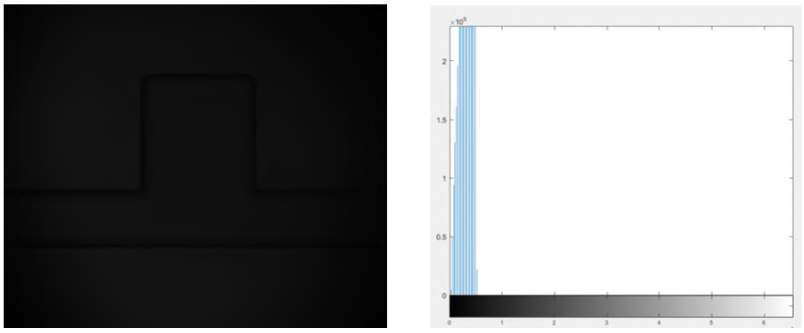

Figure B.1: Badly illuminated image of a square pore with its histogram

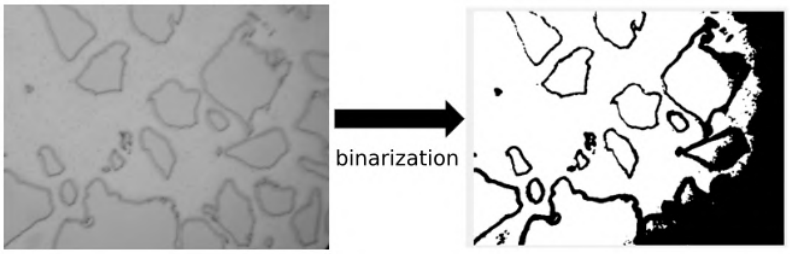

Figure B.2: Example of the binarization process on a picture of a micromodel. The right side of the picture is darker, and the binarization leads to too many black pixels in this area. To correct, a better illumination is needed, or an illumination correction process needs to be done.

details. Thus, proper illumination is required to have good-quality pictures.

From this histogram, it is possible to perform a binarization operation to obtain a black and white image. For this, a threshold in the pixel value is determined using the Otsu method[147], or by manually selecting the value. This operation will turn all of the pixels below the threshold black and all of the pixels above white, see Fig. B.2.

The binary images can then be subjected to different morphological operations, to either add or remove white pixels (for black and white pictures, the white pixels are called the object, and the black pixel is the background). The idea for the mathematical operation is to use a probe, or structuring element, that is made out of a geometrical shape composed of several pixels. This probe is then used to perform two operations: erosion and dilation. Erosion is done by displacing the center of the probe over each pixel of the image (black and white). When the probe is centered on one pixel, we check if every pixel of the probe is covered by a pixel of the object. If it is not the case, the original pixel is marked for removal, and we go to the next pixel. After every pixel has been probed, the ones that have been marked for removal are turned black. Dilation is similar, but instead of removing pixels, we add some. In the same fashion, the probe scans every pixel, but if the structural element touches any white pixel, the pixel in the center is turned from black to white at the end of the operation.

Erosion is used to remove pixels on object boundaries by shrinking the image region, see Fig. B.3. It transforms the image by removing small-scale details and disconnecting narrow parts of objects. On the opposite, dilation adds pixels to the boundaries of an object in an image, see Fig. B.4. It enlarges the image regions, filling in small holes and connecting adjacent objects in the image.

These two operations can then be combined, using the same structural element to perform a morphological opening (erosion followed by dilation) or a morphological closing (dilation followed by erosion). The goal of the opening is to remove every object smaller than the structural element, see Fig. B.5 while keeping the other objects more or less identical (depending on the choice of probe shape). On the contrary, morphological opening is used to fill the voids inside objects, see Fig. B.6.

The morphological erosion and morphological opening are used in the image analysis part of this study to remove the walls of the channels and the particles from the image, to isolate the menscci from the images. The MATLAB program used to treat the data can be found in the supplementary data.

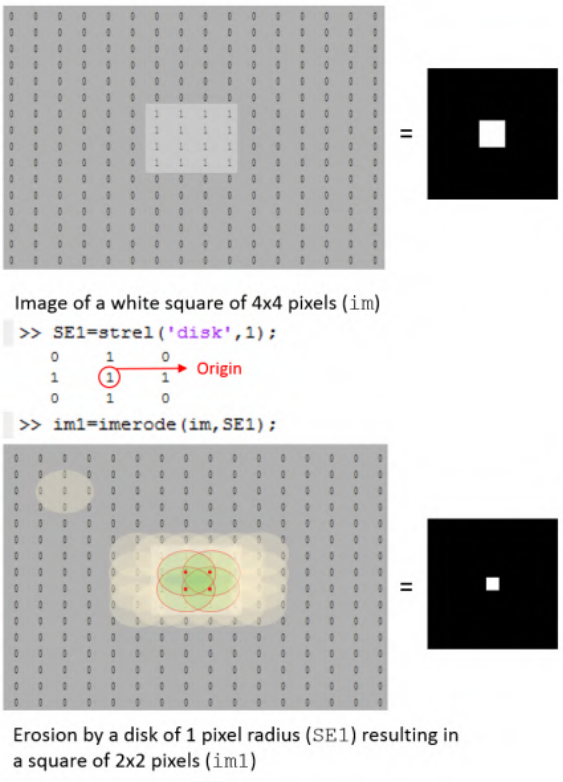

Figure B.3: Example of erosion using the software MATLAB, credits to Sophie ROMAN

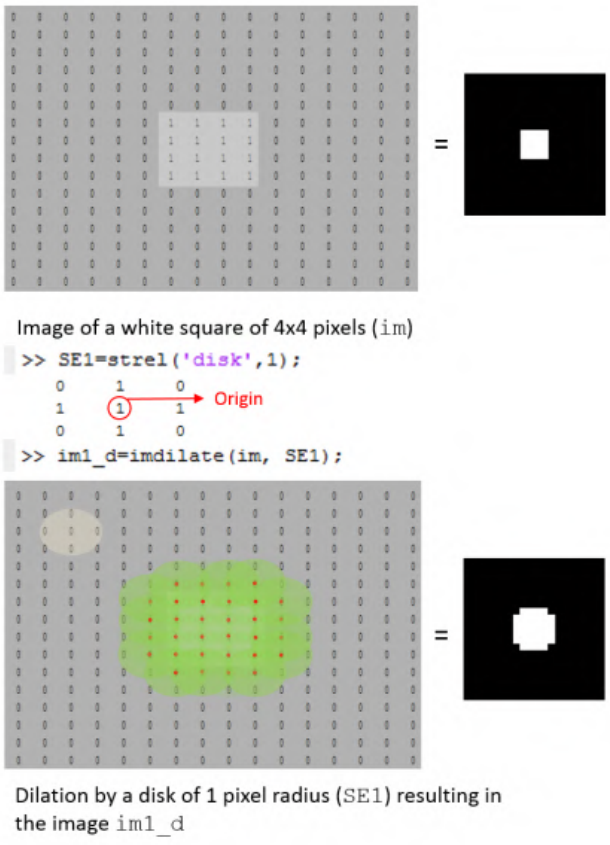

Figure B.4: Example of dilation using the software MATLAB, credits to Sophie ROMAN

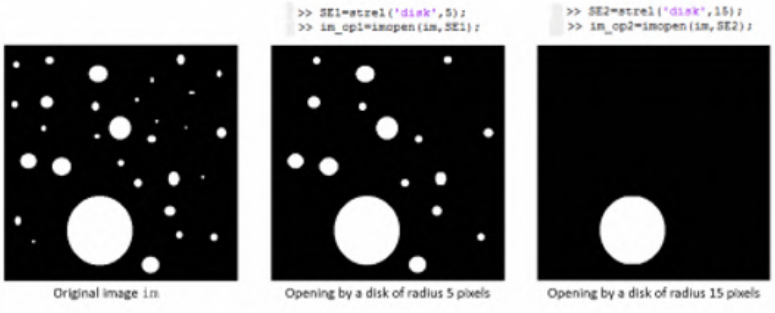

Figure B.5: Example of morphological opening, using bigger and bigger structural elements, credits to Sophie ROMAN

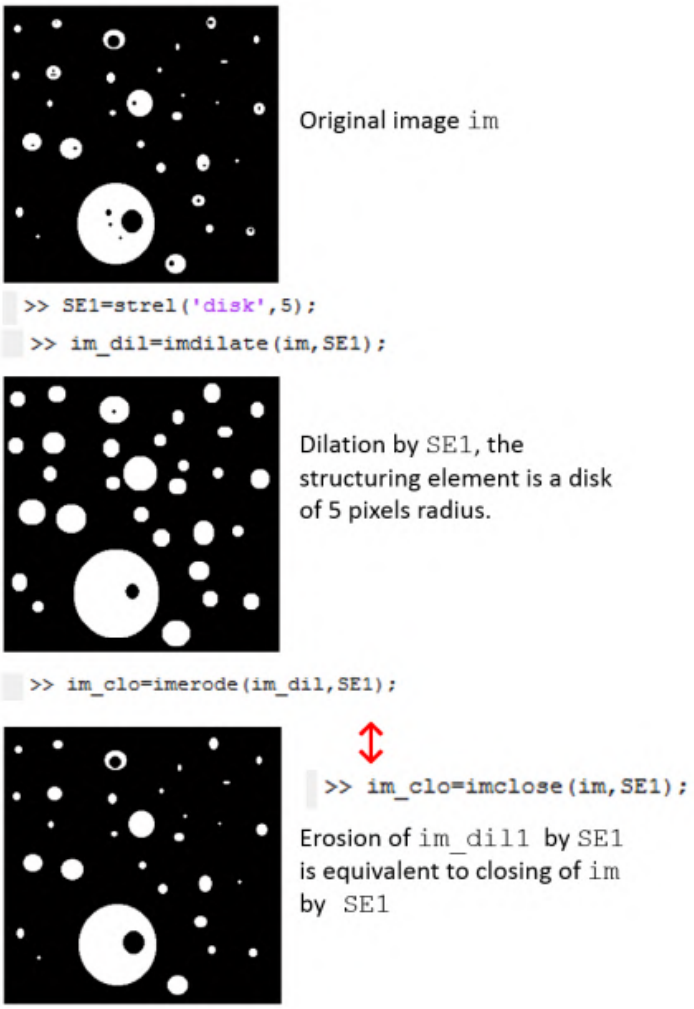

Figure B.6: Example of morphological closing, credits to Sophie ROMAN

Appendix C

$P(M)$, $Q(M)$ and $\psi(z)$ functions for calculating the value of the film thickness

According to Balestra et al. (2018), for the cylindrical geometry,

$$P(M) = \frac{0.643}{2}\left(1 + 2^{2/3} + \left(2^{2/3} - 1\right)\tanh\left(1.2\log_{10} M + 0.1657\right)\right) \tag{C.1}$$

and

$$Q(M) = \frac{1.37M^3 + 33.84M^2 + 111.25M + 2.21}{M^3 + 54.50M^2 + 44.86M + 0.89}. \tag{C.2}$$

According to Wong et al. (1995), the wet fraction in the case $Ca \to 0$ is given by,

$$\psi(z) = 1 - \frac{1 - \frac{\pi}{4}}{\epsilon(z)}\left(\frac{2\epsilon(z)}{\epsilon(z) + 1 + \sqrt{(\epsilon(z) - 1)^2 + \pi\epsilon(z)}}\right)^2. \tag{C.3}$$

Appendix D

Simultaneous flow of two fluids in a cylindrical channel

Both fluids flow in the same cylinder, with fluid 1 forming a uniform layer of thickness e along the wall of the cylinder. The fluid flow is assumed to be steady and laminar, meaning that we can use Stoke's law to describe the flow of each fluid:

$$-\boldsymbol{\nabla} P_j + \mu_j \boldsymbol{\nabla}^2 v_j + \rho_j \boldsymbol{g} = 0 \tag{D.1}$$

where μ_j is the viscosity of fluid j ($j = 1, 2$), v_j is the speed of the fluid j and $\frac{\partial P_j}{\partial z}$ is the pressure gradient in the fluid j. This leads, for the fluid 2, in the center of the channel,

$$\begin{aligned} v_2(r,z) = &\frac{\nabla P_2}{4\mu_2}\left(r^2 - (R(z)-e)^2 + 2M(R(z)-e)^2 \ln\left(1 - \frac{e}{R(z)}\right)\right) \\ &+ \frac{\nabla P_1}{4\mu_1}\left((R(z)-e)^2 - R(z)^2 - 2(R(z)-e)^2 \ln\left(1 - \frac{e}{R(z)}\right)\right) \end{aligned} \tag{D.2}$$

with the first cylindrical coordinate.

Appendix E

Slip flow in a conduit

The equation describing the flow of a single fluid of viscosity μ inside a cylindrical channel of radius R_0 under a gradient of pressure ∇P is given by,

$$v(r) = \frac{\nabla P}{\mu}\left(\frac{r^2}{4} - R_0\left(\frac{\lambda}{2} + \frac{R_0}{4}\right)\right). \tag{E.1}$$

With λ the slip lenght at the wall of the channel. After integration, we end up with a flow rate of ,

$$Q = -\frac{\pi \nabla P}{8\mu} R_0^3 (R_0 + 4\lambda). \tag{E.2}$$

We can compare this speed with the average speed of the non-wetting phase during two-phase flow in the case where a film of fluid of thickness e is present on the wall. This average speed is given by,

$$Q_{withfilms} = -\frac{\pi \nabla P}{8\mu}\left((R_0 - e)^4\left(1 - 4M \ln\left(1 - \frac{e}{R_0}\right)\right)\right). \tag{E.3}$$

Comparing Eq. E.2 and Eq. E.3, we can deduce that they give the same if the slip lenght is equal to:

$$\lambda = \frac{(R_0 - e)^4}{4R_0^3}\left(1 - 4M \ln\left(1 - \frac{e}{R_0}\right)\right) - \frac{R_0}{4}. \tag{E.4}$$

And after a Taylor expansion in e at the first order,

$$\lambda = e(M - 1). \tag{E.5}$$

Appendix F

Solution of $\phi(z_i)$ in different cases

F.1 Diverging/converging cylindrical channels

To solve Eq. (7.25), we need to integrate the first term of the right-hand side of the equation, which is non-trivial. To do this, we first need to do the variable change $X = r(z) = 1 + \alpha z$, which leads us to the integration of the inverse of a fourth-order polynomial:

$$M \int_0^{z_i(t)} \frac{dz}{r(z)^4 + 4r(z)^3 e(M-1)} = \frac{M}{\alpha} \int_1^{1+\alpha z_i(t)} \frac{dX}{X^4 + 4X^3 e(M-1)}. \tag{F.1}$$

Then, we must write that function as a sum of simpler terms. As we know, a polynomial P of order m whose expression is

$$P(X) = \alpha X^m + \beta X^{m-1} + \gamma X^{m-2} + ... + \omega, \tag{F.2}$$

with α, β, γ and ω constants, can always be written under the form

$$P(X) = \alpha \sum_{k=1}^{n} (X - \delta_k)^{a_k}, \tag{F.3}$$

where δ_k are the roots of P, n the number of root of P, and λ_k is the order of the root δ_k, which is a non null positive integer. Following this equation, we also have

$$m = \sum_{k=1}^{n} \alpha_k, \tag{F.4}$$

where m is the order of P. We use these properties to solve our integral. For that, we first need to re-write our polynomial, which we call Q :

$$Q(X) = X^3 (X + 4e(M-1)). \tag{F.5}$$

F.1.1 Case $e \neq 0$ and $M \neq 1$

One root of Q is zero, which is of order 3. And the other is $K = -4e(M-1)$, so for $M \neq 1$, we can re-write Q as a sum of simpler fractions :

$$\frac{AX^2 + BX + C}{X^3} + \frac{D}{X - K} = \frac{1}{X^3 (X + 4e(M-1))} \tag{F.6}$$

with

$$A = \frac{1}{K^3}, B = \frac{-1}{K^2}, C = \frac{-1}{K} \text{ and } D = \frac{-1}{K^3} = -A.$$

And we can now integrate the term that we are working on, which gives us

$$\int_1^{1+\alpha z_i(t)} \left(\frac{AX^2 + BX + C}{X^3} + \frac{D}{X + 2\lambda} \right) dX = A \ln r(z_i) + B\left(1 - \frac{1}{r(z_i)}\right) + \frac{C}{2}\left(1 - \frac{1}{r(z_i)^2}\right) + D \ln\left(\left|\frac{r(z_i) - K_1}{1 - K_1}\right|\right). \tag{F.7}$$

F.1.2 Case $e = 0$ or $M = 1$

In this case, $Q(X)$ has only the root of order 4, 0. In this case, the problem degenerates to the problem introduced by Al-Housseiny et al. (2014) and the integration is straightforward. So we are finally able to re-inject the previous equation in the Eq. (7.16), which gives us the following expression of $\phi(z)$,

$$\phi(z_i) = \frac{r'(z_i')^2}{(r'(z_i') - e_i')^2} \times \frac{1 - \frac{r'(z_i')^3}{r'(1)^3}}{3\alpha' r'(z_i')^3} - \frac{M}{8\alpha' \lambda_i^3}\left(-\ln r'(z_i') + 2\lambda_i\left(1 - \frac{1}{r'(z_i')}\right) + 2\lambda_i^2\left(1 - \frac{1}{r'\left(z_i'\right)^2}\right) + \ln\left|\frac{r'(z_i') + 2\lambda_i}{1 + 2\lambda_i}\right|\right). \tag{F.8}$$

F.2 Diverging/converging rectangular channels

The Eq. (7.16) for a rectangular channel can be written as :

$$\phi(z_i) = \alpha\left(M \int_0^{z_i(t)} \frac{dz}{\chi_i^2 D'^2 (w'(z) - \beta)(1 + c\lambda / R_h'(z))} + \frac{1}{\chi_i} \int_{z_i(t)}^{l} \frac{dz}{D'^2 (w'(z) - \beta)}\right), \tag{F.9}$$

with $\beta = 6(2/\pi)^5 (D_0/w_0)$. For the rest of the derivation, we set $D' = 1$ as $w_0 = D_0$ in our pore doublet. We focus on the first term of the right-hand side of the equation since it is the hardest one to integrate. We can re-write this term as:

$$\frac{1}{(w'(z) - \beta)(1 + c\lambda / R_h'(z))} = \frac{w'(z)}{(w'(z) - \beta)(w'(z)(1 + c\lambda) + c\lambda)}. \tag{F.10}$$

We now need to do a decomposition into simple elements to integrate this term.

$$\frac{w'(z)}{(w'(z) - \beta)(w'(z)(1 + c\lambda) + c\lambda)} = \frac{1}{2\alpha(1 + c\lambda)} \frac{2(1 + c\lambda)\alpha w'(z) + c\lambda\alpha - \beta(1 + c\lambda)\alpha}{w'(z)^2(1 + c\lambda) + w'(z)(c\lambda - \beta(1 + c\lambda)) - c\beta\lambda} + \frac{\beta(1 + c\lambda) - c\lambda}{2\alpha(1 + c\lambda)}\left(\frac{\alpha}{(w'(z) - \beta)(w'(z)(1 + c\lambda) + c\lambda)}\right). \tag{F.11}$$

The second term on the right hand side can be further decomposed :

$$\frac{1}{(w'(z) - \beta)(w'(z)(1 + c\lambda) + c\lambda)} = \frac{1}{A(w'(z) - \beta)} + \frac{-(1 + c\lambda)}{A(w'(z)(1 + c\lambda) + c\lambda)}, \tag{F.12}$$

with $A = (c\lambda + \beta(1+c\lambda))$. We can now integrate Eq. (7.16), which gives us:

$$\begin{aligned}\phi(z') = &\frac{M}{2\chi_i^2\alpha'(1+c\lambda)}\left(\ln\left(\frac{(w'(z_i)-\beta)(w'(z_i)(1+c\lambda)+c\lambda)}{(1-\beta)(1+2c\lambda)}\right)\right.\\ &\left.-\frac{c\lambda-\beta(1+c\lambda)}{A}\ln\left(\frac{(w'(z_i)-\beta)(1+2c\lambda)}{(w'(z_i)(1+c\lambda)+c\lambda)(1-\beta)}\right)\right)+\frac{1}{\alpha'\chi_i}\ln\left(\frac{w'(l)-\beta}{w'(z_i)-\beta}\right),\end{aligned} \tag{F.13}$$

which is a pretty ugly equation.

F.3 Sinusoidal rectangular channels

In the dimensionless case, we have

$$\phi_i(z_i, M) = M\int_0^{z_i}\frac{dz}{A(z)k(z)} + \int_{z_i}^{L}\frac{dz}{A(z)k(z)} \tag{F.14}$$

The difficulty in the integral is that the approximated value of $k(z)$ depends on which lenght scale controls the viscous dissipation [80]. If the depth controls it (if $D_0 < w_t$), the dimensioned permeability can be expressed as $k(z) = \frac{D_0^2}{12}\left(1-\beta\frac{D_0}{w(z)}\right)$, with $\beta = 6\left(\frac{2}{\pi}\right)^5\frac{D_0}{w(z)}$. If the width dominates the viscous drop (if $w_t < D_0$), then the permeability is expressed as $k(z) = \frac{w(z)^2}{12}\left(1-\beta\frac{w(z)}{D_0}\right)$. In the case of $D_0 < w_t$, the dimensionless permeability of the channel is given by,

$$k_i(z) = \left(1-\frac{\beta D_0}{Hw(z)}\right). \tag{F.15}$$

In this case, we can analytically calculate the value of ϕ. This expression has different values depending on the value of $\Omega_i = a_i - \beta\frac{D_0}{a_1}$ and b_i. For $|\Omega_i| > |b_i|$, we have,

$$\begin{aligned}\phi_i(z_i, M) = &\frac{M-1}{\sqrt{\Omega_i^2-b_i^2}}\left(\frac{2Lz_i\pi}{H} - 2\arctan\left(\frac{\left(\sqrt{\Omega_i+b_i}-\sqrt{\Omega_i-b_i}\right)\tan\left(\frac{Lz_i\pi}{H}\right)}{\sqrt{\Omega_i+b_i}+\sqrt{\Omega_i-b_i}\tan^2\left(\frac{Lz_i\pi}{H}\right)}\right)\right)+\\ &\frac{1}{\sqrt{\Omega_i^2-b_i^2}}\left(\frac{2\pi L}{H} - 2\arctan\left(\frac{\left(\sqrt{\Omega_i+b_i}-\sqrt{\Omega_i-b_i}\right)\tan\left(\frac{L\pi}{H}\right)}{\sqrt{\Omega_i+b_i}+\sqrt{\Omega_i-b_i}\tan^2\left(\frac{L\pi}{H}\right)}\right)\right)\end{aligned} \tag{F.16}$$

If $|\Omega_i| < |b|$, we have,

$$\begin{aligned}\phi_i(z_i, M) = &\frac{M-1}{\sqrt{b_i^2-\Omega_i^2}}\ln\left(\left|\frac{b_i+\Omega_i\cos(2z_i\pi)+\sqrt{b_i^2-\Omega_i^2}\sin(2z_i\pi)}{\Omega_i+b_i\cos(2z_i\pi)}\right|\right)+\\ &\frac{1}{\sqrt{b_i^2-\Omega_i^2}}\ln\left(\left|\frac{b_i+\Omega_i\cos(2L\pi)+\sqrt{b_i^2-\Omega_i^2}\sin(2L\pi)}{\Omega_i+b_i\cos(2L\pi)}\right|\right)\end{aligned} \tag{F.17}$$

For the case $a = b$

$$\phi_i(z_i, M) = \frac{M-1}{\Omega_i}\tan(z_i\pi) + \frac{1}{\Omega_i}\tan(\pi L). \tag{F.18}$$

If you are reading this and can keep up with the maths, congrats! This took me ages to derive! In the case $w(z) < D_0 \forall z \in [0, H]$, the viscous drop is controlled by the width of the channel, which means that the dimensionless permeability of the channel is given by,

$$k(z) = \frac{H^2}{D_0^2} w(z_i)^2 \left(1 - w(z_i)\frac{\beta H}{D_0}\right). \tag{F.19}$$

Finding an analytical solution for Eq. (F.19) is both long and impractical, and it is instead found by numerical integration using Matlab.

The third case, where the controlling length-scale is alternating between the depth and the width of the channel, has not been developed as it was of no use in the present research, but it would require the use of the full Fourier series, giving the exact solution for the flow of a fluid through a rectangular channel [187].

Solving ψ in rectangular and sinusoidal channels In the dimensionless case, we have,

$$\psi_i(z_i, \Gamma) = \Gamma \int_0^{z_i} \frac{dz}{w_i(z)} + \int_{z_i}^{1} \frac{dz}{w_i(z)}, \tag{F.20}$$

with $w_i(z) = a_i + b_i \cos\left(\frac{2\pi z L}{H}\right)$.

Comparing $\psi(z_i, \Gamma)$ and $\phi(z_i, M)$, we see that their expressions are similar,

$$\begin{aligned}
\phi(z_i, M) &= M \int_0^{z_i} \frac{dz}{\Omega_i + b\cos\left(\frac{2Lz\pi}{H}\right)} + \int_{z_i}^{1} \frac{dz}{\Omega_i + b\cos\left(\frac{2Lz\pi}{H}\right)}, \\
\psi(z_i, \Gamma) &= \Gamma \int_0^{z_i} \frac{dz}{a_i + b\cos\left(\frac{2Lz\pi}{H}\right)} + \int_{z_i}^{1} \frac{dz}{a_i + b\cos\left(\frac{2Lz\pi}{H}\right)},
\end{aligned} \tag{F.21}$$

with, $\Omega_i = a_i - \beta \frac{D_0}{a}$. By replacing M by Γ and Ω_i by a_i, it is clear that one can use Eqs. (F.16), (F.17), and (F.18) to compute the value of $\psi(z_i, \Gamma)$

Appendix G

PHREEQC simulations for the dissolution of calcite

Here is an example of the code used to perform the geochemical solution of the calcite dissolution in the autoclave in Chapter. 9. In Fig. G.1 we present the dissolution kinetics obtained using this code.

```
Kinetic dissolution of calcite with PHREEQC at 65°C

RATES 1
     Calcite               # rate name
     -start
     1 rem M = current number of moles of calcite
     2 rem M0 = number of moles of calcite initially present
     3 rem PARM(1) =A/V, cm^2/L
     4 rem PARM(2) = exponent for M/M0
     10  si_cc = SI("Calcite")
     20 if (M <= 0 and si_cc < 0) then goto 200
     30    k1 = 10^(0.198 - 444.0 / TK )
     40    k2 = 10^(2.84 - 2177.0 / TK)
     50    if TC <= 25 then k3 = 10^(-5.86 - 317.0 / TK )
     60    if TC > 25 then k3  = 10^(-1.1 - 1737.0 / TK )
     70    t = 1
     80    if M0 > 0 then t = M/M0
     90    if t = 0 then t = 1
     100   area = PARM(1) * (t)^PARM(2)
     110   rf = k1*ACT("H+")+k2*ACT("CO2")+k3*ACT("H2O")
     130   rate = area * 1e-3 * rf * (1 - 10^(2/3*si_cc))
     140 moles = rate * TIME
     200 SAVE moles
     -end

KINETICS 1                # Sediment: 100% Calcite, grain size 0.15 mm, por 0.1, rho_CaCO3 2071 k
     Calcite              # rate name
     -formula CaCO3
     -m0 0.004          # initial moles of calcite, measured
     -parms 100 0.66    # parameters for rate eqn. Here: A/V and exponent for M/M0
     -steps 8000 in 8000  # time in s (default)

INCREMENTAL_REACTIONS true # start integration from the previous step
```

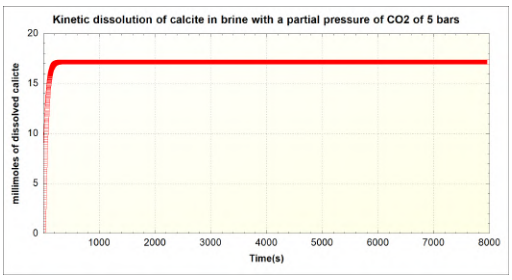

Figure G.1: Results from the kinetics of calcite dissolution obtained with the presented PHREEQC code.

```
SOLUTION 1 salty water
        pH      8.0
        temp    25
 Na 1000
 Cl 1000
 -water 0.016 #kg, volume of water in the autoclave

EQUILIBRIUM_PHASES 1
 CO2(g)  1 # log(PCO2) for this example, the partial pressure of CO2 is 10 bars

REACTION_TEMPERATURE 1
 65.0

SAVE solution 1

END
```

Nathan Bernard

Dynamique du piégeage par capillarité pour le stockage géologique du CO_2 : microfluidique expérimentale et numérique

Résumé :

La capture et le stockage du carbone (CSC) ont été proposés comme l'une des solutions à la crise écologique actuelle. Cette technologie repose sur l'injection de CO_2 dans des réservoirs géologiques souterrains, tels que les aquifères salins ou les gisements d'hydrocarbures épuisés, afin de limiter l'effet de serre. Cependant, le piégeage résiduel, l'un des mécanismes responsables de la rétention du CO_2 en profondeur, reste encore mal compris. Cette incertitude limite notre capacité à évaluer avec précision la quantité de carbone qui peut être stockée dans ces formations géologiques.

Ce travail a pour objectif d'étudier le piégeage résiduel afin de mieux prédire son impact sur le stockage du CO_2 et d'optimiser son efficacité. Pour cela, nous avons combiné des approches expérimentales et numériques pour analyser les écoulements diphasiques dans les milieux poreux. Nous avons introduit la microfluidique ainsi que le modèle du doublet de pores, ou pore doublet, afin de simplifier la description du milieu poreux. À l'aide de ce modèle, nous avons montré que les films mouillants aux parois, qui apparaissent lors des écoulements diphasiques, peuvent influencer la stabilité de l'invasion dans un doublet de pores. Nous avons également mis en évidence que l'inertie, souvent négligée dans l'étude des milieux poreux, a le potentiel de modifier le déplacement du front d'invasion lors du drainage. Enfin, nous avons proposé un protocole expérimental pour étudier comment la mouillabilité de la matrice poreuse est modifiée lors de la présence simultanée de saumure et de CO_2 dans les formations géologiques. Nous pensons que ce travail contribue à améliorer la compréhension des écoulements diphasiques en milieu géologique.

Mots clés : microfluidique, capillarité, diphasique, numérique, doublet de pores

Dynamics of CO_2 trapping by capillarity effects for carbon sequestration: experimental and numerical microfluidics

Summary:

Carbon capture and storage (CCS) has been proposed as a promising solution to the current ecological crisis. This technology relies on the injection of CO_2 into underground geological reservoirs, such as saline aquifers or depleted oil and gas fields, to mitigate the greenhouse effect. However, residual trapping—one of the key mechanisms immobilizing CO_2 underground—remains poorly understood, creating uncertainty about the long-term storage capacity of geological formations.

This work aims to improve our understanding of residual trapping in order to better predict its role in CO_2 storage and to optimize its efficiency. To this end, we combine experimental and numerical approaches to study two-phase flow in porous media. Microfluidics and a pore-doublet model are introduced to simplify the description of pore-scale processes. Using this model, we show that wetting films arising during two-phase flow can significantly affect invasion stability, and that inertial effects, often neglected in porous media, may alter the dynamics of the drainage front. Finally, we propose an experimental protocol to investigate how the wettability of the porous matrix is modified in the simultaneous presence of brine and CO_2.Overall, this work contributes to a deeper understanding of two-phase flow in subsurface environments and provides new insights into the mechanisms controlling the long-term trapping of CO_2.

Keywords : microfluidic, capillarity, two-phase flow, numerics, pore-doublet

Institut des Sciences de la Terre d'Orléans (ISTO)
1A rue de la Férollerie, 45071, Orléans, France